ATOMIC PARITY VIOLATION IN HEAVY ALKALIS: Detection by Stimulated Emission for Cesium and Traps for Cold Francium

Stefano Sanguinetti

UNIVERSITE PIERRE & MARIE CURIE
LA SCIENCE A PARIS

UNIVERSITÀ DI PISA

ATOMIC PARITY VIOLATION IN HEAVY ALKALIS:

Detection by Stimulated Emission for Cesium and Traps for Cold Francium

Stefano Sanguinetti

Laboratoire Kastler Brossel
Dipartimento di Fisica E. Fermi

Advisors

Prof. Ph. Jacquier
Prof. P. Minguzzi

Ph D thesis in Physics, 2004

UNIVERSITE PIERRE & MARIE CURIE
LA SCIENCE A PARIS

UNIVERSITÀ DI PISA

ATOMIC PARITY VIOLATION IN HEAVY ALKALIS:

Detection by Stimulated Emission for Cesium and Traps for Cold Francium

Stefano Sanguinetti

Laboratoire Kastler Brossel
Dipartimento di Fisica E. Fermi

Advisors

Prof. Ph. Jacquier
Prof. P. Minguzzi

Ph D thesis in Physics, 2004

Université Pierre et Marie Curie,
Ecole Doctorale de Physique de la région parisienne ED 107

Università di Pisa,
Scuola di Dottorato Galileo Galilei, XVI ciclo

This Ph D thesis was carried out in France (LKB) and in Italy (Dipartimento di Fisica E. Fermi), under a double-badged ('cotutelle') program between the Université Pierre et Marie Curie and the Università di Pisa.

there. And certainly the glass *was* beginning to melt away, just like a bright silvery mist.

In another moment Alice was through the

From *Through the Looking-Glass and What Alice Found There*, by Lewis Carroll (1872): illustration by John Tenniel.

Contents

Introduction

The thesis work presented in this document deals with atomic parity violation in heavy alkalis: cesium and francium. The first proposal for measuring parity violation (PV) in atoms, with laser spectroscopy techniques, dates back to 1974 [1, 2]. The interest for such experiments comes mainly from the subsequent test of fundamental Physics (Standard Model) provided by this kind of measurements, after elaboration of the results with theoretical atomic structure calculations.

Precisely, the atomic PV measurements allow to probe the effect of the weak neutral currents on atoms. The weak neutral currents and the associated gauge boson Z_0 were predicted by the electro-weak model, in the framework of the Standard Model (SM) (developed mainly around 1960 [3, 4, 5] to 1980 [6, 7, 8]), as a consequence of the gauge invariance: at that time, only the weak charged currents, mediated by the $W^{\pm}$ bosons, had been observed, essentially in the nuclear β decays or in leptons decays, and there was a strong motivation to find experimental evidence for the Z_0 boson. The observation of the neutral currents was made extremely difficult by the smallness of the associated effects, and by their charge-conserving feature which prevented them to play any role in the typical weak interaction decays (such as the well-known β decay), only governed by charged currents effects. In atomic systems, the opportunity to detect neutral currents effects comes from the associated parity violation, inherent to the weak interaction: parity violation turns out to be a necessary powerful signature to discriminate the effect of the weak neutral currents from the preponderant parity conserving electromagnetic interactions.

By now, the weak neutral currents have been experimentally observed in many systems: they have been studied in different processes, like neutrino scattering on matter, or even the direct production of the Z_0 boson by e^+e^- scattering at the LEP collider (CERN). Nevertheless, the interest of atomic parity violation (or APV) did not decrease, because it still allows to probe weak interactions at low energy scales (i.e. at low transferred momentum), providing an important complement to high energy collider searches for physics beyond the Standard Model (see for instance ref. [9] for a recent review about low energy tests of the weak interaction).

Alkalis are very interesting systems for APV experiments, because their atomic structure can be calculated with a very high accuracy. Among the alkalis, cesium and francium are the more suited atoms to perform PV measurements, since the effects of the weak interaction are larger for atoms with heavier nuclei.

Although Cs and Fr are fundamentally very similar (as they are consecutive al-

kalis in the periodic table) the implementation of a spectroscopy experiment has to be quite different for these two elements: Fr has no stable isotopes, therefore it is available only in extremely small quantities from radioactive decays or nuclear reactions, and it is not possible to study it in a simple vapour cell. The first spectroscopic measurements on Fr atoms, in 1978 [10], took advantage of the CERN ISOLDE facility for the production of unstable nuclei. The experiment was set up in such a way that a francium beam, isotopically separated, interacted at right angle with a CW tunable laser. A few years ago, thanks to the new arising trapping techniques, the possibility to spatially confine a sample of cold Fr atoms (with a magneto-optical trap or MOT) led to new high precision measurements of the Fr atomic structure [11]. The MOT allows to reach an atomic density high enough to obtain good signals with laser spectroscopy. Note that trapping techniques can also be applied to cesium atoms, to obtain a cold sample: however, for stable species, the MOT cannot compete with simple vapour cells, for the much lower number of atoms provided, and the consequent lower signal to noise ratio, for a given measurement time. For a Fr MOT, the lower signal to noise ratio with respect to a cesium vapour experiment could be compensated, at least in part, thanks to the higher magnitude of the PV effect, which is expected to be 16-18 times larger [12, 13]. An advantage of a francium PV experiment would also come from the possibility to probe different isotopes, in order to check the dependence of the so called weak charge (by analogy with the electromagnetic charge): the measurements with different isotopes would allow to reduce the uncertainties related to the distribution of the neutrons inside the nucleus.

At the present time, efforts are being done, in Europe (Legnaro) and in the United States (Stony Brook), to implement francium spectroscopy experiments: the main purpose is to maximize the number of atoms collected in a trap, and see if the obtained atomic sample is large enough to undertake parity violation measurements. The situation for parity violation in cesium is much more definite: the first results with a 12% precision were obtained in 1982-84 in Paris [14, 15, 16] and in 1985 in Boulder [17]. From that time, the second generation experiment in Boulder allowed to further improve the precision: also thanks to more accurate theoretical calculations, the total error bar on the weak charge was reduced to the 0.6% level [18]. The Boulder result, which was in slight disagreement with the Standard Model (2.5 σ), stimulated theoretical physicists to refine the cesium atomic structure calculations, which link the APV measurements to the nucleus weak charge Q_W, predicted by the SM. More than ten papers were published on this topic, eventually converging to similar results [19], and reconciliating theory with the experiment (to the 0.5 σ level).

In the light of these recent advances in cesium APV and the increased theoretical interest, this thesis work reports the progress of two spectroscopy experiments, in which the candidate has participated: the first one is the second generation cesium parity violation experiment in Paris (Laboratoire Kastler-Brossel) started in 1991, the second one is the beginning of a francium production and trapping experiment in Legnaro (INFN national laboratories).

The motivation for further PV measurements in cesium is to perform a cross-check of the Boulder result: indeed, such a high-precision measurement deserves to be confirmed with a different method, hence a different problematics of the systematic errors. This kind of measurements, as we are going to see in the development of the thesis, are very delicate, and the estimation of the systematic effects is not straightforward. The agreement between two different experiments would be a further guarantee that the results are free from any significative spurious bias. The pursued goal would be therefore to reach the 1% accuracy, sufficient for a significant comparison with the 0.6% precise result from Boulder.

The specificity of the Paris experiment is the detection technique of the parity violation observable, from the excited cesium atoms, by the stimulated emission process. Let us briefly recall the general principles common to all the cesium PV experiments. The atoms are excited by a laser on a highly forbidden transition ($6S$-$7S$), with the purpose to measure the electric dipole amplitudes (E_1^{PV}), coming from the parity violating mixing of the S levels with the P states (of opposite parity). In order to enhance the excitation rate, and provide an efficient signature of the searched effect, an electric field is applied, which also contributes to the S and P mixing, by Stark effect. We will see then how the parity violation observable comes from the interference of E_1^{PV} with the Stark amplitude. Of course, many schemes are possible (electric field longitudinal or transverse with respect to the laser beam, presence or not of a magnetic field, circular or linear polarization of the excitation beam, etc.), but the review of all the possible detailed configuration is out of our purpose. Let us just mention that there are two kinds of PV observables, according to the chosen experimental configuration:

- the PV is detected in the angular anisotropy of the excited $7S$ atoms which violates the natural symmetry planes of the system;

- the PV is detected as a difference in the excitation rate for two mirror configurations of the experiment (which are typically obtained by changing the polarization of the excitation laser, or the sign of the applied electric field). This case is referred to experiments with polarized atomic samples, like thermal beams (as in Boulder), or atomic polarized traps.

Once we have excited the cesium atoms, providing the parity violation observable, the next step is the PV detection. In the first Paris experiment, this one was based on the polarimetric analysis of the atoms fluorescence: only 0.5‰ of the emitted photons were detected. In the experiment presented here, the detection of the $7S$ is instead based on the stimulated emission effect, on a probe laser tuned to the $7S$-$6P$ transition. By this way, the detection efficiency is much higher, since all the atoms participate to amplify the probe laser, which is then detected in a dedicated polarimeter. Although the general philosophy of the previous experiment is not changed, the recourse to stimulated emission implied drastic modifications of the setup, first of all the need to change from CW laser light to a pulsed regime: thanks to the concentration of the excitation energy in 20 ns long pulses, the obtained

number of $7S$ atoms is large enough to produce a significant amplification of the probe laser.

The recent Boulder setup was radically different: the excitation CW laser, amplified in a high finesse Fabry-Perot cavity, was sent orthogonally to a polarized cesium thermal beam in the F hyperfine ground state ($F = 3$ or 4). The interesting observable is the number of excited atoms: in practice, only the ones which decay to the other hyperfine ground state F' are detected, when they arrive in the detection area and scatter the photons from a probe laser, opportunely tuned on a cycling $6S, F' - 6P_{3/2}, F''$ transition. The photodetector can thus collect many fluorescence photons scattered by each F' atom, therefore reaching a high global detection efficiency.

We will see that a remarkable feature of the detection by stimulated emission, is the characteristic exponential amplification of the detected PV asymmetry with the applied electric field E: for all the other performed experiments, with fluorescence detection, the PV observable decreases instead as $1/E$.

The goal of the Paris experiment, presented here, is to reach the 1% precision for the measurement of the weak charge of cesium. In this thesis, we report a preliminary measurement, with a 8.4% relative statistical error, which confirms the validity of our detection method. We will see that this measurement was made possible thanks to a new kind of cells, with their internal surface grooved, in order to inhibit the secondary multiplication of electrons which are emitted from the windows, following the application of the excitation laser pulse. The detailed analysis of the acquired data is presented, along with the checks for systematic errors. A qualitative analysis is reported concerning the effect of unwanted electric and magnetic fields in the cell, giving rise to anisotropies in the signals, according to the direction of the excitation laser polarization: some analysis techniques were developed, in order to estimate the impact of these fields on the measurements. A discussion is given about systematic errors within the present accuracy level. Finally, indication is given about the way to reach the experimental conditions to obtain a signal to noise ratio which will allow to achieve the 1% precision. One of the most important advances is the introduction of a dichroic element before the polarimeter, which amplifies the polarization tilts.

Unlike the Paris experiment on cesium, the francium experiment at Legnaro laboratories is in its beginning phase: in these first years, we managed to reach the conditions for a good rate production of francium isotopes, and set up a beam line to convey the francium into a MOT cell. We observed the francium MOT in several measurement runs. Further improvements of the setup will allow to meet all the experimental conditions for a high efficiency trapping of the relatively low francium flux entering the cell and a direct optimization of the MOT with the francium fluorescence signals. We are not yet ready to start a francium parity violation experiment, but this does not prevent us to make some preliminary considerations, and try to understand which could be the requirements on our francium sample for this kind of measurement.

Although the experimental conditions for the spectroscopy of francium and cesium are quite different (cold small atomic cloud vs hot extended vapour), the general

lines for the implementation of PV measurements remain common to the two considered elements. Also in Francium the PV observable to be detected will be a very small dichroism, or emitted light polarization, which violates the natural symmetry planes of the experiment. As for cesium, we suppose that the most efficient way to obtain acceptable signals on the highly forbidden $7S$-$8S$ transition will be to enhance the excitation rate by applying an electric field, whose reversal will also be an important signature for the PV observable to be measured. Hence, all the knowledge concerning the precise control and definition of the laser polarizations, and the high precision PV spectroscopy, applied to cesium, will be extremely valuable for a PV experiment on francium. Only the setup for the preparation of a good atomic sample differs completely for cesium and francium: on the one hand, a vapour cell with a sophisticated heating system, with control feedback of the temperatures in different areas of the cell; on the other hand, an accelerator facility and laser trapping setup.

In this thesis are then also discussed basic considerations on how the PV techniques, which proved to be successful for cesium, can be transposed to the somewhat different situation of a cold atomic radioactive sample. It is of primary importance to understand what can be the best scheme for an efficient francium PV measurement and how to exploit the present Legnaro facilities to reach the experimental conditions which will allow an acceptable signal to noise ratio. Before bringing a definite answer to these questions, the present Legnaro experiment must still make further progress. However, considering other experiments about stable atom trapping, and the last results in the Stony Brook francium experiment (which began a few years before Legnaro's experiment), it is possible to conclude that a francium PV measurement is not out of reach, in the following years. All the progress made in Legnaro on this topic will be discussed in detail, with a complete experimental characterization of the stages which lead from the production of francium by nuclear reactions in a gold target, to the transport of the isotopes into the MOT cell, and their successive trapping.

Chapter 1

Elements of parity violation theory in atoms

1.1 Weak interactions in atoms

There are different contributions of the weak interaction between electrons and nucleons, in atoms. The parity conserving terms do not play any role, because they are an absolutely negligible perturbation to the atomic structure imposed by electromagnetic interaction, with the same symmetry properties.

The dominant contribution of the weak interaction in heavy atoms is given by its axial-electronic vectorial-nuclear term (see fig. 1.1), which is, in the non relativistic approximation [1, 2]:

$$V_1^{PV} = \frac{G_F}{4\sqrt{2}}\, Q_W\, \frac{\boldsymbol{\sigma}\cdot\mathbf{p}}{m_e c}\, \rho_N(\mathbf{r}) + h.c.,$$

where

- G_F is the Fermi constant,
- $\boldsymbol{\sigma}$ is the electronic spin operator (Pauli matrices),
- $\mathbf{p}$ is the electronic momentum,
- $\rho_N(\mathbf{r})$ is the electric nuclear charge density, normalized to one,
- Q_W is the so called weak charge of the Cesium nucleus, by analogy with the electric charge definition for the electromagnetic interaction.

It is easy to see that this is a pseudo-scalar potential, which violates the parity symmetry.

The Standard Model [6, 7, 8] provides the value of Q_W: at the first order,

$$Q_W = Z(1 - 4\sin^2\theta_W) - N, \tag{1.1}$$

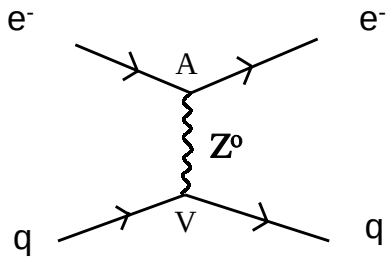

Figure 1.1: Feynman diagram for the dominant term of the weak interaction in atoms: axial electronic current and vectorial hadronic current. Z^0 is the boson for the neutral weak currents.

where Z is the number of protons of the nucleus, N is the number of neutrons, and θ_W is the angle of Weinberg ($\sin^2\theta_W \simeq 0.23$). We note that the weak charge is carried essentially by the neutrons.

1.2 Manifestation of the parity violating weak interaction

We can consider the atom as a quantum system governed by a hamiltonian with a parity conserving leading term H_0 and a very small parity violating term H_1. In such a system, the only parity violation (PV) effect which can be measurable is the very weak mixing of opposite parity eigenstates of H_0, coming from the perturbation H_1.

During a laser transition in the atom, this weak mixing manifests itself as a small parity violating term A^{PV} in the amplitude transition expression, which interferes with the parity conserving amplitude A^{PC}. The transition probability is then given by:

$$P^+ = |A^{PC} + A^{PV}|^2 = |A^{PC}|^2 + 2\Re e(A^{PC}A^{PV*}),$$

at the first order in A^{PV}.

If we make the same experiment with a mirror symmetry configuration, we will have:

$$P^- = |A^{PC} - A^{PV}|^2 = |A^{PC}|^2 - 2\Re e(A^{PC}A^{PV*}).$$

The interference term has changed sign because A^{PC} and A^{PV} have opposite behaviour under parity symmetry. The two probability transitions are then different, and we can define the left-right asymmetry as:

$$A^{LR} = \frac{P^+ - P^-}{P^+ + P^-},$$

which is equal to

$$A^{LR} = 2\frac{A^{PV}}{A^{PC}}.$$

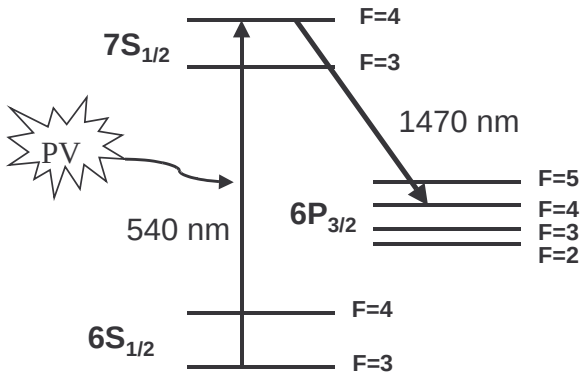

Figure 1.2: The atomic levels of Cesium for our PV measurement.

The parity violation experiment is then a measurement of the asymmetry in the results given by two parity-symmetric experimental configurations.

The order of magnitude of A^{LR} for example in hydrogen is of the order of 10^{-15} [20], and until now this is too small to be measured. Of course, it is preferable to choose a system and experimental conditions for which the asymmetry is the highest one: we have to try to exalt A^{PV} and minimize A^{PC}.

Choice of the cesium atom: M.A. and C. Bouchiat have shown that the weak amplitude in the atoms goes with Z^3, and even slightly more (Z is the atomic number) [1]. This means we are interested in heavy atoms. However, precise calculations about atomic structure are necessary in order to deduce from the A^{LR} measurement a test of the Standard Model. This is why it is preferable to use an alkali atom, for which calculations now reach a precision of at least 1%. As a consequence, we are led to use Cesium, which is the heaviest alkali atom, with one stable isotope ^{133}Cs.

Another interesting possibility is to use Francium, the heavier alkali atom, which has no stable isotope, but for which the PV effect is expected to be 16-18 times larger [12, 13]. In that case, it is necessary to produce the radioactive Fr with a nuclear reaction, and then to collect the few Fr atoms with an efficient trapping system. The main problem will be to reach a significant number of atoms in order to have a detectable signal on the $7S$-$8S$ forbidden transition. The Fr production has been achieved at the INFN National Laboratories in Legnaro, allowing to perform the first tests for the collection of Fr atoms in a magneto-optical trap.

Choice of the atomic transition: In order to have A^{PC} as smallest as possible, we choose a transition which is highly forbidden. The $6S \rightarrow 7S$ transition (see fig. 1.2) is optimal for this purpose, because it is doubly forbidden: the electric dipole moment between these two states is zero, as well as the magnetic dipole moment, in first approximation, since the radial wave functions $6S$ and $7S$ are or-

thogonal. We have a 14 orders of magnitude depression factor, with respect to a typical electric dipole transition.

1.3 Choice of the PV observable

In this section we present our experimental configuration for the cesium PV measurement on the $6S$-$7S$ transition. In particular we show how useful is the application of a large static electric field.

1.3.1 Effective transition dipole

The general form of the effective transition dipole, imposed by parity and time reversal symmetries, is given by [1]:

$$\boxed{\mathbf{d}^{eff}_{6S,F-7S,F'} = -\alpha\mathbf{E} - i\beta\boldsymbol{\sigma}\times\mathbf{E} + M'_1\boldsymbol{\sigma}\times\hat{\mathbf{k}}_\mathbf{L} - i\,\Im m(E_1^{PV})\,\boldsymbol{\sigma}} \tag{1.2}$$

where

- σ_i are the Pauli matrices, which operate on the electron spin,
- $\hat{\mathbf{k}}_\mathbf{L}$ is the wave vector of the excitation laser,
- α is the scalar polarizability,
- β is the vectorial polarizability,
- $M'_1 = M_1 + M_1^{hf}(F'-F)$ is the magnetic dipole moment,
- E_1^{PV} is the amplitude of the transition dipole between $6S$ and $7S$, due to the weak neutral currents.

It is easy to see that the term involving E_1^{PV} is a pseudo-vectorial quantity, whereas the other ones are true vectors, and hence the E_1^{PV} dipole violates the parity symmetry.

The effective transition dipole allows to calculate all the features of the $|7S,F'\rangle$ states (population, orientation, alignment) after laser excitation, with given polarization and electric field.

1.3.2 Atomic anisotropy after excitation

Thanks to the expression (1.2), it is possible to calculate the density matrix ρ of the $7S$ state. It is not difficult to see that with a circularly polarized excitation light, the excited atoms acquire an orientation ($Tr(\rho\mathbf{F})/Tr(\rho)$). With a linearly polarized pump, the excited atoms acquire an alignment[1] (we remind that the alignment of

[1]Rigorously, the alignment is given by five quantities which form a tensor of rank 2 (hence, in the geometrical space, it can be seen as an ellipsoid with three principal axes). Nevertheless, it is simpler to talk about an alignment along two orthogonal axes, to design actually a component of the tensor.

axes $(\hat{x}, \hat{y})$ is defined by $\frac{<F_x^2 - F_y^2>}{<F_x^2 + F_y^2>}$). The main formulas which allow to calculate these quantities are included in ref. [21] and [22].

In our setup, we decided to use a longitudinal electric field $\mathbf{E} = E_z \cdot \hat{z}$ and a linear excitation polarization, for example $\epsilon_{ex} = \hat{y}$. If we neglect the small magnetic dipole, we have according to (1.2):

$$\mathbf{d}^{eff} \cdot \hat{\mathbf{y}} = i\beta\sigma_x E_z - i\Im m(E_1^{PV})\sigma_y = i\beta E_z \left(\sigma_x - \frac{\Im m(E_1^{PV})}{\beta E_z}\sigma_y\right). \tag{1.3}$$

Stark alignment The first term (in σ_x) leads to the main alignment of the excited atoms, which can be seen as a revolution ellipsoid with axis $\hat{x}$. This alignment respects the symmetry planes of the experiment, given by the field E_z (or the wave vector $\mathbf{k}_L$) and the linear polarization $\hat{\epsilon}_{ex}$.

PV alignment The second term (in σ_y) leads to the so called PV alignment by interference with the first term. Looking at the right hand side of equation (1.3), it is easy to see that the total alignment is characterized by the same magnitude as the Stark alignment, but with the eigenaxis $(\hat{x} - \frac{\Im m(E_1^{PV})}{\beta E_z}\hat{y})$ instead of $\hat{x}$. This corresponds to a rotation of the Stark alignment axis by the small angle $\boldsymbol{\theta^{PV} = -\frac{\Im m(E_1^{PV})}{\beta E_z}}$ in the transverse plane, which breaks the symmetry of the experiment. It is fundamental to realize that the θ^{PV} angle changes sign when we reverse the applied electric field: this feature gives a powerful signature for the PV measurement, as will be emphasized in the next chapter.

Another way to understand the situation is to say that the PV effect consists in providing, in addition to the Stark alignment with axes $(\hat{x}, \hat{y})$ in the transverse plane, a small second alignment with axes $(\hat{u}, \hat{v})$, turned 45° from $(\hat{x}, \hat{y})$.

Since $\Im m E_1^{PV}/\beta \simeq -2$ mV/cm, with an applied electric field of 2 kV/cm magnitude, θ^{PV} is about 10^{-6} rad.

1.3.3 Detection of the alignment by stimulated emission

The specificity of our experiment, with respect to traditional PV measurements, is to detect the anisotropy of the excited atoms not by collecting fluorescence photons, but using the stimulated amplification of a probe laser tuned on the $7S \rightarrow 6P_{3/2}$ resonance. By this way the atoms emit all the stimulated photons in the same direction, so that we can collect all of them for our PV measurement.

Linear dichroism and birefringence arising from alignment

When propagating in the excited vapour, not only is the probe beam amplified by stimulated emission, but also its polarization is modified by the alignment anisotropy of the atoms: the alignment generates linear dichroism and birefringence. Let us consider the ellipse resulting from the intersection of the ellipsoidal representation of the alignment tensor and the plane normal to the wave vector of the probe beam. The

eigenaxes of the optical anisotropies (dichroism and birefringence) are given by the axes of this ellipse. When we fix the frequency of one laser and change the frequency of the other one, in the absence of magnetic field, the birefringence is dispersive-shaped whereas the dichroism is absorption-shaped (cf. Kramers-Krönig relations). As a consequence, the dichroism is maximum at the center of the resonance, hence it will be the quantity of interest for our PV measurement.

In our experimental setup, the probe and the excited beams are collinear, so that the dichroism axes are given by the two alignment axes in the transverse plane. Again, we find that the Stark alignment generates a linear dichroism with axes $(\hat{x}, \hat{y})$, and the PV effect is to tilt these axes by the angle θ^{PV}. We can also say that the PV alignment introduces an additional small linear dichroism with axes $(\hat{u}, \hat{v})$.

The best way to measure linear dichroism is to have a linear probe polarization, which possibly rotates when passing through the vapour. We will see in the next chapter how to measure very small polarization rotations (of the order of 10^{-6} rad).

Jones formalism for small optical anisotropies

It is useful for the following chapters to introduce the general expression of the matrix $\mathcal{M}$ which gives the relation between the Jones vector $\hat{\epsilon}_{in}$ for the initial polarization in the base $(\hat{x}, \hat{y})$, and $\hat{\epsilon}_{out}$, the polarization after the passage in a slightly anisotropic medium [23]:

$$\hat{\epsilon}_{out} = \mathcal{M}\ \hat{\epsilon}_{in},$$

with

$$\mathcal{M} = \mathbb{1} + (\gamma_1 + i\alpha_1)\sigma_1 + (\gamma_2 + i\alpha_2)\sigma_2 + (\gamma_3 + i\alpha_3)\sigma_3,$$

where $\mathbb{1}$ is the unit matrix and σ_i are the Pauli matrices[2].

If we set $\hat{u} = (\hat{y} + \hat{x})/\sqrt{2}$ and $\hat{v} = (\hat{y} - \hat{x})/\sqrt{2}$, we have the following physical interpretation for the real coefficients α_i and γ_i:

- $2\alpha_1$: linear birefringence with axes $(\hat{u}, \hat{v})$,
- $2\gamma_1$: linear dichroism with axes $(\hat{u}, \hat{v})$,
- $2\alpha_2$: circular birefringence (or optical activity),
- $2\gamma_2$: circular dichroism,
- $2\alpha_3$: linear birefringence with axes $(\hat{x}, \hat{y})$,
- $2\gamma_3$: linear dichroism with axes $(\hat{x}, \hat{y})$.

In the following, we will frequently use this terminology to mention these optical anisotropies. We can say that the Stark alignment generates a relatively large γ_3 effect at resonance, while the PV alignment generates a small γ_1 effect, which would be forbidden were the parity conserved.

[2]Pauli matrices: $\sigma_1 = \begin{pmatrix} 0 & 1 \\ 1 & 0 \end{pmatrix}$, $\sigma_2 = \begin{pmatrix} 0 & -i \\ i & 0 \end{pmatrix}$, $\sigma_3 = \begin{pmatrix} 1 & 0 \\ 0 & -1 \end{pmatrix}$.

Chapter 2

Parity violation detection in a cesium cell: strategy and preliminary results

In this chapter we describe the Paris experiment setup with its latest modifications, which should allow to measure the atomic Parity Violation (PV) of Cesium in a vapour cell with high precision: the ultimate purpose is to reduce to 1% the error on the final result. We report our experimental advances, which consented to perform a first measurement of the parity violation detected by stimulated emission, with a 8.4% relative statistical precision [24]. This preliminary result demonstrates the validity of this new method, and outlines the road map to reach the 1% precise experimental PV value.

2.1 Principle

As we have already seen, this experiment, performed on the $6S_{1/2}$-$7S_{1/2}$-$6P_{3/2}$ transition in a dense cesium vapour, is of the pump-probe kind. The way to reach the pump energy necessary to achieve a significant amplification of the probe laser is to operate in a pulse mode. The applied longitudinal electric field makes the transition slightly allowed, in addition it provides a valuable signature for the PV detection.

2.1.1 Experimental setup

The lasers

The probe laser @1.47 μm This laser is used to probe the $7S_{1/2} \rightarrow 6P_{3/2}$ transition, after pumping from $6S_{1/2}$ to $7S_{1/2}$ with our pulsed green laser @539 nm. It is a color-center laser (NaCl crystal doped with OH^-, irradiated by UV light), pumped by a Nd:YAG. Usually we have about 100 mW continuous power, single mode radiation, with a jitter reduced to 1 MHz thanks to a short term stabilization on an external Fabry-Perot cavity.

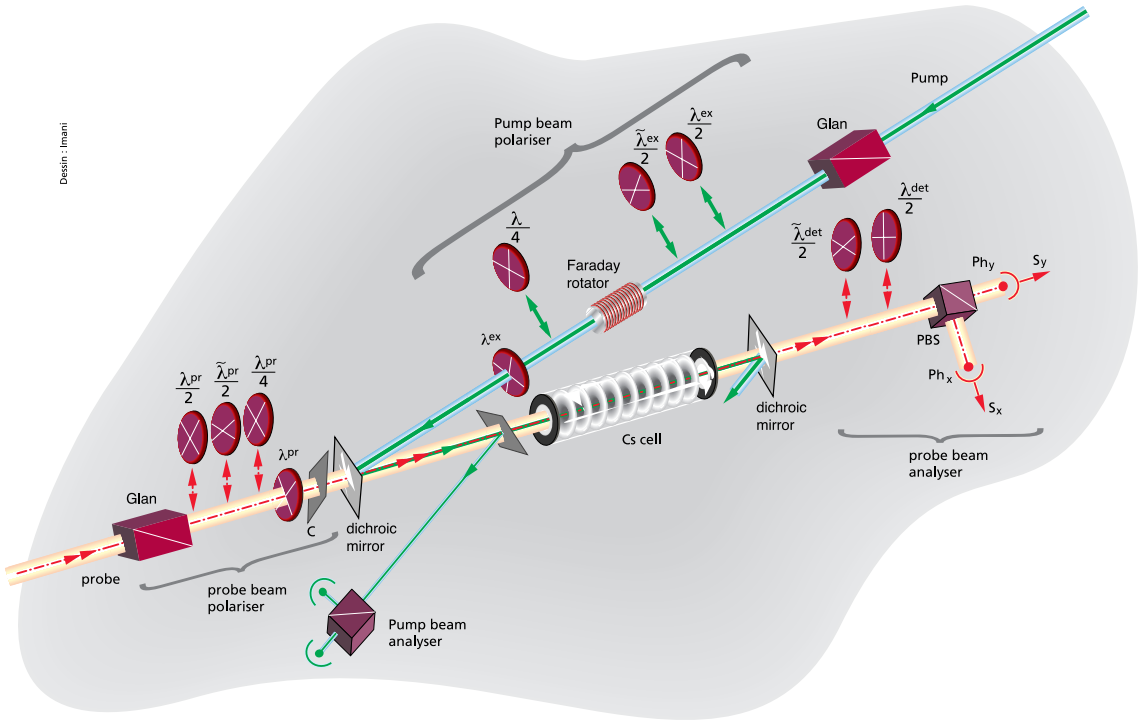

Figure 2.1: Optical elements for polarization selection, control and analysis, after [26].

A dedicated servo-lock system with a separate Cesium cell allows to stabilize the laser on the hyperfine atomic lines. In practice we always use the F=4→F=4 or the F=4→F=5 transitions, for reasons developed in the next paragraphs (2.1.2 and 2.1.3). The efficiency of the stabilization is of the order of a few megahertz.

In order to obtain short-time 20 ns square pulses from this continuous laser, the probe beam is gated by a very fast (sub ns) optical switch ($LiNbO_3$ electro-optic modulator), which is driven by low voltage (about 15 V) pulses. The 20 ns value comes from the importance to restrict our detection to the lifetime of the $7S$ excited state, during which there is amplification of the probe[1]. The extinction ratio is better than 10^{-3}, whereas the transmission when the switch is open is 8%. The number of photons detected at each outgoing pulse is about 5×10^7 in typical conditions.

The excitation laser @539 nm

In order to produce a 539 nm continuous-wave light beam, we use a tunable ring dye laser (Rhodamine 560) pumped by an Ar^+ laser @514 nm. The dye laser system can produce 200 mW continuous single-mode radiation with a jitter below 1 MHz. This

[1]The natural lifetime of the $7S$ state is 48.5 ns [25]. In the presence of the probe beam, at our typical incident intensity, it is reduced to about 20 ns.

beam is then amplified in a pulsed mode by three dye cells (Coumarine 540) pumped by UV pulses, delivered by a XeCl excimer laser. By this way we obtain 15 ns long pulses @539 nm, with an energy of typically 1.5-2 mJ, in the range 90-200 Hz. Due to the appearance of geometrical instabilities, it was not possible during this thesis work to operate at more than 150 Hz[2]. The spectral bandwidth of the pulses is close to the Fourier transform limit (30 MHz FWHM).

The polarizations

In the fig. 2.1 it is possible to see the essential optical elements of the heart of the PV experiment. The polarization of the incoming beams is first defined by two Glan prisms, one for each beam. Then, a set of switchable half-wave plates allows to rotate the excitation and probe polarizations by $45°, 90°$ or $135°$, before and after the passage in the cell. We will see that this feature is very useful to check the rotational symmetry of our apparatus.

It is possible to insert a quarter-wave plate into the path of each beam in order to produce circular polarization, which can be useful for some control measurements.

A Faraday rotator is used to perform tiny polarization tilts of the incoming excitation light. We will see that this is essential for the calibration of the PV effect.

Whole-wave plates with adjustable orientation compensate the birefringence produced on the path of the beam, essentially by the entrance cell window, and so cancel the helicity of the beams inside the cell.

The electric field

In order to assist the forbidden excitation transition $6S \rightarrow 7S$, we apply a longitudinal electric field. The use of a cell made of alumina, a dielectric insulating material, made it possible to use external electrodes to apply the field. The set of eleven annular electrodes is inserted inside an "internal" oven which is used to hold and heat the body of the cell (see fig. 2.2) [27].

A numerical simulation was performed by M.A. Bouchiat for the field map. Fig. 2.3 represents the equipotential lines of the field calculated on a 600×600 points grid for a quarter of the cell. The sapphire ring extends the alumina tube over the window and makes the electric field more homogeneous near the end of the cell. The variation of E_z along the axis of the cell does not exceed one percent; all over the interaction region, the standard deviation of E_z is 3×10^{-4} and the standard deviation of the radial field is 8×10^{-4}.

The electric field in the cell cannot be kept for too long, in order not to create discharges in the vapour. Hence, we have to use a pulsed high voltage (HV) ($\tau < 0.2\ \mu s$) which is applied by a system formed by a HV supply (10 kV maximum), two HV switches for the two ends of the cell and two decoupling capacities. A resistance

[2]The limitation came from the dye flow into the amplification cells. Since the end of this thesis, it was overcome thanks to the use of a more powerful pump for the circulation of the dye into the main amplifier cell.

bridge distributes the voltage over the eleven annular electrodes, the central one being connected to ground. By this way we can produce trapezoidal pulses of both signs, with a constant amplitude plateau over a time much longer than the duration of the laser pulses (usually 150 ns), so that the electric field can be considered static

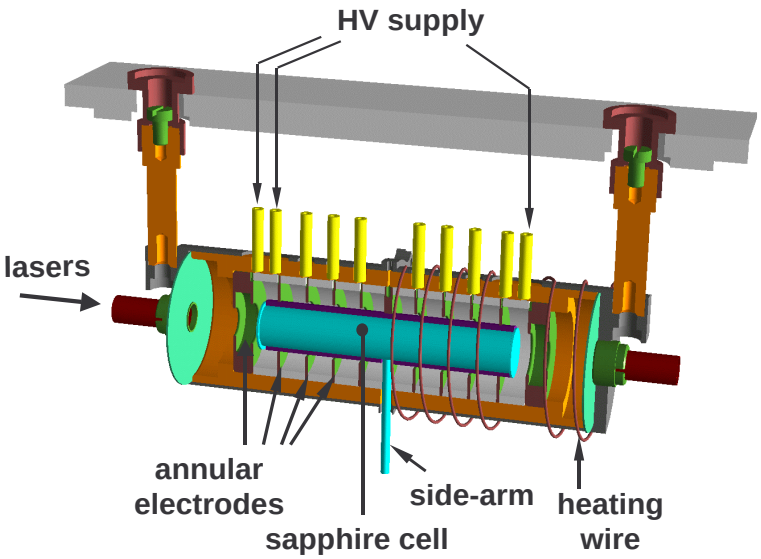

Figure 2.2: The internal oven, after [27].

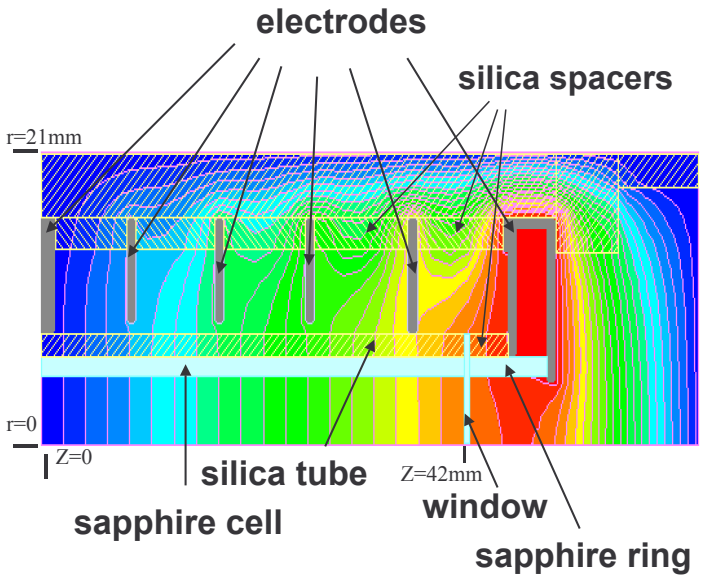

Figure 2.3: Equipotential lines of the electric field, for a quarter of the cell (numerical simulation), after [27].

for the excitation process.

During the measurements, we use to apply ±8100 V, which, according to the simulation, correspond to an electric field of about 1730 V/cm.

Moreover, in E. Jahier's thesis [28], a procedure was developed which allows to calibrate the E field seen by the atoms thanks to atomic signals analysis (paragraph 2.3.5). The typical 5% difference with respect to the previous nominal value comes from the appearance of a space charge in the cell (cf. next paragraph).

The cell

As we already said, our experiment is performed on a cesium vapour contained in a cylindrical cell, 8 cm long (see fig. 2.4). The advantage with respect to an atomic beam or a trap is the high atomic density and the high number of atoms interacting with the lasers. The typical atomic density in our cell is 2×10^{14} atoms/cm^3, i.e. 2×10^{13} atoms in the interaction region. About 10^{12} atoms have such a velocity to be resonant on their $6S$-$7S$ transition with the excitation pulsed beam (30 MHz spectral width). At this density the $7S$ state is nearly unperturbed by Cs-Cs collisions. The $7S$-$6P$ transition dipole begins to be damped but the typical damping rate $1/(14$ ns) is not prejudicial to good resolution of the $6P_{3/2}$ hyperfine structure. The cylindrical shape of the cell allows to respect the revolution symmetry as far as possible: the latter is broken only by the tube in which the cesium is collected, and by the wires which bring the voltage to the annular electrodes. Nevertheless, the reflection symmetry with respect to the vertical plane is totally preserved.

In the first years of this PV experiment, glass cells with internal electrodes were used. In the required experimental conditions, these cells give rise to serious problems. In particular, with intense green laser pulses and a large applied electric field,

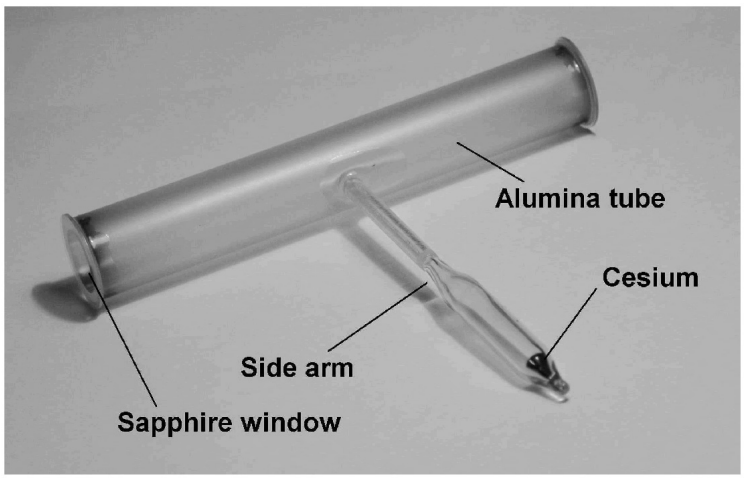

Figure 2.4: Photo of our alumina cell.

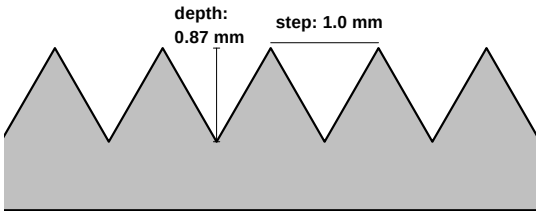

Figure 2.5: Profile of the grooved machined on the inner wall of the alumina tube.

the glass windows in contact with the cesium vapour show the appearance of dark spots, and lose their good transparency much too fast to allow for long measurement times. The other problems associated with this kind of cells are developed in [28] and [29].

A good alternative to the glass cells is to use another material: alumina. Our new cells are made of an alumina tube, at the end of which two sapphire windows have been glued (sapphire is the monocrystalline form of alumina)[3].

A complete study of the improvements and limits obtained by using sapphire cells in the current PV setup was done in E. Jahier's thesis [28]. In particular, the windows did not show any damage after many hours of measurements. Another important feature is that the resistivity of alumina is very high, even with cesium inside the cell, so that currents around the body of the cell are very small. We will see that this kind of currents could generate magnetic fields which mimic the parity violation effect.

On the other hand, an important problem which arose with the use of alumina cells was the emission of electrons from the windows hit by the intense green laser pulses. It was shown in ref. [30] that these primary electrons are amplified by secondary emission when they hit the alumina tube. This effect generates large space charge effects, which prevent serious PV data acquisition.

We will see in this thesis that a good remedy for this problem has been to groove the inner surface of the alumina tube (see fig. 2.5) [30]. Indeed, the cross-section for secondary electronic emission is particularly large at grazing incidence. In the "saw tooth" alumina tube, the primarily electrons hit the alumina surface at quasi normal incidence, hence the most part of them are stopped inside the material, thus hindering multiplication.

[3]These cells were realized by the group of D. Sarkisyan at the Institute for Physical Researches, Ashtarak, Armenia.

The internal and external ovens

In order to reach the desired density of atoms, we have to heat cesium to increase the vapour pressure. Actually, it is very important to be able to keep the temperature of the cell body higher than that of the side-arm, in order to thermally destroy the cesium dimers, which are always present for chemical equilibrium reasons ($Cs+Cs \leftrightarrows Cs_2$), and could be harmful for the PV measurements (cf. paragraph 2.4.2) [31]. Then, the temperature of the side-arm (which can be considered the "cold" finger of the cell, where the liquid part of cesium accumulates), defines the cesium vapour density.

For the separate control of the two temperatures, the heating system is composed of two ovens, called "internal" and "external". The internal oven (fig. 2.2) contains the set of eleven annular electrodes and the body of the cell, and let the side-arm out thanks to a proper small hole. The typical operating temperature, for a good suppression of dimers, is 220°C (for a side-arm temperature of about 140°C). Really, the internal oven itself is divided into two halves, each one having an independent heating thermocoax wire, in order to be able to create longitudinal temperature gradients. The purpose is to separately control the temperatures of the entrance and exit windows of the cell: we will see in paragraph 2.3.2 how this temperature tuning allows to reach, for each window, very high transmissions of the excitation laser beam, thanks to Fabry-Perot interference effects.

The internal oven is then placed inside a bigger structure, the external oven, which has been thermally insulated from outside. The external oven allows to control the side-arm temperature, kept around 140°C, and to preheat the internal oven.

The magnetic field

The stray magnetic field is compensated with the fields produced by three pairs of Helmholtz coils along the three cartesian axes $\hat{x}, \hat{y}, \hat{z}$, the last one being the axis of the cell. Other coils are used to compensate the gradient of the field along $\hat{z}$. The residual magnetic field variations over the length of the cell are of the order of 1 mG.

In order to perform control measurements about electric and magnetic fields, we must be able to apply substantial magnetic fields (of the order of 2 gauss). This is carried out by three extra pairs of coils.

The polarimeter

Parity violation is to be measured via an atomic polarization signal, namely a rotation of the polarization of the probe beam by about 1 μrad. In order to measure such a small signal, we make use of a differential polarimeter. In practice, the probe beam, after passage in the cell, falls on a polarizing beam-splitter cube (see fig. 2.6). The intensities of the two split beams are then measured by two photodiodes. The axes of the cube are tilted by 45° with respect to the probe polarization before the cell, so that the difference between the two channels is zero when there is no anisotropy. A small tilt ψ of the linear polarization of the probe beam is detected as

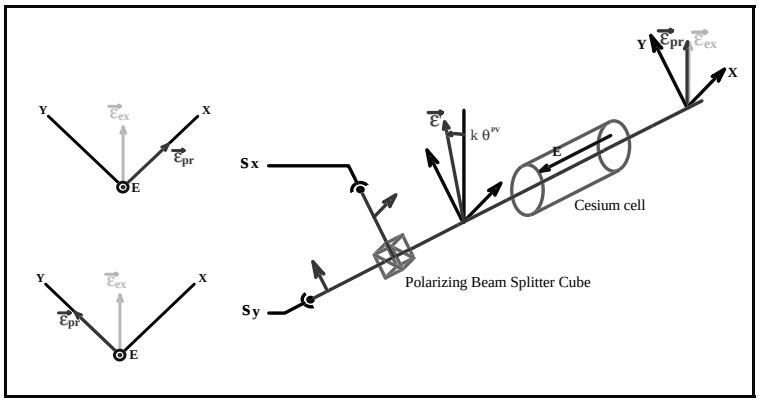

Figure 2.6: Differential polarimetry.

an imbalance of the signal received by the photodiodes. If we define the normalized imbalance D as

$$D = \frac{S_X - S_Y}{S_X + S_Y}$$

where S_X and S_Y are the signals of the photodiodes for the two channels of the polarimeter, we have at the first order

$$D = 2\psi.$$

Data acquisition

The analog signals coming from the photodiodes have to be numerically converted in a very accurate way. To this end, we use the following scheme for the data acquisition electronics: for each channel of the polarimeter, a low-noise pre-amplifier which integrates the charges, an amplifier (*Ortec*), a stretcher circuit (*Tennelec*), and a 14 bits analog to digital converter (ADC). The collection of the digital signals is then entrusted to an acquisition interface card (PIA) and an acquisition PC. This kind of electronics comes in part from the particle physics field [32].

Note that the two polarimeter channels are kept separate until the end of the acquisition process: we have two distinct electronic channels (for the amplification and the digital conversion), which are kept as symmetric as possible with respect to each other. The sum $S_X + S_Y$ and the difference $S_X - S_Y$ are then performed on the acquired data, by the computer processor, to extract the imbalance D.

2.1.2 Detection of the alignment of the cesium atoms by the stimulated emission process

PV signature and calibration

We saw in paragraph 1.3.2 that following the excitation process the cesium atom acquires a relatively large alignment. For symmetry reasons, in absence of parity violation, the axes of this Stark alignment would be exactly collinear with the natural axes of the experiment, i.e. the polarization of the green laser, the longitudinal electric field and the axis orthogonal to the previous ones. Actually, we saw that the effect of the parity violating interaction is to tilt the alignment axes in the plane orthogonal to the electric field direction. We will see in this paragraph how the rotation of the amplified probe laser polarization caused by the passage in the excited cesium vapour can give all the information about the alignment tilt.

For our experimental conditions, the angle θ^{PV} of the tilt to be measured is expected to be about 1 μrad. So tiny an angle is extremely difficult to measure: it is not even possible to define the excitation laser absolute polarization to better than 100 μrad. However, an important feature is that the tilt direction of the alignment axes depends on the sign of the applied electric field. For the experimentalist, the interesting parameter is no longer the absolute angle between the green polarization and the alignment axes, but the change in the alignment axes angle θ when we reverse the electric field, which is possible to measure.

Moreover, this kind of measurement leads immediately to a straightforward calibration procedure. Let us suppose that we have a signal S which is linear in θ, no matter whether it comes from stimulated emission of a probe laser or not:

$$S = K \cdot \theta.$$

We want to know how much is K in order to deduce from the measurement of $(S(E+) - S(E-))$ how much is $(\theta(E+) - \theta(E-) \equiv 2\ \theta^{PV})$, where $E+$ and $E-$ stand for positive and negative electric field. Now there is another very simple way to tilt the alignment axes, with a known angle θ^{cal}: we just rotate the polarization of the excitation laser by θ^{cal}. If we measure the corresponding change S^{cal} of our signal, the ratio S^{cal}/θ^{cal} gives K.

This is the basic principle for the parity violation measurement in cesium, in the longitudinal electric field configuration. We see that the reversal of the electric field is the most powerful signature for the PV measurement.

Linear dichroism during stimulated emission

Let us see now how it is possible to measure the features of the Cesium atoms alignment, with our probe laser. We saw in the previous chapter that the alignment manifests itself as a linear dichroism and a linear birefringence with the same axes, on the incident linearly polarized probe light which is amplified by stimulated emission. With our experimental conditions, the wave vector of the probe laser and the axis $\hat{z}$ of the alignment tensor are collinear. Hence, the optical anisotropy axes for the

probe laser are precisely given by the axes of the alignment lying in the transverse plane (cf. paragraph 1.3.3). If the excitation polarization is vertical ($\hat{y}$ direction), the Stark alignment creates, for the probe laser, a linear dichroism $(\hat{x}, \hat{y})$ (denoted γ_3). The parity violation effect is to tilt these axes by the tiny angle $\pm\theta^{PV}$. We can say that parity violation introduces a linear dichroism γ_1 with axes $(\hat{u}, \hat{v})$ turned 45° from $(\hat{x}, \hat{y})$, which is proportional to θ^{PV} (and changes sign when the electric field is reversed). Furthermore, it is easy to see that the effect of this PV dichroism is to tilt the probe laser polarization by an angle ψ_{pr} which is proportional to γ_1 (cf. fig. 2.7). ψ_{pr} is then measured by our polarimeter. Hence, we have for the measured imbalance D:

$$D_{PV} = 2\psi_{pr} = K \cdot \theta^{PV}.$$

Of course, K is not easy to compute; it depends on the hyperfine probe transition, and on the polarizations configuration (para, $\hat{\epsilon}_{probe} \parallel \hat{\epsilon}_{excitation}$ or ortho, $\hat{\epsilon}_{pr} \perp \hat{\epsilon}_{ex}$) too. It also depends on saturation effects induced by the probe beam. However, because D is linear in θ^{PV}, we can calibrate it independently for each configuration, in order to get rid of the K factor.

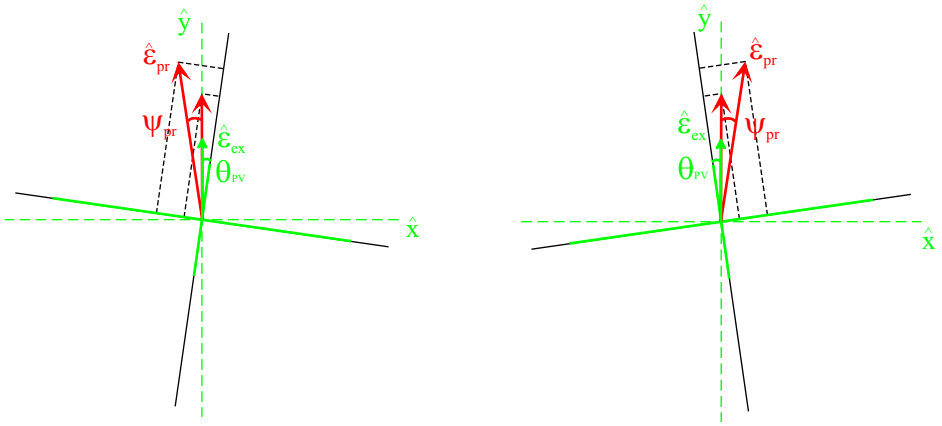

(a) (b)

Figure 2.7: Effect of the linear dichroism axes tilt $\pm\theta^{PV}$ on the probe laser polarization: the latter is rotated by $\psi_{pr} = K' \cdot \theta^{PV}$, during the passage in the vapour. The continuous green lines represent the dichroism axes: high gain and small gain for the probe light. The dashed axes $\hat{x}$ and $\hat{y}$ stand for the symmetry axes of the experiment (before the passage in the vapour, $\hat{\epsilon}_{pr} \| \hat{\epsilon}_{ex} \| \hat{y}$).

Asymmetry amplification

A very attractive feature of stimulated emission, for atomic PV experiments, is that not only the number of probe photons emitted, but also the rotation of their polarization increase with the magnitude of the longitudinal electric field. Such a characteristic is unusual since in all Stark PV experiments based on detection of spontaneous emission the asymmetry is proportional to $\theta^{PV} = -\Im m E_1^{PV}/\beta E$, so that a reduction of E which increases the asymmetry leads to an unavoidable loss of the fluorescence signal proportional to $\beta^2 E^2$.

For our experiment, if we use the most simple model for stimulated emission, the two polarization components of the probe beam which correspond to the two gain axes grow exponentially with the optical thickness of the medium, but with different gains. This leads to the following expression of the polarimeter imbalance (for the case $\hat{\epsilon}_{pr} \perp \hat{\epsilon}_{ex}$ for example):

$$D \equiv \frac{S_X - S_Y}{S_X + S_Y} = \; 2\; \theta^{PV} \cdot (\exp(\eta_\perp(F_1, F_2, F_3) \cdot \mathcal{A}_\perp) - 1), \tag{2.1}$$

where

$$\mathcal{A} \equiv \ln \frac{I^{out}}{I^{in}} \propto \; n_{\mathrm{Cs}}\; E_z^2\; I_{ex}$$

is the optical thickness, and I^{out} and I^{in} are deduced from the sum of the signals coming from the two polarimeter photodiodes. η is a computable number, which depends only on the hyperfine quantum numbers F_1, F_2, F_3 of the atomic states $(6S_{1/2}, F_1)$, $(7S_{1/2}, F_2)$ and $(6P_{3/2}, F_3)$ involved in the pump-probe transition. The choice ($F_1 = 3$, $F_2 = 4$, $F_3 = 4$), with the largest anisotropy $\eta_\perp = \frac{11}{12}$, leads to the most favorable situation for PV measurements. n_{Cs} is the Cesium vapour atomic density and I_{ex} is the intensity of the excitation laser.

A more realistic model [33, 34], which accounts for our real experimental conditions, gives slightly different expressions: for the two configurations "para" and "ortho" of $\hat{\epsilon}_{pr}$ with respect to $\hat{\epsilon}_{ex}$, we have

$$\begin{aligned} D_\perp &= \quad 2.0 \quad \theta^{PV} \cdot (\exp(\eta_\perp(3,4,4) \cdot \mathcal{A}_\perp) - 1), \\ D_\parallel &= -2.26\; \theta^{PV} \cdot (\exp(\eta_\parallel(3,4,4)\; \cdot \mathcal{A}_\parallel\,) - 1), \end{aligned} \tag{2.2}$$

with $\eta_\parallel = -\eta_\perp/(1 + 2\eta_\perp)$.

Complete signature and precise measurement of γ_1(E_z-odd)

In a general way, our polarimeter allows to measure the linear dichroism γ_1 and the circular birefringence α_2, since these are the only effects which rotate our linear (vertical or horizontal) polarization. At fixed excitation polarization $\hat{\epsilon}_{ex}$, sequences of measurements with $\hat{\epsilon}_{pr} \| \hat{\epsilon}_{ex}$ and $\hat{\epsilon}_{pr} \perp \hat{\epsilon}_{ex}$[4] allow to distinguish γ_1 from α_2, because

[4]The rotation of $\hat{\epsilon}_{pr}$ by 90° is ensured by a half-wave plate, cf. paragraph 2.1.1.

for a γ_1 effect, the polarimeter imbalance does not change sign, whereas for an α_2 effect it does. To the first order the polarimeter is only sensitive to $\gamma_1 \pm \alpha_2$.

When acquiring $\gamma_1 \pm \alpha_2$ data, not only the polarimeter imbalance D_{amp} for the amplified probe pulse is measured, but also the imbalance D_{ref} for a reference probe pulse which comes 1 ms later, when all the atoms have relaxed to the fundamental state. In such a way, the so called double imbalance $\Delta D = D_{amp} - D_{ref}$, at each excitation pulse, gives the atomic contribution for γ_1 and α_2, free of any static component coming from the optics. Actually, we measure the imbalance for four reference pulses, at 1 ms interval, in order to have less noise on D_{ref}.

The calibration procedure we have already seen allows to get immediately the calibrated quantities γ_1^* and α_2^*: γ_1^* is the one suited for the measurement of θ^{PV} and α_2^* is expected to be zero.

A very important symmetry operation during data acquisition is the periodic insertion and removal of a half-wave plate with vertical axis, just before the polarimeter: this allows to distinguish between true polarization effects and instrumental defects. For example, the electromagnetic parasites which go with the large electric field pulse can affect in a different way the two channels of the polarimeter. After the half-wave plate, the probe polarization is flipped with respect to the vertical axis. This means the optical signals on the two photodiodes of the polarimeter have been exchanged. As a consequence, the "$\frac{\lambda}{2}$-odd" imbalance eliminates the possible asymmetry on the detection channels and gives the true polarization tilt.

The rotational invariance of the experiment is the last symmetry test we perform during PV measurements, carried out with the simultaneous rotation of the polarizations $\hat{\epsilon}_{ex}$ and $\hat{\epsilon}_{pr}$, by 45° steps: we measure atomic signals with the green laser polarization alternately along $\hat{y}$, $\hat{x}$, $\hat{u}$, $\hat{v}$, where $\hat{u}$ and $\hat{v}$ are the axes turned by 45° with respect to $\hat{x}$ and $\hat{y}$. These four orientations of $\hat{\epsilon}_{ex}$ suffice for our test, because of the general form of the density matrix of the excited $7S$ atoms: $A+B\sin(2\theta)+C\cos(2\theta)$, where θ is the angle between $\hat{\epsilon}_{ex}$ and some reference axis in the transverse plane. It is easy to check that the set of half-wave plates we use can produce all the polarizations configurations we need for the excitation and the probe lasers. This revolution symmetry test is of fundamental importance, because many systematic effects (for example coming from transverse magnetic and electric fields) break this kind of symmetry.

Let us summarize the essential selection criteria for our PV measurement:

- Balanced mode differential polarimetry: dark-field detection of the probe polarization tilt, detected as an imbalance between the $\hat{u}$ ("left") and the $\hat{v}$ ("right") mirror-image components.
- Double imbalance $D_{atom} - D_{ref}$: it allows discrimination of atomic effects against optical defects.
- Reversal of the Electric field E_z: the most powerful signature for the PV signal. When we reverse E_z, θ^{PV} changes sign, whereas most of the other effects are functions of E^2.

- Flipping of the probe polarization just before the polarimeter (plate $(\lambda/2)^{xy}_{det}$): this allows discrimination between true rotation of the polarization and instrumental defects (or electromagnetic interferences).
- Rotation of the incident probe polarization $\hat{\epsilon}_{pr}$ by 90°: this is used in order to distinguish linear dichroism (PV effect) from optical rotation (e.g. Faraday effect).
- Rotation of $\hat{\epsilon}_{ex}$ and $\hat{\epsilon}_{pr}$ by 45°, 90°, 135°: by this way we can select the isotropic part of our signals, and eliminate anisotropic systematic effects.

We can define now the precise way to deduce the PV effect from our polarimetric signals (cf. [29], Annexe A). We can see in table 2.1 the 16 states which correspond to the 2^4 possibilities related to the four parameters θ^{cal}, E_z, $(\frac{\lambda}{2})_{det}$ and $(\frac{\lambda}{2})_{pr}$. Note that the most frequent reversal (of θ^{cal}), does not appear in the selection criteria enounced before: it is not a signature of the PV effect, but it is nevertheless essential, since it is the reversal which allows to calibrate our measurements.

State	1	2	3	4	5	6	7	8	9	10	11	12	13	14	15	16
θ^{cal}	+	-	+	-	+	-	+	-	+	-	+	-	+	-	+	-
E_z	+	+	-	-	+	+	-	-	+	+	-	-	+	+	-	-
$(\frac{\lambda}{2})_{det}$	-	-	-	-	+	+	+	+	-	-	-	-	+	+	+	+
$(\frac{\lambda}{2})_{pr}$	-	-	-	-	-	-	-	-	+	+	+	+	+	+	+	+

Table 2.1: The 16 possible states for a fixed excitation polarization $\hat{\epsilon}_{ex}$.

In fact, the numbering of the states does not represent the chronological order: for each parameter E_z, $(\frac{\lambda}{2})_{det}$ and $(\frac{\lambda}{2})_{pr}$, we choose the first state randomly.

For each state, we measure the double imbalance $\Delta D(j)$ ($j = 1, ..., 16$). We average this quantity over 30 pulses for each j (with a repetition rate of about 100 Hz). Then, with one set of data, we can deduce the calibrated E_z-odd angles $\theta^*_{\parallel}$ and $\theta^*_{\perp}$ defined below, which will give the value of the calibrated dichroism $\gamma^*_1(E_z\text{-odd})$:

$$\theta^*_{\parallel} = \frac{1}{2}\left\{+\theta^{cal}\left[\frac{\Delta D(1)+\Delta D(2)-\Delta D(5)-\Delta D(6)}{\Delta D(1)-\Delta D(2)-\Delta D(5)+\Delta D(6)}\right] -\theta^{cal}\left[\frac{\Delta D(3)+\Delta D(4)-\Delta D(7)-\Delta D(8)}{\Delta D(3)-\Delta D(4)-\Delta D(7)+\Delta D(8)}\right]\right\} \quad (\text{case } \hat{\epsilon}_{pr}\|\hat{\epsilon}_{ex}). \quad (2.3)$$

This is equivalent to say that:

$$\theta^* = \theta^{cal} \times \frac{1}{2} \times \times \left[\frac{\Delta D(\theta^{cal}\text{-even}; (\frac{\lambda}{2})_{det}\text{-odd}; E_z > 0)}{\Delta D(\theta^{cal}\text{-odd}; (\frac{\lambda}{2})_{det}\text{-odd}; E_z > 0)} - \frac{\Delta D(\theta^{cal}\text{-even}; (\frac{\lambda}{2})_{det}\text{-odd}; E_z < 0)}{\Delta D(\theta^{cal}\text{-odd}; (\frac{\lambda}{2})_{det}\text{-odd}; E_z < 0)}\right].$$

In paragraph 2.3.3 we explain why it is necessary to calibrate the signals separately for positive and negative applied electric fields.

In order to get $\theta^*_\perp$, we have to replace the indices $j = 1 - 8$ by $j = 9 - 16$ in the formula (2.3).

γ^*_1 and α^*_2 for a given excitation polarization are then given by:

$$\gamma^*_1(\hat{\epsilon}_{ex}) = \frac{1}{2}(\theta^*_\parallel + \theta^*_\perp), \qquad \alpha^*_2 = \frac{1}{2}(\theta^*_\parallel - \theta^*_\perp). \tag{2.4}$$

Our PV signal, for a given hyperfine transition, is the "isotropic" value when we rotate the excitation polarization $\hat{\epsilon}_{ex}$:

$$\gamma_1^{*iso} = [\gamma^*_1(\hat{y}) + \gamma^*_1(\hat{x}) + \gamma^*_1(\hat{u}) + \gamma^*_1(\hat{v})]/4.$$

There is a slightly different way to reconstruct the parity violating observable, which should in principle be less sensitive to pulse to pulse fluctuations of the excitation laser energy. We know from equation (2.2) how to deduce an estimation $\tilde{\theta}$ of the probe polarization tilt, before the calibration operation, from the double imbalance value and the measurement of the amplification:

$$\begin{aligned} \tilde{\theta}_\perp &= \quad \Delta D_\perp \ / \ 2.0 \quad (\exp(\eta_\perp \mathcal{A}_\perp) - 1), \\ \tilde{\theta}_\parallel &= -\Delta D_\parallel \ / \ 2.26 \ (\exp(\eta_\parallel \mathcal{A}_\parallel) - 1). \end{aligned} \tag{2.5}$$

Hence, this second reconstitution method, dubbed "$\tilde{\theta}$", consists in replacing all the double imbalance values ΔD of the so called "D" reconstitution method (equation (2.3)) with the relative calculated $\tilde{\theta}$. These two analysis procedure always led to practically identical results, for all our experimental runs (paragraph 2.5.4).

2.1.3 Main systematic effects arising from electric and magnetic fields

We present in this section the most important identified systematic effects coming from stray electric and magnetic fields [29].

B_z(E_z-odd) effect

The only systematic effect, which can perturb the γ_1^{PV} measurement at first order, is due to the possible presence in the interaction region of a longitudinal magnetic field which changes sign when the applied electric field is reversed. For obvious reasons this field is dubbed $B_z(E_z\text{-odd})$.

The systematic effect comes from the precession of the Stark alignment axes in the B_z magnetic field: the axes rotate by an angle $\theta^{B_z} \propto B_z$ in the transverse plane. If a component of B_z is odd with respect to the applied electric field E_z, the consequent $\theta^{B_z}(E_z\text{-odd})$ is characterized by exactly the same signature as θ^{PV}.

Note that the cylindrical symmetry of the experiment forbids in principle the appearance of this longitudinal magnetic field. Even if we take into account the side

arm and the wires which bring the voltage to the electrodes, which break the revolution symmetry, the remaining (y, z) symmetry plane still forbids the presence of a longitudinal magnetic field coming from the experiment. This means that actually such a systematic effect should be of the second order, because it has to combine a geometrical defect and a current source. The $B_z(E_z\text{-odd})$ has to be 50 μG large to produce a γ_1^* of the order of the PV effect.

Another feature of the $B_z(E_z\text{-odd})$ field is to produce an optical rotation of the probe laser by the Faraday effect. This is very useful to keep this field under control, because this α_2 effect is relatively important on the $(6S, F{=}3)$-$(7S, F{=}4)$-$(6P, F{=}5)$ transition, so that we can measure it with a relatively short data acquisition time. By this way, if the B_z field is stable, we can make corrections on the measured $\gamma_1^*(E_z\text{-odd})$ to deduce γ_1^{PV}.

(E_t, B_t) and (B_t, B_t')

Another class of systematic effects comes from transverse electric and magnetic fields. It was shown that the systematic effect is of the second order in the transverse fields. The two harmful configurations are given by:

- a couple of electric and magnetic fields (E_t, B_t) the product of which having to be E_z-even,
- a couple of two magnetic fields (B_t, B_t'), one being E_z-odd and the other one E_z-even.

In the first case, the average of γ_1^* on the four excitation polarizations is not zero: there is a systematic effect on our isotropic γ_1^{iso} measurement. In the second case, the isotropic part of the systematic effect is zero.

Note that in either case there are anisotropic effects on γ_1 and α_2 as well, which are measured during PV data acquisition and provide a useful test.

After a simple calibration procedure, if we measure γ_1 and α_2 when we apply large transverse magnetic fields (alternatively along $\hat{x}$ and $\hat{y}$), it is possible to deduce the transverse electric and magnetic fields in the cell, for different radial positions (by moving the laser beams). We will come back in detail to these topics in paragraph 2.3.4.

2.2 History and organization of the experimental work

2.2.1 Experimental background

In this paragraph, We try to give the key features of the evolution of the experiment in the past years, in order to understand the context in which this thesis began, and the improvements brought by the use of our new cells.

Already in 1995, at the early stage of the experiment, it was known that the cell was the weakest link of the experimental setup. At that time, a rectangular glass cell

with internal electrodes was used, which broke the cylindrical symmetry of the setup. The remaining specular symmetry (with respect to the vertical plane containing the laser beams) was not enough to prevent the appearance of a small 3 mG magnetic field, which reversed with the applied longitudinal electric field. From a physical point of view, this field was interpreted as the effect of currents on the body of the cell, when the high voltage was applied to the electrodes (the glass is no more a good insulator, when it is in contact with cesium vapour). This value of the so called $B_z(E_z\text{-odd})$ was not acceptable, as it produced a systematic effect which was more than 50 times the expected PV signal.

During D. Chauvat's thesis [29], a major improvement consisted in the substitution of the rectangular cell with a cylindrical one. This led to a reduced $B_z(E_z\text{-odd})$, which didn't exceed 50-100 μG. This was still comparable to the PV effect.

The next generation of cells, which was exhaustively tested within the ambit of E. Jahier's thesis [28], differs from the previous ones by the use of a new material, sapphire instead of glass. We already saw in paragraph 2.1.1 the reasons for such a choice: the sapphire windows do not report any damage under our experimental conditions, whereas the glass windows were affected by the appearance of a dark spot (in the area hit by the green laser beam), after a few tens of hours of measurements. Another reason is that sapphire is a better electric insulator than glass (in the presence of a cesium vapour), so that the $B_z(E_z\text{-odd})$ caused by currents in sapphire should be even smaller than our previous 50 μG. The high electric resistivity of sapphire also allowed to use external electrodes.

Unfortunately, the many tests made during E. Jahier's thesis revealed a very unpleasant situation: during the green laser pulse, electrons are emitted from the windows, and then accelerated by the longitudinal applied electric field. The main problem is that this stray current is amplified by secondary emission of the electrons which hit the cell tube. The amplification factor was measured to be of the order of 10, and the total current pulse in the cell was around 0.6 A during 20 ns, which corresponds to $8 \cdot 10^{10}$ electrons. The runs made with this type of cells showed that the $B_z(E_z\text{-odd})$ (presumably due to the electronic flow) was not stable from run to run, and was typically of the order of 100 μG. The consequent systematic error on γ_1^{PV} did not allow to undertake PV measurements.

In order to solve this problem, it was decided to switch back to the use of internal electrodes, which should act as diaphragms that capture free electrons, thus preventing them from reaching the tube and multiplying themselves. The choice of sapphire was not disputed, since the decisive advantages of this material, with respect to glass, were confirmed under our experimental conditions. In fact, the development of such a cell, which began at the end of 2001, was much more difficult than expected, and we had to wait 2003 for the first prototype.

In the meanwhile, we put into practice another idea, already introduced in paragraph 2.1.1. It is well known that the secondary electronic emission from materials is much more efficient at grazing incidence of primary electrons. Hence, if we groove the inner surface of the alumina tube of the cell, most electrons hit the surface at quasi normal incidence, and are stopped inside the material without multiplying

themselves. We will see that this basic idea is the one that has made possible the preliminary measurement of parity violation, which is reported in the thesis.

2.2.2 Our grooved cells

In the next section, we will introduce the standard preliminary measurements developed during E. Jahier's thesis, which allow to optimize the setup (the alignment of the laser beams with respect to the cell, for example), understand the field configuration inside the cell, deduce which are the best conditions for a PV measurement and quantify possible systematic errors.

We had the opportunity to use three grooved cells, called *Alum2*, *Alum3* and *Alum4*. The cells differ mainly by the quality of the sapphire windows, and the tilt of the windows with respect to the alumina tube.

We will see that *Alum2*, the first cell we used, despite relatively bad quality windows, had the great advantage of a low and stable $B_z(E_z\text{-odd})$. With this cell we managed to reach a first PV measurement, with 8.4% precision. The following cells allowed to continue the parity violation runs in order to reduce the statistical error on θ^{PV}, to investigate carefully which are the limits of the present setup, and determine the improvements which will lead to a 1% precision.

From January 2002 to October, we performed measurements on *Alum2*. Then we tested *Alum3*, but we realized that there were many electric problems with this cell, probably due to the presence of some residual gas (see next paragraph). Hence, in December, we decided to change again, and use *Alum4*. In the meanwhile, *Alum3* was filled again with Cesium, taking care of good vacuum conditions. On March 2003, we came back to measurements on *Alum3*. We report in the following the progress performed with the participation of the candidate to the cesium experiment, until April 2003.

We tried several configurations with each cell. Since our goal is to measure the violation of a spatial symmetry, we try to have an experimental configuration which is the most symmetric possible, in order not to introduce a systematic bias due to geometrical effects. A few examples: the cylindrical cell, the well superimposed laser beams, which are themselves centered on the axis of the cell. It is possible to test the sensitivity of the measurements with respect to this "apparent symmetry" of the apparatus by applying reflections or rotations to some elements (beam polarizations, cell), or even by breaking it: for example, we already saw that the half-wave plate before the polarimeter flips the probe polarization with respect to the vertical plane (this is the way to discriminate true polarization rotations from geometrical effects or electric interferences which disturb in a different way the two photodetectors). Regarding the cell, we decided to periodically turn it over, and observe the possible change of sign of $B_z(E_z\text{-odd})$. This is not an easy operation, because we had to take off the internal oven and the cell from the external oven every time. We also decided to break the symmetry with a tiny tilt of the cell with respect to the beam axis, in the horizontal plane or in the vertical plane. We will see that there is a clear effect, although not stable on a long scale of time.

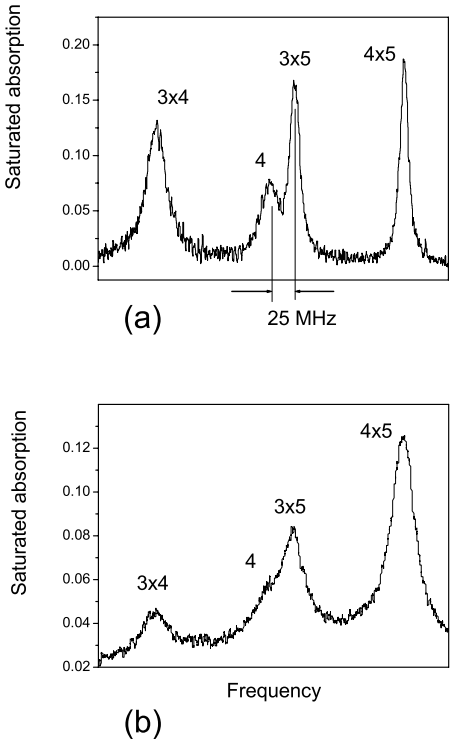

Figure 2.8: Saturation spectroscopy of the $6S$,$F = 4$ - $6P_{3/2}$,$F = (3, 4, 5)$ transitions. 3×4 (and in a similar way 3×5 and 4×5) corresponds to the cross-over between the $(6P, F = 3)$ and $(6P, F = 4)$ levels.
(a) *Alum3* cell, after new cesium filling;
(b) *Alum3* cell, before new cesium filling.

Purity of the gas inside the cell

We said in the previous paragraph that the *Alum3* cell measurements were affected by the presence of anomalous electric parasites, ascribed to the presence of spurious gas inside the cell. Actually, the hypothesis of an unwanted residual gas was confirmed later, thanks to spectroscopic measurements on the D_2 cesium line. Indeed, the high spectroscopic definition of our saturation spectroscopy setup, completed in the meantime, allowed to observe the collision broadening of the cesium lines, due to the spurious gas (see fig. 2.8). Such a broadening disappeared after filling again the *Alum3* cell with cesium.

For the other cells, the saturation spectroscopy measurements confirmed that the vacuum conditions were always good, showing there is no degradation due to the grooving of the cell.

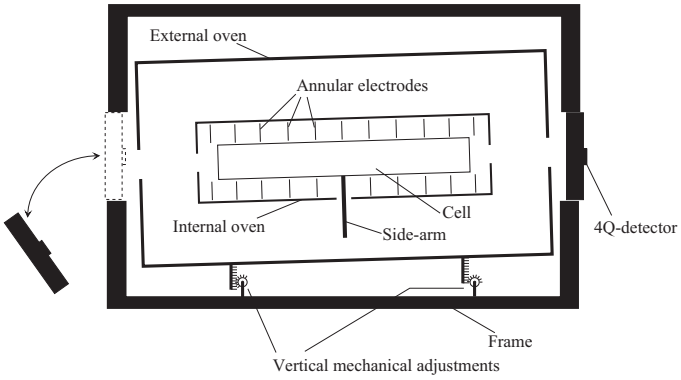

Figure 2.9: Configuration of the frame which sustains the external oven, the internal oven and the cell, as well as the magnetic coils (not reported in the figure) (side view).

2.3 First tests: characterization and optimization of the experimental conditions

2.3.1 Alignment of the PV setup

When we want to use a new cell, we install it into the internal oven and we place the latter into the external oven. The external oven itself is maintained by a rigid frame, equipped with fine adjustments (1/10 mm precision) which allow precise translation and tilt in the vertical and horizontal plane (see fig. 2.9). The tilt of the cell is monitored thanks to the reflection of the green laser by the two sapphire windows. The rigid frame also sustains the magnetic coils.

In order to superimpose the excitation and probe laser beams, we use a four quadrants photodiode (*Judson J16-4Q*), which is alternatively placed at the entrance and at the exit of the oven. The photodiode is mounted on a squared Dural® block, which fits with a 20-30 μm reproducibility the front or the back of the frame (see fig. 2.9). The resulting alignment of the beams is then constantly checked, during the measurement runs, thanks to four positiometers, which monitor separately the probe and excitation lasers before and after the passage through the cell. Each positiometer consists in a four quadrants photodiode, placed in such a way as to detect the portions of the beams which come out of the main path of the beams, from reflections and transmissions on the dichroic mirrors at the entrance and exit of the cesium cell (cf. fig. 2.1). A feedback system acting on mirrors (by means of piezos) allows to correct the alignment of the beams, if need be.

$(\lambda/2)_{pr}$

Once we have aligned the beams, we have to check the polarizations of the lasers. The probe polarization is measured thanks to our polarimeter, without atomic excitation. We want to adjust it for all the configurations of our lambda plates (in tables 2.2

$(\lambda/2)_{pr}$	$(\lambda/2)^{bis}_{pr}$	$(\lambda/4)_{pr}$
90° rotation	45° rotation	Circular polarization
Discrimination between γ_1 and α_2	Inserted when $(\lambda/2)^{bis}_{ex}$ is in, in order to have probe polarization along γ_1^{Stark} axes	The polarimeter detects atomic birefringence α_3: control for the green laser frequency, when we are on the 3-4-4 transition

$(\lambda/2)^{bis}_{det}$	$(\lambda/2)_{det}$
45° rotation	Reflection with respect to the vertical axis
When $(\lambda/2)^{bis}_{pr}$ is on, brings back the polarization along the axes of the polarimeter for balanced-mode detection	Discriminates true polarization rotation from instrumental imbalances

Table 2.2: Plates for the control of the probe beam polarization.

and 2.3, we remind which are the switchable lambda plates of the experiment, and what they are used for).

First, we switch on and off the $(\lambda/2)_{det}$ and $(\lambda/2)_{pr}$ and measure the imbalance signal for the four configurations (1:off-off, 2:on-off, 3:on-on, 4:off-on). The axes of $(\lambda/2)_{det}$ are adjusted in order to have the same imbalance in the cases 1 and 2. The axes of $(\lambda/2)_{pr}$ are adjusted in order to have the same imbalance in the cases 3 and 4. Then we have to set the orientation of the polarimeter axes to have the same imbalance in all the cases. Finally we adjust the gain of the two channels of the amplifier to set the imbalance to zero.

We insert then $(\lambda/2)^{bis}_{pr}$ and $(\lambda/2)^{bis}_{det}$, and we adjust $(\lambda/2)^{bis}_{det}$ with the same procedure. At the end of this alignment, the maximum imbalance over all the configurations is of the order of the mrad. This residual imbalance is then essentially suppressed for the double imbalance quantity.

$(\lambda/2)_{ex}$ and B_z^{res}

Once we have aligned the lambda plates for the probe beam, we can use the atomic amplification polarimetric signals to align the ones for the excitation beam. This procedure is detailed in [35]. It allows to orientate the axes of the Glan prism (which define the excitation polarization) and the plates $(\lambda/2)_{ex}$, to adjust the tilt of the lambda plates of the probe and excitation beam (in order to compensate birefringences and eliminate a possible helicity of the lasers), and also compensate the residual longitudinal magnetic field B_z^{res}.

$(\lambda/2)_{ex}$	$(\lambda/2)_{ex}^{bis}$	$(\lambda/4)_{ex}$
90° rotation	45° rotation	Circular polarization
Rotational invariance		⇒Atomic orientation in $7S$ ⇒Birefringence α_2 ⇒Control for the green laser frequency, when we are on the 3-4-5 transition

Table 2.3: Plates for the control of the excitation beam polarization.

For example, a misalignment between probe and pump polarizations is corrected by measuring and reducing to zero the consequent γ_1^{even}.

At the end, the residual polarization or misalignment defects are of the order of a few hundreds microradians. Finally, a servo-loop allows to drive the Faraday rotator placed in the excitation beam path, in order to apply a polarization tilt to maintain the defects below the noise level.

Instantaneous noise

The last step of the preliminary procedures is the fine alignment of the lens which focuses the probe laser into the polarimeter. Thanks to two translation screws, we can translate the lens in the transverse plane and minimize the instantaneous imbalance noise, being careful that the imbalance stays near zero. What we call instantaneous noise is given by the standard deviation of the imbalance of the signals, over 120 laser pulses. Just after the lens, a diaphragm is available: the polarizations of the periphery of the beam can add noise, hence it can be useful to let only the inner part of the laser go into the polarimeter.

2.3.2 Cell windows: tilt and temperature

Tilt θ

In an ideal experiment, we would have our two lasers superimposed, propagating straight away, without any reflection, passing through cesium vapour, the probe beam being amplified and then detected by the polarimeter. In the real experiment, throughout the path of the lasers, we have some optical elements which act on the beams and introduce some defects. We have already seen how the defects on the polarization of both lasers are minimized. Another element which inevitably perturbs the beams is the presence of the windows of the cell. Unfortunately, it is not possible to coat the windows against reflection, because normal coatings are attacked by cesium vapour. Hence, we have to deal with reflections of the beams on the two windows.

Experimentally, we notice that when the windows are orthogonal to the beams, the noise of the signals coming from the polarimeter dramatically increases: the probe beam is reflected many times back into the cell by the two windows, and interferes

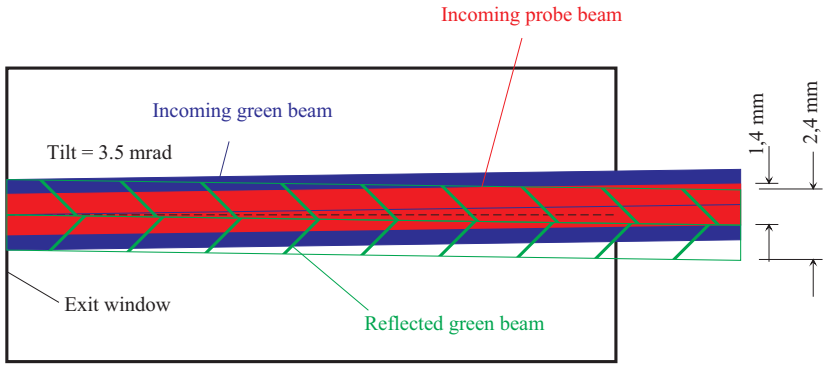

Figure 2.10: Reflection of the beams on the exit window, with a 3.5 mrad tilt (scheme not to scale).

with itself in an uncontrolled way. In order to come back to the usual noise, we have to tilt the cell by a few milliradians. We usually tilted the cell in the horizontal plane, by 1.5 to 3 mrad.

Of course, this operation breaks the natural symmetry of the setup. In order to check the possible related effect, we performed PV measurements in various configurations: tilt in the horizontal or vertical plane, up, down, right or left. We tried different magnitudes: 1 mrad, 2 mrad, 3 mrad, and even 7 mrad.

We decided, for long PV measurements, to periodically change the direction of the tilt, in order to average on a possible effect which could change sign with the tilt. This has to be considered as a symmetry reversal, in the same way as the other reversals (electric field, lambda plates...).

Many factors can affect γ_1^{odd}, when we tilt the cell. We can begin with simple geometrical considerations.

Of course, when we tilt the cell with respect to the lasers, as a consequence we tilt the longitudinal electric field too. This can be seen as a modification of the component of the transverse electric field which is odd with respect to the reversal of the longitudinal electric field ($E_\perp$-odd). The effects of the transverse fields were already studied in [28] and [29]; in the present thesis, they are discussed in paragraph 2.3.4. This is the first consequence of the tilt: the angle $\theta_{(\vec{E},\overrightarrow{k_{ex}})}$ is equivalent to an $E_\perp$-odd, which has to couple with a $B_\perp$-odd in order to create a systematic effect on γ_1^{odd}.

Let us see now the effect of the windows of the cell. The index of refraction of sapphire differs from 539 nm to 1.47 μm light, by approximately 1%. Hence, if we tilt the entrance window with respect to the incoming superimposed beams, after the window there will be a tiny translation of one beam with respect to the other one. In fact, for a 0.5 mm window thickness and a 3 mrad tilt, the displacement is negligible (of the order of 10 nm).

Then, the beam are reflected on the exit window with a tilt which is twice the tilt of the cell (see fig. 2.10). We could fear that the procedure which allows to

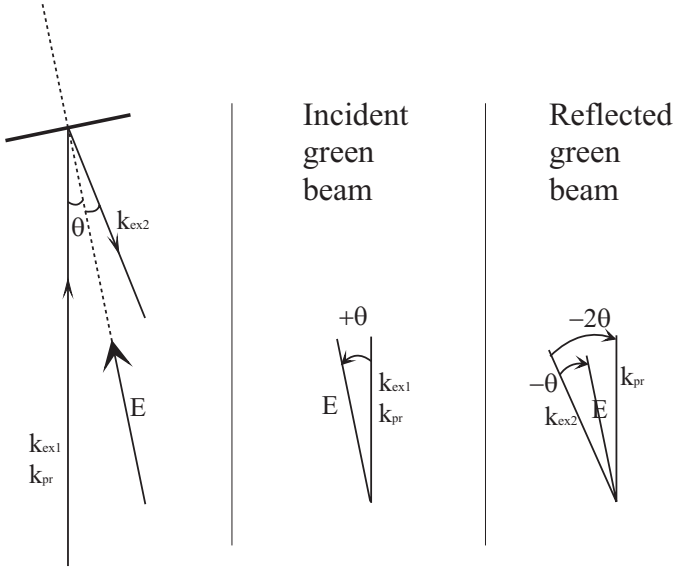

Figure 2.11: Angles between the incident and reflected excitation beams (k_{ex1} and k_{ex2}), the probe beam (k_{pr}) and the longitudinal electric field (E). The angles are relative to the excitation beam (incident or reflected), in order to account properly for systematic effects.

align the beams at the output of the oven with the four quadrants photodiode is not appropriate, because of the presence of secondary reflected beams which reach the photodiode. In fact, if the reflectance of the single window is 10%, a secondary beam has to be reflected twice to reach the photodiode, hence it would be 1% of the principal beam. This means that our error is less than one hundredth of the diameter of the beam, which is negligible.

The first reflected excitation beam comes back into the cell with an angle which is 2θ, and interacts too with the probe beam. As we can see from fig. 2.11, in this case there is the $E_\perp$-odd effect too, but this time with the opposite sign: $-\theta$. We must account as well for another effect, which is due to the angle -2θ between the probe and excitation beams. Because of this angle, the infrared beam probes alignment axes tilted by -2θ in the horizontal plane, with respect to the normal case ($k_{pr} \parallel k_{ex}$). Now, this rotation is very similar to the one which could be produced by the presence of a vertical magnetic field, by Hanle effect. It is not exactly equivalent, because the magnetic field leads to other effects too (perturbation of the atomic excitation and the probe transition [29]), but the qualitative effect is a pseudo "$B_\perp^{Hanle}$-even". We will see in paragraph 2.3.4 that this $B_\perp$-even has to couple with a $B_\perp$-odd or an $E_\perp$-even, to give a systematic effect on γ_1^{odd}. Nevertheless, only the second contribution to the systematic γ_1^{odd} ($B_\perp$-even, $E_\perp$-even) does not cancel out when we average the results over the four excitation polarizations.

Let us now review the role of the reflected probe beams, which is not easy to understand. From simple geometric considerations, we see that for small tilts the main beam arriving on the polarimeter comes with a secondary beam which has been

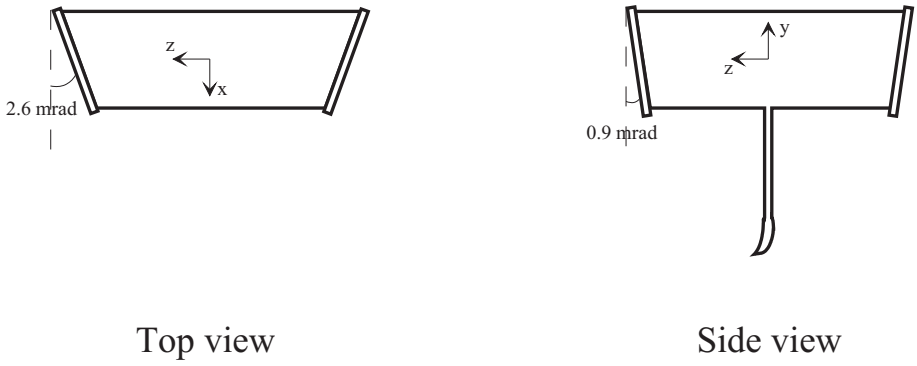

Figure 2.12: Scheme of the *Alum3* cell.

reflected twice in the cell. Such a configuration generally generates noise, due to the interference of the two beams in the polarimeter. We avoid this kind of situation by tilting the cell, typically of about 3-3.5 μrad, until the anomalous noise disappears.

Note that we have supposed the two windows of the cell were almost parallel, and this is true for *Alum2* and *Alum4*. However, the windows of *Alum3* are tilted with respect to each other (see fig. 2.12). Hence, for Alum3, the twice reflected probe beam is not parallel to the principal beam, and does not enter the polarimeter.

In conclusion, the main effects associated with the tilt of the cell come from the tilt of the electric field and the reflected green beam. We have a total effect which can be summarized by the following simplified formula:

$$E_{\perp}\text{-odd}(\theta) + \eta \cdot (E_{\perp}\text{-odd}(-\theta) + B^{Hanle}_{\text{pseudo},\perp}\text{-even}(-2\theta)), \tag{2.6}$$

where η is the fraction of the green beam which is reflected by the rear window. Each term of equation (2.6) still has to combine with another defect to generate a systematic effect (paragraph 2.3.4).

Temperature T and reflectivity of the windows

At normal incidence, for our two laser wavelengths, the reflectance at the air/sapphire interface is about 7.5%. This means that for a single window, 15% of the laser is reflected. Unfortunately, it is not easy to decrease this number by the use of an AR (anti-reflection) coating, because normal coatings are attacked by cesium vapour. But during Jahier's thesis [28], another solution was found, which takes advantage of the interference of the multiple reflections on the two sides of the window. In fact, if the sapphire plate has got high quality and parallel faces, it can be seen as a Fabry-Perot interferometer, whose optical path length varies with the temperature. By tuning separately the temperature of the two windows, it is possible to reach very good transmissions. The theory and the experimental features of this technique are described in [36]. Thanks to two digital temperature controllers from *Chauvin*

Arnoux (*statop 4849*), we manage to stabilize the temperatures T_{in} and T_{out} of the entrance and exit windows (measured by thermocouples) to better than 0.2°C, and we typically lose about 5‰ power in the passage through the two windows.

Of course, it is not possible to maximize transmission for our two wavelengths at the same time. When we take measurements, we tune the temperature in order to have optimum transmission @539 nm. The free spectral range, expressed in temperature, is about 16°C @539 nm, and 44°C @1.47 μm (these values can vary, according to the thickness of the windows). If the transmission @1.47 μm is too bad, we choose the next temperature value, which gives maximum transmission @539 nm. Experimentally, we monitor the spots of the green laser beam reflected by the two windows of the cell in order to evaluate the reflection coefficient for each one.

It was not very difficult to find the right temperatures for *Alum3*, because the windows are tilted with respect to each other, hence the two distinct reflections allowed to monitor separately the reflectivity of both windows. The sign and the magnitude of the correction ΔT to be applied to the temperature in order to decrease reflectivity is deduced by slightly detuning the laser from the desired frequency and seeing for which $\Delta\nu$ the green reflected spot dims and then disappears. Then, $\Delta T = \Delta\nu \cdot (16°\text{C})/FSR$, FSR being the free spectral range (170 GHz for a 0.5 mm thick plate). In fact, T_{in} and T_{out} are not exactly the temperature of the windows, but the one read by the thermocouple in the proximity of the windows. As a result, when we change the value of T_{in} for example, the temperature of the exit window is slightly affected too. This can be experimentally seen from the temperatures which maximize the transmission of the cell, reported in table 2.4. From the first two couples, we see that here the experimental FSR is 14°C. In the third couple, we have decreased T_{in} more than the FSR (from 214.4°C to 194.7°C), and we see that in order to maintain the same temperature on the exit window (to have the same low reflectivity), we need to increase T_{out} from 217.4°C to 222.0°C. If we suppose the relation between the monitored (T_{in}, T_{out}) and the windows (τ_{in}, τ_{out}) temperatures is linear (except for an insignificant offset),

$$\begin{cases} \tau_{in} = a_{in}\, T_{in} \;+\; b_{in}\, T_{out} \\ \tau_{out} = b_{out}\, T_{in} \;+\; a_{out}\, T_{out}, \end{cases}$$

presuming $a + b = 1$, we can deduce from the data in table 2.4 the numeric coefficients, thanks to a simple linear fit:

$$\begin{cases} \tau_{in} = 0.76\, T_{in} \;+\; 0.24\, T_{out} \\ \tau_{out} = 0.18\, T_{in} \;+\; 0.82\, T_{out}. \end{cases} \tag{2.7}$$

Now, for the cells with parallel windows, the spots of the two reflected beams are superimposed, and it becomes more difficult to know which temperature has to be changed to improve the overall transmission. However, it is possible to use a simple trick to quickly converge to the right values. We first try to put in phase the two windows, i.e. to set their temperatures such that for one wavelength, the

T_{in}(°C)	T_{out}(°C)
228.4	231.4
214.4	217.4
194.7	222.0

Table 2.4: Some of the windows temperatures which maximize the transmission of the *Alum4* cell.

transmission of the two windows is maximum: this is done by looking at the spot while smoothly varying the frequency. When the phase between the windows is opposite, the brightness of the spot does not quite change (the contrast is almost zero). Then, if we change the relative temperature of the windows (for example decrease T_{in} and increase T_{out}), the contrast increases, and then becomes maximum when the windows are in phase: for a frequency ν_0 of the laser, we have minimum reflectivity for both windows, so that the spot is very dim, and for $\nu + FSR/2$, the reflectivity is high for both windows, so that the spot reaches its maximum brightness. Once we are in this situation, we only have to change both temperatures by the same quantity to match ν_0 with the atomic transition.

For 1.47 μm light, it was not possible to use the same technique, because the eye cannot see infrared light. We had to use a detector, placed alternately before and after the cell, in order to monitor the incident and the transmitted light, and deduce the transmission coefficient. In fig. 2.13, we can see some of the measurements for *Alum4*, along with the theoretical transmission (we have used equation (2.7) to

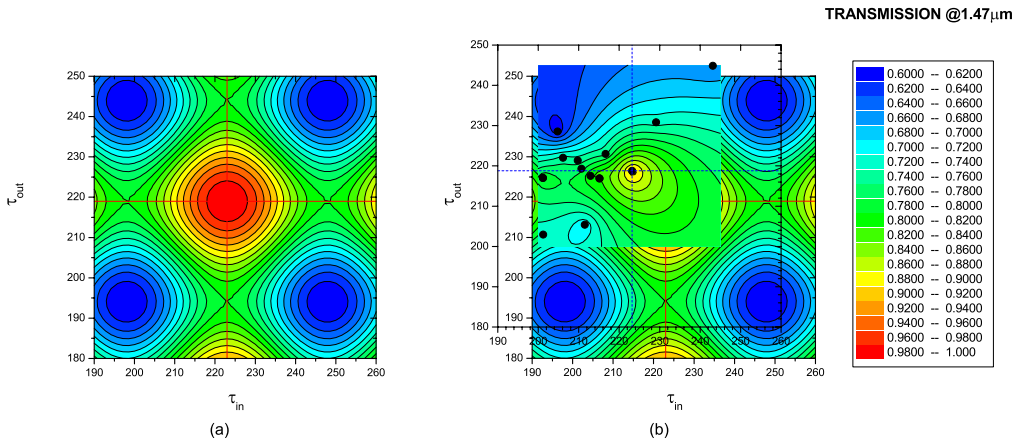

Figure 2.13: Transmission of the *Alum4* cell @1.47 μm. (a) Theoretical graph. (b) Experimental measurements (black dots) and relative false colours, placed above the theoretical graph.

deduce τ from the measured temperature T). The agreement seems pretty good: thanks to the comparison of the theoretical and experimental graph, it seems not too difficult to reach high transmission @1.47 μm, but unfortunately we did not have time to look for the optimal temperatures (it was not our priority, since we wanted high transmission @539 nm).

Order of magnitude of the systematic effects

Since the effects associated with the tilt of the cell are tightly correlated with the effects due to the presence of electric and magnetic fields, we report the discussion about the magnitude of the related systematic errors to the end of the paragraph 2.3.4, about the transverse fields.

2.3.3 First examples of asymmetry

Absorption

One of the first steps, when we want to test a new cell, is the measurement of the amplification of the probe beam, in the presence of the excitation light. This quantity depends essentially on two parameters, the intensity of the green pulses and the density of cesium atoms, itself governed by the side-arm temperature. The amplification $\mathcal{A}$ is deduced from the measurement of the five probe pulses energies by the polarimeter photodiodes, the first one being amplified, and the following being reference pulses: it is defined as

$$\mathcal{A} = \ln \frac{I^{amp}}{I^{ref}},$$

where I^{amp} is the sum of the two polarimeter photodiodes signals for the amplified pulse, and I^{ref} the average of the signals sum for the reference pulses.

Now, if we shift the green laser 2 GHz from the resonance, we expect no amplification. In fact, we measure an absorption, typically of the order of 2 to 15%, which can be explained by Franck-Hertz collisions: the electrons photo-emitted from the windows and accelerated by the longitudinal field collide with the cesium atoms, and produce transitions from $6S$ to $6P$. Then, the probe light is absorbed by the $6P \rightarrow 7S$ transitions. This is not crippling, since the remaining photons are not depolarized at all: indeed the absorption does not affect the experimental calibration $\Delta D/\theta^{cal}$ at all. However it is better to keep it low in order not to lose amplification signal too much.

The absorption does not depend very much either on the magnitude of the electric field or the energy of the excitation pulses. On the other hand, it increases with the vapour pressure, hence we have to choose the side-arm temperature in order to have a good amplification, with a relatively low absorption. We noticed that when we tested a new cell, the absorption was always very high in the beginning (of the order of 15%), and then, after a few weeks, it became more reasonable (3%). We also noticed that very often, during a run (typically at least 5 hours), the

HV	$\mathcal{E}_{ex}$	$\mathcal{N}_{pr}$	τ	η_τ	$\mathcal{A}_\tau$	$(\mathrm{d}a/\theta^{cal})_\tau$	$Abs+$	$Abs-$
9500V	1.5 mJ	$4 \cdot 10^7$	$\parallel$	$-\frac{11}{34}$	0.82	0.52	-0.034	-0.028
			$\perp$	$\frac{11}{12}$	0.37	0.80		

Table 2.5: Some experimental parameters, for typical measurement conditions (we report the parameters for the run performed on July 14th, 2002). $\mathcal{N}_{pr}$ is the number of photons for each probe pulse, τ is the polarization of the probe with respect to the excitation laser, η the coefficient in equation (2.1). $\mathrm{d}a/\theta^{cal}$ is the ratio of the imbalance $\mathrm{d}a$ over the calibration angle, and gives the sensibility of the polarimeter to polarization rotations. $Abs+$ and $Abs-$ are the absorptions measured for positive and negative applied electric field.

absorption slowly decreases. There are probably some relaxation effects of the cell and the windows during the electric and laser pulses, which turn out to improve the situation (e.g. less electron photoemission).

An important parameter which is critical for the absorption is the extinction coefficient of the optical switch: immediately after the pulse, the few transmitted photons are absorbed by the long lasting (a few microseconds) $6P$ population of cesium atoms. Since the time constant of the pulse amplifiers (*Ortec*) is of the order of the microsecond, this spurious signal, following the true pulse, cannot be rejected, an we measure the relative absorption. When the conditions are good, the typical extinction ratio, better than 1‰, is good enough to have the lowest possible absorption, which is around 2 or 3%. However, due to a high sensitivity of the switch to weather changes (temperature and humidity), it happened more than one time that the performances of the switch decreased, after what it could take several days to come back to a reasonable situation. Sometimes, we reached extinctions of the order of 1%, which implied absorptions of the order of 10%, a level at which it generates noise in the polarimeter imbalance because of a consequent deformation of the pulses given by the pre-amplifiers. For this reason, we decided to place a Pockels cell in series with the optical switch, in order to improve the extinction coefficient. This is developed in paragraph 2.4.2.

Usually, the measured absorption is not the same for the two signs of the longitudinal electric field: there is a little difference, which is bigger when the absorption is high. Table 2.5 shows typical measured values, for the *Alum4* cell. This difference comes from the asymmetry of the cell: the two windows do not emit the same number of electrons, the distribution of the electrons and the fields inside the cell cannot be the same for the two signs of the applied voltage.

Anyway, this little asymmetry is not worrying, for a PV measurement, since it does not affect the transmitted photons, and also because the measurement and the calibration of the parity violation are based on purely polarimetric effects. However, it can have indirect consequences, for example on the measurement of the amplification and the relative asymmetry, which have to be corrected with the measured absorptions (during a run, the absorption can change: usually it slowly decreases, and so does the asymmetry, hence it is not easy to know the correction to apply on

the amplification). Nevertheless, it is not important at all to have a precise evaluation of the amplification, since the exploited measurements for the parity violation detection are all polarimetric measurements, which are much more accurate.

Amplification, calibration, and applied electric field

In fact, if it were reliable, the measurement of the amplification asymmetry could be used to evaluate the asymmetry of the applied electric field, whose reversal cannot be perfect, for instance due to a slight asymmetry between the two HV switches. Nevertheless, there is another quantity we can use to this purpose, which is directly dependent on the magnitude of the electric field: the calibration measurement,

$$D_{cal}(E) = D_{cal}(|E|) \equiv D_{cal+}(E) - D_{cal-}(E),$$

which is equal to

$$4\theta^{cal} \cdot (\exp(\eta_\tau A_\tau) - 1) = 4\theta^{cal} \cdot (\exp(\alpha E^2) - 1),$$

according to equation (2.1) (the + and − subscripts are referred to positive and negative applied calibration angles $\pm\theta^{cal}$; here D represents the measured double imbalance, after taking into account the $(\lambda/2)_{det}$ signature, for the selection of polarization effects). The calibration, being a polarimetric measurement, has the advantage not to be affected by the absorption.

The calibration asymmetry, defined as

$$AsCal \;=\; \frac{D_{cal}(E_+) - D_{cal}(E_-)}{D_{cal}(E_+) + D_{cal}(E_-)},$$

is then proportional to the difference between the moduli of the positive and negative electric fields, $\Delta E = |E_+| - |E_-|$:

$$AsCal \;=\; \frac{\eta_\tau \mathcal{A}_\tau \exp(\eta_\tau \mathcal{A}_\tau)}{\exp(\eta_\tau \mathcal{A}_\tau) - 1} \cdot \frac{\Delta E}{E} \;\simeq\; (1 + \frac{\eta_\tau \mathcal{A}_\tau}{2}) \cdot \frac{\Delta E}{E}.$$

Thanks to the measurement of this quantity, we have implemented a feedback loop which allows to maintain low asymmetries, by acting on the applied electric field. Concretely, the acquisition program averages $AsCal$ in order to reach a good precision, and then automatically corrects the applied voltage for the two signs of the electric field, by means of two amplifiers (±100 V maximum). It is possible to correct asymmetries $\Delta E/(2E)$ up to ∼1%. Thanks to this system, we typically have asymmetries less than 1‰.

Note that in general the E_z-odd part of a measured polarimetric quantity D_α is affected by the coupling of its E_z-even part with the asymmetry of the electric field, in the same way as the E_z-odd part of the calibration D_{cal}:

$$D_\alpha^{odd} = D_\alpha^{even} \cdot \frac{\eta_\tau \mathcal{A}_\tau \exp(\eta_\tau \mathcal{A}_\tau)}{\exp(\eta_\tau \mathcal{A}_\tau) - 1} \cdot \frac{\Delta E}{E}.$$

We could fear that such a behaviour would bias our parity violation measurement. If we take the example of an asymmetry $\Delta E/2E = 1‰$, E_z-even defects of the order of 300 μrad, and the typical values of the amplification (cf. table 2.5), it seems we could expect effects of the order of 0.7 μrad on the E_z-odd quantities (70% of the PV effect). Actually, this kind of effects, as well as the way to avoid any consequence on our measurements, are well-known since a long time: in the data analysis, the angles are calibrated separately for the two signs of the electric field, before the extraction of the E_z-odd contribution (cf. equation (2.3)),

$$\theta^{odd} = \theta^{cal} \cdot \left\{ \left(\frac{D_{cal+} + D_{cal-}}{D_{cal+} - D_{cal-}} \right)_{E+} - \left(\frac{D_{cal+} + D_{cal-}}{D_{cal+} - D_{cal-}} \right)_{E-} \right\} / 2 \,.$$

The results are then essentially independent on an imperfect reversal of the electric field.

2.3.4 The transverse fields

Another very important test to characterize the cell is the measurement of the transverse fields, $E_\perp$, $B_\perp$. In this paragraph, following [29], we give some hints to understand how these fields can mimic the PV effect, and how it is possible to deduce them from polarimetric measurements (see [37] for a recent quantitative analysis).

For an applied electric field along the $\hat{z}$ axis, if we take the polarization $\hat{\epsilon}_{ex} = \hat{y}$, we have the following expression for the Stark dipole of the $6S \rightarrow 7S$ transition (cf. equation (1.3)):

$$\mathbf{d}^{Stark} \cdot \hat{\epsilon}_{ex} = i\beta\sigma_x E_z,$$

which produces an alignment in the excited state $7S$, along the $\hat{x}$ axis. The alignment is then detected by the probe beam propagating along $\hat{z}$, as a linear dichroism with axes $(\hat{x}, \hat{y})$.

The electric field: systematic effect produced by a $(\mathbf{E}_\perp \cdot \mathbf{B}_\perp)_{even}$

Let us consider a transverse electric field $\mathbf{E}_\perp = E_x\ \hat{x} + E_y\ \hat{y}$. Then, we have to include another term for the alignment:

$$\mathbf{d}^{Stark} \cdot \hat{\epsilon}_{ex} = i\beta(\sigma_x E_z - \sigma_z E_x).$$

The alignment axis is now $(\hat{x} - \frac{E_x}{E_z}\ \hat{z})$; but this new component along $\hat{z}$ cannot be detected by the probe beam (which is sensitive to dichroisms in the $(\hat{x}, \hat{y})$ plane). However, if we introduce a magnetic field $\mathbf{B}_\perp$ along $\hat{x}$, the alignment precession rotates the $\hat{z}$ component into an $\hat{y}$ one. This component is very similar to the PV term, already discussed in paragraph 1.3.2, and generates the same γ_1 effect.

Of course, only the E_z-odd part of this signal can mimic the PV effect, which corresponds to have both $\mathbf{E}_\perp$ and $\mathbf{B}_\perp$ odd or even with respect to E_z. Then, we have to check the behaviour of this $\gamma_1^{(E_\perp, B_\perp)}$ under excitation polarization rotations

(the rotational invariance of γ_1, by steps of 45°, is the last typical signature tested during PV measurements). It has been shown [29] that the angular dependence of $\gamma_1^{(E_\perp, B_\perp)}$ is given by:

$$\boldsymbol{S_1 \cdot (\cos\psi - \cos(\psi - 2\phi)),}$$

with $\psi = (\mathbf{E}_\perp, \mathbf{B}_\perp)$ and $\phi = (\hat{\epsilon}_{ex}, \mathbf{B}_\perp)$. Hence, there is an isotropic part $S_1 \cos\psi$ which is a real systematic effect, having the complete PV signature.

The magnetic field: systematic effect produced by a $(\mathbf{B}_\perp \cdot \mathbf{B'}_\perp)_{odd}$

A transverse magnetic field can rotate the alignment originally produced along $\hat{x}$, but the $\hat{y}$ component (i.e. the only one which can perturb the probe polarization), is of the second order with respect to the precession angle ($\propto B_\perp^2$). Since we search for E_z-odd effects, we need two components of the magnetic field, the first one odd with respect to E_z (we call it $\mathbf{B}_\perp$), and the second one even ($\mathbf{B'}_\perp$). To tell the truth, there are other effects of the second order, related to transverse magnetic fields [29], but the resultant behaviour does not change.

This time, the angular dependency of the $\gamma_1^{(B_\perp, B'_\perp)}$ is given by:

$$\boldsymbol{-S_2 \cdot \cos(\psi' - 2\phi),}$$

with $\phi = (\hat{\epsilon}_{ex}, \mathbf{B}_\perp)$ and $\psi' = -\frac{\pi}{2} + (\mathbf{B'}_\perp, \mathbf{B}_\perp)$. It means the effect is purely anisotropic. If we average the effect over the four possible excitation polarizations $(\hat{x}, \hat{y}, \hat{u}, \hat{v})$, we obtain zero. Note that it is sufficient to average over two polarizations, $\hat{x}$ and $\hat{y}$, or $\hat{u}$ and $\hat{v}$ to cancel the effect (and this is true for the anisotropic part of $\gamma_1^{(E_\perp, B_\perp)}$, too).

The atomic diagnosis for the transverse fields: *2B4POL*

During D. Chauvat's thesis [29], a procedure was implemented, which allows to deduce from polarimetric measurements the magnitude and the direction of the transverse electric and magnetic fields. Here we give only the basic principles.

The main idea of the procedure is to exploit the second order dependence of the effects with respect to the fields: if we apply a known fixed magnetic field $\mathbf{B}_\perp$, the γ_1 measured by our polarimeter will be proportional to $(B_\perp \cdot B'_\perp)$ and $(B_\perp \cdot E_\perp)$. Hence, the application of $B_\perp$ is a good way to amplify an effect which is proportional to $B'_\perp$ and $E_\perp$, which are the quantities we want to measure. It can be shown that, in addition to γ_1, the transverse fields produce α_2 effects too, with the same angular dependencies (S_1 and S_2), but different magnitudes. The so-called *2B4POL* procedure consists in measuring γ_1^{even}, γ_1^{odd}, α_2^{even} and α_2^{odd} for a fixed magnetic field $B_\perp$, alternately applied along $\hat{x}$ and $\hat{y}$, and for all the excitation polarizations $(\hat{x}, \hat{y}, \hat{u}, \hat{v})$. The collected data is then enough (and even redundant) to deduce the eight components:

$$E_x(E_z\text{-odd}),\ E_y(E_z\text{-odd}),\ E_x(E_z\text{-even}),\ E_y(E_z\text{-even}),$$

$E_\perp$ measurement	γ_1(3-4-5)(S_1)	-4.5	μrad/(V/cm)/G
	α_2(3-4-5)(S_1)	18	μrad/(V/cm)/G
$B'_\perp$ measurement	γ_1(3-4-5)(S_2)	6	μrad/mG/G
	α_2(3-4-5)(S_2)	-2	μrad/mG/G

Table 2.6: Sensitivity of the signals γ_1 and α_2 to the electric ($\mathbf{E}_\perp$) and magnetic ($\mathbf{B'}_\perp$) transverse fields, on the (3-4-5) transition, in presence of a high magnetic field $\mathbf{B}_\perp$, for a 2 kV/cm longitudinal applied electric field.

$$B_x(E_z\text{-odd}),\ B_y(E_z\text{-odd}),\ B_x(E_z\text{-even}),\ B_y(E_z\text{-even}).$$

This kind of measurements can be done on the (3-4-5) transition, and on the (3-4-4) one as well. In order to calibrate the procedure, it is possible to apply two fields: the usual $\mathbf{B}_\perp$ and $\mathbf{B'}_\perp$ for the calibration of the magnetic field, or $\mathbf{B}_\perp$ and $\mathbf{E}_\perp$ for the calibration of the electric field, all of them being much larger than residual fields). Of course, the proportionality of the effect with respect to the product of the fields has been checked. We report in table 2.6 (taken from [28]) the sensitivity of γ_1 and α_2 to the transverse fields, on the (3-4-5) transition.

We use to apply 2.1 G for the $B_\perp$ magnetic field, which allows to extract all the transverse fields after a few minutes of measurements, with typical statistical errors of ± 0.3 V/cm and ± 1 mG for electric and magnetic fields.

Measurements and results

Thanks to *2B4POL*, during Erwan Jahier's thesis, the typical transverse fields in the smooth-wall sapphire cells were probed, for different positions of the laser beams. They appear to be small or zero near the axis of the cell (as expected from symmetry considerations), and increase linearly when the pump and probe beams are translated away from the center. The electric field E_r is centripetal, and does not change sign when the applied E_z is reversed. The magnetic field B_θ is orthoradial, and is odd with respect to the E_z reversal (cf. fig. 2.14).

This result indicates that a distribution of negative charges fills the cell. The

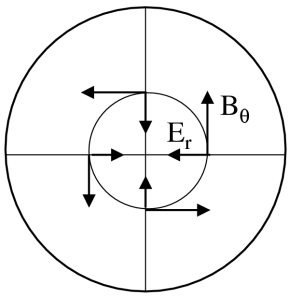

Figure 2.14: Geometry of the measured transverse fields in sapphire and alumina cells.

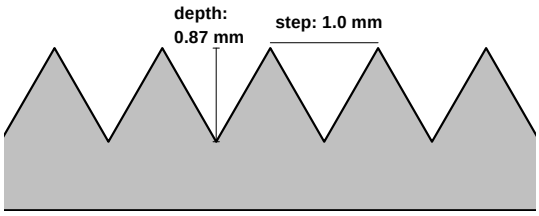

Figure 2.15: Profile of the grooved machined on the inner wall of the alumina tube.

gradient of the Electric field in a smooth-wall alumina cell (see fig. 2.16) was about 30 V/cm/mm. From Gauss' law, the charge density was then estimated to be of the order of 2.5 to $4.5{\cdot}10^8$ e/cm^3. These charges, accelerated by the longitudinal electric field, flow through the cell and create the measured magnetic field. The flow velocity, deduced from the B_θ amplitude, appears compatible with what is expected for charges of mass m_e, hence electrons. It was evaluated that around $4 \cdot 10^{10}$ charges per pulse flow through the cell. This order of magnitude was confirmed by a direct measurement of the electronic current which reach the anode window, detailed in [28]. This measurement showed that the current pulse is concomitant with the excitation laser pulse. However the electrons leaving the cathode window are at least one order of magnitude less than the electrons reaching the anode: the electrons are photoemitted from the window, accelerated by the field E_z, and then multiplied by secondary emission when they hit the tube of the cell. This last phenomenon is responsible for at least 90% of the charges which reach the anode window.

A conceptually simple remedy to the multiplication of charges would be to use internal electrodes, which could act as diaphragms: by this way, the charges would be collected before hitting the tube and producing secondary emission. This kind of cell is under development since the beginning of this thesis, but unfortunately, it resulted much more difficult than what it seemed to reach a satisfying result.

In the meanwhile, another simple idea to inhibit secondary electronic emission (*SEE*) was tested during this thesis, which then revealed itself to be the beginning of viable PV measurements. We know from literature [38] the *SEE* depends on incidence: it is higher at grazing incidence, because the secondary electrons are produced very close to the surface and have a large escape probability. If we could prevent grazing incidence on the cell tube, the *SEE* efficiency would be much lower. It was decided then to replace the smooth internal surface of the cell by a grooved surface, prepared by machining regular circular grooves inside the alumina tube (cf. fig. 2.15).

Actually, the result was spectacular: as we can see from fig. 2.16, the transverse fields are reduced by one order of magnitude, with the new cell (the gradient of the electric field is about 3 V/cm/mm). We will see in the following sections the tests

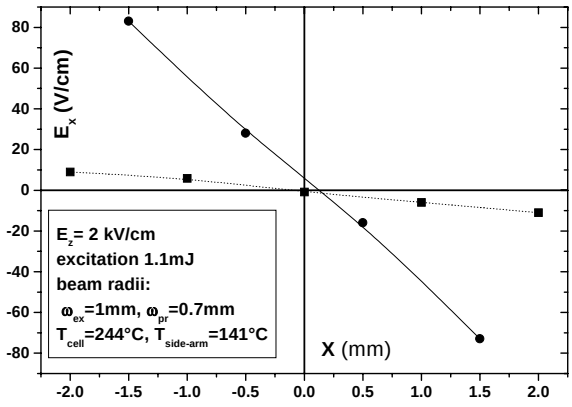

Figure 2.16: Transverse electric field component E_x observed when the excitation and probe beams, while kept superposed, are translated in the transverse x direction of the cell. *Circles*: smooth-wall sapphire cell; *squares*: grooved-wall alumina cell. Similar behaviour is observed for E_y, for translations along y. The $x = 0$ position defined mechanically is arbitrary to within 0.5 mm.

which highlight other good properties, with respect to smooth-wall cells.

Note that *2B4POL* is actually the procedure we use in order to center the beams on the axis of the cell, in the region where the fields are minimum: the $E_\perp$-even signals indicate how far we are from the axis, whereas the $E_\perp$-odd (divided by E_z) is merely the tilt of the applied longitudinal electric field, hence practically the tilt of the cell.

Theoretical magnitude of the systematic errors associated to the transverse fields

The study of the systematic errors which can derive from the presence of transverse fields has already been reported in Erwan Jahier's thesis [28] (p. 110), for the case of non grooved sapphire cells. We report the values of the considered fields in table 2.7, which of course are a little larger than for the case of the grooved alumina

Average value	Physical origin
$< E_\perp^{even} > \leqslant$ 2 V/cm	electronic charge
$< E_\perp^{odd} > \leqslant$ 5 V/cm	tilt of the cell (3 mrad)
$< B_\perp^{even} > \leqslant$ 3 to 5 mG	residual field
$< B_\perp^{odd} > \leqslant$ 3 mG	electronic flow

Table 2.7: Magnitude of the unwanted transverse electric and magnetic fields deduced from *2B4POL*, in smooth-wall cells, for typical PV acquisition conditions (from [28]).

cells (but not so much, because the measurement and the centering of the cell do not provide a better precision than 1 V/cm and 1 mG). The false signals generated by the transverse fields were found to be small: about 0.05 μrad $\simeq \gamma_1^{PV}/16$ for $(E_\perp^{even} B_\perp^{even})$, 0.075 μrad $\simeq \gamma_1^{PV}/10$ for $(E_\perp^{odd} B_\perp^{odd})$, and less than $3 \cdot 10^{-8}$ rad $\simeq \gamma_1^{PV}/30$ for $(B_\perp B'_\perp)$.

If we try to take into account the effects of the excitation beam reflected by the rear window of the cell (cf. equation (2.6)), the important term being given by $B^{Hanle}_{\text{pseudo},\perp}$-even, we see that the effect is not always negligible. The order of magnitude of the "$E_\perp^{even} B_\perp^{Hanle}$" systematic error is given by the angle of the pseudo $B_\perp^{Hanle}$ (which is twice the tilt of the cell), times the angle of the electric field with respect to the longitudinal axis, when we take into account the presence of an $E_\perp^{even}$. If we consider a 3 mrad tilt θ, a 2 V/cm $E_\perp^{even}$, and the usual E_z ($\simeq$ 1650 V/cm), the resulting systematic error will be of the order of:

$$\eta \cdot 2 \cdot 3 \cdot 10^{-3} \cdot \frac{2}{1650} \text{ rad} \simeq \eta \cdot 7.3 \ \mu\text{rad},$$

with η the fraction of the green beam reflected by the window.

In conclusion, the effects of the transverse fields are very small, except for the effect of the reflected excitation beam: for the *Alum2* cell, the coefficient η was around 5%, so that the systematic error could be as high as 35% the PV angle, for a given sign of the tilt. For the successive cell, we used to manage to reach reflection coefficients better than 3‰, so that a possible systematic error would be less than 2% the PV effect. Anyhow, a regular reversal of the cell tilt allows to considerably lower the incidence of this effect on the final results, by averaging the measurements on the two configurations (see paragraph 2.5.4 on page 77); this reversal operation also allows to check the magnitude of the dependence of the signals on the tilt.

2.3.5 The measurement of the applied longitudinal electric field

We saw we use to apply a longitudinal electric field to assist the forbidden transition $6S \rightarrow 7S$ in cesium. The reversal of this field (performed every 0.5 s, on average), is the most powerful signature to detect the parity violation effect. In paragraph 2.3.3, a method was described, which allows to keep under control the asymmetry of the reversal of the field, but we didn't talk about the magnitude of the field itself, yet. Note that the PV angle is given by $\theta^{PV} = -\frac{\Im m(E_1^{PV})}{\beta E_z}$ (cf. paragraph 1.3.2), hence, in order to deduce $\Im m(E_1^{PV})$ from the measurement of θ^{PV}, it is fundamental to know how much is E_z.

We remind here the procedure, already used during E. Jahier's thesis [28], which exploits atomic signals to extract the value of the electric field "seen" by the cesium atoms.

The atomic signal sensitive to E_z

We already saw the expression of the effective dipole for the $6S \rightarrow 7S$ transition in cesium (equation (1.2)):

$$\begin{aligned}\mathbf{d}^{eff}_{6S,F-7S,F'} &= -\alpha\mathbf{E} - i\beta\boldsymbol{\sigma} \times \mathbf{E} + M_1'\boldsymbol{\sigma} \times \hat{\mathbf{k}}_\mathbf{L} - i\,\Im m(E_1^{PV})\,\boldsymbol{\sigma} \\ &= \qquad - i\beta\boldsymbol{\sigma} \times \mathbf{E} + M_1'\boldsymbol{\sigma} \times \hat{\mathbf{k}}_\mathbf{L},\end{aligned}$$

if $F \neq F'$ and we neglect the parity violating term.

A simple idea to evaluate the longitudinal electric field would be to use the amplification signal $\mathcal{A}$, which is proportional to $(|M_1'|^2 + \beta^2|E_z|^2)$. However, if we want to calibrate the result, we should measure the amplification without the applied field too (cf. below), which is proportional to $|M_1'|^2$, hence much smaller than the background absorption, and subject to a dominant pulse to pulse noise.

A better way to make a precise measurement is to use a polarimetric signal. If we excite the cesium atoms from $6S$ to $7S$ with a circularly polarized laser beam, the atoms acquire a polarization which is proportional to $(|M_1'|^2 + \beta^2|E_z|^2)$, and odd with respect to the helicity of the laser light ξ_{ex} [39]. This polarized population produces a circular dichroism γ_2 on the infrared probe beam: in order to detect γ_2, we just have to use our usual polarimeter in circular mode, i.e. with a quarter-wave plate before the polarizing beam-splitter cube. We have then an atomic imbalance da proportional to $(|M_1'|^2 + \beta^2|E_z|^2)$.

If we measure $\gamma_2(\xi_{ex}\text{-odd})$, alternately with and without the presence of the applied electric field, and we make the ratio R of the results, we obtain

$$R = 1 + \frac{\beta^2|E_z|^2}{|M_1'|^2}, \tag{2.8}$$

from which we deduce the value of $|E_z|$.

The orientation signal measured with an applied field is dubbed $P^{(2)}$ (or d$aP^{(2)}$, da staying for "imbalance"), recalling it is quadratic in E_z, whereas the zero field counterpart is dubbed $P^{(0)}$ (or d$aP^{(0)}$).

Note that, when we measure γ_2 at zero electric field, we have to take into account the presence of a background signal, although this is a polarimetric measurement. An interpretation for this polarized background has already been given in [28] (p. 178). Concretely, we measure $\gamma_2(\xi_{ex}\text{-odd})$ out of the resonance (e.g. with a detuning of the excitation laser of about 2 GHz[5]), and we subtract the result to the $\gamma_2(\xi_{ex}\text{-odd})$ measured at resonance.

We finally have to include small corrections for the measurement at zero applied field, due to the electric quadrupole transition E_2 [28, 40], which cannot be neglected, and to the presence of a residual random electric field [28]. These corrections appear as a multiplying factor before M_1', which will give a new quantity M_1'' to be substituted to M_1' in equation (2.8).

[5] We have checked the background is flat over several GHz.

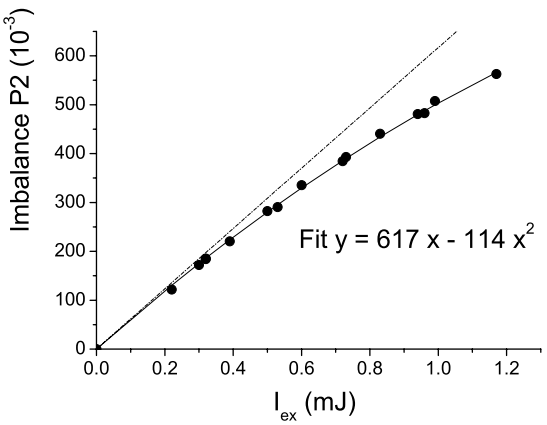

Figure 2.17: Imbalance $daP^{(2)}$ as a function of the energy of the excitation laser pulses, measured on the 3-4-5 transition.

For the 3-4-5 transition we have

$$\begin{aligned} M_1' &= M_1 + M_1^{hf} \\ \frac{M_1'}{\beta} &= (\frac{M_1}{M_1^{hf}} + 1) \cdot \frac{M_1^{hf}}{\beta} \\ &= 35.103 \pm 0.073 \text{ V/cm} \end{aligned}$$

where we have made use of the quantities presented in paragraphs A.1.2 and A.1.3.
After including the corrections for the quadrupole transition (3.8(2)‰, see A.1.7) and for the residual electric field (7.3(2.4)‰)[6], we obtain

$$\frac{M_1''}{\beta} = 35.49 \pm 0.11 \text{ V/cm},$$

from which

$$E_z \simeq (35.49 \pm 0.11) \text{ V/cm} \cdot R^{1/2}.$$

Measurements

We have performed the calibration of the longitudinal electric field for different values of the relative applied high voltage. For low voltages, the amplification is low, but even for fields as low as 100 V/cm the signal to noise ratio is enough to reach a 1% precision. For high voltages, the signal is much higher; However, in this case we have to deal with non linear phenomena due to saturation effects. We report

[6] cf. E. Jahier's thesis [28], p. 175. We assume that the residual field in alumina grooved cells is the same as in smooth-wall sapphire cells.

Measured $\mathbf{d}aP^{(2)}$ (10^{-6})	$\mathbf{d}aP^{(2)}_{lin}$ (10^{-6})	**Measured** $\mathbf{d}aP^{(0)}$ (10^{-6})	**Measured Background** (10^{-6})	$\frac{\mathbf{d}aP^{(2)}_{lin}}{\mathbf{d}aP^{(0)}_{corr}}$	$\frac{E_z^{real}}{E_z^{nom}}$
319000	350000	337	35	1157	94%

Table 2.8: Example of measured and calculated quantities, which take part in the calibration of the applied electric field. Measurements from 1/2/2002, with a nominal field $E_z = 1290 \pm 14$ V/cm.

in fig. 2.17 the aspect of the imbalance signal for a 1700 V/cm nominal electric field, as a function of the energy of the excitation laser pulses. The imbalance $\mathrm{d}aP^{(2)}$ is evidently non linear, but it can be well fitted by a polynomial of the second order. Thanks to this fit, we have been able to correct our $\mathrm{d}aP^{(2)}$ measurements from this nonlinearity, defining:

$$\mathrm{d}aP^{(2)}_{lin} \;=\; \mathrm{d}aP^{(2)} + \frac{114 \cdot 10^3}{617^2}\,(\mathrm{d}aP^{(2)})^2.$$

An example of the quantities which are measured and calculated to deduce the real E_z is given in table 2.8. The nominal field E_z^{nom} is deduced from the numerical simulation presented in paragraph 2.1.1, and from the measurement of the pulsed voltages applied to the two end electrodes (each one read on a digital oscilloscope, after a resistive divider), with a 1% precision.

In fig. 2.18, we report the results of our calibration measurements, for nominal fields between 100 and 1200 V/cm. The weighted average of the ratio between the measured E_z^{meas} and the nominal E_z^{nom} is 95.2(6)%: this 5% lack with respect to the expected value has already been interpreted as a probable consequence of the presence of free charges inside the cell, during E. Jahier's thesis [28].

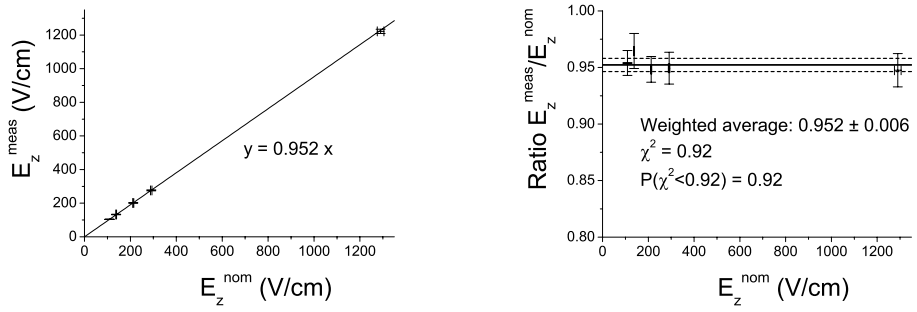

Figure 2.18: Calibration of the longitudinal electric field, for different values of the applied high voltage. The measurements were performed on 1/2 and 4/2/2002.

For our 1730 V/cm nominal electric field, the real electric field is then $E_z = 1647 \pm 10$ V/cm. Hence, from Boulder group's result [41] (see equation (A.7)), we expect the following value for the parity violating angle:

$$\theta^{PV}_{\text{expected}} \equiv \Im m \frac{E_1^{PV}}{\beta E_z} = 0.967 \pm 0.007 \ \mu\text{rad}.$$

2.3.6 The longitudinal magnetic field B_z(E_z-odd)

Once we have made all our preliminary controls, which allow to check the good properties of alumina grooved cells, before beginning PV measurements, we still have to test the most important systematic effect, which comes from the component of the longitudinal magnetic field which changes sign when the applied electric field is reversed. As we already saw in paragraph 2.1.3, this is the only effect which perturbs the γ_1^{PV} measurement at the first order. When the cells used for the cesium spectroscopy were made of glass, such a "B_z-odd" arose from the superficial currents on the cesiated internal surface, and an imperfect symmetry of the cell. Now, with the last kind of cells, thanks to the high resistivity of alumina even with the presence of cesium, this phenomenon cannot occur any longer. However, because of the electrons emitted from the windows, and then accelerated by the applied field, there is a current inside the cell, whose imperfect cylindrical symmetry gives rise to another B_z-odd [28].

Fortunately, the longitudinal magnetic field not only expresses itself into a precession of the axes of the linear dichroism γ_1, which biases the PV measurement, but also into a circular birefringence α_2 which is particularly sensitive on the F=3 - F=4 - F=5 transition. Since in the normal configuration, our polarimeter detects both γ_1 and α_2, we have only to change the probe transition (from 4-4 to 4-5) to deduce the magnitude of B_z-odd from the measurement of α_2^{odd}. In practice, we also perform a calibration measurement on the two transitions by applying an external known longitudinal magnetic field, so as to deduce the exact conversion factors between α_2(3-4-5) and B_z, and γ_1,α_2(3-4-4) and B_z (see table 2.9).

3-4-5	3-4-4	
α_2/B_z	γ_1/B_z	α_2/B_z
-176 mrad/G	18 mrad/G	3.2 mrad/G

$$\Longrightarrow \boxed{\begin{array}{l}\gamma_1^{B_z}(\text{3-4-4}) = 0.10 \ \ \alpha_2^{B_z}(\text{3-4-5}) \\ \alpha_2^{B_z}(\text{3-4-4}) = 0.018 \ \alpha_2^{B_z}(\text{3-4-5})\end{array}}$$

Table 2.9: Calibration of the B_z-odd effect (from the measurements of 25/10/2002).

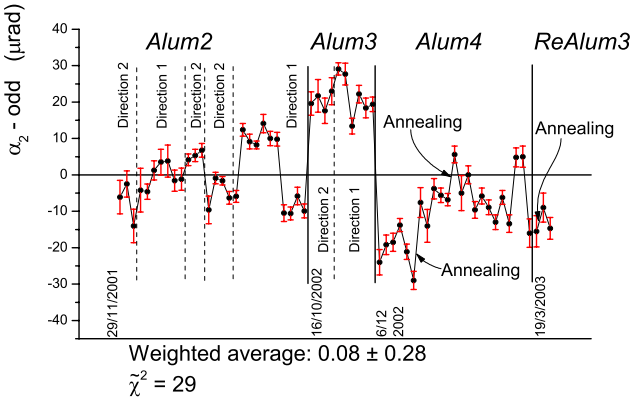

Figure 2.19: α_2^{odd} for the three alumina grooved cells, measured on the 3-4-5 transition. For *Alum2* and *Alum3*, we changed the direction of the cell inside the external oven many times, in order to see the possible effects on our measurements. Note that *Alum3* contained spurious residual gas. *ReAlum3* is the same cell as *Alum3*, after filling it again with Cesium, without spurious gas.

Magnitude of the effect

With the glass cells, the observed B_z-odd was of the order of 50 μG [29], which gave a systematic effect of the same order as the parity violation angle θ^{PV}. With sapphire and alumina cells, the B_z-odd was found to be of the same order, associated with the unwanted electronic flow inside the cell [28]. Actually, the measurement of the magnetic field was subject to drifts and sudden variations. This was attributed to come from the changes in the surface properties of the sapphire windows of the cell, which are typical from any insulated surface, irradiated by charged particles. In these conditions, it was impossible to undertake PV measurements.

The grooved alumina cells led to a much better situation: the drastic reduction of the secondary electronic emission from the body of the cell led to a smaller B_z-odd. For the first grooved cell, *Alum2*, it seldom exceeded 50 μG (v. fig. 2.19). The drift of the B_z-odd was slower, and the sudden variations rare enough to allow to perform meaningful and precise measurements. For each run, the measurement of B_z-odd was then used to correct the value of the γ_1^{PV} measurement, affected by the B_z-odd systematic error (see paragraph 2.5.4).

In fig. 2.19, we report the B_z-odd measurements, chronologically ordered, for the three grooved cells we have tested. The very high value of the χ^2 indicates the value of the B_z-odd is not constant over a long period[7]. At the beginning of the year 2003,

[7]We remind the definition of the χ^2 for the weighted average over a sample of N measurements: $\chi^2 = \sum_1^N (X_i - \bar{x})^2/\sigma_i^2$, where σ_i is the standard deviation of each measurement X_i, and $\bar{x}$ the weighted average. The $\tilde{\chi}^2$ of fig. 2.19, also called reduced χ^2, indicates the χ^2 divided by the number of degrees of freedom $(N-1)$.

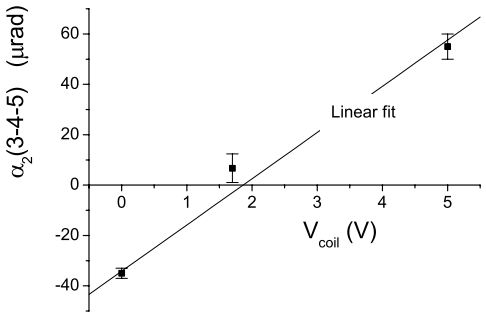

Figure 2.20: Effect of an applied external magnetic field, odd with respect to E_z, on the optical activity α_2^{odd} (3-4-5 transition).

we found a very interesting property: the B_z-odd can be reduced by annealing of the cell, between measurement periods. In practice we increase the temperature of about 50 or 60^oC for one or two days, and then we come back to our usual 210-220^oC.

Compensation of the B_z-odd

It is possible to compensate the unwanted B_z-odd by the application of an external magnetic field, which has to be of the same magnitude of the measured value of the B_z-odd, and opposite in sign. Of course, we have to reverse the magnetic field simultaneously with the applied longitudinal electric field. This procedure has been implemented and tested: in fig. 2.20, we have reported the values of α_2^{odd} measured for different values of the voltage V_{coil}, given to the coils which produce the external magnetic field along the $\hat{z}$ axis. We see that, by this way, for $V_{coil} = 1.7$ V, we manage to obtain an α_2 which is close to zero, hence to strongly reduce the incidence of the B_z-odd systematic effect on the PV measurement. Of course, since the B_z-odd can vary with time, we have to check regularly its magnitude, and accordingly change the value of the external correction.

Measurement of an α_2^{odd}, with an external gradient of the magnetic field: the pseudo B_z-odd

The test presented in this paragraph has been developed during E. Jahier's thesis [28]. It allows to understand the importance of the inhomogeneities of the longitudinal electric field inside the cell. Indeed, the electric field cannot be constant over all the length of the cell as the numerical simulation predicts, because of the electronic flow which follows each laser pulse: the electrons emitted are stopped when they reach the end of the cell, and they accumulate near the window, creating there a sudden drop of the electric field. When the applied field is reversed, the electronic flow changes direction, so that the location of the electric field drop changes, from one window to the other one.

	$\Delta B_z = 13$ mG		
	Alum2	*Alum3*	*Alum4*
α_2^{odd}(3-4-5) (μrad):	-6 ± 3	-16 ± 3	-26 ± 3

Table 2.10: Pseudo B_z-odd measurement: α_2^{odd} with an applied gradient of B_z (13 mG between the two windows of the cell).

Since there is amplification of the probe laser only where the electric field is present, in a simple scheme, we can say the cesium vapour near each window contributes to the detected signals only for one sign of the applied electric field. For example, let us say the electric field has to be "positive" for the vapour near the window "1" to contribute to the signal, so that the vapour near the window "2" contributes when the electric field is "negative".

Now, let us consider the case in which an external longitudinal magnetic field is applied, with a constant gradient along the cell (and average zero). If the electric field were homogeneous, the measured birefringence α_2^{odd} would be zero. However, in the real case, when the electric field is positive, the region "1" of the cell, where the magnetic field is $+B_z^{grad}$, for example, is probed, whereas the region "2" of the cell, where the magnetic field is $-B_z^{grad}$, is not. When the electric field is negative, we have the opposite situation: it is the region with a negative $-B_z^{grad}$ which contributes to the birefringence signal. Hence, by reversing the electric field, we alternately probe regions in which the longitudinal magnetic field is positive or negative. This creates a birefringence α_2^{odd}, which changes sign when we change the sign of the gradient of the external magnetic field. Since the effect and the measurement is identical to the one due to the presence of a B_z-odd, and the consequent systematic effect on γ_1^{PV} is the same, we call this measurement **"pseudo B_z-odd"**.

For an applied gradient of 13 mG between the two windows of the cell, the sapphire cell has a pseudo B_z-odd of the order of 800 μG, which gives a pseudo B_z-odd of the order of 30 μG if we consider the inhomogeneities of the residual magnetic field, carefully reduced to 0.5 mG. We could expect then a systematic effect on γ_1(3-4-4) of the order of 0.5 μrad [28].

For the alumina grooved cells, the situation is much better, as it is possible to see from table 2.10. If we use the calibration (cf. table 2.9), we see that the pseudo B_z-odd is below 150 μG, and for the first cell (*Alum2*), it is even below 50 μG with the applied 13 mG gradient, thus less than 2 μG for 0.5 mG residual field inhomogeneities.

2.4 Improvements of the experimental setup

2.4.1 Stabilization of the excitation laser frequency

During this thesis, we realized that the external thermalized Fabry-Perot cavity, on which the frequency of the excitation laser was locked, was not perfectly stable: the excitation laser frequency was subject to slow drifts. This didn't imply any

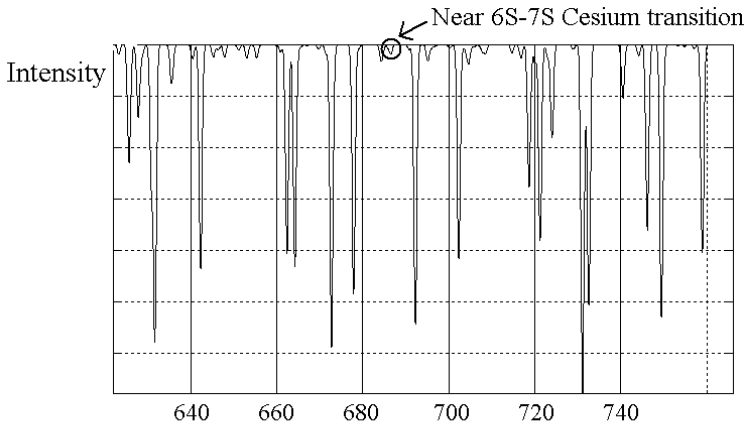

(a)

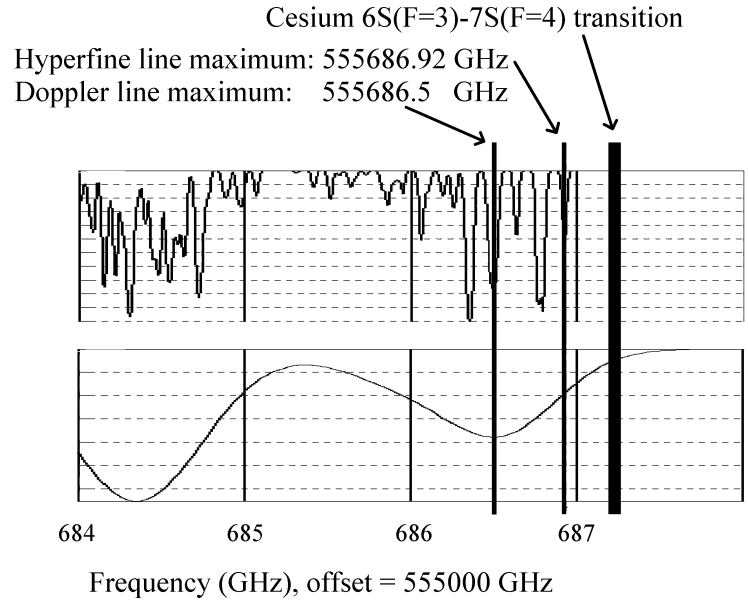

(b)

Figure 2.21: Theoretical spectrum of the iodine molecule, in the 539.5 nm region.
(a) Wide Doppler spectrum.
(b) Doppler and hyperfine lines, in the region of interest. We have indicated with vertical lines the maximum of the Doppler profile of the (J''=36, ν''=1- J'=37, ν'=31) transition, the hyperfine component $a15$, and the cesium frequency of interest.

systematic error on our measurements, since our calibration procedure eliminates any dependence of the signals on the line shape. However, it is necessary to be at resonance, to have the maximum possible amplification of the probe laser. In practice, during our measurements, when we noticed a decrease of the amplification

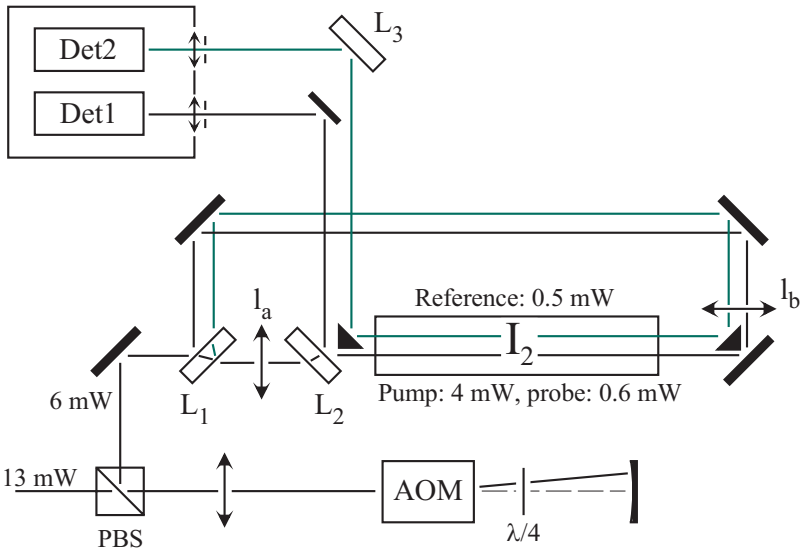

Figure 2.22: Experimental setup for the saturation spectroscopy of I_2. The 13 mW laser light enters the setup from the polarizing beam-splitter cube (PBS).
AOM is the acousto-optic modulator, which shifts and modulates the frequency of the laser (after the double passage of the light).
L_1, L_2 and L_3 are thick glass plates (whose surfaces reflect about 10% each). The probe and reference beams come from the reflections of the main beam on the two surfaces of L_1. L_2 transmits the pump beam (which arrives then in the cell), and reflects the probe beam which comes from the opposite direction (superimposed to the pump beam).
l_a and l_b are two 30 cm focal lenses, which focus the beams into the cell, in order to enhance saturation effects. In order to make the alignment of the pump beam into the cell easier, l_a is mounted on two translation stages, which allow fine mechanical adjustments along transverse horizontal and vertical axes.

signal, we paused the data acquisition and manually centered the frequency of the green laser in order to maximize the probe signals on the polarimeter.

In order to solve the problem, we decided to investigate the possibility to stabilize the laser on a iodine molecule (or I_2) line. In fig. 2.21, the theoretical spectrum of I_2, taken from the program *IodineSpec* [42] supplied by *Toptica*, is reported. By monitoring the frequency of our laser and the visible fluorescence in a iodine cell, we managed to individuate the closest line to the cesium $6S$-$7S$ transition: from (J''=36, ν''=1) to (J'=37, ν'=31). As you can see from fig. 2.21 (a), the intensity of the line is relatively low. The shift between the maximum of the iodine Doppler line, and the $(6S, F{=}3)$-$(7S, F{=}4)$ transition was measured to be between 670 and 750 MHz. Considering the theoretical frequencies of the iodine lines, these values lead to a $\Delta\nu = 330 \pm 40$ MHz shift between the closest hyperfine line ($a15$) and the cesium $6S$-$7S$ transition.

We then decided to use saturation spectroscopy in order to resolve the hyperfine lines. Thanks to a beam-splitter, a small portion of light (about 13 mW) is taken

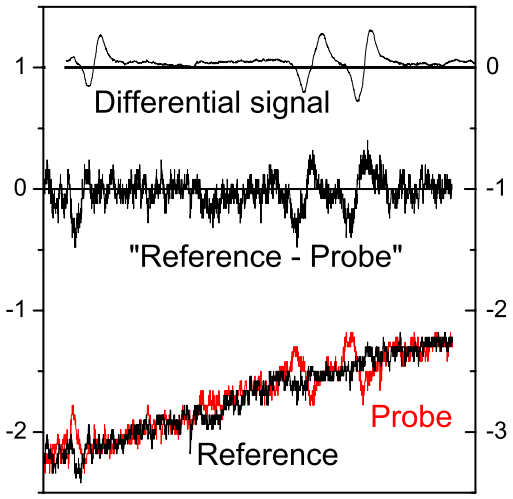

Figure 2.23: Experimental probe and reference signals from iodine spectroscopy saturation (Pump intensity = 5 mW, $\Delta\nu(AOM)$ = 180 MHz, modulation amplitude = 1.8 MHz, modulation frequency = 19 kHz, integration time = 300ms). From left to right, we have the following hyperfine lines: $a15$, $(a14, a13)$ and $(a12, a11)$.
Probe is the probe signal seen after lock-in detection, *Reference* is the reference signal seen after lock-in detection, *"Reference-Probe"* is the difference between the first two spectra (*Reference* and *Probe*). *Differential signal* is the lock-in output, when the input is directly the difference between Reference and Probe.
Note how clean is the *Differential signal*, compared to *"Reference-Probe"*, which is affected by the Doppler background noise.

from the main CW dye laser, and enters the setup described in fig. 2.22. Note that the order of magnitude of $\Delta\nu$ allows to use a double-passed acousto-optic modulator (AOM) in order to shift the frequency of the laser by $\Delta\nu$. By this way, when the light which comes from the AOM is stabilized on the $a15$ hyperfine iodine line, the main laser is stable on the frequency which correspond to the $6S$-$7S$ cesium transition. Since we want to use lock-in detection, we use the AOM also to modulate the frequency of the radiation.

The idea of the setup is to probe the iodine sample with two laser beams, called *probe* and *reference*, which are detected then by $Det1$ and $Det2$. The two beams are subject to Doppler absorption in the same way, since they interact with the same quantity of iodine molecules. However, the probe beam is superimposed with the 4 mW pump beam, and is then subject to spectroscopy saturation effects too. By detecting the difference between $Det1$ and $Det2$, we obtain hyperfine lines from saturation spectroscopy, with a significantly reduced Doppler background. The first harmonic lock-in detection, of the frequency-modulated signal, gives directly dispersion lines, on the zero of which it is possible to stabilize the laser (see fig. 2.23).

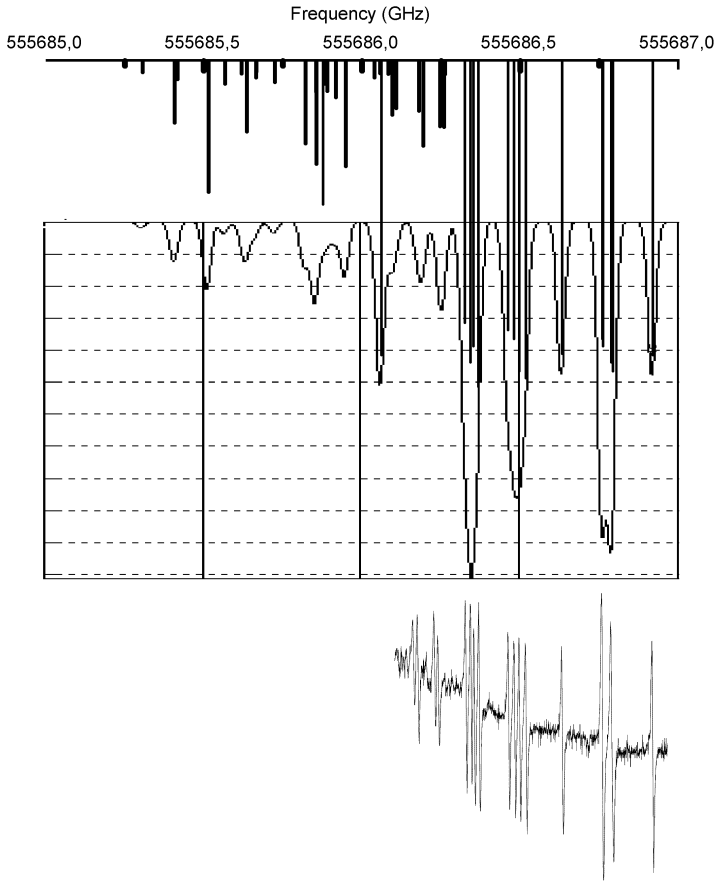

Figure 2.24: Comparison between theoretical and experimental data: theoretical lines, theoretical spectrum, and first harmonic lock-in measurements (Pump intensity = 4 mW, $\Delta\nu(AOM) = 180$ MHz, modulation amplitude = 1.8 MHz, modulation frequency = 19 kHz, integration time = 300ms). Note the presence of a varying offset, due to imperfect elimination of the Doppler background.

Another advantage of the differential detection is the reduction of the laser intensity noise: the two detected beams are subject to the same intensity fluctuations, which cancel out in the subtraction process. Since the iodine line of interest is very weak, we have to enhance saturation effects by focusing the laser beams into the cell, with 30 cm focal lenses, and we use a long iodine cell (50 cm), in order to increase the absorption signal.

We realized during the first tests that a problematic feature of our setup was the existence of a large offset in the final signal, which resulted to be of the same order of magnitude as the height of the dispersion lines. In order to minimize the offset due to an imperfect removal of the Doppler background (performed by subtracting the reference signal from the probe), the optics was already placed in such a way as to have almost the same light intensities for the probe and the reference, which go in

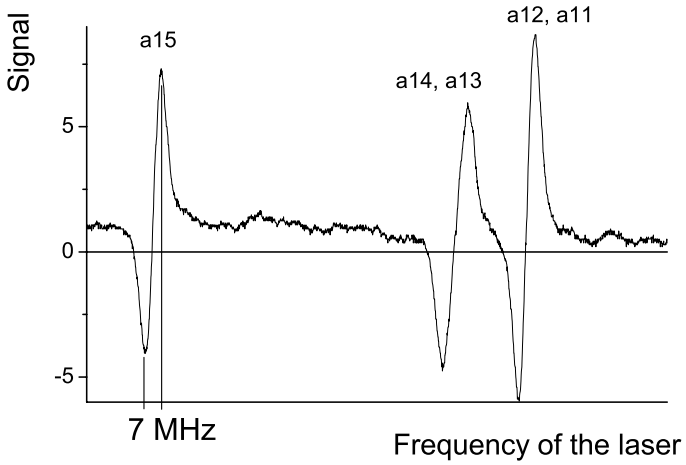

(a)

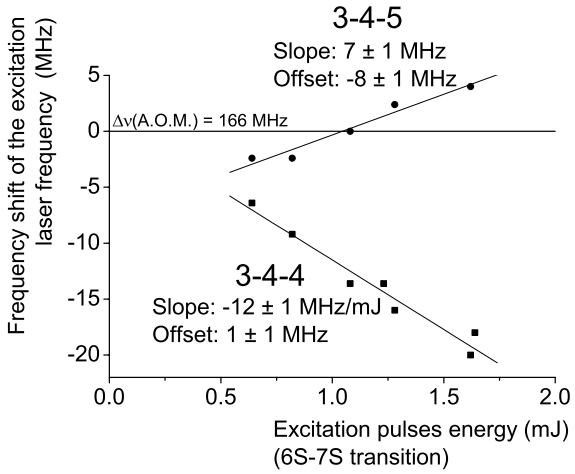

(b)

Figure 2.25: Stabilization of the laser.
(a) Experimental spectrum (Pump intensity = 5 mW, $\Delta\nu(AOM) = 180$ MHz, modulation amplitude = 1.8 MHz, modulation frequency = 19 kHz, integration time = 300ms): the width of the $a15$ line (between the minimum and the maximum) is 7 MHz (if we suppose the hyperfine line is Lorentzian, this corresponds to $\sqrt{3} \cdot 7 = 12$ MHz FWHM). The $a15$ line is the one we use to stabilize the laser.
(b) Light shift: shift of the excitation laser frequency, with respect to the iodine $a15$ line, for different energies of the green pulses. (Since there is double passage into the AOM, the shift of the laser $\Delta\nu(laser)$ is twice $\Delta\nu(AOM)$).

*Det*1 and *Det*2. The remaining asymmetries between the two channels (*Probe* and *Reference*) were corrected thanks to a potentiometer, acting on the signals coming from *Det*2 for example, just before performing the subtraction.

However, two other processes contribute to the offset: along with the frequency modulation, the *AOM* cannot prevent a small amplitude modulation of the light, and there is also a very tiny modulation of the direction of the light which comes from the *AOM*, which depends on the alignment. In order to minimize the consequent displacement of the light on the detectors (which could produce modulation of the signals), we focus the laser on *Det*1 and *Det*2, with the help of short focal lenses. With regard to the amplitude modulation, the possible effect is already greatly reduced thanks to the subtraction of the *Reference* signal from the *Probe* signal. However, we realized that the detectors were reached by stray amplitude modulated light, in different proportions, which created in the final signals a big offset. Protecting the detectors with a black screen, and diaphragms before the focusing lenses, solved the problem. Of course, there is still a great sensitivity of the offset to the global alignment of the setup (for example, if the diaphragms are not well centered around the beam, the tiny modulation of the direction of the light turns into an amplitude modulation, after the diaphragm). In practice, if necessary, the remaining offset is compensated thanks to our potentiometer (but at this point the resulting offset will not be constantly 0, in general, for all the hyperfine lines, cf. fig. 2.24).

Since the end of this thesis, the group has solved the problem of the offset with an upgrade of the setup, by using two acousto-optic modulators. With the first one, the frequency of the pump is shifted and modulated. With the second one, the frequency of the probe is shifted, without any modulation, this time. By this way, only saturation effects are modulated, and then there is no Doppler background, nor offset, in the resulting signals. There is no more unwanted intensity modulation on the probe beam, and no more need for the reference signal.

Once the spectroscopy saturation setup was fully functional, we could use the correction signal coming from the lock-in to stabilize the excitation laser at the center of a hyperfine iodine line. Actually, the laser is still stabilized on the external Fabry-Perot cavity, which is now itself driven by the iodine correction signal (by means of suitable integration). In fig. 2.25, we present some of our results. The laser, stabilized on the iodine molecule, can now be used to excite the cesium atoms in the PV setup. The shift $\Delta\nu$ is chosen in order to have the laser centered on the cesium transition. We report in fig. 2.25 (b) some values of $\Delta\nu$, measured with respect to the iodine reference, for the 3-4-4 and 3-4-5 transitions, as a function of the excitation pulses energy (cf. light shift effects).

2.4.2 Reducing the absorption of the probe beam

We saw in paragraph 2.3.3 the existence of an absorption on the probe beam, of the order of 5%, which is basically not harmful on polarization signals. However, it happened during our runs to have absorptions as high as 15%, and the consequent

drop of signal did not allow to continue measurements in good conditions. In this paragraph, we review the mechanisms of the appearance of the absorption, and explain how the temperamental behaviour of the extinction coefficient of the optical switch (which produces 20 ns long probe pulses from the continuous laser @1.47 μm, cf. paragraph 2.1.1) causes an anomalous increase in the absorption. We then describe the implemented solution: a Pockels cell, cascaded to the optical switch.

Origins of the absorption

The absorption of the probe beam on the $7S$-$6P_{3/2}$ transition comes from the appearance of an atomic population in the $6P_{3/2}$ state. We know two mechanisms for this phenomenon to occur, following the exposure to the excitation pulse @539 nm [31]. The first one is the photodissociation of the cesium dimers Cs_2, which produces, after deexcitation, atoms in the $6P$ state:

$$\begin{aligned} Cs_2 \;+\; \gamma(539\,\mathrm{nm}) \;&\rightarrow\; Cs(5D_{5/2}) \;+\; Cs(6S) \\ Cs(5D_{5/2}) \;&\rightarrow\; Cs(6P_{3/2}) \;+\; \gamma(3.49\,\mu\mathrm{m}). \end{aligned}$$

From the characteristic times of the decay reactions from $5D$, the maximum of the absorption was found to occur for a pump-probe delay of 2 μs.

The second mechanism is the excitation from $6S$ to $6P$, due to Franck-Hertz collisions with the electrons photo-emitted from the windows of the cell, and accelerated by the longitudinal electric field. Since the transit time of the electrons across the cell is very small (about 2 ns), the excitation to the $6P$ level takes place only during the green laser pulse (20 ns long).

In order to reduce the effects of the photodissociation of dimers, the density of Cs_2 is reduced by keeping the temperature of the body of the cell higher (around 220 ^{o}C) than the temperature of the side arm (140 ^{o}C), therefore favouring thermodissociation of the molecules.

Note that it is not possible to bring up the temperature of the body too much: above 250-260 ^{o}C, there is a sudden increase in the absorption, even without the application of excitation pulses. This phenomenon is explained by the appearance of a thermoelectronic emission of the windows, assisted by the electric field: again, this leads to Franck-Hertz collisions, which populate the $6P$ level.

In the end, for our typical experimental conditions, the phenomenon which mainly contributes to the absorption is the electronic photo-emission.

The leakage photons

The extinction coefficient of the optical switch is usually better than 10^{-3}. 10^{-3} means that, following the probe pulse, 1‰ of the photons leak through the switch and continue to probe the cesium sample: the leakage photons participate to the detected signals for a time of the order of 1 μs, which is tightly related to the characteristic time of the detection amplifier (cf. next paragraph).

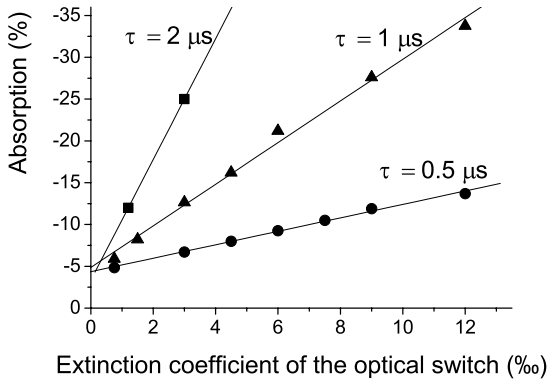

Figure 2.26: Absorption measured on the 3-4-5 transition, as a function of the leakage photons flux, for different values of the time constant τ of the pulse amplifiers. The intensity of the probe light reaching the cell was about 250 μW (with the optical switch on).

But this is just the time when the amplification has finished, and the absorption effects continue to grow, and become important (cf. photodissociation of dimers). As a result, the leakage photons are particularly sensitive to the absorption, and this is evident in the experiment: if we increase the leakage flux[8], the measured absorption increases (see fig. 2.26).

The pulse amplifier

In the end, the way the leakage photons act on our measurements depends on our detection chain. We remind the stages which lead to the digitalization of the signals coming from the two photodiodes of the polarimeter: for each channel, integration of the pulse with a low-noise pre-amplifier; use of a pulse amplifier (*Ortec* spectroscopy amplifier), which produces 3 μs long, gaussian-shaped pulses; production of 5 μs long, rectangular pulses, thanks to a stretcher circuit (*Tennelec*); digital conversion with a 14 bits ADC.

It is possible to choose the time constant of the pulse amplifier, among the following values: 0.5, 1 or 2 μs. We realized, during our tests, the measured absorption is very dependent on this parameter: when we increase the time constant, the leakage photons contribute to the signals for a longer time, leading therefore to a higher measured absorption (see fig. 2.26). However, it is not desirable to choose the smallest time constant for our measurements, because in this case we observe an important increase in the noise: the less the signals are filtered, the noisier they are (see fig. 2.27). Actually, we realized that, if we don't apply the longitudinal electric field, we obtain cleaner signals, with a noise which does not depend on the

[8]It is possible to degrade artificially the extinction coefficient of the optical switch by slightly changing the applied voltage.

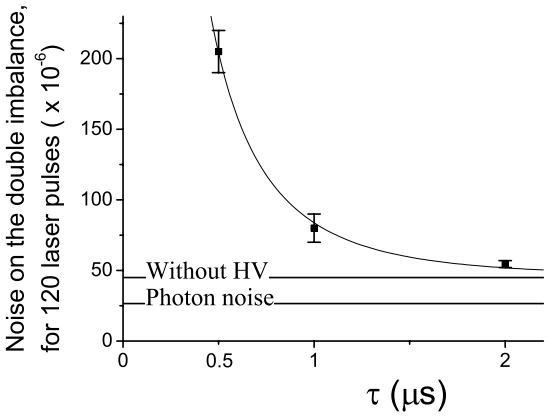

Figure 2.27: Instantaneous noise measured on the 3-4-4 transition for the different values of the *Ortec* time constant (*Alum4* cell). We report the noise of the double imbalance, for 120 laser pulses of $1.5 \cdot 10^7$ photons each, without amplification (the excitation laser was off). The noise in the absence of the electric field, and the theoretical photon noise are indicated with a horizontal line.

time constant. This means our detection is affected by the electric parasites which come with the pulsed high voltage. In this respect, we plan to carefully investigate the question, and find how to protect the polarimeter from this kind of noise when the latter is not negligible (the magnitude of the electric parasites was found to be dependent on the tested cesium cell).

Problems with the optical switch

As it is possible to see from fig. 2.26, the problem of the absorption arises for anomalous leakages of photons: in normal experimental conditions, the absorption is low. However, it happened too often to have temporary deteriorations of the performances of the optical switch, generally coming from sudden climatic changes (temperature, humidity). In these cases, the extinction coefficient worsens, and can become even higher than 5‰. This implies a large increase in the absorption, and therefore a reduction of the signals. We also noticed a spectacular raise in the noise of the signals which come from the pre-amplifier. In the end, several times, the too low signal to noise ratio did not allow to undertake serious measurements.

In order to avoid this annoying dependance on the optical switch performance, we decided to implement a system which cuts off the leakage photons: a Pockels cell, which closes immediately after the end of the probe pulse.

The Pockels cell: setup

We placed the Pockels cell at the output of the CW probe laser, before the optical switch. The beam is let through when the high voltage (600 V) is applied to the two

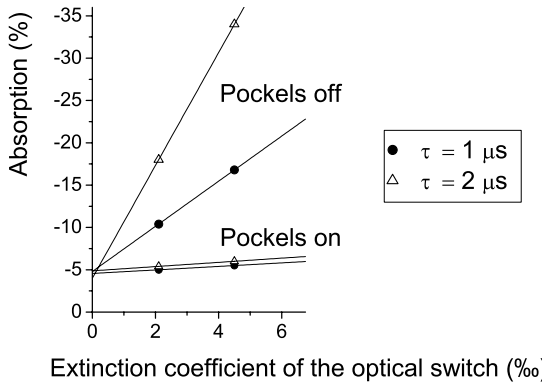

Figure 2.28: Effect of the Pockels cell on the absorption measurements, on the 3-4-5 transition. The effect on the 3-4-4 transition is almost the same.

Pockels electrodes. The transmission was measured to be 91%, and the extinction ratio 4‰.

In order for the Pockels cell to stop the probe beam as soon as the optical switch closes, we have to be able to drive our device with high voltage pulses, whose transient times are small. We had the occasion to test two pulse generators, from the *DEI* company[9]: *FPX800* and *FPX1000*. For the first one, the rise and fall times are about 20 ns, whereas for the second one, they are less than 10 ns.

First tests

For our first tests, the Pockels was triggered in such a way that it closed only after the first probe pulse, for 3 μs, and was open for the rest of the time, letting through the four reference pulses. This configuration, which was easy to implement, since we only had to synchronize the trigger with the first laser pulse, allowed to check how good was the effect on the measured absorption, before spending time to settle the definitive scheme, described in the next paragraph.

In this way, we had to take care about the asymmetry between the first laser pulse and the following reference pulses, still affected by the presence of leakage photons, therefore giving rise to slightly larger detected signals. This was seen as a "false" absorption (measured in the absence of excitation laser or longitudinal electric field), an offset which had to be subtracted from our "true" absorption measurements.

The results are reported in fig. 2.28: thanks to our system, the absorption is reduced to the possible minimum value. Since the two pulse generators we tested gave identical results, we decided to keep the *FPX800*, which was the cheapest one.

Note that it is not possible to have an absorption lower than 4 or 5%, even if we extrapolate the curves in fig. 2.28 to a null extinction coefficient: the 20 ns probe

[9]For our first tests, the pulse generators were generously lent by the French distributor Armexel.

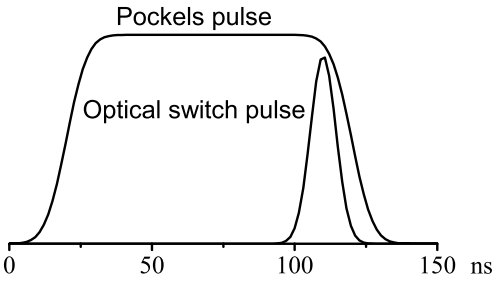

Figure 2.29: Timing of the pulses which govern the optical switch and the Pockels cell.

pulse is itself already subject to the absorption which comes from the Franck-Hertz collisions.

A penta-pulse trigger for the Pockels

The very encouraging results prompted us to implement a trigger synchronized with the penta-pulse which governs the optical switch. The *FPX800* provides high voltage pulses of 80 ns minimum duration. We decided then to let the Pockels open only for the 100 ns which precede the end of the usual 20 ns long laser pulse (see fig. 2.29). Note that, since the Pockels cell has been placed before the optical switch, a further benefit of this system is the largely reduced exposure of the optical switch to the 50 mW probe light. This is very welcome, since in many occasions we noticed a deterioration of the performances of this device, consecutive to the introduction of the probe beam.

The trigger for the first pulse was easy to implement, since it was directly taken (with the suitable delay) from the quartz clock which governs all the experiment: the pulses of the excimer laser, of the high voltage for the longitudinal electric field, etc.

Concerning the reference pulses, originally the trigger which drove the optical switch (four 20 ns long pulses, separated in time by 0.9 ms) was generated from the first pulse, thanks to a simple dedicated circuit. From these four pulses, it would have been possible to generate four other synchronized pulses, with a small adjustable delay, to govern for example the Pockels cell. However the trigger of the Pockels has to start before the trigger of the optical switch. Hence, we decided to consider the opposite point of view: from the first pulse, a circuit produces four 100 ns long pulses (separated in time by 0.9 ms) to drive the Pockels cell. Then, from this set of four pulses, a second "tetra-pulse" with an adjustable delay (around 80 ns) is generated to drive the optical switch. This scheme is summarized in the diagram of fig. 2.30.

At this point, it seems right to ask why not to choose the following simpler solution: to generate all the five optical switch pulses from the Pockels penta-pulse. Actually, we did not talk yet about another constraint, which prevents this possibility. When

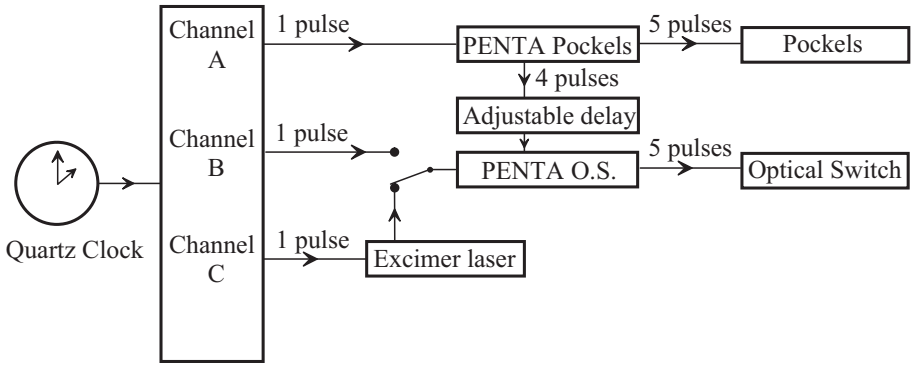

Figure 2.30: Block diagram for the generation of the triggers, for the Pockels cell and the optical switch. It is possible to adjust the delays of each channel (A, B, etc.). The first pulse of the optical switch can be triggered by the channel B (for auxiliary measurements), or by the excimer laser pulses (for real measurements).

we perform measurements with the excitation laser at resonance, in order to maximize the amplification on the probe laser, the delay between the excitation and the probe pulses has to be short (a few nanoseconds), and exactly determined, without any jitter nor drift at the 1 ns level. However, there is an unavoidable jitter between the trigger which drives the excimer laser (which pumps the dye cells, providing the excitation pulses @539 nm) and the produced excimer pulses, which is small (less than 5 ns) but enough to affect the amplification. Therefore, when we undertake measurements, the first probe pulse generated by the optical switch is triggered with respect to the excimer pulse instead of the clock. This is realized thanks to the signal coming from a photodiode which receives a small portion of the excimer beam[10].

Once we managed to implement the triggers, we repeated the absorption measurements, this time without any problem of "false" absorption, and we confirmed the results presented in fig. 2.28. This new device proved then to be very useful, to protect the measurements from the whims of the optical switch, and to allow to choose a longer time constant of the *Ortec* amplifier, so as to minimize the noise coming from the high voltage pulses parasites (see fig. 2.27).

2.4.3 Use of a polarization magnifier: the dichroic cube

Description and motivations

During this thesis work, we tested and implemented a system, placed before the polarimeter, which allows to amplify the probe beam polarization rotations [43]. It consists of a dichroic cube made of two coated prisms stuck together, with two natural axes $\hat{x}$ (horizontal) and $\hat{y}$ (vertical). The internal surfaces of the prisms have been coated so as to obtain a transmission coefficient which depends on the

[10]It is possible to change from the "clock trigger" to the "excimer trigger" with a simple switch. Indeed, the "clock trigger" is very useful for all the measurements which don't need the presence of the excitation pulses.

polarization of the incident probe beam: $T_x \simeq 1$ for the component along $\hat{x}$, and $T_y \simeq 20\%$ for the component along $\hat{y}$, T staying for the intensity transmission (as opposed to the field transmission t). The amplification of the tilt occurs when the incident beam polarization is nearly vertical: it easy to see that after the passage through the cube, the angle between $\hat{y}$ and the light polarization has been multiplied by a factor $K = \sqrt{T_x/T_y}$, and the number of photons reduced by T_y. Note that if we consider $T_x = 1$, the introduction of the cube does not modify the signal to photon noise ratio: nevertheless, with this system it is possible to gain on the non photonic sources of noise. The other main advantage of the use of the cubes is the reduction of the number of transmitted photons, which allows to increase the probe pulses energy, hence increase the detected signals, without saturating the detection electronics. In paragraph 2.5.5, we will quantify the experimental benefits obtained from the use of the magnifier, presenting the features of the measurements on the *Alum4* cell, with and without the implemented cube.

Experimental characterization of the cube

With respect to the dichroic plate described in [43], the cube has the advantage not to translate the laser beam, allowing to insert and remove it in the setup without need to a drastic realignment of the detection optics each time.

The cube must have dichroic properties along the $\hat{x}$, $\hat{y}$ axes, without introducing defects on the polarizations, in particular unwanted birefringences. The desired T_y was about 10%: enough to have a good magnification ($\sqrt{10}$) of the polarization rotations, without suppressing the number of detected photons too much. Because of the so specific asked properties, the magnifier had to be made to measure. It was ordered to *Optique J.Fichou S.A.*, which realized several prototypes to be tested in our experiment. Unfortunately, the step of the two prisms gluing process introduced uncontrolled modification of the coating features, and the resulting cubes did not match our severe initial specifications: they were characterized with a too low T_y,

T_y	T_x/T_y	$\Delta\phi$	$M.F.$
0.98	24	50°	3.2
0.9	18	10°	4.0
0.9	23	9°	4.8
0.96	6.6	17°	2.4
0.95	5.6	13°	2.3

Table 2.11: Characterization of the tested cubes. T_x and T_y are the transmission coefficients for $\hat{x}$ and $\hat{y}$ polarizations, $\Delta\phi$ is the phase difference coming from the birefringence, $M.F.$ (magnification factor) is the amplification of the polarization rotation, measured as described in the paragraph. The relatively small values of T_y (about 90%) concerned cubes whose external faces had no antireflection coating. The last two cubes were the one used to test the system on true PV measurements.

and above all a very high linear birefringence along the $\hat{x}$ and $\hat{y}$ axes (cf. table 2.11). It was possible to modify the parameters by slightly tilting the cube with respect to the incident beam, but if we tried for example to improve T_y by this way, the birefringence became worse.

The amplification of the polarization rotations, obtained with the cube, was measured by rotating the Glan prism which defines the linear probe polarization, and measuring the effect on the simple imbalances measured by the polarimeter. This method was performed with and without the cubes to be tested, in order to compare the results.

The measurement of the birefringence is slightly more complicated [43]. First, note that the birefringence affects the tilt amplification by a $\cos\Delta\phi$ factor (where $\Delta\phi$ is the phase difference between the $\hat{x}$ and $\hat{y}$ components of the polarization, acquired after the passage through the cube). However there is a much more sensitive quantity, which allows a precise measurement: for a circular polarized incident beam, the imbalance detected by the polarimeter, after the cube, is [43]:

$$D^{circ} = \sin(\Delta\phi)\ \frac{2|K|}{1+|K|^2}.$$

The circular polarization σ_+ is obtained with the insertion of a quarter-wave plate. In order to obtain the part of the imbalance due to the birefringence, we perform the measurement for the σ_- polarization too (obtained with the insertion of a half-wave plate), and we consider the semi-difference of the two results. Then, from D^{circ} and the measured transmission coefficients T_x, T_y, it is easy to deduce the birefringence $\Delta\phi$.

Alignment of the magnifier system

Since the specifications of the last tested cubes were not so far from what we wanted, we decided to implement the magnifier system. There are two possible configurations of the probe polarizations, before the polarimeter (and hence before the cube), along the vertical ($\hat{y}$) or the horizontal ($\hat{x}$) axes. This means we had to find a system to use the magnifier for both configurations. Our first try was to build a supporting framework, similar to the insertable lambda plates holders, which allowed to switch between two cubes, the first one normally aligned, and the second one rotated by 90°, so as to attenuate the $\hat{x}$ component of the polarization instead of the $\hat{y}$ component. However, this made the alignment of the two cubes more difficult, and we also had to accept to work with two relatively different cubes, since the making process did not allow to produce cubes identical enough (the gluing step casually modified the properties of the coating). We then decided to implement another system, with a single cube normally aligned in the setup, for the amplification of the nearly vertical polarizations rotations. Then, in order to exploit the cube for horizontal incident polarizations, we placed just before the cube, a switchable half-wave plate (which is obviously not inserted for $\hat{y}$ polarizations), in such a way that the horizontal polarizations are brought near the vertical axis.

With this system we could perform several measurement runs on the *Alum4* cell. This allowed to observe the clear improvement of the signal to noise ratio (cf. paragraph 2.5.5). However, the high birefringence was source of systematic effects, which were detected from anomalous variations of the signals over the four different excitation laser polarizations $\hat{y}$, $\hat{x}$, $\hat{u}$, $\hat{v}$ (also called anisotropies of the signals). Nevertheless, after the end of this thesis another kind of magnifier (a set of Brewster plates, without annoying birefringences) was implemented, and confirmed the improvement on the polarimetric signals, without introducing any systematic effect.

2.5 Parity violation measurements and analysis

We have already presented in paragraph 2.1.2 the general method to measure parity violation, with all the useful signatures which discriminate the true PV effect from the instrumental defects. In the following, after a brief recall about some important aspects of the acquisition work, we describe the analysis method used to exploit the experimental data at best. Of course, since at the beginning of the thesis we had just reached the experimental conditions which consented to undertake long PV measurements, it was not imaginable to reach our 1% precision goal in only one step: we had to perform a preliminary measurement [24], with a 8.4% precise result, presented in this chapter with the relative analysis of the possible systematic effects (anisotropies). The experience acquired with the achievement of this milestone allowed to understand the problematics to face in order to be able to obtain the conditions which will bring the 1% precision within our reach. In the end, we report our analysis of the short-term and long-term noise, which highlights the benefits coming from the use of the polarization magnifier introduced in paragraph 2.4.3.

2.5.1 Organization of the PV acquisition

Data acquisition sequence

We have seen in paragraph 2.1.2 that a complete PV data set includes the polarization measurements over a set of states, each one defined by the position of the half-wave plates (inserted or not), the sign of the longitudinal electric field E_z and the sign of the calibration angle θ^{cal}.

The acquisition proceeds at a rate between 80 Hz and 150 Hz[11], with 1.5-2 mJ excitation pulses, immediately followed by the amplified probe pulse (about $4 \cdot 10^7$ photons before amplification), and the four reference pulses, which give a measurement of the double imbalance. After thirty excitation pulses (i.e. thirty double

[11]The rate is limited by the performance of the pulsed dye amplifier, which is itself critically dependent on the goodness of the optics alignment. In the last months, after a revision of the alignment of the whole system from scratch (which took one day), it was possible to measure with a 150 Hz rate without any problem on the geometrical stability of the excitation pulses: the shape of the beam, observed with a CCD camera, was excellent, and the position at the cell level, monitored with a 4-quadrants photodiode, did not significatively changed from pulse to pulse.

State	1	2	3	4	5	6	7	8	9	10	11	12	13	14	15	16
θ^{cal}	+	-	+	-	+	-	+	-	+	-	+	-	+	-	+	-
E_z	+	+	-	-	+	+	-	-	+	+	-	-	+	+	-	-
$(\frac{\lambda}{2})_{det}$	-	-	-	-	+	+	+	+	-	-	-	-	+	+	+	+
$(\frac{\lambda}{2})_{pr}$	-	-	-	-	-	-	-	-	+	+	+	+	+	+	+	+

Table 2.12: The 16 possible states for a fixed excitation polarization $\hat{\epsilon}_{ex}$. $(\lambda/2)_{det}$ is the half-wave plate placed at the entrance of the polarimeter to select true polarization effects, whereas $(\lambda/2)_{pr}$ is the the half-wave plate which rotates the probe polarization by 90^o to distinguish γ_1 from α_2.

imbalance data), we change configuration, according to table 2.12, which summarizes all the possible states at fixed excitation polarization. Actually, the choice of the initial states of E_z, $(\lambda/2)_{det}$ and $(\lambda/2)_{pr}$ is random, in order to avoid possible spurious effects on our measurements, synchronous with the frequency of the parameter reversals, and also to obtain quantities odd with respect to reversals performed in both directions (for example, from positive to negative and from negative to positive electric field). The reversal of θ^{cal} and E_z is performed four times, before inserting or removing the plates, in order to take advantage of their relatively low dead times, the dead time for mechanical operation being much higher (this implies a factor 4 in addition to our 16 states when we count the collected data). Before changing the excitation polarization, the measurement sequence is repeated 5 times. In the end, for a single excitation polarization, we have $4 \times 16 \times 5$ bunches of 30 double imbalance measurements.

The excitation polarization is then changed according to the scheme $\hat{y}$, $\hat{x}$, $\hat{u}$, $\hat{v}$, $\hat{v}$, $\hat{u}$, $\hat{x}$, $\hat{y}$, and we therefore obtain, from the double imbalances analysis, the correspondent quantities (γ_1^y, α_2^y), (γ_1^x, α_2^x), (γ_1^u, α_2^u), (γ_1^v, α_2^v), (γ_1^v, α_2^v), (γ_1^u, α_2^u), (γ_1^x, α_2^x), (γ_1^y, α_2^y) etc. From these ones, we deduce

- the anisotropies, i.e. the differences between the results for the four polarizations, which allow to understand and keep under control a certain class of systematic effects, which break the cylindrical symmetry (cf. paragraph 2.5.3);
- the isotropic γ_1 and α_2: the first one is exactly the PV violation angle we are interested in, whereas the second one is expected to be zero (cf. paragraph 2.5.4). Each couple of values (of γ_1 or α_2), along $\hat{x}$ and $\hat{y}$ or along $\hat{u}$ and $\hat{v}$, gives an isotropic value S_{xy} or S_{uv}, defined as the mean.

Dynamics of the measurements

Before undertaking a long PV measurement, we have seen we have to check and optimize many parameters. In particular, the tilt of the cell has to be minimized, taking care not to introduce interference noise from the reflected beams. Of course, according to the procedure described in the paragraph 2.3.1, we align the probe

and excitation beams and keep them superimposed, with the help of the four quadrants photodiode, and we minimize the polarizations defects by acting on the optic elements (half-wave plates etc.). We also use to check the shape of the excitation pulse, which is very sensitive to the alignment of the dye amplifiers, with the help of a CCD camera: the cylindrical symmetry of the beam is important, since we exploit the cylindrical symmetry of the whole setup (cf. the rotations of the excitation laser polarization) when we analyze our polarimetric signals. Another fundamental preliminary test is the measurement of the transverse fields (cf. *2B4POL*, paragraph 2.3.4), which are kept minimum thanks to the compensation of the residual magnetic field with coils, and the centering of the beams inside the cell.

Once we have found the optimum conditions for our PV measurement, we can begin to acquire data, according to the method described above. However, the spirit of the PV acquisition is not to settle definitively the experimental conditions, and then undertake long-term averages, without touching anything any more.

Firstly, this would not be possible, because we have to check from time to time the alignment of the setup, and accordingly adjust it (the mechanical stability cannot be optimal for more than one day).

Secondly, from run to run, we desire to change some experimental parameters, always keeping the best operating conditions, in order to check for possible dependencies of the signals, and eventually average them. We emphasize that the purpose of our preliminary PV measurement (whose results are presented in paragraph 2.5.4) is not only to demonstrate the validity of our experimental method, characterized by stimulated emission detection, but also to understand which are the important parameters we have to care about, and in which direction we have to put our efforts to reach the experimental conditions which will allow the 1% precise measurement. For example, we realized during the first months of measurements that it is important to frequently change the tilt of the cell, with respect to the laser beams (cf. paragraph 2.5.4). This has simply to be considered as an additional reversal, in the same way as the other ones (insertion of half-wave plates etc.). We also tried sometimes to reverse the direction of the cell, in order to check for possible differences of the measured signals, in particular also control signals, as the $B_z(E_z\text{-odd})$. Since this reversal requires time (we have to take down the external oven), it was not carried out frequently (three times for the first analyzed cell, *Alum2*). In the end, we did not notice any correlation of our measurements with the direction of the cell.

Before and/or after each PV run, some test measurements are performed. The *2B4POL* procedure on the 3-4-4 and 3-4-5 transitions allows to check the transverse fields, and the centering of the beams inside the cesium cell. The $B_z(E_z\text{-odd})$ measurement on the 3-4-5 transition allows to monitor the relative systematic error, and consequently correct the analyzed PV data (see paragraph 2.5.4).

In the next three paragraphs, we present the PV analysis method, applied to the data collected with the *Alum2* cell: the measurements on *Alum3* could not be exploited, because of the presence of a spurious gas, and the *Alum4* cell was mainly used to implement and test our polarization magnifier system.

2.5.2 Noisy data rejection

After an experimental run (which can last about five or six hours), we have to analyze the collected data in order to obtain the maximum information about the results of our measurements.

The first step of the analysis is to "clean" the experimental data. Indeed, a small part of our measurements is unavoidably affected by some extra non gaussian noise, generally due to external interferences (for example occasional electric parasites which affect the signals coming from the photodiodes). Already during the measurement, a procedure allows to avoid acquiring the clearly unsuited data: the variance of each bunch of thirty double imbalance measurements is computed at once, and if it exceeds a certain value (120 μrad on the 3-4-4 transition and 150 μrad on the 3-4-5) the measurement of the bunch is repeated.

Then, after the run, the same kind of analysis of the noise is performed on each sequence of data (one sequence consisting of 4×16 bunches), and the sequences which show a dispersion more than three times higher than the average noise are rejected.

In the end, we obtain our pairs (γ_1, α_2), for the successive excitation polarizations $\hat{y}$, $\hat{x}$, $\hat{u}$, $\hat{v}$, $\hat{v}$, $\hat{u}$, $\hat{x}$, $\hat{y}$, cleared of bad data, from which we directly extract the anisotropies and, above all, the isotropic contributions (in sequence, S_{xy}, S_{uv}, S_{uv}, S_{xy} etc.). Since these last quantities S are our final result, we perform one last time a selection on them, in order to be sure to obtain the minimum error bar. In practice, we use the so called self-consistent truncation at 3 standard deviations. The mean and variance of the data set are computed (separately for γ_1 and α_2), and all the data which are more than three standard deviations away from the mean are removed. Since after the procedure the mean and variance of the truncated data set are different, the operation is repeated until all the retained data are consistent with the 3σ limit. Eventually, since γ_1 and α_2 come from the same measured quantities $\theta_{\parallel}$ and $\theta_{\perp}$ (cf. equation (2.4)), for each rejected γ_1, it is logical to eliminate the respective α_2 datum too, and vice versa.

2.5.3 Anisotropies

In a general way, the systematic errors which break the cylindrical symmetry of the experiment can be detected as anisotropies in the collected data, i.e. variations of the signals according to the direction of the excitation polarization.

We saw in paragraph 2.3.4 how the presence of transverse electric and magnetic fields can cause such undesirable effects. We also presented the *2B4POL* procedure, which allows to monitor the transverse fields, and keep them as low as possible (with better centering of the beams inside the cell, and compensation of the residual magnetic field). Note that the effect of the transverse fields on our polarimetric measurements is quadratic (proportional to $(E_{\perp}B_{\perp})$ and $(B_{\perp}B'_{\perp})$), whereas our control measurement *2B4POL* gives the mean values $<\mathbf{E}_{\perp}>$ and $<\mathbf{B}_{\perp}>$. Even if we imagine to be in the best conditions, with $<\mathbf{E}_{\perp}>=<\mathbf{B}_{\perp}>= 0$, in general, a non-zero value of

$<E_\perp B_\perp>$ and $<B_\perp B'_\perp>$ can be present. Therefore, the best way to understand the real impact on our PV measurement is to analyze the associated anisotropies, present in the PV data. We present in the following the analysis method of the anisotropies for our preliminary measurement. The considered theoretical model was developed during D. Chauvat's thesis [29], when the experimental situation didn't require a more thorough analysis. After the end of this thesis, a significant theoretical effort allowed to totally review the situation of the systematic effects which break the cylindrical symmetry [37], confirming the validity of the following simplified analysis for a 8.4% precise result, and adding theoretical information which will allow to examine at best the situation for the future 1% precise measurement.

According to the model described in D. Chauvat's thesis, in the presence of transverse fields, γ_1^{odd} for a given excitation polarization $\hat{\epsilon}_{ex}$ is given by

$$\begin{aligned}\gamma_1^{odd} &= \gamma_1^{PV} + \gamma_1^{(E_\perp^{odd},B_\perp^{odd})} + \gamma_1^{(E_\perp^{even},B_\perp^{even})} + \gamma_1^{(B_\perp^{odd},B'^{even}_\perp)} \\ &= \gamma_1^{PV} + S_1^o \cdot (-\cos\psi_o + \cos(\psi_o - 2\phi_o)) \\ &\qquad + S_1^e \cdot (-\cos\psi_e + \cos(\psi_e - 2\phi_e)) \\ &\qquad + S_2 \cdot \cos(\psi' - 2\phi_o),\end{aligned}$$

where $\psi_o = (\mathbf{E}_\perp^{odd}, \mathbf{B}_\perp^{odd})$, $\phi_o = (\hat{\epsilon}_{ex}, \mathbf{B}_\perp^{odd})$, $\psi_e = (\mathbf{E}_\perp^{even}, \mathbf{B}_\perp^{even})$, $\phi_e = (\hat{\epsilon}_{ex}, \mathbf{B}_\perp^{even})$, and $\psi' = -\frac{\pi}{2} + (\mathbf{B}'^{even}_\perp, \mathbf{B}_\perp^{odd})$.

For α_2, the effect of the transverse fields, although coming from different physical processes (there is no Hanle precession here), gives rise to the same kind of systematic effects, with different coefficients:

$$\begin{aligned}\alpha_2^{odd} &= \alpha_2^{(E_\perp^{odd},B_\perp^{odd})} + \alpha_2^{(E_\perp^{even},B_\perp^{even})} + \alpha_2^{(B_\perp^{odd},B'^{even}_\perp)} \\ &= -0.56 \cdot \{S_1^o \cdot (-\cos\psi_o + \cos(\psi_o - 2\phi_o)) \\ &\qquad + S_1^e \cdot (-\cos\psi_e + \cos(\psi_e - 2\phi_e))\} \\ &\qquad - 0.31 \cdot S_2 \cdot \cos(\psi' - 2\phi_o),\end{aligned}$$

where the numerical values, which show the relative magnitude of α_2 effects with respect to γ_1, on the 3-4-4 transition, have been taken from [29].

The difference between the isotropic contributions S_{xy} and S_{uv}

We already mentioned that we define the isotropic contributions S_{xy} and S_{uv} as the mean of the successive pairs of data, for the excitation polarization along $\hat{x}$ and $\hat{y}$, and along $\hat{u}$ and $\hat{v}$. One could fear that the anisotropies give rise to incompatible values of S_{xy} and S_{uv}, but we easily see from the formulas above that this is not possible, in the case of our transverse fields. Actually, the equality between S_{xy} and S_{uv} is a general principle, which comes from the general form of the density matrix of the excited 7S atoms, $A + B\sin(2\theta) + C\cos(2\theta)$, quoted in paragraph 2.1.2.

Note that we assume that the fields configuration does not change when the excitation laser polarization rotates. Actually, we cannot exclude that the electrons

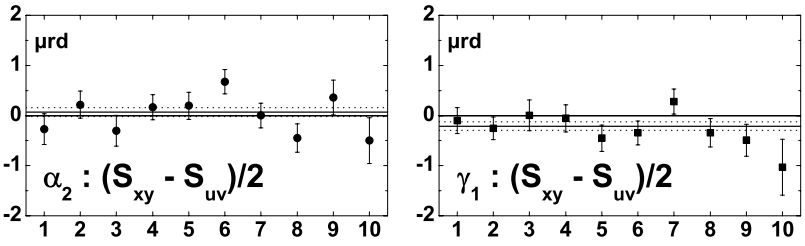

Figure 2.31: Difference between the isotropic contributions S_{xy} and S_{uv}, for γ_1 and α_2 signals, on the 3-4-4 transition: experimental values obtained for the *Alum2* cell (47 measurement runs).

photoemitted from the windows, have not a privileged escape direction, correlated with the polarization of the light, which would give rise to fields which are partially dependent on the polarization. Such a behaviour, which has been shown to be unlikely [37], would not modify the anisotropies described in the next paragraph, but it would lead to a difference between S_{xy} and S_{uv}.

In our measurements (fig. 2.31), we never noticed any statistically significative difference between the two isotropic contributions S_{xy} and S_{uv}.

The anisotropies D_{xy} and D_{uv}

From the general formulas of γ_1^{odd} and α_2^{odd} reported at the beginning of the paragraph, we see that the efficient way to isolate the anisotropy of the signals from the isotropic contributions is to consider the differences $D_{xy} \equiv \frac{1}{2}(S_x - S_y)$ and $D_{uv} \equiv \frac{1}{2}(S_u - S_v)$, S being referred to γ_1 or α_2.

We have then:

$$\begin{cases} D_{xy}^{\gamma_1} = S_1^o \cdot \cos(2\phi_o - \psi_o) + S_1^e \cdot \cos(2\phi_e - \psi_e) + S_2 \cdot \cos(2\phi_o - \psi') \\ D_{uv}^{\gamma_1} = S_1^o \cdot \sin(2\phi_o - \psi_o) + S_1^e \cdot \sin(2\phi_e - \psi_e) + S_2 \cdot \sin(2\phi_o - \psi'), \end{cases} \tag{2.9}$$

where the angles ϕ are now referred to $\hat{x}$, instead of $\hat{\epsilon}_{ex}$.

For α_2 signals,

$$\begin{cases} D_{xy}^{\alpha_2} = -0.56 \cdot \{S_1^o \cdot \cos(2\phi_o - \psi_o) + S_1^e \cdot \cos(2\phi_e - \psi_e)\} \\ \qquad\qquad - 0.31 \cdot S_2 \cdot \cos(2\phi_o - \psi') \\ D_{uv}^{\alpha_2} = -0.56 \cdot \{S_1^o \cdot \sin(2\phi_o - \psi_o) + S_1^e \cdot \sin(2\phi_e - \psi_e)\} \\ \qquad\qquad - 0.31 \cdot S_2 \cdot \sin(2\phi_o - \psi'). \end{cases} \tag{2.10}$$

The α_2 terms are all opposite in sign with respect to the corresponding γ_1 terms, and lower in magnitude.

In order to graphically represent the anisotropy, we plot each couple of data (D_{xy}, D_{uv}) in a cartesian coordinate system. Then, we look for a possible deviation of the center of gravity of the resulting cloud of points (see fig. 2.33). For each run, when the anisotropy is different from zero, it is useful to define the modulus $S_{ani} = \sqrt{D_{xy}^2 + D_{uv}^2}$ and the angle $\theta_{ani} = \arctan(D_{uv}/D_{xy})$. Note that if we had a dominant term in equation (2.9), for example the first term, S_{ani} and θ_{ani} would simply correspond to S_1^o and $(2\phi_o - \psi_o)$.

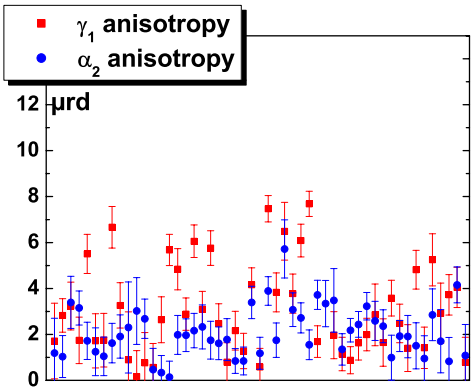

Figure 2.32: Modulus S_{ani} of the γ_1 and α_2 anisotropies, obtained in the successive runs of the *Alum2* cell, on the 3-4-4 transition. As expected from equations (2.9) and (2.10), the α_2 anisotropies are usually lower than the γ_1 ones.

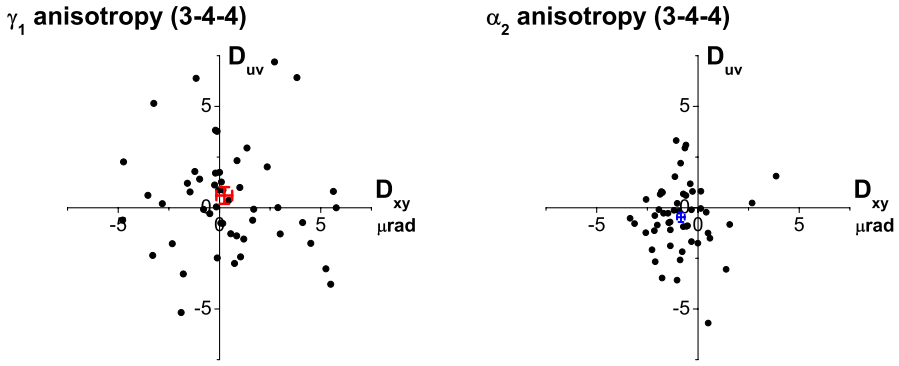

Figure 2.33: Anisotropy plots for γ_1 and α_2, on the 3-4-4 transition. We have reported here the result for the whole set of measurements on *Alum2*: each data point represents the mean D_{xy} and D_{uv} of an experimental run (5-6 hours long).

The correlation test. In fig. 2.32, where the modulus of the anisotropies of γ_1 and α_2 is reported, as measured for all the runs of the *Alum2* cell, on the 3-4-4 transition, we see that many runs show no significant anisotropy. However, we have many other runs for which the anisotropy is statistically different from zero: for more than 20% of the runs, the moduli S_{ani} are even equal or higher than 6 μrad. In these conditions, it is necessary to check if there can be an associated systematic error on the isotropic contribution. This would appear as a correlation between the isotropic and the anisotropic parts of the signals, S_{xy} and D_{xy}, or S_{uv} and D_{uv} [37]. We decide then to evaluate the correlation coefficients r_{xy} and r_{uv}, defined as:

$$r_{xy} = \frac{\left(\sum_{i=1}^{n} S_{xy}^{(i)} D_{xy}^{(i)}\right)/n - <S_{xy}><D_{xy}>}{s_S \; s_D} \tag{2.11}$$

(and similarly for r_{uv}), where $<S_{xy}>$ and $<D_{xy}>$ are the average values and s_S and s_D are the standard deviations of S_{xy} and D_{xy} taken over the sample population.

This kind of analysis was applied for the single runs, as well as for the whole set of data of *Alum2*. When we analyze the single runs, we consider the four values D_{xy}, S_{xy} and D_{uv}, S_{uv} given by each measurement cycle, whereas when we want to compute the correlation for the whole set of data, the $D^{(i)}$ and $S^{(i)}$ in equation (2.11) actually represent the average D and S on each run, in order to deal with more precise data. In both cases, we never found any significant correlation. This means we do not expect any systematic error on γ_1^{PV}, coming from transverse electric and magnetic fields, at the present accuracy level of our measurements (8.4%).

Anisotropy of the whole set of data We have reported in fig. 2.33 the anisotropy plots of γ_1 and α_2, for all the collected data on the *Alum2* cell. The cloud of points of the γ_1 plot is centered well enough at the origin of the graph. Indeed, we have a mean value which is 0.24 ± 0.39 for D_{xy} and 0.60 ± 0.41 for D_{uv}, consistent with zero. This means the anisotropy, though clearly present for some runs, averages to zero for long-term measurements. This is expected, since we know the fields inside the cell are not stable at all: for example, the electron emission from the windows of the cell is sometimes subject to variations, which cause changes of the electric and magnetic field configurations (we saw that B_z(E_z-odd) is affected too by these sudden variations).

The case of α_2 is more surprising: here the cloud is clearly shifted to the left side of the plot. We have indeed a mean value $D_{xy} = -0.84 \pm 0.19$, which is 4.5 standard deviations away from zero. It is not completely clear why we observe this, but the fact that the anisotropy comes mainly for the $\hat{x}, \hat{y}$ part of the signals suggests that it could be related to symmetry breaking along these axes, for example because of the horizontal tilt of the cell. Note that for this cell the reflection coefficient of the windows for the excitation beam could not be kept lower than 5% (cf. paragraph 2.3.2). We conclude by mentioning that the cells analyzed after the end of this thesis work, with windows characterized by a very low reflection coefficient, did not show this kind of effect on the α_2 anisotropy any longer.

2.5.4 Isotropic contribution of γ_1 and α_2

We review in this paragraph the important aspects of the analysis method which extracts the isotropic γ_1 and α_2 from the measurements.

The θ_0(E_z-odd) test

The entire acquisition procedure has been tested by simulating the parity violating effect, thanks to a suitably programmed tilt of the excitation laser polarization. Indeed, we already saw in paragraph 2.1.2, where the calibration procedure of the γ_1 angles is described, how the tilt of the excitation polarization generates the same effects as the parity violation, i.e. a rotation of the alignment axes which is detected as a γ_1 signal. In order to mimic the PV observable, we have to give to this tilt θ_0 the same E_z-odd signature as γ_1^{PV}. The tilt and the field are then switched in accordance with the following pattern: $(\theta_0 + \theta^{cal}, +E)$, $(\theta_0 - \theta^{cal}, +E)$, $(-\theta_0 + \theta^{cal}, -E)$, $(-\theta_0 - \theta^{cal}, -E)$. The detected γ_1^{odd} is thus expected to be equal to the sum $\theta_0 + \gamma_1^{PV}$.

The test was performed with θ_0 chosen to be about 200 μrad (by appropriately programming the current delivered to the Faraday rotator), and the usual $\theta^{cal} =$ 1.76 mrad. The excitation polarization was monitored by a dedicated polarimeter, with the same design as the probe polarimeter, but sensitivity about 2.5 times better. This allowed to measure directly, with a good precision, the tilt given to the green polarization. In the end, the expected θ_0 was measured to be 191.7 ± 2.6 μrad. The analysis of the collected data for the probe beam gave for the isotropic contributions the values $\gamma_1^{odd} = 192.1 \pm 1.4$ μrad and $\alpha_2^{odd} = 0.1 \pm 1.5$ μrad, which are in perfect agreement with what is expected. Note that this procedure allowed also to check the good discrimination between γ_1 and α_2, based on the para/ortho reversal.

Note also that during our normal PV measurements, the presence of the polarimeter for the excitation laser is very useful, as it allows to check the possible presence of an unwanted E_z-odd tilt of the excitation laser polarization. Such an effect could arise from a possible influence of the electromagnetic interferences associated with the pulsed applied electric field, on the faraday rotator. The measurements on *Alum2* proved the total absence of such an effect, at the 0.034 μrad statistical level.

The cell tilt reversal

We already cited that during our first runs on *Alum2*, we understood the importance of frequently changing the tilt of the cell, in order to average on possible related systematic errors. Practically, this operation has to be considered as a reversal, in the same way as the other ones (insertion of half-wave plates etc.). Of course, since it is a mechanical operation which takes some time, the tilt cannot be changed as frequently as the other reversal parameters of the experiment: we decided to perform at least one tilt reversal per day of measurements.

In our analysis, we then consider, for the average value of γ_1 (or α_2), the mean of the measurements performed for positive and negative tilts, with the same weight for

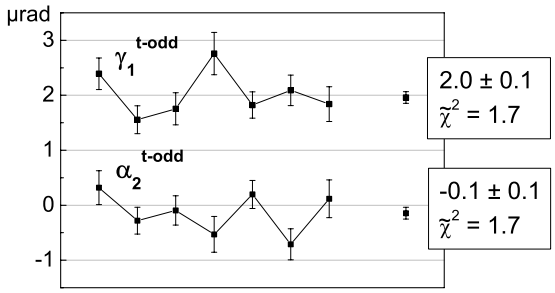

Figure 2.34: Tilt-odd part of the isotropic γ_1 and α_2. Each data point represents the average over four consecutive runs, on the *Alum2* cell.

the two tilts. It is also worth defining the "*tilt*-odd" quantity $\gamma_1^{t-odd} = (\gamma_1(\text{tilt}+) - \gamma_1(\text{tilt}-))/2$ (and the analog α_2^{t-odd}), which can be considered as an evaluation of the effect of the tilt on our measurements. A plot of this quantity has been reported in fig. 2.34: for γ_1, the effect is remarkable, whereas α_2 does not seem affected too much. For α_2, note however that there is a possible effect which averages at zero, but expresses itself as a higher dispersion on the *tilt*-odd contributions, than the *tilt*-even α_2: indeed, we found that the reduced χ^2 is 1.7 for α_2^{t-odd}, and only 0.3 for the mean α_2 on the same set of data. If, as we think, the tilt-dependent contributions on our signals came in part from the excitation laser reflected by the rear window of the cell (about 5% of the incident beam), the use of cells with better quality windows, which allow to reduce the reflection coefficient below 3‰ (cf. paragraph 2.3.2), should much improve the situation. Indeed, the latest measurements performed by the group since October 2003 with new cells report absence of *tilt*-odd contributions.

The B_z-odd correction

Once we have the *tilt*-even values of the isotropic γ_1 and α_2, if necessary, we have to correct them from the $B_z(E_z\text{-odd})$ systematic effect, according to the procedure described in paragraph 2.3.6. Each run on the 3-4-4 transition is preceded or followed by a run on 3-4-5, which allows to deduce the magnitude of $B_z(E_z\text{-odd})$ from the α_2^{odd} measurement. For each run (on 3-4-4 and 3-4-5), the calibration of $B_z(E_z\text{-odd})$ (cf. table 2.9) is performed at least three or four times, in order not to introduce uncertainties on the proportionality coefficients we use to correct our signals.

The time spent on the 3-4-5 transition for this control measurement is about 25% of the time spent for the PV averagings on 3-4-4. The precision of the corrections to be applied is high enough not to increase the uncertainty on γ_1^{odd} by more than 10% of the statistical error (and only 1% for the error on α_2).

Results for γ_1^{odd} and α_2^{odd}

For the *Alum2* cell, we have accumulated 3207 experimental isotropic values of γ_1^{odd} and α_2^{odd}, distributed over 47 parity violation measurement runs. The result is shown in fig. 2.35. The two analysis methods "D" and "$\tilde{\theta}$" led to practically identical results (cf. paragraph 2.1.2), showing by this way that the pulse to pulse variation of the excitation laser energy is low enough not to affect our measurements.

γ_1^{odd} The weighted average of the measured values of γ_1^{odd} gives the experimental $|\gamma_1^{PV}| = 1.082 \pm 0.091$ μrad, which agrees both in sign and magnitude with the expected value $\theta^{PV}_{\text{expected}} = 0.9675 \pm 0.0070$ μrad, presented in paragraph 2.3.5.

α_2^{odd} The case of our α_2^{odd} measurement is more difficult to interpret. Indeed, α_2^{odd} is clearly positive, 0.367 ± 0.090 μrad, whereas we expect it to be zero. In the light of the similar situation encountered for the measured anisotropies (cf. paragraph 2.5.3), it is not so surprising to have a non zero value of the isotropic α_2, without consequences on our γ_1 measurement: indeed, we found an average γ_1 anisotropy compatible with zero, whereas for α_2 we have a negative value of D_{xy} (-0.84 ± 0.19). We quoted a possible link between this unexpected effect and the undesirable 5% reflection of the excitation laser on the rear window of the cell. Actually, the measurements performed after the end of this thesis work, on cells with good quality windows (less than 3‰ reflection), did not show such birefringence effects any longer.

Note that, although until now we have reviewed only systematic effects which affect both γ_1 and α_2 (coming for example from the presence of electric and magnetic fields), it is absolutely possible to have physical processes which act only on α_2. For example, we can mention the propagation of light in a medium with a variable

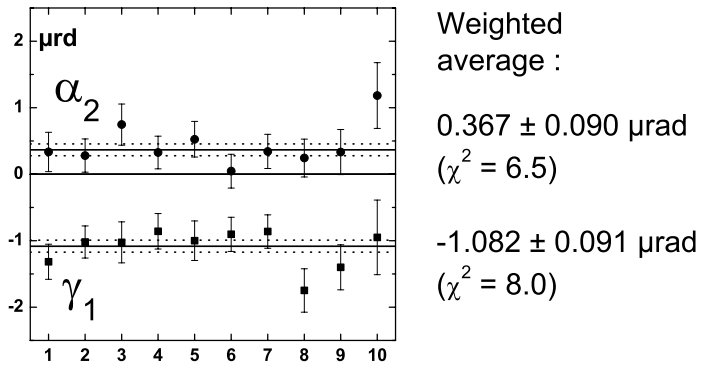

Figure 2.35: Experimental values of γ_1^{PV} and α_2^{odd}, obtained for the *Alum2* cell (47 measurement runs on the 3-4-4 transition). Each plotted datum represents the weighted average over several successive runs, after correction from the $B_z(E_z$-odd) effect.

refraction index (in our case, the excited vapour): the non planar path followed by the light determines the rotation angle of the polarization. Such an optical activity effect would surely have an E_z-odd contribution, since the refraction index depends on the excited atomic population, which significatively changes in the proximity of the windows, when the electric field is reversed (cf. paragraph 2.3.6, about the pseudo B_z-odd).

The *Alum3* and *Alum4* cells. We do not present the PV measurements performed on the next two cells, *Alum3* and *Alum4*, because they do not bring more information with respect to *Alum2*. For *Alum3*, the presence of a spurious gas inside the cell was cause of electric discharges, which perturbed the measurements: the anisotropies of the signals were relatively high. *Alum4* was mainly used to implement and test our polarization magnifier system (dichroic cubes). In the next paragraph we present the first encouraging results.

2.5.5 Measurements with and without the use of the polarization magnifier: considerations about the noise

We review in this paragraph some important experimental aspects about the statistical noise which characterizes our measurements. In particular we show how the use of the polarization magnifier allows to obtain a substantial improvement of the signal to noise ratio.

Noise contributions without the polarization magnifier

Our measurements are subject to different sources of noise. The first one comes from the particle nature of the photons: each single photon incident on the polarimeter polarizing cube has a certain probability (around 50%, since we work in a balanced mode) to be reflected or to be transmitted (we neglect the absorption). In the end, for N incident photons, the standard deviation of the number of photons arriving on one photodiode, coming from the choice process ("transmitted" or "reflected"), is $\sqrt{N/4}$ (cf. binomial distribution). Thus, we find for the imbalance signal a $1/\sqrt{N}$ uncertainty, which has to be multiplied by the calibration coefficient in order to deduce the noise on the calibrated angles. Of course, all the probe pulses (the first pulse and the four consecutive reference pulses) are affected by this fundamental noise. We still have to account for the noise added by the presence of the photodiodes dark current and the amplification chain to deduce the theoretical noise, which is then given for a single excitation pulse by:

$$\sigma_\theta = \frac{\theta^{cal}}{\mathrm{d}a^{cal}} \sqrt{\frac{1 + 1.2 \cdot 10^7/N}{N} + \frac{1 + 1.2 \cdot 10^7/N_{ref}}{N_{ref}}}\,, \tag{2.12}$$

where σ_θ is the statistical error on the calibrated angle, in the "ortho" or "para" configuration (of the probe with respect to the excitation laser), N and N_{ref} are respectively the number of photons of the amplified probe pulse and the total number

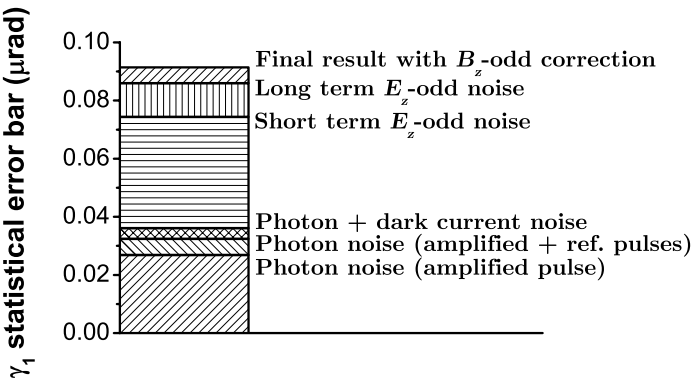

Figure 2.36: Different contributions to the final error on our preliminary γ_1 measurement, performed with the *Alum2* cell.

of photons for the reference pulses, extracted from the sum signal of the polarimeter; $(1.2 \cdot 10^7/N^2)$ is the electronic noise term. The experiment was conceived from the beginning in such a way as to get as close as possible to the quantum noise of the first amplified probe pulse: we have four reference pulses, in order to increase the number of reference photons N_{ref}, and we use low noise electronics.

In order to monitor the true noise on our measurements, we define two quantities, which allow to characterize the noise on our E_z-odd measurements, for two scales of times. The first one, which we will call "short term E_z-odd noise", is defined as the standard deviation of the eight E_z-odd double imbalances we obtain for each group of sixteen states, at fixed lambda plates configuration. The standard deviation is then quadratically averaged over all the run, in order to obtain a precise value. The second noise quantity, the "long term E_z-odd noise", is no other than the standard deviation of the isotropic γ_1^{odd}, over all the run. In the following, all the kinds of noise are normalized to the single cycle of measurements (over the four excitation polarizations), in order to be able to compare them.

In fig. 2.36 we can see the contributions of all these sources of noise to the final error bar on the preliminary PV measurement presented in paragraph 2.5.4 (cf. fig. 2.35). We reported the small increase of the error due to the $B_z(E_z$-odd) correction too. Note that the short term experimental noise is relatively high with respect to the theoretical noise. We will see in the next paragraph how the use of the polarization magnifier allows to reduce this noise component.

It is also interesting to observe the situation for each single run reported in fig. 2.37: if we take the example of the short term noise (which is much more accurate than the long term noise, hence easier to analyze), we see that even without considering the first very noisy runs, the noise varies regularly from run to run, between 2.5 and 3 μrad per cycle. This is because the experimental conditions depend on many parameters (excitation laser energy, shape of the beams, cell tilt, possible presence

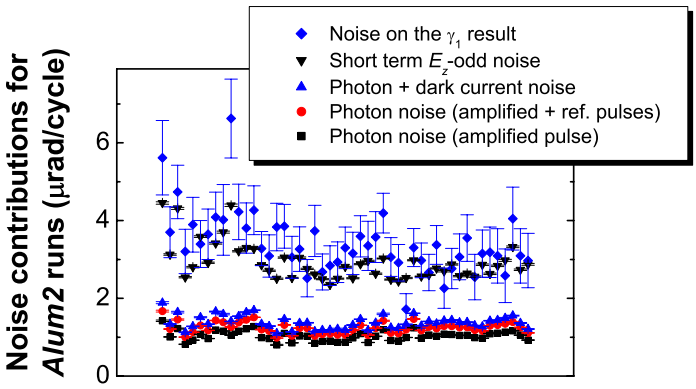

Figure 2.37: Different noise contributions on γ_1 for each run on the 3-4-4 transition, in the *Alum2* cell.

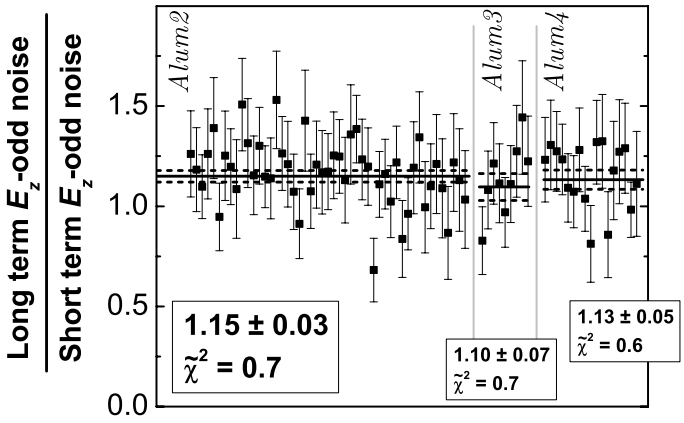

Figure 2.38: Ratio $\frac{\text{Long term noise}}{\text{Short term noise}}$, for each run on the 3-4-4 transition, with the three tested cells. We have reported the weighted average for each cell.

of microdischarges, extinction coefficient of the optical switch for the probe beam etc.) and it is not easy to keep all of them optimal simultaneously.

Note that the accuracy on the short term E_z-odd noise makes this quantity ideal to quickly evaluate, at the beginning of the run, how noisy will be the measurement and how long time we will have to spend to average γ_1^{odd} to reach an established error bar in these conditions. Of course the long term noise is a little higher than the short term noise, but the ratio seems to be constant with an excellent reproducibility, even when we change cell (cf. fig. 2.38).

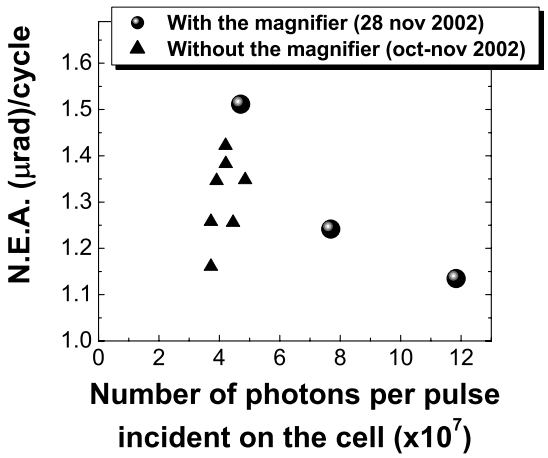

Figure 2.39: Minimum theoretical noise (photon + dark current, defined by eq. (2.12)), with and without use of the polarization magnifier. For the case with the magnifier, we see how the noise decreases for higher probe photon fluxes. (The number of photons for the amplified and reference pulses was deduced from the polarimeter sum signals.)

Use of the polarization magnifier: improvement of the signal to noise ratio

We have seen in paragraph 2.4.3 the implementation of a dichroic cube before the polarimeter, which allows to amplify the tilt of the probe laser polarization. This system should allow to reduce the noise on our polarimetric measurements. Actually, if we consider only the photon noise, there is no variation of the signal to noise ratio because the gain obtained thanks to the amplification of the angles is equitably counterbalanced by the loss of the total number of photons [43]. However, the idea is to take advantage of the reduction of the number of photons which are transmitted by the cube and enter the polarimeter: indeed, we can now increase the probe laser energy, without fearing to saturate the detection electronic chain. By this way, we detect more photons and reduce the statistical error on our measurements.

Fig. 2.39 shows our first test of the signal to noise ratio ($N.E.A.$ standing for Noise Equivalent Angle) which compares the two situations: with and without the dichroic cube (for the *Alum3* cell). Without our polarization magnifier, the theoretical $N.E.A.$ (which includes photon and dark current noise, cf. equation (2.12)) was typically between 1.2 and 1.4 μrad per cycle. With the cube, for the same incident probe intensity, we had a small deterioration of the situation, due to the dark current noise, which is no more negligible for low photon fluxes incident on the polarimeter. We recover a good situation if we increase the probe photons flux N, even if at first sight, the result doesn't seem to be spectacular. Actually, the noise decreases less than $1/\sqrt{N}$, because of saturation effects on the probe transition: the amplification of the probe photons by stimulated emission and consequently the amplification of

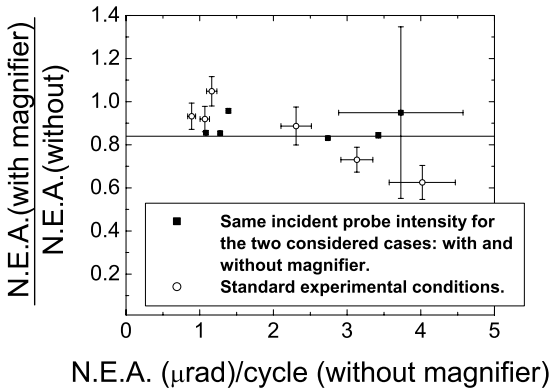

Figure 2.40: Noise equivalent angle: ratio of the values obtained with and without the use of the polarization magnifier. Each group of six points represents, from left to right, the quantities relative to the following kinds of noise: photon noise of the amplified pulse, photon noise of the five probe pulses, photon and dark current noise, short term noise, short term E_z-odd noise, long term E_z-odd noise. The short term noise is defined as the standard deviation of the angle measurements (with the suitable normalization), over the 30 pulses which form each of the 16 possible states, averaged on all the run.

the probe polarization tilt decrease for higher probe pulses energies.

Nevertheless, a gain in the signal to noise ratio was present, and we continued to test and use the system for our measurements on the *Alum4* cell. We found that the real gain, on the γ_1^{odd} error bar, was better than what we could expect from the previous photon noise analysis. Indeed, the increase of the probe beam saturation on the cesium atoms leads to a lower noise on our E_z-odd quantities. This statement is confirmed by fig. 2.40, where the comparison between the measurements with and without the use of the magnifier is presented, for two different cases:

- a dedicated run, in which the incident probe intensity is kept constant with and without the cubes, in order to put in evidence possible differences due only to the detection part of the experiment, and not related to changes of the atomic saturation. When we did not use the cube, we had to place an attenuator before the polarimeter, in order not to saturate the detection electronics;

- our standard PV measurement conditions: high probe intensity (about $8 \cdot 10^{10}$ photons per pulse) when we use the cube, and normal intensity ($5 \cdot 10^{10}$ photons per pulse) when we use the normal detection system.

In the first case, the ratio between the $N.E.A.$ with and without the magnifier, is the same for all the noise contributions[12]. In the second case, we clearly see that the

[12]Except when we account for the dark current noise, since it is no more negligible for the low photon fluxes we have after the passage through the cube.

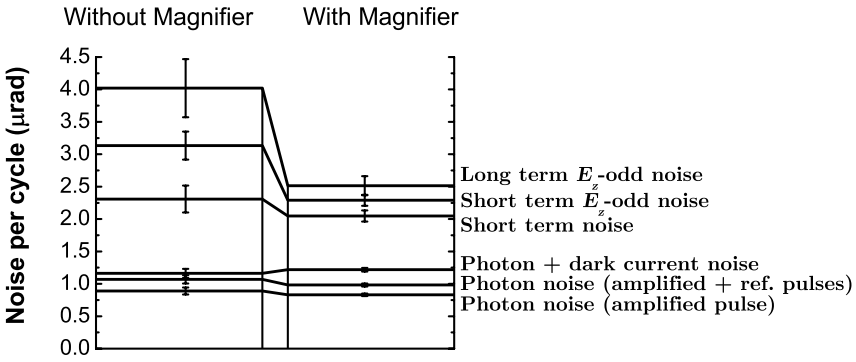

Figure 2.41: Different contributions to the noise for the runs performed on *Alum4*, with and without using the polarization magnifier. The short term noise has been defined in fig. 2.40.

short and long term E_z-odd noises benefit from the increase of the probe intensity, much more than the photon noise.

The resulting contributions to the noise for the runs performed on the *Alum4* cell are presented in fig. 2.41. The gain coming from the use of the magnifier, on the final γ_1 (and α_2) error bar was 1.6. This means it took us, on average, 2.6 times (the square of the 1.6 factor) less time to reach the same precision on γ_1 (and α_2), when we performed measurements with the magnifier.

Unfortunately, it was not possible to exploit the collected data, because of the high birefringence of the cube we used. This one gave origin to very high anisotropies in our γ_1 and α_2 signals, and biased the isotropic values. After the end of the thesis, another kind of dichroic element[13] was implemented which succeeded in avoiding the inconvenience of the birefringence. It confirmed definitely the gain for the signal to noise ratio.

2.5.6 Conclusion

We have seen in this chapter how the preliminary tests allow to choose the best conditions to undertake a parity violation measurement. Some particularly important parameters are the alignment of the beams inside the cell, the tilt of the cell with respect to the axis of the beams, the temperature of the cell windows (and hence the reflectivity @539 nm). It is fundamental to have a good knowledge of the electric and magnetic fields inside the cell and to be able to keep them as low as possible, in order to prevent the appearance of systematic effects.

This thesis work began with the analysis of a new kind of cells whose tube was grooved in order to inhibit the secondary emission of electrons coming from the

[13]Precisely a set of Brewster plates. We remind that the gluing step of the two prisms which form the cube was the process which introduced the uncontrolled birefringences.

photoionization of the windows, and disturbing the field map in the cell. We soon could show this modification totally changed the situation, suppressing by more than one order of magnitude the annoying fields in the cell.

We decided then to perform a preliminary measurement. We indeed obtained a 8.4% precise result which succeeded to validate the stimulated emission detection method. We put the emphasis on the originality of the measurement: our PV experiment appreciably differs from the traditional ones, since here the detection is based on the stimulated emission of a laser, which probes on an allowed transition the cesium $7S$ state after the excitation on the highly forbidden $6S$-$7S$ transition. Unlike the fluorescence detection schemes, here there is amplification of the asymmetry when the applied electric field is increased.

This preliminary measurement allowed to bring out the most important features of the experiment, for example what kind of systematic effects we have to expect and to study in order to make possible our 1% precision goal. We managed to correct for the most dangerous systematic effect, coming from the presence of a longitudinal magnetic field B_z-odd which changes sign when we reverse the applied electric field.

A simple study of the anisotropies showed that at the 8.4% accuracy level reached during this thesis work we don't expect any associated systematic error on our PV observable γ_1. We presented a test on the collected data, which allows to confirm the absence of correlation between the anisotropies and the isotropic γ_1.

In the end, we showed the improvements given to the experiment: the excitation laser stabilization on the I_2 line, the use of a Pockels cell for a better extinction of the probe pulses, and the introduction of a dichroic element before the polarimeter, which acts as a polarization magnifier and increases the signal to noise ratio.

Chapter 3

The first steps for a parity violation experiment with radioactive francium: production and trapping

We saw that, besides cesium, francium is a very promising candidate for precise atomic parity violation measurements. Indeed, as for cesium, the alkali structure of francium should allow very accurate theoretical atomic calculations, essential to link the PV measurements to the weak charge (predicted by the Standard Model). The advantage of francium comes from the larger PV effect in this atom with respect to cesium (due to the higher number of protons and neutrons in the nucleus). Theory shows that the relativistic effects enhance PV even more than what expected from the Z^3 law presented in paragraph 1.2: $\Im m E_1^{PV}$ for francium has been calculated to be 16-18 times higher than for cesium [12, 13].

However, an important drawback for a parity violation experiment on francium is that this element is radioactive: the longest-lived isotope (^{223}Fr) has a half-life of 22 minutes. Therefore, francium has to be continuously produced, from radioactive decays or nuclear reactions (by an accelerated beam colliding a target). The resulting available quantity of francium is then far much lower than the number of cesium atoms available for the Paris PV experiment. The laser cooling and trapping techniques are currently used to obtain a substantial francium sample for high resolution spectroscopy on allowed transitions: two research groups in the United States have measured energy levels of different francium isotopes confined in a magneto-optical trap (MOT) [11, 44]. Note that the possibility to probe different isotopes is very attractive for APV measurements because it can lower the incidence of the theoretical calculations accuracy on the final value of the weak charge given by the PV experiment [45].

In this chapter we will describe the Legnaro francium experiment, started three years ago: the first purpose was to obtain a francium MOT. In the next paragraph we

make some preliminary considerations to show how it can be possible to implement a parity violation experiment with francium on the highly forbidden $7S$-$8S$ transition, guided by the features of the two cesium PV experiments (in Paris and Boulder).

3.1 Considerations for a PV measurement with cold francium

Many important aspects have to be considered for the definition of a PV experiment on cold atoms. First of all we can ask ourselves what kind of cooling/trapping scheme is more suited for a PV measurement. There are two main possibilities: the production of a cold francium beam, or a francium trap (preferably an optical trap because we want to avoid the presence of magnetic fields which could disturb PV measurements). The cold beam would have the advantage to allow a simple continuous mode operation, whereas an optical trap could be used only during one trap lifetime, after which it would have to be loaded again from a MOT. Another pleasant property of a cold beam scheme would be the possibility to probe two interaction regions simultaneously and then allow for direct differential measurements (cf. paragraph 4 of the paper [46] presented in the following (paragraph 3.1.2)). Nevertheless for an optical trap, the localization of francium in a small volume would allow the concentration of the excitation laser power on the sample and an easier collection of the fluorescence photons.

In the two following paragraphs we give some considerations about a possible parity violation measurement on francium, for the two kinds of samples: cold beam and trap.

3.1.1 Cold beam

The case of a parity violation experiment on cold atomic beams (stable cesium or radioactive francium) has been considered in [46]. This article is reported in the following paragraph.

We briefly outline here the main feature. A cold spin-polarized (**P**) atomic beam is excited on the highly forbidden transition nS-(n+1)S (n=6 for cesium, 7 for francium), by circularly polarized (σ_+ or σ_-) light, in the presence of a transverse applied electric field **E**. The PV is then detected as a circular dichroism for the excitation light absorption, monitored by the collection of the fluorescence photons (n+1)$S \rightarrow$nP.

The setup considered in the article should allow to minimize the systematic effects related to the presence of unavoidable birefringences in the path of the laser beam. We show that with a very high production rate (of the order of what is currently attainable at the ISOLDE facility) a PV measurement could be envisaged.

3.1.2 Prospects for forbidden-transition spectroscopy and parity violation measurements using a beam of cold stable or radioactive atoms

Eur. Phys. J. D **25**, 3–13 (2003)
DOI: 10.1140/epjd/e2003-00215-5

THE EUROPEAN PHYSICAL JOURNAL D

Prospects for forbidden-transition spectroscopy and parity violation measurements using a beam of cold stable or radioactive atoms

S. Sanguinetti[a], J. Guéna, M. Lintz, Ph. Jacquier, A. Wasan, and M.-A. Bouchiat[b]

Laboratoire Kastler Brossel[c], Département de Physique de l'École Normale Supérieure, 24 rue Lhomond, 75231 Paris Cedex 05, France

Received 5 March 2003
Published online 17 July 2003 –

Abstract. Laser cooling and trapping offers the possibility of confining a sample of radioactive atoms in free space. Here, we address the question of how best to take advantage of cold atom properties to perform the observation of as highly forbidden a line as the 6S-7S Cs transition for achieving, in the longer term, atomic parity violation (APV) measurements in radioactive alkali isotopes. Another point at issue is whether one might do better with stable, cold atoms than with thermal atoms. To compensate for the large drawback of the small number of atoms available in a trap, one must take advantage of their low velocity. To lengthen the time of interaction with the excitation laser, we suggest choosing a geometry where the laser beam exciting the transition is colinear to a slow, cold atomic beam, either extracted from a trap or prepared by Zeeman slowing. We also suggest a new observable physical quantity manifesting APV, which presents several advantages: specificity, efficiency of detection, possibility of direct calibration by a parity conserving quantity of a similar nature. It is well adapted to a configuration where the cold atomic beam passes through two regions of transverse, crossed electric fields, leading both to differential measurements and to strong reduction of the contributions from the M_1-Stark interference signals, potential sources of systematics in APV measurements. Our evaluation of signal-to-noise ratios shows that with available techniques, measurements of transition amplitudes, important as required tests of atomic theory, should be possible in ^{133}Cs with a statistical precision of 10^{-3} and probably also in Fr isotopes for production rates of $\gtrsim 10^6$ Fr atoms s^{-1}. For APV measurements to become realistic, some practical realization of the collimation of the atomic beam as well as multiple passages of the excitation beam matching the atomic beam looks essential.

PACS. 32.80.Ys Weak-interaction effects in atoms – 32.70.Cs Oscillator strengths, lifetimes, transition moments – 32.80.Pj Optical cooling of atoms; trapping – 39.90.+d Other instrumentation and techniques for atomic and molecular physics

1 Introduction: motivations

Atomic parity violation (APV) measurements have proved successful for probing at low energy one of the most fundamental predictions of the standard model (SM), namely the existence of a weak electron-nucleus interaction mediated by the exchange of neutral gauge bosons Z_0 [1–3]. Up to now the efforts have been focused on the comparison between the experimental determination of the weak charge of the atomic nucleus, Q_W, and its SM prediction at the 0.5% level of precision, the cesium atom lending itself to the most precise comparison [4–6]. Actually, it looks somewhat too early to assert definitely either the absence or existence of a deviation, most likely less than 2.5σ [6,7]. On the other hand, it has not been possible, yet, to test another important SM prediction concerning the variation of Q_W along a string of isotopes belonging to the same element. An original experimental approach is currently pursued for rare-earth elements namely Yb [8] and Dy [9], but it also would be extremely valuable to extend the measurements which have proved successful for natural cesium, ^{133}Cs (the sole stable Cs isotope), to a few of its numerous radioactive isotopes, as well as to other alkali isotopes, most excitingly radioactive francium. With $Z = 87$, francium is expected to lead, due to the fast increase with Z [1], to APV effects 18 times larger than cesium, while it does not look unrealistic to have a theoretical prediction of its weak charge as precise as that for cesium [10]. Indeed, atomic structure calculations for alkalis

[a] *Also at* E. Fermi Physics Dept., Pisa Univ., Pisa, Italy.
[b] e-mail: marianne@lkb.ens.fr
[c] Laboratoire de l'École Normale Supérieure associé au CNRS (UMR 8552) et à l'Université Pierre et Marie Curie.

are (barring H and He) the most precise available. This, added to the fact that many isotopes can be produced, makes this element often considered as one of the most interesting candidates for forthcoming experiments. Moreover, since up to now, the nuclear anapole moment [11] has been detected only for ^{133}Cs [2] (an even neutron-number isotope), it is important to measure it for another isotope (preferably one with an odd neutron-number). Regardless of APV, measurements on the forbidden line in alkali-metal atoms are important since forbidden magnetic dipole amplitudes are "the most sensitive among electromagnetic transition amplitudes to the accuracy of the relativistic description of an atomic system" [12], *i.e.* rigorous tests of atomic theory.

Francium, and more generally short-lived radioactive atoms, either obtained from a radioactive source or produced on line by an accelerated ion beam colliding with a target, are produced at a limited rate with a thermal or even superthermal velocity distribution. In order to perform APV measurements the first prerequisite is to avoid their spreading out in space and their loss inside the wall. Only radiative cooling and trapping techniques [13] possibly combined with light induced atomic desorption (LIAD) [14] can succeed in this kind of operation. Several successful attempts to load radioactive alkali atoms in a neutral atom trap have been reported with ^{21}Na [15], ^{38}K^{m}, ^{37}K [16], ^{79}Rb [17], ^{135}Cs [18], $^{207-211}$Fr [19], ^{221}Fr [20]. Observation of several allowed Fr transitions has been realized for atoms trapped inside a MOT, leading to precise spectroscopic measurements [21]. But never, yet, has it been reported for a transition as highly forbidden as the Fr 7S-8S transition. Therefore, before attempting APV measurements with cold atoms, a preliminary — and by no means straightforward — objective consists in observing the 6S-7S transition with trapped Cs atoms. Since the precise value of the parity conserving transition amplitudes, in particular the Stark induced amplitude associated with the vector polarizability β, is still a somewhat open question (see below), as an assessment of the potential of trapped atoms for this kind of experiment, we suggest a new precision measurement of the ratio $M_1^{\rm hf}/\beta$. Here, the magnetic dipole amplitude $M_1^{\rm hf}$ induced by hyperfine interaction serves as a precisely known amplitude used for calibration [22,23]. This would be all the more precious since the previous measurements [3] were made in acrobatic conditions (background equal to 100 times the signal [3]) and have led to a result for β which differs from a recent independent semi-empirical determination by (0.7±0.4)% [24]. Though small, such a difference is sufficient to narrow the gap between theoretical and experimental values of Q_W(Cs) from 2.2 to 0.9σ. A measurement of $M_1^{\rm hf}/\beta$ in cesium will allow us to assess the feasibility of similar measurements in francium, knowing the production rate. Finally, we also attempt to evaluate the feasibility of an even more ambitious project, namely a new high precision measurement of the parity violating electric dipole amplitude $E_1^{\rm pv}$ in cesium, and hence Q_W(Cs) by an independent method using cold atoms. Indeed, such an independent measurement would be extremely valuable as a cross check of this fundamental quantity [25]. Beyond this, we cannot understate how welcome a measurement of Q_W(Fr) would be, if some day feasible.

Our paper is a prospective work suggesting preparatory experiments for much more ambitious projects. Once a sample of cold alkali atoms is produced at the center of a trap, there remains a still unsolved point at issue: what is the best way to use it for exciting and probing the forbidden Cs 6S-7S transition, or the analogous 7S-8S transition in Fr, in the Stark electric field necessary to previous APV measurements? Even for the stable isotope ^{133}Cs, the biggest difficulty is linked to the small number of atoms available in a trap. It is the purpose of the present paper to quantify such a difficulty by making comparisons with conditions realized in previous APV experiments performed with stable, thermal atoms and to suggest an experimental approach using their different specific properties. We suggest advantageous means to exploit their low velocity and we also propose a new physical observable which, we believe, is well adapted to this situation. It is shown to be well suited to the measurement of first $M_1^{\rm hf}/\beta$ and later $E_1^{\rm pv}/M_1^{\rm hf}$. Concerning the measurement accuracy, in an approach of this kind two parameters play an essential role: (i) the number of atoms present at a given time in the interaction region, (ii) the probability for such an atom to contribute to the APV signal, which takes into account the nature of the physical observable, and both the excitation and detection efficiencies. We have not found the ideal compromise between simplicity and outstanding performances, transferable from Cs to Fr. According to the exact goal to be reached the experimental scheme to be chosen will probably have to change. We consider three different experimental approaches, all of them relying on the production of a cold, slow atomic beam. They differ by the method of production of the beam and its parameters. This will appear explicitly in Section 2. The observable physical quantity is presented in Section 3, while Section 4 describes a method to suppress the dangerous systematic effect which might arise from the Stark-M_1 interference effect when one wants to measure $E_1^{\rm pv}$. Finally (Sect. 5), we make predictions for the signal-to-noise ratio for measuring the interesting physical quantities mentioned above, in these three different, well-defined and realistic experimental configurations.

2 Use of a slow and cold atomic beam excited by a colinear laser beam

The energy levels and wavelengths relevant to APV measurements and to laser trapping operation for both cesium and francium are shown in Figure 1. A precise value of the measured energy difference between the Fr $8S_{1/2}$ and $7S_{1/2}$ levels is given in [26]. Performing the PV measurements *inside* an optical molasses or a magneto optical trap (MOT), precisely where the atoms are cooled and stored presents some inconvenience. Indeed, both laser cooling and APV measurements require specific conditions which

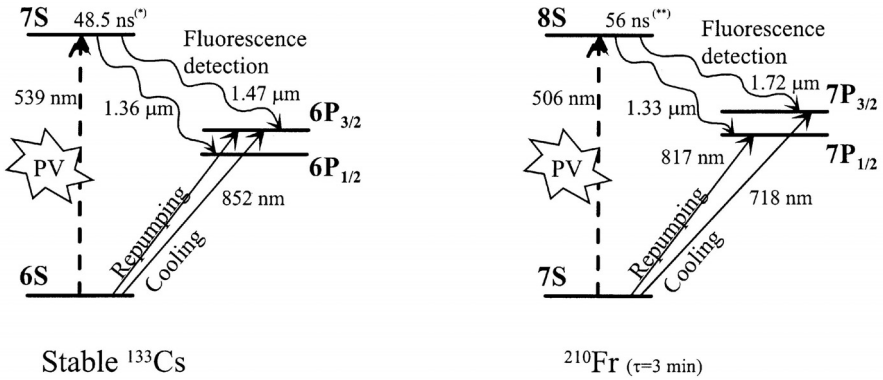

Fig. 1. Energy levels and wavelengths relevant for APV experiments and atomic cooling and trapping in cesium and francium. (*) Cs 7S state lifetime from experiment [31], and (**) Fr 8S state lifetime from theory [32].

look difficult to reconcile: for instance, the presence of excited atomic species in the interaction region and the interception of the wide cooling light beams by the necessary electrodes are both difficult to avoid. Among a large variety of techniques available for manipulating atomic velocities by electromagnetic forces [27], several of them offer the possibility of producing a well collimated beam of slow, cold atoms. In order to concentrate the discussion on a well defined situation, we shall choose the example of a pyramidal MOT built according to the judicious and simple suggestion of Lee *et al.* [28], now used by several groups [29,30]. The trap is built with four mirrors, standing as the four faces of an inverted pyramid. A single cooling beam, circularly polarized, is enough to create, after reflection on the four mirrors, the same field configuration as a standard six-beam MOT. When the pyramidal trap is vapor-loaded, a beam of slow and cold atoms escapes continuously through the hole bored through the pyramid apex because of local imbalance of intensities. In typical conditions this kind of device can provide a continuous flux $\Phi_{\rm at}$ of $\gtrsim 2\times10^9$ cesium atoms/s with a mean velocity v tunable around 10 m/s and a velocity spread less than 1.5 m/s [30]. The transverse velocity spread of the beam is found to lie close to the transverse Doppler limit for cesium $\sqrt{\hbar\Gamma/m} = 0.13$ m/s.

The pyramidal trap has advantages of low cost and simplicity, but still better performances can be achieved with more sophisticated devices. In particular, references [33,34] describes how an even slower and colder rubidium beam can be obtained using a vapor loaded laser trap which ensures two-dimensional magneto-optical trapping, as well as longitudinal cooling by a moving molasses (MM-MOT). The average velocity can be as low as 1 m/s and the velocity distribution has been evaluated: $\Delta v/v < 1/10$. When either one of those slow atomic beams is illuminated by a co- or counter-propagating narrow line-width cw laser beam, *the dispersion of the longitudinal velocities is small enough for all atoms excited on the 6S-7S transition to belong to a single velocity class.* Moreover, at optimum alignment, the divergence of the atomic beam (26 mrad FWHM) going out of the pyramidal trap is small enough for avoiding any significant atom loss out of a 1 mm radius laser beam over an interaction length of 4 cm. In contrast, the larger divergence of the ultra-cold beam [34] unavoidably complicates the design of the experiment (see proposal 2, Sect. 5.2). Other 2D-MOTs, among those delivering larger atomic fluxes [35–37], have, for the present application, the drawback of either a larger divergence or a larger velocity spread. On the other hand, the features needed here, high flux, moderate velocity and low divergence are met by other techniques, namely Zeeman slowing. In particular, the Zeeman slower apparatus described in reference [38] has very attractive features: a flux of Cs atoms exceeding 10^{10} s^{-1}, very small spread of longitudinal velocities, $\sim$1 m/s and much better collimation (divergence angle less than 1 mrad). This gives the possibility of lengthening the interaction region (see proposal 3 in Tab. 1 and Sect. 5.3). Although some adaptation will be necessary to make the system work with radioactive isotopes, depending on their method of production, it is interesting to evaluate its potentiality as compared to that of a thermal atomic beam or a vapor cell.

After a short path beyond the trap exit (or the collimation module [38]), the atomic beam enters the interaction region which includes capacitor plates generating the Stark field, with the plane electrodes parallel to the beam direction. The first relevant parameter to be compared here to previous experimental configurations is the number of atoms $N_{\rm at}$ interacting with the excitation laser beam in the interaction region of length l.

For an atomic beam experiment $N_{\rm at} = \Phi_{\rm at}\times l/v$. For a vapor in thermal equilibrium (Paris experiment [40]) we take into account the fact that only a fraction of the atoms can absorb the resonant light beam which has a spectral width much smaller than the Doppler width. By averaging the velocity-dependent transition probability over the thermal distribution, one finds that this can be accounted for by the reduction factor: $R = \sqrt{2\pi}\Gamma/4\Gamma_D$ (see Ref. [41]), where $\Gamma_D = \omega_0\sqrt{kT/Mc^2}$, and $\omega_0/2\pi$ is the transition frequency; Γ is the radiative linewidth of the 7S state, including both the emission rate of spontaneous and stimulated photons. In the conditions realized experimentally, we arrive at $R \approx 0.035$. The factor R yields the fraction of atoms sufficiently slow to be in interaction with the

Table 1. Number of atoms in the interaction region for the cold atomic beam proposals compared to the previous situations in which APV measurements have been performed. Figures collected in the last column, clearly illustrates that, for stable atoms, a vapor experiment presents from the outset a large advantage.

	Atom flux $\Phi_{\rm at}$ (at s^{-1})	Velocity v (cm s^{-1})	Length l (cm)	Int. time $\tau(s)$	Number of atoms in the interaction region $N_{\rm at}$
Slow, cold beam [30] (proposal 1)	2×10^{9}	0.8×10^{3}	4	5×10^{-3}	1×10^{7}
Ultra-cold beam [34] (proposal 2)	2×10^{9}	1×10^{2}	5	5×10^{-2}	$1\times10^{8}\,(\times\frac{1}{10})^{\star}$
Zeeman slower [38] (proposal 3)	2.6×10^{10}	9×10^{3}	60	6.7×10^{-3}	1.7×10^{8}
Thermal beam (Boulder [2]) completed expt.	1×10^{13}	3×10^{4}	0.08	2.6×10^{-6}	2.6×10^{7}
Vapor (Paris [40])	density (cm^{-3})	volume (cm^{3})	R		
current expt.	2×10^{14}	0.1	3.5×10^{-2}		7×10^{11}

* This additional factor is a rough estimate of the loss occasioned by spreading of the beam, unless special design of the experiment (*e.g.* multiple passages of the excitation beam) solves this difficulty.

resonant excitation laser, thus we obtain $N_{\rm Cs} = n_{\rm Cs}V\times R$, $n_{\rm Cs}$ being the cesium vapor density, and V the interaction volume.

Table 1 collects the value of this important parameter $N_{\rm at}$ expected in the present proposals, for comparison with those obtained in the experiment having previously yielded APV data in Cs. It clearly appears that the effect of the much larger atomic flux available with the thermal beam used by the Boulder group [2,42] is counterbalanced by the much shorter interaction time resulting from a ∼30 times larger velocity and an interaction length ∼50 times shorter to ensure transverse excitation of the beam. By comparison, the vapor experiment developed in Paris takes complete advantage of having at one's disposal a number of atoms in the interaction region up to tens thousands times larger. The thermal beam experiment compensates for this deficit by use of a huge laser power in the interaction region owing to a Fabry-Perot cavity with a finesse of $\sim 10^5$. From the point of view of systematics each approach has its advantages and its drawbacks.

Cold atomic beams of several kinds have been described in the literature. Since our purpose is to assess how well each one is adapted to performing APV measurements, with comparison in view, we introduce a quality factor aiming at taking into account the divergence of the atomic beam, $\Delta v_\perp/v$, the main limitation to measurement efficiency. We first define the optimum length of interaction $l_{\rm opt}$, as the length over which the atomic beam radius r, does not exceed 1 mm, a reasonable value for a laser beam radius[1]. For proposals 1, 2 and 3, we obtain

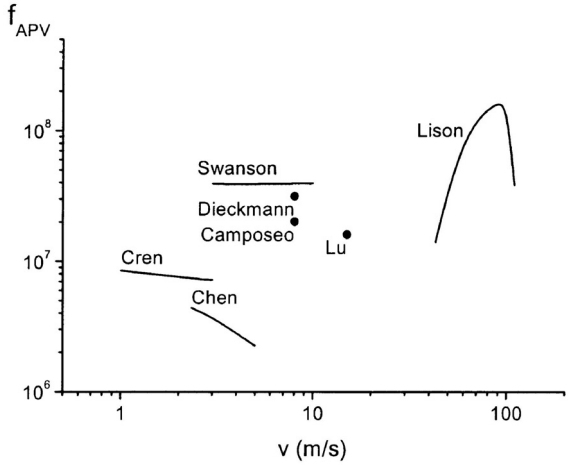

Fig. 2. The quality factor $f_{\rm APV}$ *versus* atomic longitudinal velocity for several alkali sources of cold atomic beams. Camposeo *et al.* [30] (Cs), Chen *et al.* [33] (Rb), Cren *et al.* [34] (Rb), Dieckmann *et al.* [35] (Rb), Swanson *et al.* [36] (Rb), Lison *et al.* [38] (Cs), Lu *et al.* [39] (Rb).

$l_{\rm opt}$ = 4 cm, 1.5 cm and 60 cm respectively[2]. Then, the quality factor is defined as the number of atoms in the interaction region of length $l_{\rm opt}$, namely $f_{\rm APV} = \Phi_{\rm at}\times l_{\rm opt}/v$.

In Figure 2 we plot the quality factor versus the velocity for several beams of cold stable atoms chosen among those having a small spread of longitudinal velocities. The existing designs present themselves as grouped into three categories: ultra-cold beams using a moving molasses

[1] More precisely, $l_{\rm opt}$ is defined by the condition: $r = r_0 + (\Delta v_\perp/v)l_{\rm opt} = 1$ mm, where r_0 is the atomic beam radius at the pyramidal MOT or collimator output and $\Delta v_\perp = \sqrt{kT_\perp/m}$.

[2] The beam can be horizontal: the vertical displacement $gl^2/2v^2$ over these distances, due to gravity, does not exceed 0.5 mm.

[33,34], cold beams extracted from a 2D-MOT [30,35,36, 39] and a Zeeman-slowed device using a collimator [38]. In view of optimizing APV measurements on stable atoms, this last device is expected to lead to the best results, although the pyramidal trap remains of real interest due to its simplicity and probably better adaptability to radioactive isotopes. As we noted previously, the performances expected with the cold atomic beams are limited essentially by their divergence. However one may imagine two means of palliating this kind of difficulty.

(i) *Multiple passages of the excitation beam:* it looks possible to widen the interaction region, at fixed density of excitation energy, by performing forward-backward passages of the beam between two spherical mirrors. The two mirrors should be pierced, one for providing the passage of the atomic beam at the output of the MOT and the other the passage of the counterpropagating excitation laser [43].

(ii) *Insertion of a collimator at the output of the MOT:* it would seem very interesting to insert at the output of a two dimensional MOT a collimator similar to that described in [38]. Besides the beam collimation this device has the attractive feature of deflecting the atomic beam by a small angle, thus making possible to place the interaction region inside a Fabry-Perot cavity which provides enhancement of the excitation energy density. However we must be aware that a transverse temperature at the output of the collimator less than 50 μK looks difficult to achieve. Therefore the divergence of the slow beam remains well above that of the faster Zeeman-slowed beam.

3 A well adapted observable physical quantity and two interaction regions

The choice of the observable physical quantity which manifests APV also plays an important role, since it determines the specific nature of the signal (absence or presence of a background), its signature and it also conditions the detection efficiency. In our first experiment in Paris [44], as well as in our current second-generation one [40], we have chosen to detect an angular momentum anisotropy in the excited state (either an atomic orientation in the first version, or an atomic alignment in the latter) providing a very specific signal without background. However, fluorescence detection efficiency of the 7S state orientation was low ($\sim 10^{-3}$), due to the need of polarization analysis on a single fine structure line. Alignment detection can be conducted efficiently using stimulated emission detection [40,45]. However, in view of the very small number of atoms available in a trap, there is no possibility of signal amplification by the stimulated emission process advantageously used in a dense vapor. Therefore, with a cold beam there is a strong incentive for detecting the PV effect on the absorption rate.

We suggest creating a spin polarization $\mathbf{P}_e$ of the atomic beam at the output of the trap in a direction perpendicular to its velocity. Then, an specially well adapted observable physical quantity is a contribution to the absorption rate involving this spin polarization. It results from an interference between the parity-violating electric dipole amplitude $E_1^{\rm pv}$ and the Stark amplitude induced by a transverse electric field. More precisely, the manifestation of APV would then rely on the presence in the absorption rate of the pseudoscalar quantity $\mathbf{E} \wedge \xi\hat{\mathbf{k}} \cdot \mathbf{P}_e$, where $\xi\hat{\mathbf{k}}$ represents the angular momentum of the light beam which excites the transition and $\mathbf{E}$ is the applied static electric field. It has the advantage of appearing in the total population of the excited state. It can be detected by monitoring the total intensity of the fluorescence light emitted during the two-step desexcitation process, involving either the $6P_{1/2}$ or the $6P_{3/2}$ state. No polarization analysis nor even light filtering (except for stray light) is necessary in principle. The APV signal is odd under the separate reversals of the electric field, the spin polarization and the helicity of the photons which excite the transition. We relegate to the appendix the derivation of the signal expression in the most general conditions. Here we present the result in the particular case of ^{133}Cs ($I = 7/2$), for the experimental configuration shown in Figure 4, supposing no magnetic field and a total circular polarization of the excitation beam, $\xi = 2\,\mathrm{Im}\{\epsilon_x^* \epsilon_y\} = \pm 1$ (hence $|\hat{\boldsymbol{\epsilon}} \cdot \hat{\mathbf{u}}\,|^2 = 1/2$ whatever $\hat{\mathbf{u}} \perp \hat{\mathbf{k}}$)

$$N_{7\mathrm{S}} \propto \beta^2 E^2 - \frac{3}{4}\,(M_1' + \xi\ \mathrm{Im}E_1^{\rm pv})\ \beta \mathbf{E} \wedge \hat{\mathbf{k}} \cdot \mathbf{P}_e \quad \text{for the 6S, } F = 3 \to 7\mathrm{S}, \quad F = 4 \text{ line,} \quad (1)$$

$$N_{7\mathrm{S}} \propto \beta^2 E^2 - \frac{5}{4}\,(M_1' + \xi\ \mathrm{Im}E_1^{\rm pv})\ \beta \mathbf{E} \wedge \hat{\mathbf{k}} \cdot \mathbf{P}_e \quad \text{for the 6S, } F = 4 \to 7\mathrm{S}, \quad F = 3 \text{ line,} \quad (2)$$

where β denotes the vector polarizability of the transition[3] and M_1', the magnetic dipole amplitude, which is the sum of the many-body contribution M_1 and that induced by the hyperfine interaction $M_1^{\rm hf}$. Here we assume the applied electric field large enough to neglect the field-independent contribution proportional to $M_1'^2$.

We note that *this circular dichroism of a transversally polarized sample*, $\mathbf{E} \cdot \xi\hat{\mathbf{k}} \wedge \mathbf{P}_e$, could not be envisaged in a dense vapor where the spin polarization is rapidly destroyed by collisions. By contrast, (co-)counterpropagation of the atomic and light beams provides the attractive possibility of having both beams passing *through two interaction regions leading to circular dichroism of opposite sign*. For instance, one can choose two orthogonal directions of $\mathbf{E}$ in these two regions, with the direction of $\mathbf{P}_e$ taken at $\pm 45°$ to the direction of $\mathbf{E}$ in one and the other region (see configurations 1 and 2, or 3 and 4, represented in Fig. 4). Then, the difference of fluorescence rates in the two regions can selectively provide the $\mathbf{P}_e$-dependent contribution of interest. In the next section,

[3] From the radial matrix elements and the experimental energies compiled in [46], we have obtained estimates of the scalar and vector Fr 7S-8S transition polarizabilities, $\alpha = -361\ ea_0^3$, $\beta = 50\ ea_0^3$ hence $\alpha/\beta \approx -7.2$ (instead of $-261\ ea_0^3$, $27\ ea_0^3$ and -9.9 for the Cs 6S-7S transition).

we shall show that such a differential measurement also offers the important additional advantage of suppressing some dangerous systematic effects.

It is important to notice that real time calibration of the PV signal is easy to obtain. By selecting in the fluorescence rate the contribution odd under the separate reversals of the electric field and the spin polarization, but even in the reversal of the light helicity, we can isolate the M_1'-Stark interference signal. Thereby the amplitude $\mathrm{Im}E_1^{\mathrm{pv}}$ is directly calibrated[4] in terms of M_1'. If one reminds that $M_1' = M_1 \pm M_1^{\mathrm{hf}}$, depending on the hyperfine transition $\Delta F = \pm 1$, we see that absolute calibration of $\mathrm{Im}E_1^{\mathrm{pv}}$ in terms of the theoretically well-known amplitude M_1^{hf} is possible.

Another observable physical quantity appearing in the absorption rate has been proposed in [47]. It does not require any spin polarization of the ground state, but it involves the application of a magnetic field $\mathbf{B}$, transverse to the light beam, which enters explicitly into the definition of the pseudoscalar manifesting parity violation, $\mathbf{E} \cdot \xi\hat{\mathbf{k}} \wedge \mathbf{B}$. However, for observing this effect the field has to be large enough for the Zeeman components to be resolved, otherwise compensations occur [48]. This is, actually, the APV effect which has been detected by the Boulder group [49]. In the most recent version of their experiment [2] (see Fig. 3a for a schematic representation of the configuration), the atomic beam is spin polarized in a preparation zone before entering the interaction region, but a magnetic field (6.4 G), whose purpose is to resolve the Zeeman lines is still applied, although the atomic spin polarization prepared in the ground state makes this unnecessary, as equation (1) shows. With the same set-up, a much weaker field would be sufficient for preserving the direction of the atomic orientation between the preparation and the interaction regions. This would avoid slight line overlap of adjacent Zeeman lines and the associated difficulties.

Let us now comment on the conditions to be fulfilled by the magnetic field, which obviously cannot be perfectly cancelled. There are strict requirements: the magnetic field of the MOT has to be screened. Instead, a small $\mathbf{B}$ field along the direction wanted for the spin polarization is needed in the optical pumping region as well as in the two interaction regions and, consequently, in between those two regions: otherwise the rapid spin precession might result in spin disorientation (when the spins do not follow adiabatically the field direction). Finally, the exact direction of $\mathbf{P}_e$ inside the interaction regions, involved in the pseudoscalar manifesting APV, is actually determined by the $\mathbf{b}$ field direction in those regions, even though this field (typically 100 mG) is small enough to avoid broadening of the transition. We note that those conditions are easier to fulfill than those realized in [2], since the field direction remains the same between the preparation and the interaction regions (see Fig. 3), instead of having to be rotated by $\pi/2$.

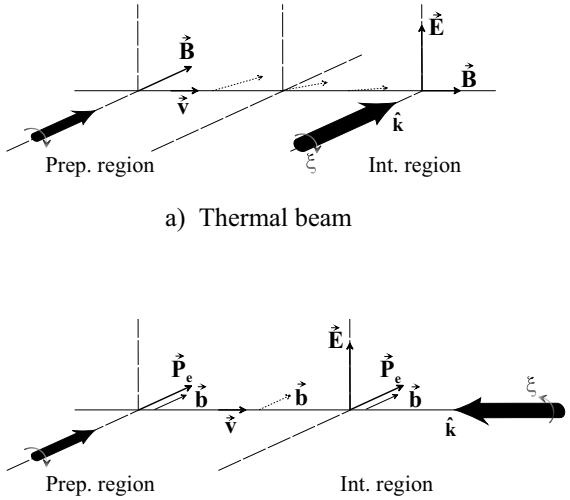

Fig. 3. Schemes of the geometrical configurations relative (a) to the Boulder experiment performed with a thermal atomic beam [2] and (b) to the present proposal using a cold and slow atomic beam. Both exploit the spin polarization $\mathbf{P}_e$ of the atoms performed in a preparation region and use a transverse Stark electric field $\mathbf{E}$ in the interaction region. Both make use of a circularly polarized excitation beam (helicity ξ). With the thermal beam, the excitation beam has to be transverse to the velocity and the magnetic field $\mathbf{B}$, large enough to resolve the Zeeman components, has to rotate its direction by $\pi/2$ between the preparation and interaction regions, while with the cold beam the excitation can be longitudinal and only a small magnetic field $\mathbf{b}$, of uniform direction, is required, to preserve the spin polarization between the two regions. The pseudoscalar $\mathbf{E}\cdot\xi\hat{\mathbf{k}}\wedge\mathbf{B}$ manifesting APV in case (a) is replaced by $\mathbf{E} \cdot \xi\hat{\mathbf{k}} \wedge \mathbf{P}_e$ in case (b).

4 Suppression of the systematic effect arising from the M_1'-Stark interference via optical birefringences

As we may note in equation (1), when the sign of the true scalar $\mathbf{P}_e \cdot \mathbf{E} \wedge \hat{\mathbf{k}}$ is reversed, the discrimination between the E_1^{pv}-Stark and the M_1'-Stark interference signals hinges on their opposite behaviour under reversal of the pseudoscalar ξ, the excitation light helicity. Since in ^{133}Cs, the latter is the larger of the two signals, by a factor 2×10^4, this is a major source of potential systematic effect[5]. Indeed, APV measurements previously performed in a transverse electric field have all met the difficulty

[4] This calibration procedure performed in each region independently, eliminates the magnitude of the spin polarization and the exact value of $|\mathbf{E}\cdot\xi\hat{\mathbf{k}}\wedge\mathbf{P}_e|$ as well as other geometrical parameters (beam spreading, detection efficiency, etc.) which may differ from one region to the other.

[5] From the calculated magnetic dipole transition amplitudes [12], we can expect $M_1(\mathrm{Fr})/M_1(\mathrm{Cs}) \sim 13$, while from [10] we expect $E_1^{\mathrm{pv}}(\mathrm{Fr})/E_1^{\mathrm{pv}}(\mathrm{Cs}) \sim 18$, hence a similar order of magnitude is expected for the ratio M_1/E_1^{pv} in both alkalis.

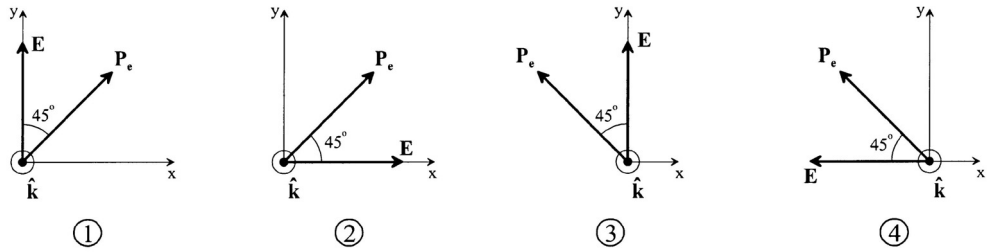

Fig. 4. The four geometrical configurations considered in the text, specified by the relative directions of the Stark field, $\mathbf{E}$, the spin polarization created in the ground state, $\mathbf{P}_e$, and the wave vector of the excitation laser $\hat{\mathbf{k}}$; ξ is assumed the same in the four configurations; the atom velocity is along $\hat{\mathbf{k}}$, orthogonal to the page. By combining measurements performed in those four configurations, the PV signal is obtained with considerable reduction of the systematic effect arising from the M_1'-Stark interference signal *via* optical birefringences.

associated with the presence of the parity conserving interference effect, which can mimic the PV signal if the reversal of the light helicity ξ is imperfect, *i.e.* if a small component of linear polarization changes its sign simultaneously with ξ. This kind of problem occurs when the optics on the path of the excitation beam possess some birefringence, a defect difficult to avoid completely at the level required.

For the complete discussion given below, we have to write down the expression for the M_1'-Stark signal assuming the most general description of the excitation light polarization. It is expressed in terms of the four Stokes parameters, which give a general representation of the beam polarization properties: $u_0 = |\epsilon_y|^2 + |\epsilon_x|^2$; $u_1 = \mathrm{Re}\{\epsilon_x\epsilon_y^* + \epsilon_x^*\epsilon_y\}$; $u_2 \equiv \xi = \mathrm{Im}\{\epsilon_x^*\epsilon_y - \epsilon_x\epsilon_y^*\}$; $u_3 = |\epsilon_y|^2 - |\epsilon_x|^2$. The first parameter u_0 represents the unpolarized intensity. If it is normalized to unity, the other parameters represent polarization ratios measured by a linear analyzer directed along x, then y (u_3) or along the bisectors of x and y (u_1) or by a direct then inverse circular analyzer (u_2).

According to equation (19) of Appendix A, the general expression for the M_1'-Stark interference signal $\mathcal{S}(M_1)$ is given by:

$$\mathcal{S}(M_1) = -2M_1' \,\mathrm{Re}\{(\beta\mathbf{E} \wedge \hat{\mathbf{k}} \cdot \hat{\boldsymbol{\epsilon}})(\hat{\boldsymbol{\epsilon}}^* \cdot \mathbf{P}_e)\}. \qquad (3)$$

We consider the four distinct geometrical configurations represented in Figure 4. Measurements relative to configurations 1 and 2 (or 3 and 4) can be performed simultaneously in the two distinct interaction regions, whereas reversal of $\mathbf{P}_e$ by $\pi/2$ is needed for changing configuration 1 into 3 and 2 into 4. It is interesting to compare the $\mathcal{S}(M_1)$ signals expected in those four configurations:

$$\begin{aligned}
\mathcal{S}_1(M_1) &= -2M_1'\beta E\left(|\epsilon_x|^2 + \mathrm{Re}\{\epsilon_x^*\epsilon_y\}\right) \\
&= -M_1'\beta E\,(u_0 - u_3 + u_1)\,, \qquad (4)\\
\mathcal{S}_2(M_1) &= \;\; 2M_1'\beta E\left(|\epsilon_y|^2 + \mathrm{Re}\{\epsilon_x^*\epsilon_y\}\right) \\
&= M_1'\beta E\,(u_0 + u_3 + u_1)\,, \qquad (5)\\
\mathcal{S}_3(M_1) &= \;\; 2M_1'\beta E\left(|\epsilon_x|^2 - \mathrm{Re}\{\epsilon_x^*\epsilon_y\}\right) \\
&= M_1'\beta E\,(u_0 - u_3 - u_1)\,, \qquad (6)\\
\mathcal{S}_4(M_1) &= -2M_1'\beta E\left(|\epsilon_y|^2 - \mathrm{Re}\{\epsilon_x^*\epsilon_y\}\right) \\
&= -M_1'\beta E\,(u_0 + u_3 - u_1)\,, \qquad (7)
\end{aligned}$$

Furthermore configurations 1 and 2 provide opposite circular dichroism *i.e.* opposite PV signals, $\mathcal{S}_1(PV) = -\mathcal{S}_2(PV) = (\mathrm{Im}E_1^{\mathrm{pv}}\beta\mathbf{E} \wedge \xi\hat{\mathbf{k}} \cdot \mathbf{P}_e)$, and the same result holds for 3 and 4. From the above set of four equations one can form the linear combination

$$\mathcal{S}_1 - \mathcal{S}_2 - \mathcal{S}_3 + \mathcal{S}_4 = 4\,(\mathcal{S}_1(PV) - M_1'\,\beta E\,u_0)\,, \qquad (8)$$

which shows up an important property: the contribution of the M_1'-Stark interference signal involves only the unpolarized intensity, u_0. Thereby when ξ is reversed, so as to isolate the E_1^{pv} contribution, we reduce considerably the risk which would have come from $\xi - odd$ contributions contaminating either u_3 or u_1, *via* the birefringence of the optics[6].

As a convenient and reliable means of performing helicity reversal, one can use the polarization modulator described in reference [51]. It provides specific labeling of the three Stokes parameters, u_1, $\xi \equiv u_2$, and u_3, by distinct modulations. In this way both signals $\mathcal{S}(PV)$ and $\mathcal{S}(M_1)$ appearing at different frequencies are detected by synchronous detection.

Additional discrimination of $\mathcal{S}(PV)$ against $\mathcal{S}(M_1)$, respectively even and odd under $\hat{\mathbf{k}}$ reversal, can be obtained by arranging multiple passages of the beam between two mirrors pierced in their center, following a procedure used in [43,44].

5 Magnitude of the expected signals

In the preceding sections we have made precise suggestions for adapting APV measurements to a source of cold atoms. Now we give an estimate of both the APV and the M_1'-Stark interference signals, $\mathcal{S}(PV)$ and $\mathcal{S}(M_1)$, and their signal-to-noise ratios (SNR), assuming reasonable magnitudes of the Stark field and the laser intensity. We note that the shot noise limited SNR is independent of the magnitude of the Stark field. We take the example of ^{133}Cs in order to make easier comparison with

[6] More precisely, the birefringence α_3 of axes x and y induces a small polarization $u_1 = 2\alpha_3\xi$ and the birefringence α_1, with axes oriented at 45°, a small polarization $u_3 = 2\alpha_1\xi$.

other atomic sources already exploited. First, we need to evaluate the excitation probability per unit of time: $\mathcal{R}_{\rm ex} = ({\rm d}N^*_{\rm Cs}/{\rm d}t)/N_{\rm Cs} = \sigma_{\rm ex}(E)\Phi_{\rm ex}$, where $\Phi_{\rm ex}$ is the flux of excitation photons. The excitation cross-section without electric field, $\sigma_{\rm nat} = \sigma_{\rm ex}(E = 0)$, without Doppler broadening, for an isotope without nuclear spin, excited by a single-mode laser centered in frequency at the transition peak, is given in reference [41]:

$$\sigma_{\rm nat} = \frac{\lambda^2}{2\pi}\,\frac{\Gamma_{M_1'}}{\Gamma_{\rm 7S}} = 2.45\times 10^{-23}\ {\rm cm}^2. \qquad (9)$$

Here $\Gamma_{\rm 7S}$ denotes the natural width of the 7S state and $\Gamma_{M_1'}$ the partial width associated with the M_1' amplitude. Assuming excitation of the $6{\rm S}_F \rightarrow 7{\rm S}_{F'}$ line in an electric field, using the results of Appendix A, we obtain:

$$\sigma_{\rm ex}(E) = \frac{(2F'+1)}{2(2I+1)}\frac{2}{3}(1-g_{_{F'}})\left(\frac{\beta E}{M_1'}\right)^2\sigma_{\rm nat}. \qquad (10)$$

5.1 Measurement of $M_1'/\beta E$ with a cold atomic beam (proposal 1)

For a Stark electric field of 1000 V/cm, leading to $\sigma_{\rm ex}(E) = 0.89\times 10^{-20}$ cm^2 for the $6{\rm S}_{F=3} \rightarrow 7{\rm S}_{F'=4}$ line and $\beta E/M_1 = 1000/30$, for an excitation beam of waist radius 1 mm, delivering 500 mW at 539.4 nm ($\Phi_{\rm ex} = 0.95\times 10^{20}$ photons s^{-1}/cm^2), we predict $\mathcal{R}_{\rm ex} = 0.89\times 10^{-20}\times 0.95\times 10^{20} = 0.84$ s^{-1}. Using the number of Cs atoms in the interaction region, given in Table 1 (proposal 1), we expect ${\rm d}N^*_{\rm Cs}/{\rm d}t = 0.84\times 10^7$ s^{-1} for the two interaction regions, each 20 mm long. Supposing a fluorescence detection efficiency of 10%, we predict a collected fluorescence rate of $\sim 10^6$ s^{-1}. Using equation (1) (and (2)), with $|\mathbf{E}\cdot\hat{\mathbf{k}}\wedge\mathbf{P}_e| = 1/\sqrt{2}$, we expect a SNR $\simeq 15/\sqrt{\rm Hz}$ for $\mathcal{S}(M_1)$ for the $6{\rm S}_{F=3} \rightarrow 7{\rm S}_{F'=4}$ line (and $\simeq 20/\sqrt{\rm Hz}$ on the $6{\rm S}_{F=4} \rightarrow 7{\rm S}_{F'=3}$ line). Hence a statistical precision of 10^{-3} can be obtained with an integration time of about one hour. For the measurement of $M_1^{\rm hf} \sim M_1'/5$ at the same level of precision, the integration time has to be 25 times longer, for both $\Delta F = 1$ and -1 lines. This looks possible to achieve. We believe that the conditions for observing this signal could be made excellent: thanks to the very good vacuum realized by differential pumping in the beam compartment which is well separated from the MOT by the pyramidal assembly, we can expect nearly no background. In this respect the signature given to $\mathcal{S}(M_1)$ by modulating u_3 and u_1 (see Eqs. (4–7)) should be of great help.

On the other hand, with ${\rm Im}E_1^{\rm pv}/\beta E = 1.6\times 10^{-6}$, there is no chance to achieve APV measurements without recourse to some amplification process. A possibility might rely on multiple passages of the excitation beam which can also provide efficient suppression of the M_1'-Stark interference signal and hence further reduction of the associated systematics. If we denote by κ the signal enhancement factor, the SNR for $\mathcal{S}(PV)$ becomes $\sim\sqrt{\kappa}\times 10^{-3}/\sqrt{\rm Hz}$, hence the time required for observing the PV effect with SNR = 1 is $10^6/\kappa$ seconds. An enhancement factor larger than 100 would be necessary for obtaining worthwhile conditions of measurement.

We can now examine the situation with francium. As mentioned earlier we can expect the francium M_1' amplitude to be one order of magnitude larger than the cesium one. This increases the $\mathcal{S}(M_1)$ without adding noise. The shot noise limited SNR ratio is thus increased by a factor of 10. On the other hand, the atom flux will certainly be reduced. The best production rates of Fr^+ ions available in the world is, to our knowledge, at the ISOLDE facility at CERN: it amounts to $\sim 10^9$ s^{-1}. We are presently uncertain about the efficiency of neutralization and collection in the MOT, ζ, one may expect. A fairly conservative estimate might be $\zeta \sim 10^{-2}$. However, taking into account that a 80% ion to atom conversion efficiency has been reported for the converter used on-line at ISOLDE [52] and that a 16% collection and trapping efficiency has been achieved with Fr atoms [39], we can reasonably hope that $\zeta \approx 0.1$ is achievable. The SNR is reduced by $\sqrt{\zeta}$. All in all, we can consider that not only does the observation of the forbidden 7S-8S transition look feasible but so too does a measurement of its magnetic dipole amplitude with an accuracy better than 10%. This would provide an important test of atomic models [12]. Such an experiment would also give invaluable insight into how to perform a future measurement of Q_W(Fr): for such a measurement to become possible with an efficiency $\zeta = 10^{-2}$, the same enhancement factor $\kappa = 100$ as for cesium is required.

5.2 Prospect for APV observation with an ultra cold atomic beam (proposal 2)

As shown in Table 1, the ultra-cold beam can in principle offer better performances owing to the possibility of lengthening the interaction time. However, this advantage is spoiled by the effect of the beam divergence, which one would like to reduce by a factor of ~ 3. One possibility consists in making additional transverse cooling of the atomic beam simultaneously at the output of the MM-MOT, using an auxiliary 2D MOT according to a scheme used by the authors of reference [34] for loading the beam into a magnetic guide. If one wants to benefit from the lowest velocities, ~ 20 cm/s reported in [34], *a priori* very interesting here, one has to solve the problem of collisional losses of the slow atomic beam with atoms in the vapor cell on its way to the interaction region, possibly by using other means for loading the trap.

Another important technical question, beyond the scope of the present paper, concerns the possibility of combining the advantages of multiple passages of the longitudinal excitation beam with those of the ultra-cold atomic beam.

5.3 APV observation with a Zeeman-slowed atomic beam (proposal 3)

The number of atoms in the interaction region obtainable with the Zeeman slower is given in Table 1. It corresponds

to a gain by a factor of $\sqrt{17}$ with respect to the slow and cold atomic beam (proposal 1). The shot noise limited S/N ratio for $\mathcal{S}(PV)$, increased by that same factor, becomes $\sqrt{17\kappa}\times 10^{-3}/\sqrt{\text{Hz}}$. To become competitive with the thermal beam Boulder experiment, from the sole point of view of SNR ratio, an enhancement factor κ of $\sim 6\times 10^3$ is necessary. In this experiment, the collimator causes a deflection of the atomic beam and a Fabry-Perot cavity enhancing the intensity of the excitation beam all along the interaction region does not look too unrealistic, but the enhancement factor required for obtaining the same SNR is comparable to that achieved in Boulder. One may, however, expect that the high power stored inside the cavity will have here somewhat milder drawbacks. Indeed, longitudinal excitation allows all the excited atoms to explore the interference pattern over several wavelengths during their lifetime, hence the difficulty associated with inhomogeneous light shifts causing asymmetric line shapes should be suppressed. In conclusion, for APV measurements on the stable ^{133}Cs atom the Zeeman slower is an interesting possibility but, with respect to the thermal beam [2], we expect neither simplifications of the set-up, nor drastic improvement of the SNR ratio.

6 Conclusion

In this paper we have addressed the question of how to best use a cold atom source for performing APV measurements. To combat the large drawback associated with the small number of atoms compared with cells, one must take maximum advantage of their narrow velocity distribution. This advantage makes it possible to excite a beam of slow and cold atoms by a (co-)antico-linear laser, spatially matching the atomic beam over several centimeters, without any Doppler broadening. With respect to a thermal beam, the lengthening of the interaction time thus achieved ranges between 10^3 and 10^4. In addition, we have made a new proposal concerning the observable physical quantity manifesting APV. The atomic beam should be given a transverse spin polarization, $\mathbf{P}_e$. The new observable reflects existence of a circular dichroism. It involves the pseudoscalar $\mathbf{E}\cdot\xi\hat{\mathbf{k}}\wedge\mathbf{P}_e$ and appears in the population of the upper state, hence in the total fluorescence light. Therefore fluorescence detection efficiency is a crucial parameter to be optimized. Moreover, with two interaction regions leading to opposite circular dichroism, it is possible to make differential measurements. If, in addition, the spin polarization $\mathbf{P}_e$ can be sequentially rotated by $\pi/2$, then by combining the four results obtained in the two interaction regions for the two orientations of $\mathbf{P}_e$, it is also possible to achieve important reduction of the systematic effects that birefringence of the optics may generate from the 10^4 times larger M_1-Stark interference signal.

The merit of cold atom sources relies on their potential to localize atoms, only one of the conditions required to extend APV measurements in the long term to radioactive isotopes. Suppression of Doppler broadening and lengthening of the interaction time are other important benefits. However, our estimate of the S/N ratio shows that, in the present state of the art, these do not appear sufficient to solve the difficulty of precise APV measurements. Nevertheless, exploratory experiments performed on stable alkali highly forbidden transitions can provide a valuable step enabling us to define the beam specifications required for APV experiments with radioactive isotopes. We have shown that by combining experimental techniques proven elsewhere, there is a reasonable hope of observing the 6S-7S transition for ^{133}Cs and of making a 10^{-3} accurate measurement of M_1^{hf}/β with a beam of slow, cold atoms with an unsophisticated set-up. Furthermore, such an experiment could be considered as a prototype to evaluate the production rate of Fr atoms needed to extend such measurements from stable ^{133}Cs to radioactive Fr. With a Zeeman slower providing a monokinetic beam of high flux and low divergence, PV measurements on ^{133}Cs as precise as those presently existing do not look impossible, but real progress with respect to a thermal beam does not look obvious to us. We hope that our present contribution will stimulate both reflections and experimental work towards advances in this emerging field of research.

We thank particularly D. Guéry-Odelin, L. Moi, C.J. Foot, D. Cassettari, A. Camposeo and F. Cervelli for very stimulating discussions and practical advice for preparing the ongoing construction of a laser trap. We are grateful to M.D. Plimmer for critical reading of the manuscript. A.W. acknowledges support from CNRS (IN2P3) and S.S. from the European Commission.

Appendix A

We now present the derivation of the population signal in the experimental configuration specified in this paper. The nS, $F\rightarrow(n+1)$S, F' transition amplitudes can be obtained from the effective transition matrix T acting on the electronic spin states of the form:

$$T = a\mathbb{I} + \mathbf{b}\cdot\boldsymbol{\sigma} \tag{11}$$

where $\mathbb{I}$ is the two-by-two unit matrix and the components of $\boldsymbol{\sigma}$ are the three Pauli matrices. The parameters a and $\mathbf{b}$ are given by:

$$a = \alpha\mathbf{E}\cdot\hat{\boldsymbol{\epsilon}} \tag{12}$$

$$\mathbf{b} = \mathrm{i}\beta\,\mathbf{E}\wedge\hat{\boldsymbol{\epsilon}} - M_1'\hat{\mathbf{k}}\wedge\hat{\boldsymbol{\epsilon}} + \mathrm{i}\,\mathrm{Im}E_1^{\text{pv}}\hat{\boldsymbol{\epsilon}} \tag{13}$$

where α and β are the scalar and vector transition polarizabilities, M_1' and E_1^{pv} are the magnetic dipole and the parity-violating electric dipole transition amplitudes, and $\hat{\boldsymbol{\epsilon}}$ represents the laser polarization.

In the present situation, stimulated emission is totally negligible compared with spontaneous emission and optical coherences between the two S states can be ignored. We assume that the laser selects one hfs component nS, $F\rightarrow(n+1)$S, F'. The excited state density matrix, up to a normalization factor, is then given by:

$$\rho = P_{F'}\,T P_F\,\rho_g P_F\,T^\dagger\,P_{F'}\,, \tag{14}$$

where ρ_g is the restriction of the density operator to the nS ground state. $P_{_F}$ is the projector on the nS, F sublevel and $P_{F'}$ the projector on the $(n+1)$S, F' sublevel. We assume an electronic orientation, $\mathbf{P}_e$, has been created in the ground state:

$$\rho_g = \mathbb{1} + \mathbf{P}_e \cdot \boldsymbol{\sigma}. \tag{15}$$

This definition implies that $\mathrm{Tr}\rho_g = 2(2I+1)$. So, a common normalization factor $1/2(2I+1)$ has to be applied to all the quantities computed below. This is taken into account in equation (10).

In order to compute the 7S population and its spin polarization, proportional respectively to Tr ρ and Tr $\rho\boldsymbol{\sigma}$, we apply the Wigner-Eckart theorem to the spin operator $\boldsymbol{\sigma}$ acting in the hyperfine subspace F:

$$P_{_F}\,\boldsymbol{\sigma}\,P_{_F} = 2g_{_F}\,P_{_F}\,\mathbf{F}, \quad \text{where} \quad g_{_F} = 2(F-I)/(2I+1). \tag{16}$$

Using equations (1–6) we obtain for the $\Delta F = F' - F$ transition:

$$\begin{aligned}\mathrm{Tr}\rho = {} & n_{_{F'}}(\delta_{_{FF'}} aa^* + h_{_{FF'}}\,\mathbf{b}\cdot\mathbf{b}^*) \\ & + [n_{_{F'}}p_{_{F'}}\delta_{_{FF'}}(a\mathbf{b}^* + a^*\mathbf{b}) - n_{_F}p_{_F}g_{_{F'F}}\mathrm{i}\mathbf{b}\wedge\mathbf{b}^*]\cdot\mathbf{P}_e,\end{aligned} \tag{17}$$

$$\begin{aligned}\mathrm{Tr}\rho\boldsymbol{\sigma} = {} & n_{_{F'}}p_{_{F'}}[\delta_{_{FF'}}(a\mathbf{b}^* + a^*\mathbf{b}) + g_{_{FF'}}\mathrm{i}\mathbf{b}\wedge\mathbf{b}^*] \\ & + \mathbf{P}_e\ -\text{dependent contributions}\,,\end{aligned} \tag{18}$$

where $n_{_{F'}} = 2F'+1$, $p_{_{F'}} = (1+2g_{_{F'}})/3$, and,

if $\Delta F = 0, h_{_{FF'}} = p_{_{F'}}$, and $g_{_{FF'}} = g_{_{F'}}$;
if $\Delta F = \pm 1, h_{_{FF'}} = 2(1-g_{_{F'}})/3 \equiv 4g_{_F}^2 F(F+1)/3$ and $g_{_{FF'}} = 1 - g_{_{F'}}$.

The second term in the RHS of equation (17) represents the contribution to the upper state population which depends on the initial state orientation $\mathbf{P}_e$, while equation (18) gives the orientation of the upper state created by the excitation process, the observable physical quantity that we detected in our first APV experiment [44]. We note the close connection between those two contributions in which the role of the initial and final states is interchanged. (Note the appearance of F, and not F', in the last term of the RHS of Eq. (17)).

Keeping only the terms which depend on the Stark field, we obtain for a $\Delta F = \pm 1$, nS, $F \to (n+1)$S, F', transition:

$$\begin{aligned}\mathrm{Tr}\rho = {} & (2F+1)\frac{1-g_{_F}}{3}\Big[2\beta^2|\mathbf{E}\wedge\hat{\boldsymbol{\epsilon}}|^2 - (1+2g_{_F}) \\ & \times\Big(\mathrm{Im}E_1^{\mathrm{pv}}\beta\mathbf{E}\wedge\xi\hat{\mathbf{k}}\cdot\mathbf{P}_e + 2M_1'\mathrm{Re}\{(\beta\mathbf{E}\wedge\hat{\mathbf{k}}\cdot\hat{\boldsymbol{\epsilon}})(\hat{\boldsymbol{\epsilon}}^*\cdot\mathbf{P}_e)\} \\ & + \beta^2\xi(\mathbf{E}\cdot\hat{\mathbf{k}})(\mathbf{E}\cdot\mathbf{P}_e)\Big)\Big].\end{aligned} \tag{19}$$

The last $\mathbf{P}_e$-dependent contribution in equation (19) vanishes when there is no longitudinal component of the electric field.

References

1. M.A. Bouchiat, C. Bouchiat, J. Phys. France **35**, 899 (1974); Rep. Prog. Phys. **60**, 1351 (1997)
2. C.S. Wood *et al.*, Science **275**, 1759 (1997)
3. S.C. Bennett, C.E. Wieman, Phys. Rev. Lett. **82**, 2484 (1999)
4. V.A. Dzuba, V.V. Flambaum, O.P. Sushkov, Phys. Lett. A **141**, 147 (1989); *ibid.* **142**, 373 (1989); S.A. Blundell, W.R. Johnson, J. Sapirstein, Phys. Rev. Lett. **65**, 1411 (1990); Phys. Rev. D **45**, 1602 (1992)
5. A. Derevianko, Phys. Rev. Lett. **85**, 1618 (2000)
6. A.I. Milstein, O.P. Sushkov, I.S. Terekhov, Phys. Rev. Lett. **89**, 283003 (2002)
7. V.A. Dzuba, V.V. Flambaum, J.S.M. Ginges, Phys. Rev. D **66**, 076013 (2002); M.Yu. Kuchiev, V.V. Flambaum, Phys. Rev. Lett. **89**, 283002 (2002)
8. D. DeMille, Phys. Rev. Lett. **74**, 4165 (1995)
9. A.-T. Nguyen, D.E. Brown, D. Budker, D. DeMille, D.F. Kimball, M. Zolotorev, in *Parity Violation in Atoms and Electron Scattering*, edited by B. Frois, M.A. Bouchiat (World Scientific, 1999), p. 295; A.-T. Nguyen, D. Budker, D. DeMille, M. Zolotorev, Phys. Rev. A **56**, 3453 (1997)
10. V.A. Dzuba, V.V. Flambaum, O.P. Sushkov, Phys. Rev. A **51**, 3454 (1995)
11. Y.B. Zel'dovich, Sov. Phys. JETP **6**, 1184 (1957); V.V. Flambaum, I.B. Khriplovich, Sov. Phys. JETP **52**, 835 (1980); C. Bouchiat, C.A. Piketty, Z. Phys. C **49**, 49 (1991)
12. I.M. Savukov, A. Derevianko, H.G. Berry, W.R. Johnson, Phys. Rev. Lett. **83**, 2914 (1999)
13. H.J. Metcalf, P. van der Straten, in *Laser cooling and trapping of atoms* (Springer, New-York, 1999)
14. S.N. Atutov *et al.*, Phys. Rev. A **60**, 4693 (1999)
15. Z.-T. Lu *et al.*, Phys. Rev. Lett. **72**, 3791 (1994)
16. J.A. Behr *et al.*, Phys. Rev. Lett. **79**, 375 (1997)
17. G. Gwinner *et al.*, Phys. Rev. Lett. **72**, 3795 (1994)
18. M.D. Di-Rosa, S.G. Crane, J.J. Kitten, W.A. Taylor, D. Vieira, X. Zhao, SPIE-Int. Soc. Opt. Eng. **34-45**, 4634 (2002)
19. J.E. Simsarian *et al.*, Phys. Rev. Lett. **76**, 3522 (1996)
20. Z.-T. Lu *et al.*, Phys. Rev. Lett. **79**, 994 (1997)
21. J.S. Grossman, L.A. Orozco, M.R. Pearson, G.D. Sprouse, Phys. Scripta **TIE1**, 1 (2000)
22. M.A. Bouchiat, J. Guéna, J. Phys. France **49**, 2037 (1988); C. Bouchiat, C.A. Piketty, J. Phys. France **49**, 1851 (1988)
23. W.R. Johnson, Phys. Rev. A **60**, R1741 (1999); V.A. Dzuba, V.V. Flambaum, Phys. Rev. A **62**, 052101 (2000)
24. A.A. Vasilyev, I.M. Savukov, M.S. Safronova, H.G. Berry, Phys. Rev. A **66**, 020101 (2002)
25. R. Casalbuoni *et al.*, Phys. Lett. B **460**, 135 (1999); J. Erler, P. Langacker, Phys. Rev. Lett. **84**, 212 (2000); D.E. Groom, `http://pdg.lbl.gov/` (Ch. 10)
26. J.E. Simsarian, W.Z. Zhao, L.A. Orozco, G.D. Sprouse, Phys. Rev. A **59**, 195 (1999)
27. See for example: S. Chu, Rev. Mod. Phys. **70**, 685 (1998); C.N. Cohen-Tannoudji, Rev. Mod. Phys. **70**, 707 (1998); W.D. Phillips, Rev. Mod. Phys. **70**, 721 (1998)
28. K.I. Lee, J.A. Kim, H.R. Noh, W. Jhe, Opt. Lett. **21**, 1177 (1996)
29. J.J. Arlt *et al.*, Opt. Commun. **157**, 303 (1998)
30. A. Camposeo *et al.*, Opt. Commun. **200**, 231 (2001)
31. M.A. Bouchiat, J. Guéna, L. Pottier, J. Phys. Lett. **45**, 523 (1984)

32. E. Biémont, P. Quinet, V. van Renterghem, J. Phys. B **31**, 5301 (1998)
33. H. Chen, E. Riis, Appl. Phys. B **70**, 665 (2000)
34. P. Cren, C.F. Roos, A. Aclan, J. Dalibard, D. Guéry-Odelin, Eur. Phys. J. D **20**, 107 (2002)
35. K. Dieckmann, R.J.C. Spreeuw, M. Weidemüller, J.T.M. Walraven, Phys. Rev. A **58**, 3891 (1998)
36. T.B. Swanson, N.J. Silva, S.K. Mayer, J.J. Maki, D.H. McIntyre, J. Opt. Soc. Am. B **13**, 1833 (1996)
37. J. Schoser *et al.*, Phys. Rev. A **66**, 023410 (2002)
38. F. Lison, P. Schuh, D. Haubrich, D. Meschede, Phys. Rev. A **61**, 013405 (1999)
39. Z.T. Lu *et al.*, Phys. Rev. Lett. **77**, 3331 (1996)
40. J. Guéna *et al.*, Phys. Rev. Lett. **90**, 143001 (2003)
41. M.A. Bouchiat, C. Bouchiat, J. Phys. France **36**, 493 (1975)
42. C.S. Wood *et al.*, Can. J. Phys. **77**, 7 (1999); B.P. Masterson *et al.*, Phys. Rev. A **47**, 2139 (1993)
43. D. Herriott, H. Kogelnik, R. Kompfner, Appl. Opt. **3**, 523 (1964); M.A. Bouchiat, L. Pottier, Appl. Phys. B **29**, 43 (1982)
44. M.A. Bouchiat, J. Guéna, L. Hunter, L. Pottier, Phys. Lett. B **117**, 358 (1982); *ibid.* B **134**, 463 (1984); J. Phys. France **47**, 1709 (1986)
45. D. Chauvat *et al.*, J. Guéna, Ph. Jacquier, M. Lintz, M.A. Bouchiat, Eur. Phys. J. D **1**, 169 (1998); M.A. Bouchiat, C. Bouchiat, Z. Phys. D **36**, 105 (1996)
46. V.A. Dzuba, V.V. Flambaum, J.S.M. Ginges, Phys. Rev. A **63**, 062101 (2001)
47. M.A. Bouchiat, L. Pottier, in *Proceedings of the International Workshop on Neutral Current Interactions in Atoms*, edited by W.L. Williams, M.A. Bouchiat (Univ. of Michigan Press, Ann Arbor, 1979), p. 122; Science **234**, 1203 (1986)
48. M.A. Bouchiat, M. Poirier, C. Bouchiat, J. Phys. France **40**, 1127 (1979)
49. S.L. Gilbert, C.E. Wieman, Phys. Rev. A **34**, 792 (1986)
50. M.A. Bouchiat, Ph. Jacquier, M. Lintz, L. Pottier, Opt. Commun. **56**, 100 (1985)
51. M.A. Bouchiat, L. Pottier, Opt. Commun. **37**, 229 (1981)
52. F. Touchard *et al.*, Nucl. Instrum. Meth. **186**, 329 (1981)

3.1.3 Dipole trap

Among the several kinds of traps for neutral atoms, the optical dipole trap [47] seems to be most suited for a parity violation experiment with francium: the first very attractive feature is the absence of magnetic field, which could be very harmful for PV measurements. Let us briefly remind the concept for this trapping technique: a laser with a very large red detuning from the D_1, D_2 transitions is focused to a small spot, with a waist typically of the order of 30-100 μm. Thanks to the forces induced by the gradient of the laser power, the atoms are attracted to the center of the spot. Because the spontaneous scattering rate of the laser photons is very low (we are off-resonance), the effect of the dipole trap on the atoms can be seen as a nearly conservative potential. The heating due to fluorescence is negligible, and long trapping times of the order of several seconds can be easily reached.

The transfer efficiency from a magneto-optical trap (MOT) to a dipole trap can be relatively high, up to 40% [48]. Note that the possibility to collect 40% of the atoms present in a MOT into a small volume (50 μm radius) is attractive: by concentrating the excitation laser power in a 50 μm waist, it is possible to reach a higher power per surface unit, hence a higher excitation rate for forbidden transitions.

The use of circularly polarized laser beams for the optical trap allows to obtain spin polarized samples of atoms [48].

If we consider the last results for the francium trapping experiment in Stony Brook [49] (an average of 50000 atoms in a MOT), we deduce that it is possible to obtain 20000 francium atoms in a dipole trap.

The excitation on the 7*S*-8*S* transition

As for cesium, the excitation of francium atoms on a highly forbidden transition ($7S$-$8S$) in the presence of a static applied electric field is a good way to induce a measurable parity violating observable. We consider in the following the same PV experimental configuration described in the article enclosed in paragraph 3.1.2, adapted to the case of an optical trap. The polarized trapped atoms are excited by a circularly polarized laser from $(7S, F)$ to $(8S, F')$ with $|F' - F| = 1$, in the presence of a transverse applied electric field. The laser is focused to the dimensions of the sample (waist $w_0 = 50$ μm). An additional circularly polarized laser (dubbed repolarizing laser) on the D_2 transition will be necessary to repump the atoms which decay to the wrong polarization (F, F_z) states, and maintain a polarized sample. The parity violation is deduced from the variations of the excitation rates when the polarizations and electric field are reversed, as described in the article.

We want now to review the orders of magnitude expected for the signals under simple assumptions for the experimental parameters, in order to show that a precise PV measurement is absolutely reasonable for trapped francium. Of course, we do not pretend to describe precisely the future PV experiment: in order to draw up a definite scheme, it will be necessary to make practice with francium spectroscopy in a dipole trap and understand better what are the most important related features.

We suppose to have 100 mW laser power P tuned on the $7S$-$8S$ transition (@506 nm, see fig. 1 of the article for a scheme of the energy levels). This power can be enhanced in a Fabry-Perot cavity, for instance by a factor $\zeta = 100$. Let us consider a 1000 V/cm applied transverse electric field $\mathbf{E}$. The main contribution to the excitation rate is given by (cf. equation (19) of the article, with the proper normalization of ρ_g defined in equation (15)):

$$\frac{\mathrm{d}\mathcal{P}}{\mathrm{d}t} \simeq \frac{1}{\hbar}\,\frac{1}{\hbar\Gamma}\,\frac{1}{3}\,\beta^2 E^2\,\frac{4\pi}{c}\,\frac{\zeta P}{S}\,, \tag{3.1}$$

where β is the vector polarizability for the considered transition (cf. paragraph A.2.2), $S = \pi w_0^2$ and Γ is the inverse of the $8S$ state lifetime (56 ns from theory, cf. [50])[1]. The angular factors (whose expressions are reported in the article) have been neglected. We expect[2]

$$\frac{\mathrm{d}\mathcal{P}}{\mathrm{d}t} \sim 9.4\cdot 10^{-5}\,\frac{\zeta P(\mathrm{mW})}{S(\mathrm{cm}^2)}\ \mathrm{s}^{-1}.$$

For the considered parameters, we obtain then:

$$\frac{\mathrm{d}\mathcal{P}}{\mathrm{d}t} \sim 12000\ \mathrm{s}^{-1}. \tag{3.2}$$

Heating due to photon scattering

For each scattered photon from the excitation laser, a francium atom receives average recoil energies $E_r = (\hbar k)^2/2m$ from absorption ($7S$-$8S$) and from spontaneous emissions ($8S$-$7P$ and $7P$-$6S$), possibly followed by recoil energies from the interaction with the repolarizing laser. Each atom which performed the forbidden transition acquires then an average energy of the order of 0.3 μK. Considering the rate in equation (3.2), we find a heating rate of the order of 3-4 mK/s. If we have a potential depth of 3 mK for the optical trap, we can then expect a lifetime of the order of the second for the trapped atoms submitted to the excitation laser.

Detection scheme

The simplest way to detect the atoms which perform the $7S$-$8S$ transition is to monitor their fluorescence when they decay to the $7P$ and to the ground state. If we consider 20000 trapped atoms, the rate in equation (3.2) and a photon detection efficiency of 2%, we should detect $5\cdot 10^6$ photons/s, which correspond to a power of 0.6 pW for the $8S$-$7P$ wavelength or 1.3 pW for the $7P$-$6S$. Very low-noise detectors are able to detect such low photon fluxes.

A more efficient system allows to detect the atoms which decay to the $(7S, F')$ state: if we probe the atoms with a laser tuned to the cycling D_2 transition $(7S, F')$-$(7P, F'')$, many fluorescence photons (of the order of one thousand) are emitted

[1] We have implicitly made use of Fermi's golden rule and Poynting's theorem to deduce equation (3.1).

[2] The following expression can be useful: 1 a_0^3 V/cm $\simeq 1.0\cdot 10^{-18}$ e cm.

for each $(7S, F')$ atom before coming back to the $(7S, F)$ state. We can expect total efficiencies of the order of 50% (the excited atoms which come back to $(7S, F)$ instead of $(7S, F')$ cannot be detected). Note that because of the relatively strong fluorescence emission on the D_2 transition for the $(7S, F')\leftrightarrow(7P, F'')$ atoms, the heating rate is much higher with this detection method. Therefore, it may be better to use lower electric fields, in order to decrease the excitation rate (and accordingly the total photon fluorescence emission on the cycling transition). Another possibility would be to try to cool the $(7S, F')$ atoms with additional laser beams.

Signal to noise ratio

$\boldsymbol{E_1^{PV}}$ We are now going to give an estimation of the signal to noise ratio for the parity violation measurement. If we consider only the reversal for the PV signature (helicity h of the excitation light), we can say that we measure the number of excited atoms N_1 for a time $t/2$ with a given sign of h, for which the rate is $R+\epsilon$, and N_2 for the following $t/2$ with the other sign of h, for which the rate is $R-\epsilon$, with a total efficiency η: we will measure the values ηN_1 and ηN_2 for each t-long cycle. The quantity of interest deduced from the experimental data will be $(\eta N_1-\eta N_2)/(\eta N_1+\eta N_2)\equiv\epsilon/R$ which turns out to be $\simeq(\Im m E_1^{PV})/\beta E\sim 9\cdot 10^{-6}$ (from equation (19) of the article without the small correction from angular factors).

The shot noise on $(\eta N_1-\eta N_2)/(\eta N_1+\eta N_2)$ is given by $\sqrt{\eta N}/(\eta N)=1/\sqrt{\eta N}$, with $N=N_1+N_2$ ($N_1\simeq N_2\simeq RtN_0/2$, with N_0 the number of trapped atoms). The expression of the signal to noise ratio does not depend on the value of the electric field: from equation (3.1) we find

$$\mathrm{SNR}(E_1^{PV}) \;\sim\; \Im m E_1^{PV}\,\sqrt{\frac{1}{\hbar}\,\frac{1}{\hbar\Gamma}\,\frac{4\pi}{3c}\frac{\zeta P}{S}\,\eta N_0}\quad\sqrt{t}.$$

If we suppose that the lifetime of the trap is of the order of 1 s, and we need a time of the order of 10 s to trap again atoms with the help of the MOT, we still have to account for a factor $1/\sqrt{10}$. We obtain then from the considered parameters $\mathrm{SNR}(E_1^{PV})\sim 6\cdot 10^{-3}\ \sqrt{\mathrm{Hz}}$ for the fluorescence detection and $\mathrm{SNR}(E_1^{PV})\sim 3\cdot 10^{-2}\ \sqrt{\mathrm{Hz}}$ if we manage to implement the detection on the cycling transition.

Therefore, we see that a SNR of 10 should be reachable in 30 days with fluorescence detection (30 hours with detection on the cycling transition). It seems even possible to consider a SNR of 100, if we consider improved parameters with respect to the conservative ones presented before:

- the power laser can be appreciably higher (500 mW instead of 100 mW), resulting in a higher excitation rate;
- it is possible to have very high reflective Fabry-Perot cavities (amplification $\zeta=10000$ instead of 100);
- cooling techniques applied to dipole traps should allow to reach longer trapping lifetimes, in the presence of the excitation laser;

- by transferring the francium atoms from the first MOT to a second trap in a ultra-high vacuum environment, it should be possible to accumulate atoms with reduced losses from residual vapour pressure. Stony Brook researchers plan to reach 10^6 trapped atoms.

M_1 The signal to noise ratio for the measurement of M_1 (or more precisely $M_1/\beta E$) is much higher than SNR(E_1^{PV}), by a factor of $M_1/(\Im m E_1^{PV}) \sim 13000$. Therefore, even without the enhancement Fabry-Perot cavity and the fluorescence detection method, we expect to have a very high signal to noise ratio SNR(M_1) $\sim 8\ \sqrt{\text{Hz}}$, which would allow to reach SNR=100 with a 3 minutes integration time.

Note that the measurement of M_1 is very interesting not only because it gives important information about the francium atomic structure (the M_1 theoretical calculation accuracy being relatively poor) but also because it is similar to the E_1^{PV} measurement: measuring M_1 is a good way to prepare a PV experiment. A precise experimental value of M_1 is also essential for the calibration of the PV measurement, as described in the article [46].

3.2 The present Francium experiment at Legnaro laboratories: from production to trapping

In spite of the difficulty coming from the meagre availability of atoms, experiments performing spectroscopy on radioactive atoms already existed before the advent of laser trapping techniques. The first measurements with francium, on thermal atomic beams at the ISOLDE facility, date back to more than 20 years ago [10, 51]. The new possibilities coming from laser cooling and trapping stimulated this research field even more: thanks to magneto-optical traps (MOT), it was possible to obtain more substantial atomic samples, whose very low temperature allowed high resolution laser spectroscopy measurements. Interesting results for trapping Na, K, Rb and Fr atoms in a MOT have been reported in several American laboratories [11, 44, 52, 53]. Recently, Stony Brook researchers, thanks to an upgrade of their experimental setup and careful optimization, managed to furthermore improve their collection method of francium atoms in a MOT. They reached average trap sizes of about 50000 atoms (to be compared to typically 1000 atoms before the upgrade), and even peak values of 350000 atoms, coming from their usual initial isotope production rate of the order of 10^6 ions/s [49].

Note that the operation with necessarily very low amounts of produced atoms entails a proportional dependence of the number of trapped atoms from the production rate, as well as the collection and trapping efficiency. In order to maximize the final number of trapped atoms, it is essential to optimize each one of the parameters of the setup which drive francium from its initial state (generally produced in a solid bulk) to the trapping area: extraction efficiency from the bulk, transport efficiency from the production region to the MOT etc. These aspects will be developed in this chapter.

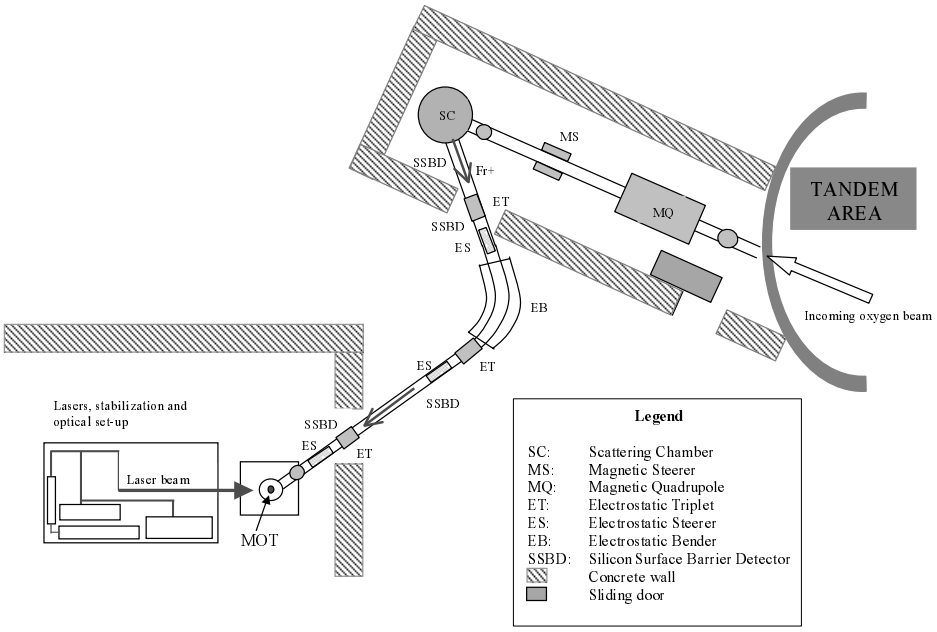

Figure 3.1: General scheme of the francium experiment beam line, from the production of radioactive isotopes, to the neutral atoms trapping.

The general concept of our setup at Legnaro laboratories follows the one used by Orozco's group at Stony Brook [11, 52]. The Francium is produced in a gold (^{197}Au) heated target, following the nuclear reaction with an incoming oxygen (^{18}O) beam from Legnaro Tandem accelerator. The francium is then extracted in its ionic form, accelerated and guided to the MOT area, thanks to the application of suitable electrostatic potentials along the beam line (see fig. 3.1). After neutralization, the francium atoms are ready to be trapped in the MOT. The physical separation of the production and the MOT zones by concrete walls, which shield from dangerous ionizing radiations, allows to safely operate with the lasers even when the radioactive ^{18}O beam is on.

The beam time has to be divided among all the thirteen experiments depending on the Legnaro Tandem accelerator. This sharing resulted in a limited number of days dedicated to our on-line tests: 8 days were assigned to the francium setup for the year 2001 (beginning of the first tests), 20 days for 2002, and 16 days for 2003.

Of course we had to build the experiment step by step: at each stage we checked the setup progress with one or two days of measurements, in order to optimize the conditions or to understand possible mistakes when the measurements went wrong. Let us emphasize that for each run it was necessary to define precise experimental conditions which allowed to perform all the scheduled tests without need for opening the vacuum system (operation which takes several precious beam-time hours away[3]). In practice, in spite of our efforts to anticipate problems, because of unexpected

[3]Opening the vacuum setup in order to perform modifications means:

events (target melting for example), for several runs we were forced to open the vacuum chamber during our beam time.

In the next paragraphs, the elements of the setup are described in detail, along with the tests which allowed to optimize their integration in the experiment: in the natural order (cf. fig. 3.1),

- the target assembly, for the production and extraction of ionic francium isotopes,
- the electrostatic optical elements, which convey the francium to the MOT,
- the neutralizer,
- the MOT setup: main laser, repumping laser and magnetic gradient,
- the trapped atoms detection system.

3.2.1 Francium production and extraction

The nuclear fusion-evaporation reaction

Francium isotopes can be produced via α-decay from Th samples (favouring neutron-rich nuclei) [44], via high energy fragmentation reactions [51, 54], or via fusion-evaporation reactions. This last method, which is an excellent compromise between the request for high production rates and the use of a common low energy (of the order of 100 MeV) accelerator facility, is the one retained by Stony Brook group, as well as by our collaboration[4]. The considered nuclear reaction is

$$^{18}\mathrm{O} + ^{197}\mathrm{Au} \longrightarrow {}^{(215-x)}\mathrm{Fr} + x\ \mathrm{n},$$

where n represents neutrons. It allows the production of $^{208\text{-}212}$Fr (from $x = 3$ to $x = 7$), whose lifetimes are long enough to make them absolutely suited for laser trapping, cf. table 3.1 (actually the production of ^{212}Fr is almost negligible).

The reaction is performed by bombardment of a thick gold target with an oxygen ion beam (charge state +6 or +7), whose energy is chosen in the 100-120 MeV range, according to the desired francium isotope (a higher ^{18}O energy favouring lower mass number isotopes production). Gold is not the only target material which can be used for the francium production, but it has the main advantage of being chemically inert (noble metal) and naturally monoisotopic.

- wait for the hot target to come back to room temperature;
- wait for the radioactivity to become low enough to allow operation;
- once the fix-up is finished, close and wait until we reach an acceptable vacuum level, and the suitable temperature for the target.

In the end, all this implies a minimum 8 hours loss of beam time.

[4]The ISOLDE facility [55], injected with 1 GeV protons coming from the CERN's PS booster, allows even higher francium production rates, using the spallation production method.

Isotope	α energy (MeV)	α decay branching	Half life $T_{1/2}$ (s)
^{208}Fr	6.641	90%	59
^{209}Fr	6.646	89%	50
^{210}Fr	6.543	60%	191
^{211}Fr	6.534	>80%	186

Table 3.1: Nuclear properties of francium isotopes, from $A = 208$ to $A = 211$ (after [56]).

The primary ^{18}O beam

The ^{18}O beam is produced by the 15 MV Tandem accelerator, available in the INFN-Legnaro National Laboratories. It is possible to reach beam intensities up to 1-1.5 μA (i.e. 1-1.5 $\cdot 10^{12}$ ions/s). The primary beam line, which brings the oxygen ions from the exit of the accelerator to the gold target, basically consists of a magnetic quadrupole and a steerer, both at $\simeq$ 4 m from the target point. At the entrance of the scattering chamber, a 4-slits device, namely four movable tantalum scrapers which define a window through which the beam has to pass, allows a first rough centering of the beam, near the target (misalignments being detected by the currents induced from the collisions of the ions onto the slits). The precise alignment on the target is achieved by temporarily inserting a Macor® disk, with a pinhole in order to individuate the center, just in front of the target: even weak beam intensities produce localized fluorescence on Macor®, which is detected by a CCD camera placed in front of a quartz viewing port of the scattering chamber. Higher intensities also allow to directly monitor the position of the beam, thanks to the fluorescence produced on the steel electrode which surrounds the gold target (see the description of the target assembly, p. 109); with a beam current higher than 800-1000 nA it is even possible to see directly the impact point on the target (always thanks to the induced fluorescence).

Cross section: calculations and measurements

Calculations. Given the primary beam flux and energy, it is interesting to have a theoretical estimation of the francium production rate. This quantity is necessarily higher than the real measured rate, because not all the francium is extracted from the target material. Therefore, the comparison between theoretical and experimental rates gives an estimation of the extraction efficiency.

In order to evaluate the theoretical production rate, we need to know the cross section for the nuclear fusion-evaporation reaction we are interested in. This one can be calculated for each produced isotope, in the framework of the HIVAP statistical-evaporation model [57, 58], which assumes that the process includes two stages: firstly the total fusion of the projectile and target nucleus to an excited compound

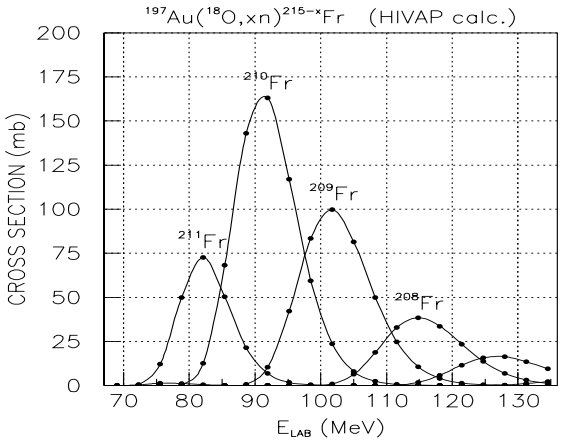

Figure 3.2: Theoretical cross sections for the francium isotopes production, via the ^{197}Au(^{18}O,xn)$^{215-x}$Fr reactions. Calculations have been performed with the HIVAP code.

nucleus CN, which is described by the Barrier Passing Model (BPM); then the deexcitation of the CN by light particles emission (evaporation process) or fission, described by the Standard Statistical Model (SSM). The result of calculations is shown in fig. 3.2.

We see that the maximum cross section is obtained for the ^{210}Fr isotope, at a projectile energy of 91 MeV. However, from our experimental tests, we found the maximum ^{210}Fr production rate at 104 MeV. This is explained by the energy loss of the oxygen ion into gold: the ion enters the target with a 104 MeV energy, corresponding to the end of the cross section curve for ^{210}Fr in fig. 3.2, then is slowed down, getting through all the energies which contribute to the ^{210}Fr production, from $E = 104$ MeV to $E = 80$ MeV.

According to the SRIM program [59], the energy loss for the considered range of energies is between 2.8 MeV/μm (for $E = 104$ MeV) and 3.1 MeV/μm (for $E = 80$ MeV). The 104 MeV ^{18}O ions penetrate 29 μm into gold, before stopping. The francium, produced in the first 8 μm, can drift to the target surface and then be extracted from it. The target is heated near its melting point (about 1300 K) in order to increase the mobility of francium and favour its migration to the surface.

The probability P for an oxygen ion to produce ^{210}Fr is then given by the following integral:

$$P = \rho \cdot \int_{104\mathrm{MeV}}^{0\mathrm{MeV}} \frac{\sigma(E)}{\frac{\mathrm{d}\mathcal{E}}{\mathrm{d}x}}\ \mathrm{d}E,$$

where ρ is the atomic density of gold, σ the cross section for the ^{210}Fr production, and $\frac{\mathrm{d}\mathcal{E}}{\mathrm{d}x}$ the energy loss of ^{18}O ions into gold. If we consider the density of gold near its melting point to be about 18.5 g/cm^3 (value deduced from the density at room

temperature and the thermal expansion coefficient [60]), we obtain the probability $P \simeq 3.7 \cdot 10^{-6}$. In the next paragraphs, we will see from francium production measurements and from this value of P that in the usual conditions the extraction efficiency is about 25%.

We expected a higher value for the extraction efficiency, because the drifting time from the bulk to the surface of the target was estimated to be of the order of 100 ms, i.e. much shorter than the ^{210}Fr lifetime. However, besides the transport efficiency from the bulk to the surface, the extraction efficiency also includes the contribution of the release efficiency from the surface. This one may be appreciably lower than 1, if we consider that it can strongly depend on target inhomogeneities (for example temperature, or surface quality). Also in Stony Brook, the conclusion that the quality and the design of the target are critical for a good francium production was reached [61]. In these conditions, we felt important to check our theoretical estimate for P, by an experimental measurement of the absolute cross section.

Measurements. This experiment was performed in collaboration with researchers from Legnaro Laboratories who had already measured the cross section for similar fusion-evaporation reactions [62]. The setup is different from our francium production setup, since for this experiment a thin target is needed. The ^{18}O beam is sent onto a 150 μg/cm^2 ^{197}Au target, and goes through the target, along with the reaction products. The produced francium isotopes are then separated from beam-like particles by means of an electrostatic deflector [63]. A silicon surface-barrier detector (SSBD) is placed behind the deflector in order to collect francium (which is stopped at the entrance of the detector). The SSBD detects then the emitted α particles, and measures their energy. The energy of the α allows to identify the isotope it was emitted from. Four monitor silicon detectors are arranged inside the scattering chamber, at a 15° angle with respect to the oxygen beam, in order to detect the Rutherford scattered beam particles, for absolute normalization of α counts to the beam current. These detectors are also used to correct for beam positions on the target. Measurements of the 0° differential cross sections were performed at different bombarding energies E_{lab}, in the range 75-130 MeV, with a 15 particle-nA beam current. The angular distribution was measured at $E_{lab} = 90$ MeV in the angular range from $-6°$ to $+8°$ in order to get the total cross section (since the ratio of the total to differential cross section at 0° is expected to be rather constant within the considered energies, it was necessary to measure the angular distribution only at one incident energy). The last parameter to know, in order to extract the cross sections from the francium rate measurements, is the transmission factor of the electrostatic deflector, relatively to the solid angle subtended by the SSBD. This one has been derived through a Monte-Carlo simulation and compared with the measured yield of ^{210,211}Fr at 90 MeV as a function of the high voltage applied to the deflector. Uncertainties in the estimates of the transmission coefficient were the main contribution to overall errors in the final cross sections values, which was quoted to be within $\pm$20%. The results for the total cross sections, as a function of the ^{18}O energy, is

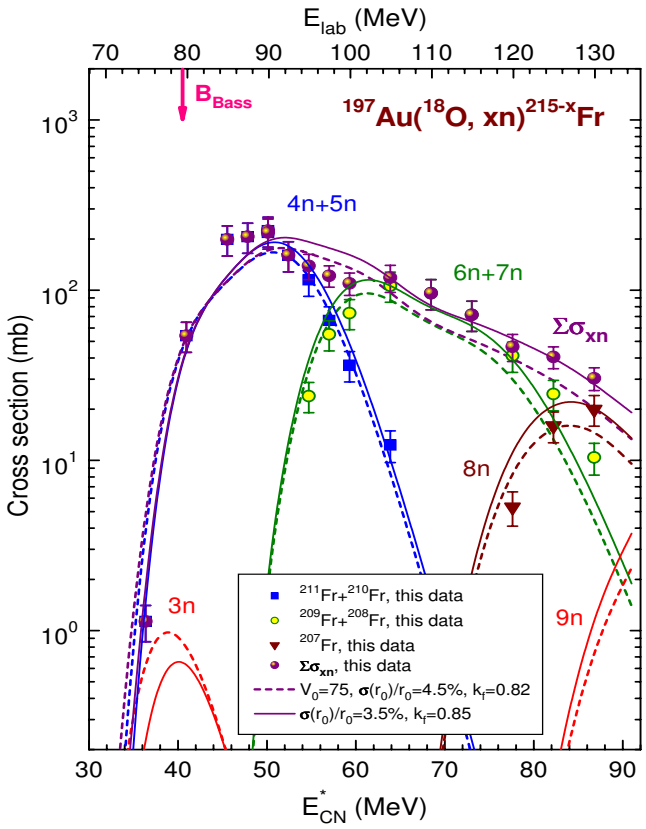

Figure 3.3: Experimental cross sections for the francium isotopes production, via the ^{197}Au(^{18}O,xn)$^{215-x}$Fr reactions. The dashed and continuous lines correspond to theoretical predictions (HIVAP code), for two different sets of nuclear parameters.

shown in fig. 3.3, along with the theoretical predictions from the HIVAP code for two plausible sets of nuclear parameters. It was not possible to distinguish between ^{208}Fr and ^{209}Fr, and between ^{210}Fr and ^{211}Fr, because the energy of the corresponding emitted α (table 3.1) was within the SSBD resolution (30 keV FWHM). The calculations are clearly in good agreement with our measurements.

The target assembly

The target is an 8.6 mm diameter ^{197}Au disk, with a thickness of about 1 mm. It is placed on one end of a cylindrical tungsten rod of the same diameter. For the preparation of the target, the tungsten stick is kept vertical into a small oven and heated until the gold melts. This ensures a good thermal contact between gold and tungsten.

Then, for normal use, the supporting rod is placed in the scattering chamber, as in

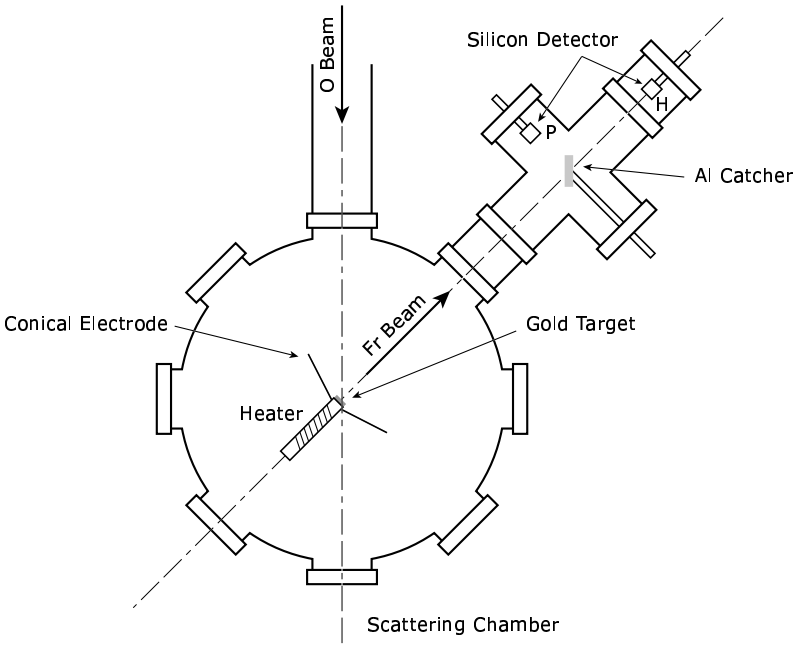

Figure 3.4: Schematic diagram of the scattering chamber. In the figure, the francium beam is detected by the setup used during the first test runs (with two silicon alpha detectors).

fig. 3.4: the oxygen beam impinges on the target surface at 45° with respect to the surface normal, so that the extraction of the reaction products can be perpendicular to the surface itself.

We already saw that the target is heated just below its melting point, in order to improve the francium mobility. The heater, which can provide up to 200 W power, consists of a current-carrying wire wrapped around a cylindrical ceramic sleeve containing the tungsten supporting rod. The ceramic sleeve (Shapal™) electrically insulates the heating wire from the target and the tungsten stick, and has been chosen according to its relatively good thermal conductivity. The heating system is surrounded by two cylindrical molybdenum heat shields. Note that the primary beam, focused to a few millimeters diameter at the target position, locally contributes to heat the target: a 100 particle-nA beam of 100 MeV oxygen ions brings about 10 W of kinetic energy. The target surface is monitored by a CCD camera, and its temperature is measured by a pyrometer positioned in front of a quartz viewing port. The pyrometer calibration is provided by a thermocouple, which can be put in thermal contact with the gold when the 3 kV high voltage (see the description of the extraction electrode below) is turned off.

Thanks to the high temperature of gold, the produced francium embedded in the bulk diffuses rapidly to the surface and evaporates, mainly in its ionic form: accord-

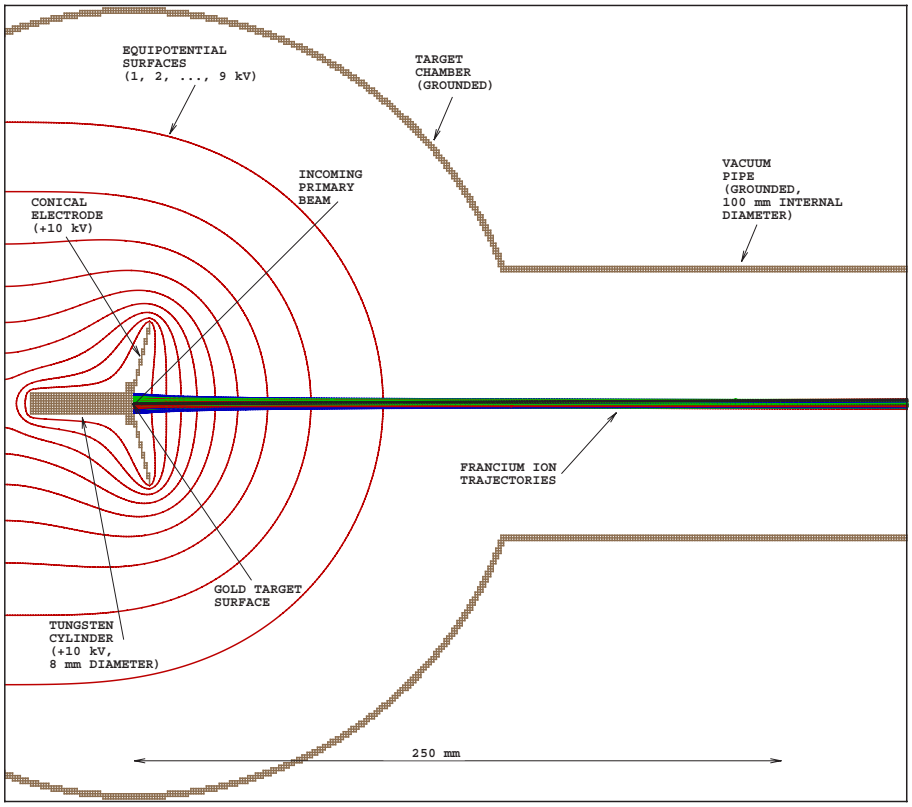

Figure 3.5: Simulation of the francium ions trajectories, performed with the SIMION program [64]. The target voltage was supposed to be 10 kV (with respect to the grounded chamber). The simulation gives quasi identical results for a 3 kV applied voltage, which corresponds to our standard experimental conditions.

ing to the Saha-Langmuir equation,

$$\frac{n_+}{n_a} = \frac{\omega_+}{\omega_a}\, e^{\frac{\phi - I}{kT}},$$

where n_+ and n_a are the number of desorbed ions and neutral atoms, ω_+ and ω_a are the statistical weights ($\frac{\omega_+}{\omega_a} = \frac{1}{2}$ for alkalis), ϕ is the surface work function at temperature T, I the atomic ionization energy, and k the Boltzmann constant. In our case, for a 5.1 eV target work function and 4.1 eV ionization potential of francium [65, 66], the ratio (n_+/n_a) is above 10000. The emitted ions can be then easily sent to the MOT thanks to a dedicated electrostatic channel.

An extraction electrode, which surrounds the gold end of the supporting rod, is submitted to a 3 kV voltage (with respect to the scattering chamber, which is kept at ground potential), in order to inject the francium ions into the secondary beam line. The stainless steel electrode is fixed on the tungsten rod by means of three screws, therefore achieving the electrical contact with the rod and the target.

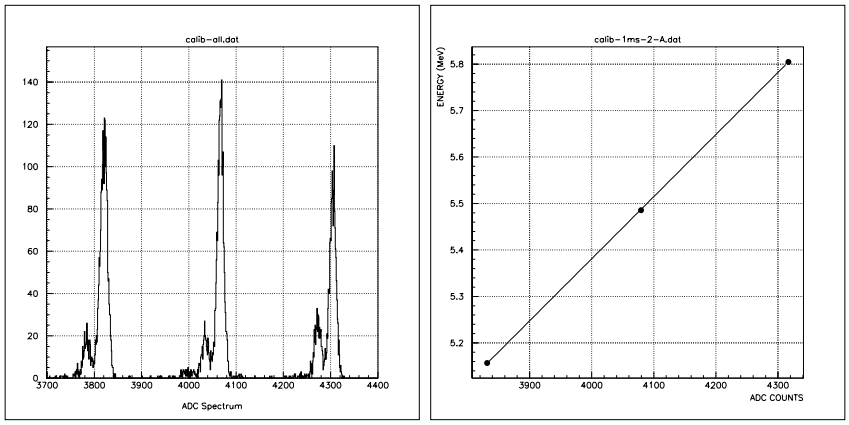

Figure 3.6: Calibration of the SSBD with a 3-peaks α source (^{239}Pu, ^{241}Am, ^{244}Cm). Left: the three main α peaks. Right: linear fit of the three peaks calibration.

Note the conical shape of the electrode (fig. 3.4): the outer diameter (69 mm) and the half-aperture angle (75°) were designed to minimize the beam divergence and guarantee that all ions are collected, independently of their initial position on the gold surface [67] (see fig. 3.5).

The whole assembly is mounted on a rigid frame, conceived to minimize possible thermal stresses (the first simpler prototype having had the drawback to break after a few days of measurements) and to allow fine positioning and alignment with respect to the secondary beam line.

Tests of Francium production

In the same way as for the cross section measurements we presented before, the francium production from our thick gold target is monitored thanks to the detection of its α decays, by the usual silicon surface-barrier detectors (SSBD). After amplification and shaping, the analog outputs are sent to analog to digital converters (ADC), and the α energy spectra are recorded. The SSBD were calibrated with a standard composite 3-peaks α particles source (^{239}Pu, ^{241}Am, ^{244}Cm, cf. fig. 3.6).

The first production tests were performed with the arrangement of the SSBD displayed in fig. 3.4. There are two silicon detectors, H and P. H is aimed directly at the target surface, when the acceleration voltage is turned off, in order to check the presence of francium in the target. Note that with this configuration, the α particles lose energy before exiting the gold: therefore the α peaks of the recorded spectra show a broad low-energy tail. In order to see the number of extracted francium ions, the acceleration voltage is turned on: it is possible to continue to use the H detector, which counts the α emitted from the collected francium, intercepted by the SSBD surface (cf. cross section measurements). However, this measurement is very critical with respect to the alignment of the secondary francium beam, since the

SSBD surface (150 mm^2 area) and the transverse beam dimensions are comparable. Especially for the first tests, it was better to use the P detector, in the following manner: the francium ions are collected on an aluminum catcher foil, which is inserted in front of H, at a 45° angle with respect to the incoming beam. A fraction of the isotropically emitted α is then detected by P, positioned in such way that it can see the exposed catcher surface. This second method results in a smaller number of detected α, but allows a much more accurate determination of the francium rate production from the α counts, since the α collection efficiency (essentially the geometrical acceptance) is well defined, and not very sensitive to the alignment of the secondary beam (the catcher intercepts all the extracted ions). In fig. 3.7, a typical spectrum of the detected α is reported: we see the two ^{208,209}Fr and ^{210,211}Fr peaks, as well as other weaker peaks, due to the decays of daughter nuclei. Then, from simple algebra, involving α decays branching ratios, and detector efficiency and geometrical acceptance [67], the α rate measurements allow to deduce the francium production rate.

The optimization of the production rate is a crucial point for the francium experiment. For this reason, many tests have been made, as a function of different parameters.

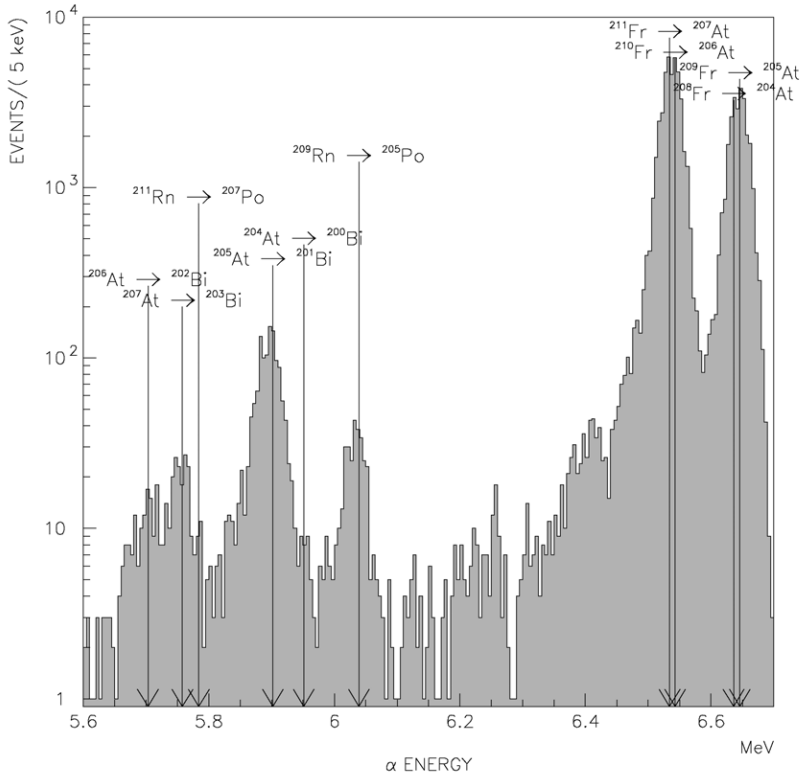

Figure 3.7: α particles spectrum, emitted from the isotopes implanted on the catcher.

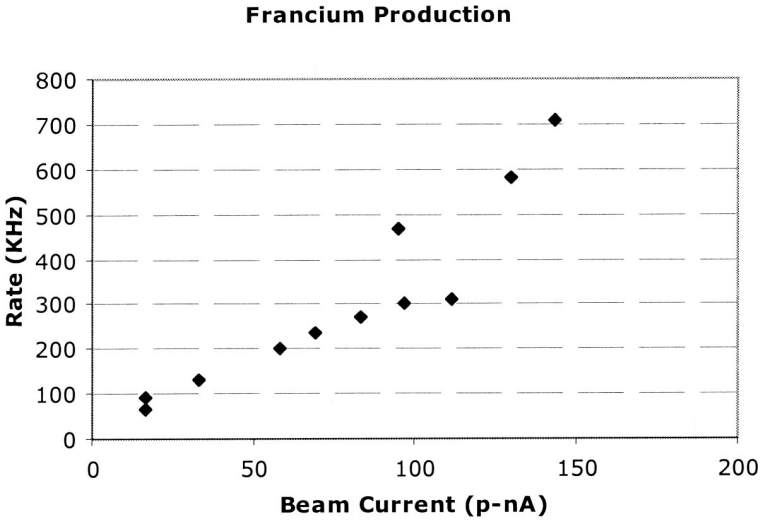

Figure 3.8: ^{210}Fr production rate as a function of the oxygen beam current. The target temperature was $T \simeq 1188$K, and the beam energy was 104 MeV.

Primary beam current. The francium production rate has been measured as a function of the primary beam current, at fixed energy and heating power (fig. 3.8). As expected, the rate increases for higher currents, more than linearly because the temperature of the target slightly increases too. The reproducibility of the measurements is not perfect, because it was not easy to keep exactly the same conditions during all the run, but it is sufficient to understand the general trend.

Target temperature. During the many runs at Legnaro laboratories, we observed how dependent the francium production rate is on the target temperature. As already noted by Stony Brook researchers [68], the way to reach the best francium production is to heat the target as close as possible to its melting point. It is possible to reach a very special temperature condition, for which the target is locally melted, in the small irradiated region. This local phase transition manifests itself with a sudden high increase of the francium rate: at the beginning of the transition, a tiny change of the heating power ($\Delta P/P \sim 10^{-4}$) resulted in doubling the production rate. This kind of situation could be permanently maintained for several runs. With the CCD camera we saw clearly the change of the target appearance when local melting occurred: in the affected zone, the gold material seemed to move, or better, to beat. After the end of the run, it was possible to observe the cold target: the local fusion had produced small holes, each one corresponding to a different position of the beam (after several hours, because of the melting of the gold, the francium production decreased, and we had to slightly move the beam to another region to come back to normal values). Of course, in order to keep the temperature of the target under control, it was very important to have a good homogeneous thermal

Figure 3.9: Example of target destroyed after melting. In the center we see the gold fused into a big drop, no more usable for francium production. The cone which surrounds the gold target is the extraction electrode.

contact between the target and its heating tungsten holder.

Unfortunately, it was not always possible to have experimental conditions good enough to reach the controlled partial fusion of the gold target. Indeed, it is very important not to exceed the melting point, in order not to destroy the target. The instabilities of the ^{18}O primary beam current did not always allow to keep the temperature under strict control (cf. fig. 3.9). For our last runs, the ^{210}Fr production rate was usually of the order of 10^6 ions/s for a primary beam current of 1 μA: considering the value of the probability P for an oxygen ion to produce ^{210}Fr (cf. p. 108), the extraction efficiency was then about 25%.

Supporting rod. We saw that the gold target is fixed at the end of a cylindrical tungsten rod (p. 109). Actually, we also tried to use steel rods, because this metal is easier to work than tungsten. However, the tests showed that this material was not suitable for the francium production. With a new target, after the first few hours of stable conditions, the production rate suddenly decreased up to a stop. During the following run, with the same target, the francium could be extracted only for the first 15 minutes. This annoying behaviour was interpreted as the result of the contamination of the gold target by steel: at high temperature, the impurities from the steel material diffused up to the surface, probably modifying the francium release properties. As a consequence, we decided to definitely use tungsten supporting rods.

Primary beam energy. From fig. 3.2, as already said, it is evident that the choice of the ^{18}O ions energy E allows to favour the production of a selected francium isotope. The production of lower mass number isotopes corresponds to higher primary beam energies. This property was checked during the first tests, aimed at the determination of the energy which maximizes the production of ^{210}Fr (we chose

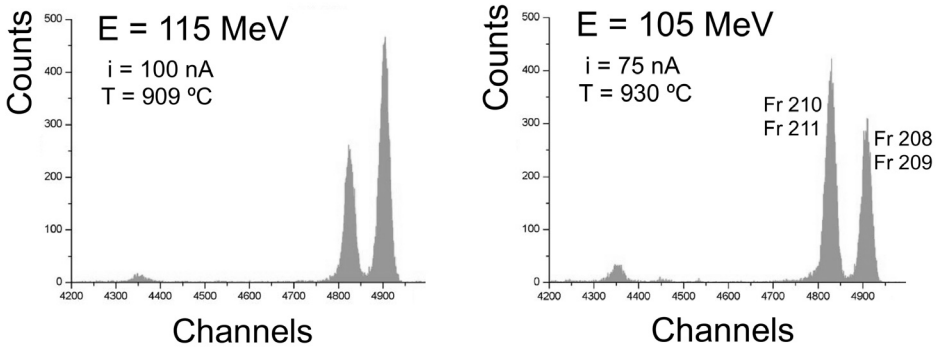

Figure 3.10: Francium isotopes production rate, at two different energies E of the primary oxygen beam. The Fr nuclei are detected thanks to their α decay, whose experimental spectrum has been reported in figure.

this isotope as the reference one because it corresponds to the maximum production cross section). It is evident from fig. 3.10 how the relative yield of ^{210,211}Fr with respect to ^{208,209}Fr decreases, from $E = 105$ MeV to $E = 115$ MeV.

3.2.2 The secondary beam line

The secondary beam line (see fig. 3.1) conveys the extracted francium ions to the MOT cell, about 8 meters away. The physical separation of the MOT environment from the scattering chamber, by thick concrete walls, is essential for the trapping operation in a radiation-safe environment even while the primary beam is on.

The beam line consists of a series of electrostatic bending and focusing elements: three quadrupole triplets (ET), three steerers (ES) and a curved electrode bender (EB) (see fig. 3.11). The bend was necessary because of the layout of the experimental hall. Since space constraints force the last triplet to be two meters away from the MOT cell, a small einzel lens[5] was built and placed on the glass tube just upstream of the cell.

The line is set up so that rubidium ions can also be transported. A Rb dispenser was placed inside the target chamber; the release of atoms can be adjusted with the power supply, located in the laser laboratory. Atoms from the vapour which come in contact with the hot gold surface are ionized and accelerated to the same kinetic energy of francium. Rb^+ currents of 30 nA can be obtained. With this diagnostic tool one can adjust some transport, neutralization and trapping parameters, even when the primary ^{18}O beam is not available.

The beam optics was designed with the aid of two computer programs. SIMION

[5]The einzel lens consists of three concentric ring electrodes: two outer rings typically held at ground potential and a center ring held at a dissimilar voltage (positive or negative with respect to the outer electrodes). In our case the central electrode operates at 3.5 kV.

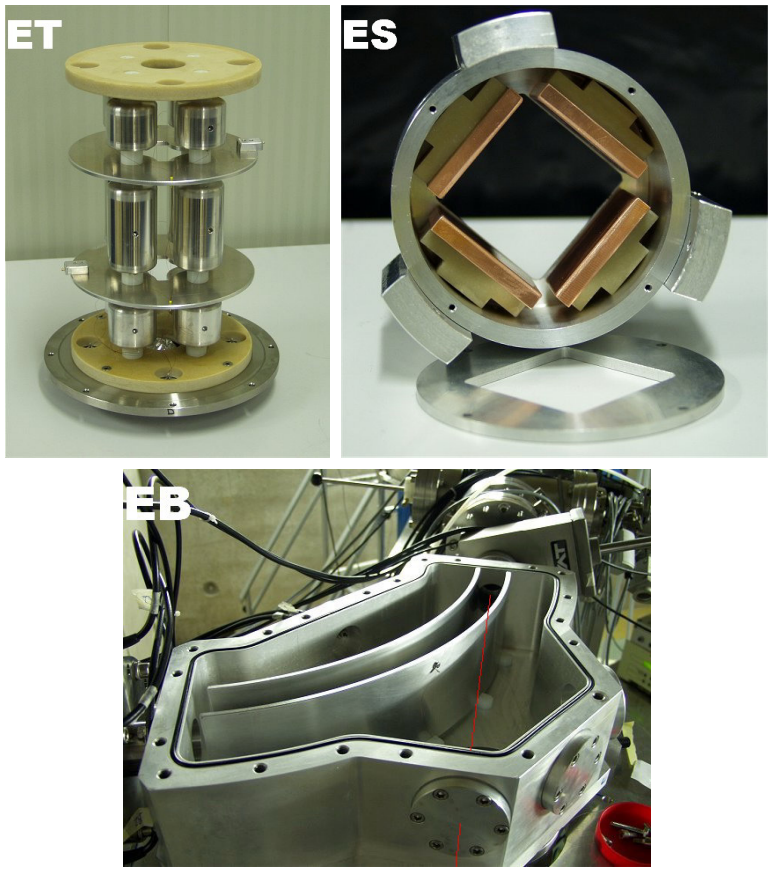

Figure 3.11: Photos of the electrostatic elements for the secondary beam line optics: quadrupole triplet (ET), steerer (ES) and curved electrode deflector (EB). The red line in EB represents the He-Ne laser beam used for the alignment of the extraction electrode.

3D [64] was used for the detailed ions trajectories, starting from the electrode shapes defined on a discrete grid: in particular, the initial beam features (emittance and Courant-Snyder parameters), after extraction from the target, were computed with this program. TRACE 3-D (within the PBO Lab environment) [69, 70] was instead used for beam envelope calculations. The result for the whole beam line is presented in fig. 3.12.

Each triplet consists of three groups of four electrodes (alternately submitted to positive and negative voltages, in the range 70-150 V), mounted on four bars of insulator material (Stesalit). Each group is separated from the next one by an aluminum disk, for better control of fringe fields. The steerer is constituted of two pairs of parallel copper plates, for orbit corrections in the horizontal and vertical planes. The bender is made of two parallel curved aluminum electrodes (actually arcs of a cylinder) operating at ± 270 V, housed in a case obtained from a single solid block of aluminum. It is possible to easily remove the electrodes and the exit flanges, in order to perform alignments by optical means, towards the target on one

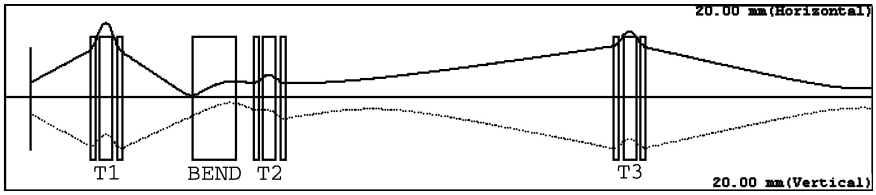

Figure 3.12: Beam profile calculated with TRACE 3-D. The horizontal and vertical scales are respectively given by the upper and lower frames (which correspond to 20 mm). T1, T2 and T3 indicate the triplets, and BEND stays for the deflector.

side, and the MOT on the other side.

The alignment procedure

Extraction electrode: optical alignment. The mechanical adjustment of the extraction electrode is performed with the help of a He-Ne laser beam (cf. fig. 3.11). We use this sophisticated method to reach a good precision, because the transmission of the electrostatic bender is very sensitive to the alignment of the extraction electrode, as expected.

A plane mirror is kept in contact with the conical electrode, in order to be perpendicular to the extraction axis of the francium ions. It reflects the incident laser light, which has been aligned on the secondary beam line axis defined by the center of the exit port and the center of the gold target (the curved electrode having been removed from its stand, in order to let the laser pass). The electrode frame is then fixed in such a way that the beam is reflected back onto itself.

Fine tuning of the voltages applied to the electrostatic elements. The voltages of the triplets, steerers and the deflector are initially chosen according to the results from the numerical simulation. However, in order to account for imperfections of the setup, it is necessary to optimize the values of the applied voltages, with a direct monitoring of the francium rate after the passage through the electrostatic elements. To this purpose, four solid-state detectors (SSBD) have been placed along the beam line, in order to count the α particles emitted from the francium isotopes. The first SSBD is the P detector of fig. 3.4, which is used to measure the production rate, when the catcher is inserted. The other three SSBD are placed according to fig. 3.1: they can be inserted in order to intercept the secondary beam, and count the α decays of the Fr embedded in them.

The voltages are individually changed in order to maximize the francium rate on each detector. The operation is iterated since there is no further improvement on the final SSBD (the one just before the MOT). This procedure, which takes more than one hour, has to be done whenever the target is changed, because of the unavoidably different alignment of the extraction electrode. From run to run (without changing the target), the optimal voltages, which are quickly checked, show an excellent reproducibility, thanks to the good rigid target frame. During one of

our shifts, an additional silicon detector was placed inside the MOT cell to check the Fr flux at the position of the neutralizer: we found that about 40% of francium extracted from the target enters the MOT cell. The beam profile has been checked by sliding the silicon detectors across the beam, and recording count rates as a function of position.

The thermionic current

We found the presence of a thermionic current, when the gold target is heated and biased at 3 kV. This current was detected on the deflector outer electrode and on the neutralizer (inside the MOT cell), which can be considered as unsuppressed Faraday cups (connected to a picoammeter). We have found that the thermionic current is a strong function of temperature and voltage; on the neutralizer it can reach 300 nA. It is not appreciably affected by the presence of the primary oxygen beam. A few months ago, thanks to the cleaning of the scattering chamber and the removal of the rubidium dispenser in the scattering chamber, it was reduced to 10 nA. The possible disturbing effects of the thermionic current on the MOT are reviewed in section 3.2.4 on page 126. For the alignment of the secondary beam line, the thermionic current can help because it is easily detected on the neutralizer. Therefore, especially for the choice of the last steerer and triplet voltages, we always take into account the value of the detected thermionic current during the alignment procedure.

3.2.3 The neutralizer

When they arrive into the MOT cell, the Fr^+ ions have to be neutralized, in order to form an atomic sample which can then be trapped in the MOT. To this purpose, we use as a neutralizer a $(11.0 \pm 0.5$ mm$) \times (9.0 \pm 0.5$ mm) rectangular yttrium foil, placed inside the cell, in the opposite side of the incoming beam. The francium beam is focused on the neutralizer: since the Y work function (table 3.2) is lower than the ionization potential of Fr (4.07 eV), francium is released in its atomic form. In the same way as for the target, the neutralizer is heated in order to enhance the diffusion of the atoms outside its surface. In practice, the two short sides of the 25 μm thick yttrium foil are attached to small 9 mm long bars (with screws), themselves connected to two rigid wires coming from a small feedthrough metal flange, which provide the heating current and also act as a holder. The bars act as electrodes, ensuring the homogeneity of the current flowing through all the surface

Element	Atomic number	Work function (eV)	Melting point (K)
Y	39	3.1	1799
Zr	40	3.8	2128

Table 3.2: Selected atoms suitable as neutralizer for francium and their properties.

of the yttrium foil: it is important to avoid cold spots where the francium could be trapped [71].

The temperature of the neutralizer should be in principle as high as possible. However, an excessive heating can damage the cell coating (described in paragraph 3.2.4), which permanently loses its good properties when submitted to temperatures above 250 °C. By keeping the neutralizer at a distance of about 1 cm from the cell surface, temperatures of the order of 850 °C are attainable without deteriorating the coating. Another effect of heating the yttrium neutralizer is the emission of impurities which can degrade the quality of the coating: this behaviour was noticed by Crane *et al.* [72], which report a damage of their SC-77 dry-film coating, caused by continuous heating of their yttrium neutralizer for several hours at temperatures of about 750 °C. They solved the problem by switching to the use of a zirconium neutralizer (cf. table 3.2), which has a significantly lower vapour pressure than yttrium at the same temperature. In our case, after tests with both materials, we decided to continue to use yttrium (in the same way as Stony Brook group), because its release efficiency was appreciably better, and after appropriate cleaning, yttrium didn't seem to damage our PDMS coating.

Measurement of the release efficiency

The release efficiency of the neutralizer can be estimated by measuring the activity of the francium ions which stay embedded into it, after a definite exposure to the Fr^+ beam, and comparing the results for different operating temperatures. In order

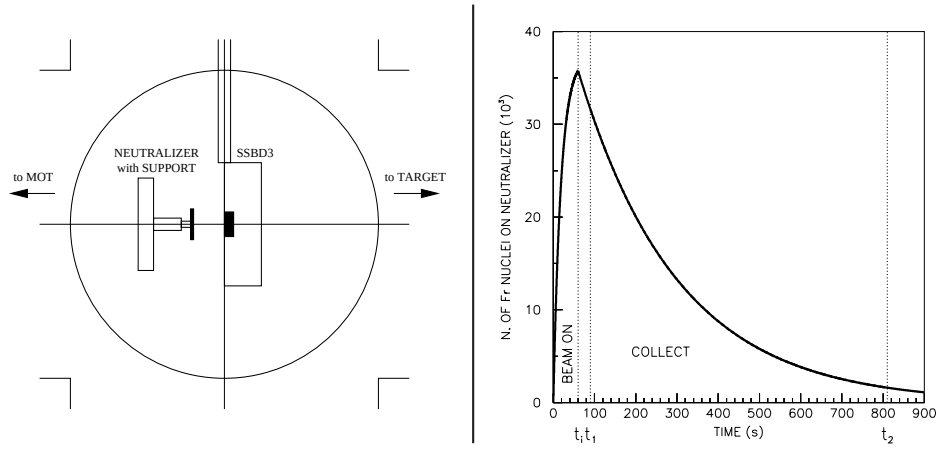

Figure 3.13: Left: scheme of the third SSBD and of the neutralizer, installed in the secondary beam line for the measurement of its release efficiency. The SSBD could be moved up and down; it could also be rotated around the vertical axis of its supporting rod. The neutralizer could be moved in and out perpendicularly to the plane of the page.
Right: number of Fr nuclei on the neutralizer, during each step of the release efficiency measurement (from simple calculations).

to obtain precise results, we decided to spend a few hours of our beam time for this measurement, with a small dedicated setup. A second neutralizer, identical to the first one, was installed in the secondary beam line, just in front of the third silicon detector (see fig. 3.13, left). The measurement was performed by the following steps (cf. fig. 3.13, right):

- Initial conditions: the SSBD is kept out of the beam, the neutralizer is at room temperature, the current of the oxygen beam is stable at 90 nA. The francium beam is controlled thanks to the voltage applied to the curved electrode deflector: when the voltage is zero, the beam is not transmitted to the neutralizer (by this way, with the primary beam always on, the temperature of the gold target is left constant).
- With the francium beam off, we measure the α background level for 60 seconds.
- The neutralizer is heated with current I. The temperature could not be directly measured, hence our measurements are referred to the measured current I instead of the temperature.
- The curved electrode is turned on for 60 s, in order to irradiate the hot neutralizer with francium.
- The curved electrode and the neutralizer heating are turned off.
- The SSBD is lowered to face the neutralizer's surface. The data acquisition starts 30 s after the beam has been stopped, and lasts 720 s.
- The SSBD is moved out.
- The α background level is measured again, for 60 s.

The secondary beam flux was estimated by intercepting the incoming francium ions with the SSBD. We measured the flux only one time, in order not to leave a large francium background on the detector. The francium flux ϕ hitting the neutralizer was of the order of $2 \cdot 10^3$ ions/s (the accuracy was poor, because the areas of the SSBD and of the neutralizer are different).

Three sets of measurements were taken: the first two sets with a fresh neutralizer, and the third one with the same neutralizer, but after exposure for one hour to the thermionic current coming from the target (0.2 μA, measured on the neutralizer as an unsuppressed Faraday cup).

From the acquired data, and after simple calculations and analysis, it was possible to deduce the escape time τ_e of francium from yttrium, as a function of the heating current I. Since, according to our definition of τ_e, the probability for a francium atom to escape from the neutralizer is $\frac{1}{\tau_e}$, the differential equation governing the accumulation of francium on the neutralizer (for $0 \leq t \leq t_i$, in fig. 3.13) is the following:

$$\frac{\mathrm{d}N}{\mathrm{d}t} = \phi - \frac{N}{\tau} - \frac{N}{\tau_e},$$

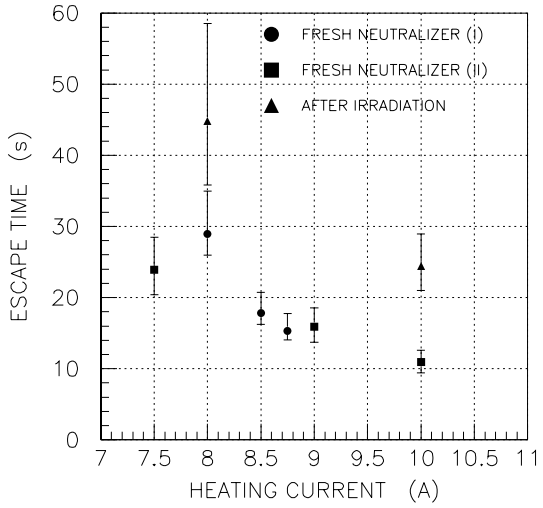

Figure 3.14: Results for the escape times τ_e, as a function of the heating current I, for the three data sets.

with τ the lifetime of the considered isotope. Therefore, the number of nuclei is given by:

$$N(t) = \phi\ \tau' \left[1 - \exp\left(-\frac{t}{\tau'}\right)\right] \qquad (0 \leq t \leq t_i), \tag{3.3}$$

where $\tau'^{-1} \equiv \tau^{-1} + \tau_e^{-1}$. Then, the number of the collected α is proportional to $N(t_i)$, as well as other factors, namely the geometrical acceptance A of the SSBD, the branching ratio f_α for the α decay, and a factor which accounts for the α emitted after the end of the acquisition step (at t_2), which are not detected. These last two factors depend on the isotope, but they don't change with the heating current I. In the end, the considered factors are important only for the estimation of the initial francium rate: they are not relevant for the comparison of the results for the different values of I. The acceptance $A = (2.99 \pm 0.27)\%$ was estimated by a Montecarlo calculation [73].

The analysis of the experimental data was performed with a general fit for the following parameters: the incoming fluxes ϕ_a, ϕ_b, ϕ_c for the three data sets, the relative flux w of ^{210}Fr with respect to ^{209}Fr[6], and the escape times τ_e for each value of I (τ_e being independent on the isotope). The χ^2 was minimized with the help of the MINUIT program [74]. The resulting escape times are presented in fig. 3.14.

The release efficiency is directly related to the escape time. In the case of an incoming steady flux ϕ_{in} (which is what we have inside the MOT cell), the number of nuclei in the neutralizer tends to a constant value, $N = \phi_{in} \cdot \tau'$ (cf. equation (3.3),

[6]The ^{208}Fr and ^{211}Fr isotopes are also present, although in a minor quantity, and cannot be distinguished from ^{209}Fr, ^{210}Fr, due to the unresolved α spectrum. Luckily, the Fr lifetimes of each couple are very similar, so that considering only the most abundantly produced ^{209}Fr and ^{210}Fr does not introduce any significative systematic error.

with $t \to \infty$). The outcoming flux is $\phi_{out} = N/\tau_e$. Therefore, the release efficiency is given by:

$$\epsilon \equiv \frac{\phi_{out}}{\phi_{in}} = \frac{N/\tau_e}{N/\tau'} = \frac{\tau}{\tau + \tau_e}.$$

In other words, the release efficiency is large when there is a small fraction of nuclei decaying inside the neutralizer. Note that it depends on the lifetime τ. Therefore, it is not the same for the different isotopes.

From the analysis, it seems clear that it takes 10-20 s for francium to leave the neutralizer, for currents above 8 A. This escape time, low with respect to Fr lifetime, corresponds to high release efficiencies: about 95% for ^{210}Fr, and 80% for ^{209} Fr. There is also evidence for a lower efficiency after the one hour exposure to the thermionic current (about 90 % for ^{210}Fr, and 70% for ^{209} Fr).

Our measurements did not allow to check if francium leaves in its atomic or ionic form. In a successive run, we decided to repeat the experiment with the application of a voltage (varying between -10 V and -100 V) to the neutralizer: if the francium that leaves the yttrium tended to be Fr^+, the applied negative voltage would prevent it to escape from the surface, and the resulting release efficiency would be found to be much lower. This doesn't occur: the collected data with the applied voltage were similar to those presented above.

3.2.4 The magneto-optical trap

The cell and the PDMS coating

We saw that the neutralizer was placed in the MOT cell in such a way that the atoms are released in the trapping region. The cell, made of Pyrex, is spherical (13 cm diameter) with six plane optical windows sealed on it (4 cm diameter) for the passage of the laser beams. The Fr^+ beam enters the cell through a 2.5 cm diameter entrance port, corresponding to the metal-glass connection which joins the cell to the beam line. A rubidium reservoir has been connected to the glass cell: a small valve allows to open or stop the flux of Rb atoms into the cell. Rb was chosen for testing the MOT, because the spectral lines used for trapping are close enough to francium trapping frequencies, in such a way that it is possible to use the same trapping laser for both elements.

The cell internal surface has been coated with a siloxane (polydimethylsiloxane, also named PDMS), in order to reduce the sticking of francium atoms on the pyrex walls. With respect to the SC-77 (or Dry-film) in use at Stony Brook [11], PDMS has the advantage to have light-induced atomic desorption (or LIAD) properties [75, 76]: after a short weak illumination (with a photographic flash, a pocket lamp or a laser), part of the francium which eventually stuck on the coating is desorbed. This is a very interesting property, for a radioactive atoms MOT, since the quantity of atoms at our disposal is very low. The LIAD effect shall allow to use the PDMS coating as a pulsed source for Fr atoms, triggered by light [77].

The vacuum

For a good operation of the trap, one of the most important parameters to keep under control is the residual gas pressure in the MOT area. Vacuum turbomolecular pumps are placed along the secondary line in order to keep a good vacuum level in the whole setup. The residual pressure in the MOT cell is usually higher than in the secondary beam line, because the cell is connected to the vacuum system only through the small entrance port. During the last year, two ionic pumps were added, the first one just after the last steerer, and the second one smaller in such a way as to place it as close as possible to the MOT (80 cm away from the cell entrance). All the secondary beam-line has been baked, in order to improve the vacuum level. The resulting pressure was below 10^{-8} mbar (whereas without the second ionic pump, it was about $4 \cdot 10^{-8}$ mbar).

The laser system

The atomic levels of the ^{210}Fr isotope involved in the trapping process are reported in fig. 3.15. The MOT has the standard configuration: six laser beams, circularly polarized, cross in the center of the cell. Two 8 cm diameter coils fed with opposite currents generate a constant gradient magnetic field near the center of the cell [78], up to 20 G/cm.

The laser light for trapping operation, on the D_2 cycling transition $7S_{1/2}, F{=}13/2 \; - \; 7P_{3/2}, F{=}15/2$, @718 nm, is provided by a tunable Ti:Sa laser (*Coherent 899-21*). The Ti:Sa crystal is pumped by a *Coherent Innova* Ar^+ laser of

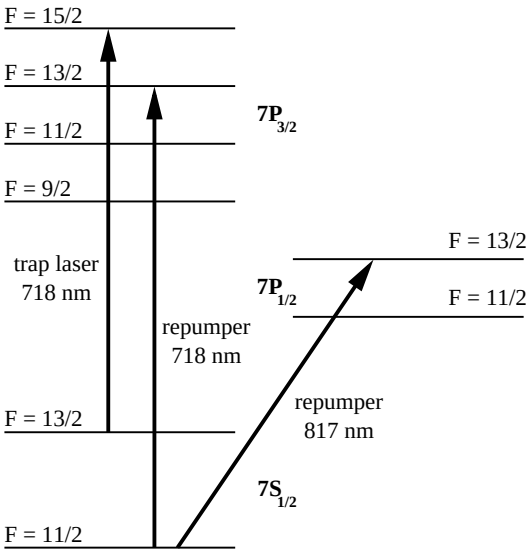

Figure 3.15: ^{210}Fr atomic levels relevant for the MOT (not to scale). The two possibilities for the repump transition are reported. In our experiment we use the 817 nm repumper. The ground state hyperfine splitting is 46.8 GHz.

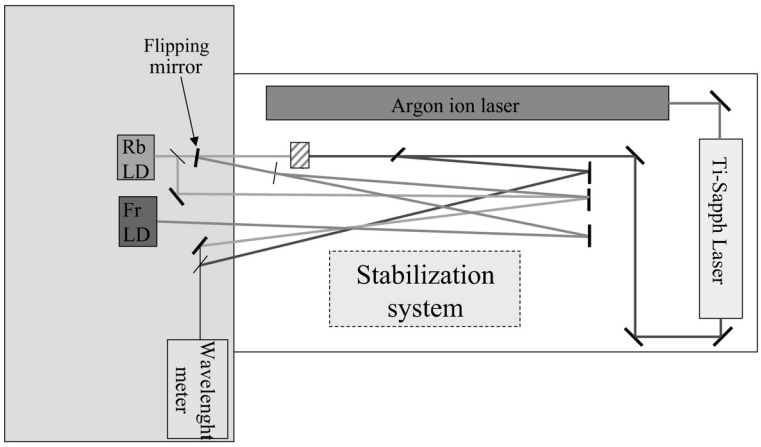

Figure 3.16: Layout of the lasers for trapping of Rb and Fr atoms.

20 W maximum power. The light power obtained @718 nm is 1.0 W. A free-running diode laser (*SDL-5421-G1*) @817 nm repumps the atoms to the cycling transition via $7S_{1/2}, F{=}11/2 \rightarrow 7P_{1/2}, F{=}13/2$. The wavelengths are measured with a wavemeter (*Burleigh WA-1500*), with a resolution of ± 0.0001 nm.

The lasers are placed on two optical tables (fig. 3.16), physically separated from the MOT region: the overlapped trapping and repumping laser beams travel for about 5 m, at 3 m height (following a periscope-like path), before reaching the cell region, where they are divided (by beam splitters) to form the six MOT beams. This layout allows an easy and full access to the MOT region. For the tests with the Rb MOT, the trapping light (@780 nm) is provided by the Ti:Sa laser, whereas the repumping light (@780 nm) comes from an additional diode laser. A very accurate description of the Rb MOT can be found in [67]. Each of the six MOT arms has a 2 inches mirror, a quarter wave plate, a telescope (magnification 10×), and a large diaphragm. The $\lambda/4$ plate is used to obtain circular polarizations @718 nm. When we switch to the Rb wavelength (780 nm), the plate still introduces a delay close to $\lambda/4$, in such a way that the obtained polarization is quasi-circular. Since rubidium is available in large quantities, the remaining ellipticity of the polarization does not prevent from trapping a large Rb sample. The diaphragm is used to limit the size of the beam below the windows diameter: indeed, the stray light produced on the edge of the windows would produce a harmful background signal (and consequent noise) on the light detectors used to observe the trapped atoms.

The short-term stabilization of the Ti-Sa laser is ensured by an external Fabry-Perot: the frequency of the light is locked on a side of the transmission fringes. The frequency can then be changed by varying the length of the external cavity, with the help of a piezo. The Fabry-Perot has proved to be very stable: the frequency drift is slow, and we seldom have to correct the frequency. However, it is better to have a long-term stabilization system, in order not to be forced to check regularly the wavelength any longer. We plan to automatically correct for long-term frequency

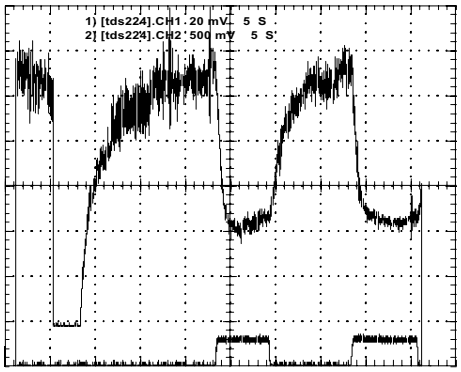

Figure 3.17: Trap signal (upper curve) and thermionic current (lower curve) vs time. The horizontal scale is 5 s per division. At $t = 5$ s, the magnetic field was turned off for 3 s in order to show the background level due to stray light.

drifts, with the help of a stabilized He-Ne laser, as of course no francium cell (hence no frequency reference at the francium D_2 or D_1 transitions) is available. In this scheme, described in detail in [67, 76, 79], the lasers are coupled to a Fabry-Perot interferometer, and the stabilization procedure works in such a way that the separation between the laser peaks transmitted by the interferometer is kept constant. The coating of the Fabry-Perot reflects the three wavelengths 633 nm (He-Ne laser), 718 nm (trapping laser) and 817 nm (repumper), in such a way that the two MOT lasers can be both stabilized with respect to the He-Ne laser frequency.

Effects of the thermionic current

We have tried to understand if and how the thermionic current (paragraph 3.2.2 on page 119) can influence the trap. The effect has been tested on the Rb MOT [80]. The gold target was heated until a 300 nA current was measured on the yttrium neutralizer. The presence of the thermionic current was controlled by turning the outer curved electrode on and off (in order to keep vacuum conditions unchanged, we chose not to use the vacuum valves on the secondary beam line). Nevertheless, we observed a small deterioration of the vacuum condition, when the beam was turned on: a gauge placed before the entrance of the MOT cell revealed an increase of the pressure from $4.9 \cdot 10^{-8}$ to $5.5 \cdot 10^{-8}$ mbar (hence a pressure variation even higher inside the MOT cell).

The fluorescence signal from trapped Rb atoms was detected by a simple photodiode. We observed the MOT signal with and without the application of the thermionic current (fig. 3.17). When we send the thermionic current into the MOT cell, we observe a decrease of about 60% of the MOT signal. Stopping the thermionic current results in recovering the original fluorescence signal of trapped atoms.

For the first test, The MOT was located in the center of the cell and therefore submitted to the direct passage of the 300 nA current. In order to understand if the deterioration of the trapping efficiency depends on direct collisions with the

thermionic beam, in a successive test we tried to move the MOT location by 2 cm, out of the passage of the ions, by varying the compensation magnetic field. The thermionic current was about 140 nA. The trap suppression did not depend on the position of the MOT, and was found to be about 30%. In conclusion, the effect of the thermionic current is roughly proportional to the beam current, and seems related to the degrading of vacuum rather than direct beam-trap collisions. The thermionic current could also affect the neutralization and trapping of Fr ions by charging the cell, and therefore distorting the electric field near the neutralizer.

In the last months, we managed to reduce the thermionic current to 10 nA (paragraph 3.2.2), so as to highly reduce its incidence on the MOT quality. In order to eliminate completely the thermionic current, we plan to install a velocity selector (Wien filter) on the secondary beam line, which will prevent the transmission of elements with a mass different from francium ions.

The detection system

The detection of the Rb MOT is relatively easy: a CCD camera is used to monitor the shape and the position of the cold atom cloud. In addition to the CCD camera, a photodiode is used to monitor the fluorescence coming from the trapped atoms. As seen in fig. 3.17, the background light is low with respect to the MOT signal.

The case of the francium is trap is different, since the number of trapped atoms is extremely small: for our first trapping tests, we don't expect to reach better conditions than the first version of the Stony Brook MOT, which contained about 1000 atoms [11]. Before reaching optimal conditions for our trap, the spatial selectivity provided by CCD cameras is not sufficient to distinguish the low trap signal from the background light. The best way to detect the Fr MOT is to use a sensitive photodetector, and separate the signals due to the trapped atoms from the unwanted stray light with lock-in techniques: a parameter on which the trap fluorescence depends is modulated, and the part of the signals synchronous with the applied modulation corresponds to the searched signal.

Since it was not obvious a priori to know which kind of modulation would lead to the highest signal to noise ratio, we tried to modulate different parameters, and checked the corresponding noise magnitudes. The validity of the different methods was checked on the Rb MOT, in order to determine the most favourable conditions (frequency and amplitude of the modulations).

Modulation of the trapping laser intensity. The simplest scheme for lock-in detection is usually to modulate the laser beam which is at the origin of the searched effect, with a chopper. In our case, the modulation of the trapping beam resulted in a background, due to the unavoidable modulation of the stray light scattered from the MOT cell and entering the photodiode detector. The scattered light being much higher than the expected MOT fluorescence, the background signals were crippling for the observation of the MOT.

Modulation of the repumper frequency. Another typical lock-in detection scheme is to modulate the frequency of the laser: this is more efficient than the previous method for the rejection of stray light, since the fluorescence from an atom depends on the light frequency, whereas the scattered light does not.

We decided to modulate the frequency of the repumping laser, rather than the Ti:Sa laser, because it was technically easier: it was sufficient to modulate the diode laser current. However, this solution was not ideal, because with this method the frequency modulation was accompanied by a small intensity modulation. Moreover, the frequency modulation lock-in detection gives a dispersive output (roughly, the first derivative of the line shape), which is less easy to detect: when the repumping laser is centered on the maximum fluorescence, the output signal is zero. The tests on rubidium atoms also showed that the modulation of the repumping laser frequency results in a loss of the number of trapped atoms (of a factor 3 or 4).

Modulation of the magnetic field. We then found a much more efficient lock-in scheme: we modulated the current of an additional MOT coil, at a frequency of the order of 160 Hz, placed in such a way as to modulate the offset of the magnetic field. There are two possible effects:

- the atoms which stay in their original position are subject to a variation of the magnetic field, hence a variation of their line frequencies by Zeeman effect: the resulting signal is similar to the one obtained with the previous method (dispersive);
- the atoms move following the MOT: we obtain a modulation of the cold sample position, hence a lock-in signal which is maximum when the fluorescence from the MOT is maximum.

The tests on Rb showed that the second effect is preponderant. We even found an increase of the Rb fluorescence (by a factor 2) with respect to the case in which there is no modulation, explained by the larger collection area swept by the MOT when the zero magnetic field region varies.

MOT detection

The search for francium trapping transitions was not trivial at all, since we had to deal with two laser frequencies (repumper and trapping laser) and very small signals. The laser frequencies were measured by Stony-Brook researchers; however, we could not be sure that the wavemeter they used was calibrated in the same way as our wavemeter, hence when we did not see any signal, we had to scan the frequency of the two lasers around the nominal values, in order to be sure to get the right frequencies. For the first measurement runs, the vacuum conditions did not allow to trap francium at all. After a few improvements, with the last lock-in detection scheme and acceptable residual pressure in the cell, the francium MOT trap was seen several times (fig. 3.18). The frequency width of the obtained curve,

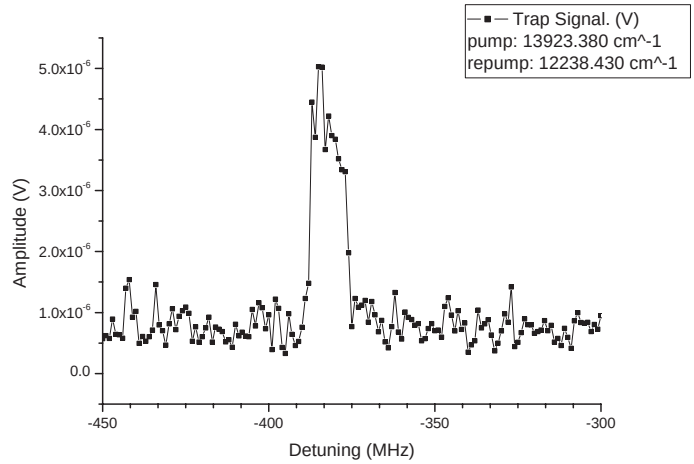

Figure 3.18: Fluorescence signal from the francium trap.

which corresponds to the expected value, confirms this is a trap signal. However, the fluorescence intensity is much lower than expected (by a factor 10 to 100, according to the different runs). The cause could be the thermionic current (since its reduction to 10 nA, it was not possible to test again the francium MOT). Another possibility which we still have to check is that the PDMS coating might adsorb Fr atoms more than Rb. We therefore plan to use a Dry-film coated cell, which has proved to be well suited for francium trapping in the Stony-Brook experiment, for comparison with PDMS.

3.2.5 Conclusion

We have presented the Francium production and trapping setup. During the past three years with 44 beam-time days, after a few initial accidents (target destroyed by melting for example), we managed to improve the experimental conditions and observe the francium MOT [81]. The MOT setup could not yet be optimized on francium atoms, because the signal was too low, and small variations of the experimental conditions resulted in losing the trap. One of the most fluctuating parameter was the intensity of the oxygen primary beam. We have learned to be very attentive to this parameter: at high intensity, a sudden increase in the oxygen current can melt the target. A feedback system has been built to shut the beam down if the intensity reaches a certain threshold, and will be tested in the next runs. Among the last improvements, we can cite a better vacuum in the MOT area, a lower thermionic current, a better definition of the neutralizer best operating conditions. For the next runs, the test with the Dry-film coated cell will allow to understand if the use of PDMS limited the trapping efficiency of our system. The implementation of the Wien filter will definitely solve the problem of the thermionic current.

Combining all these improvements, we hope to reach the conditions which will allow to obtain a stable francium trap and optimize it.

Conclusion

The work carried out in this thesis allowed to obtain important results for two spectroscopy experiments on cesium and francium, both aiming at a precise measurement of the parity violation in these atoms.

The specificity of the cesium experiment in Paris is the detection method, different with respect to all the previous PV setups: once the atoms have been excited on the highly forbidden transition $6S$-$7S$, a probe laser induces stimulated emission on the $7S$-$6P$ allowed transition. The PV observable which corresponds to an anisotropy of the excited $7S$ state is then deduced from the polarimetric analysis of the stimulated emitted photons: all the excited atoms participate to the PV detection. Precisely, the measured PV quantity is a calibrated tilt of the probe polarization detected as a PV linear dichroism (γ_1) which reveals a tilt of the alignment axes in the $7S$ excited state out of the symmetry planes of the experiment.

Among the interesting properties inherent to our setup, let us remind the line-shape independent calibration of the PV effect and the amplification of the asymmetry with the increase of the longitudinal applied electric field. The most specific signature used to discriminate the parity violation from the polarimetric experimental defects is the reversal of the electric field, which produces the change in sign of the PV tilt. The many other parameter reversals provide important control signals: we saw for example how important the analysis of the signal anisotropies is for the test of the cylindrical symmetry and for the evaluation of the systematic effects which break this symmetry.

At the beginning of the thesis work in Paris (January 2002), the cesium experiment, started in 1991, was almost ready for its first reliable PV measurements. The only remaining problem was connected to the presence of a photoinduced electronic flow in the used sapphire vapour cell. The tests on new grooved alumina cells showed that the problem could be overcome, thanks to the strong reduction of electron multiplication on the cell walls. Therefore, it was possible to undertake the preliminary PV measurements presented in the thesis.

These measurements allowed to reach a statistical precision of 8.4% and to test all the features of the experiment at this accuracy level, hence validating the detection by stimulated emission method.

Thanks to the work provided during the preliminary PV measurement and in the following months, it was possible to envisage a 1% accurate measurement. The efforts initiated in the last months of the candidate work in Paris (until April 2003)

with the view of improving the signal to noise ratio were actively pursued by the group afterwards. They have permitted to achieve a gain on the signal to noise ratio by a factor of 3.3 with respect to the preliminary measurement. Therefore, we can expect that the Paris group will manage to reach the 1% precision within the next year.

Whereas the idea to measure parity violation in cesium for a test of the Standard Model dates back to 1974, the possibility to detect parity violation in francium has been considered only in these last years. Indeed only the advent of efficient trapping and cooling techniques for atoms, together with the production of francium isotopes at an accelerator facility, could allow to reach a significant number of radioactive francium atoms for such a delicate measurement. If we combine the results for the optical trapping of alkalis published in these last years with the neutral francium production and collection efficiency into a MOT (performed in Stony Brook), it seems it would be possible to reach a significant signal to noise ratio SNR for a PV measurement, according to the scheme suggested in [46]. If the progress in these two research fields continue with the same rate encountered these last years, we can reasonably hope to obtain the conditions for a relevant PV measurement on francium. One of the advantages of using francium would be the possibility to test the PV variation with the atomic mass of several isotopes.

We reviewed then the progress made by the francium trapping experiment at the INFN national laboratories in Legnaro. At the beginning of the thesis, only the primary beam line for the francium production and a first prototype for the target were present. Since then, with the implementation of the secondary beam line and the many tests for the production of francium ions, we managed to bring into the MOT cell a francium flux comparable with the one obtained in Stony Brook. The better understanding of the important experimental features for the francium production and electrostatic transport (target preparation and temperature, critical alignment of the extraction electrode) allowed to reach a good reliability for this part of the experiment. The last runs in Legnaro were dedicated to the neutralization and trapping of francium atoms. The first tries allowed to test the efficiency of the neutralization process: for these runs, the residual pressure inside the MOT cell was not low enough to allow francium trapping. Thanks to additional ionic pumps, we managed to reach the vacuum condition necessary for the observation of the MOT. Nevertheless the MOT signals were found to be lower than expected, thus making the detection of the trapped atoms difficult. The problem could come from the use of the PDMS coating for the MOT cell internal surface, which is the only substantial difference between our setup and the Stony Brook experiment (Dry-film coating). Future tests will allow to compare MOT signals with the two kinds of coatings. Thanks to the last improvements of the setup, we then hope to reach MOT signals large enough to allow a direct optimization of the francium MOT (magnetic gradient etc.). The next step will consist in the implementation of techniques for improving the collection of francium atoms into the MOT: desorption of francium from the PDMS coating with the LIAD effect and use of a “white light” laser [82] for a higher velocity capture limit.

It was very instructive for me to have the opportunity to work on two experiments with very similar goals, even being at different stages: with cesium it was possible to achieve a first PV measurement with detection by stimulated emission, whereas with the young francium experiment we managed to begin to implement a cold sample, which will be the starting point for future measurements on the $7S$-$8S$ transition.

Appendix A

Important quantities for parity violation experiments in cesium and francium

In this appendix, we review some atomic physical quantities (which are deduced from theory or from experiment) which play an important part in parity violation. We report numerical values for cesium and francium atoms.

A.1 The case of cesium atoms

A.1.1 M_1^{hf} given by theory

We already saw in paragraph 1.3.1 that the magnetic dipole amplitude M_1' of the $6S(F) \rightarrow 7S(F')$ transition depends on the considered hyperfine levels F and F':

$$M_1' = M_1 + M_1^{hf}(F' - F),$$

where the M_1^{hf} term is the transition amplitude induced by the hyperfine interaction.

It turns out that atomic semi-empirical calculations for the determination of M_1^{hf} are very reliable: indeed, this quantity is known with a very high precision (2.5‰) for cesium, since 1988 [83, 40]. Thanks to the accuracy of the result, M_1^{hf} is currently used as a valid reference for the calibration of several experiments, among them the measurement of the vector polarizability β (cf. section A.1.3) and the measurement of M_1. From the semi-empirical calculations of ref. [40],

$$\begin{aligned} M_1^{hf} &= (-0.8094 \pm 0.0020) \cdot 10^{-5} \left|\frac{\mu_B}{c}\right| \\ &(= -151.86 \pm 0.38 \quad \frac{\mathrm{V}}{\mathrm{cm}}\, a_0^3), \end{aligned}$$

with μ_B the Bohr magneton and a_0 the Bohr radius.

Another precise evaluation has been performed in the 2000 year, by V.A. Dzuba and V.V. Flambaum [84], which gives:

$$\boxed{M_1^{hf} = (-0.8074 \pm 0.0008) \cdot 10^{-5} \ \left|\frac{\mu_B}{c}\right|}$$
$$(= -151.49 \pm 0.15 \quad \frac{\mathrm{V}}{\mathrm{cm}} \ a_0^3).$$

A.1.2 M_1: experimental measurement of $\frac{M_1^{hf}}{M_1}$

The last measurement of M_1 has been performed by C.E. Wieman's group in Boulder [18, 85]:

$$\frac{M_1^{hf}}{M_1} = 0.1906 \pm 0.0003. \tag{A.1}$$

From the value of M_1^{hf} given above [84], we deduce that

$$\boxed{M_1 = (-4.236 \pm 0.008) \cdot 10^{-5} \ \left|\frac{\mu_B}{c}\right|}$$

A.1.3 The vector polarizability β

Measurement of $\frac{M_1^{hf}}{\beta}$

One of the most recent measurements of the vector polarizability of the $6S \rightarrow 7S$ transition in cesium was published by C.E. Wieman's group, in the same work as the measurement of M_1 [18, 85]. We have

$$\frac{M_1^{hf}}{\beta} = -5.6195 \pm 0.0091 \text{ V/cm},$$

from which the value of β was deduced to be

$$\beta \ = \ (\ 27.024 \pm 0.043|_{expt} \pm 0.067|_{theor} \ ) \cdot \ a_0^3,$$

thanks to the M_1^{hf} value given in ref. [40].
If we use the slightly more precise value given in ref. [84], we obtain:

$$\beta \ = \ (\ 26.957 \pm 0.043|_{expt} \pm 0.027|_{theor} \ ) \cdot \ a_0^3 \tag{A.2}$$
$$= \ \boxed{(\ 26.957 \pm 0.051 \ ) \cdot \ a_0^3} \tag{A.3}$$

Note that in [18], Wieman's group uses the precise measurement of β itself as a calibration for the determination of the parity violating amplitude $\Im m(E_1^{PV})$, exploiting the previously published measurement of $(\Im m(E_1^{PV})/\beta)$ [41].

Measurement of α and $\frac{\alpha}{\beta}$

Another way to deduce β from the experiment has been used by A.A. Vasilyev *et al.* [86]. From the transition rates of the $6S \rightarrow 7P$ transition they measured, and with the help of semi-empirical calculations, they found the scalar polarizability of the $6S \rightarrow 7S$ transition α. Then, they deduced β from the ratio $\frac{\alpha}{\beta}$ measured by D. Cho and Wieman's group [87]:

$$\alpha = (-269.7 \pm 1.1\ ) \cdot a_0^3 \tag{A.4}$$

$$\frac{\alpha}{\beta} = -9.905 \pm 0.011 \tag{A.5}$$

$$\beta = (\ 27.22 \pm 0.11\ ) \cdot a_0^3 \tag{A.6}$$

This value of β is less precise than the previous one, but the two results differ by $(0.98 \pm 0.45)\%$, i.e. 2.2 standard deviations. These different values lead to different calibrations for the parity violation measurement, hence slightly different results for the weak charge Q_W (cf. paragraph A.1.6).

A.1.4 $\Im m(E_1^{PV})$

From the measurement [41]

$$\frac{\Im m(E_1^{PV})}{\beta} = -1.5935 \pm 0.0056 \text{ mV/cm}, \tag{A.7}$$

and the calibration $\beta = 26.96(5)a_0^3$ (equation (A.3)), we have:

$$\boxed{\Im m(E_1^{PV}) = (-8.354 \pm 0.033) \cdot 10^{-12}\ e\ a_0}$$

($\frac{e}{a_0^2} \simeq 5.1422 \cdot 10^{22}$ mV/cm).

A.1.5 k_{PV} from atomic calculations

The parity violation amplitude $\Im m(E_1^{PV})$ can be written in the form [84]

$$\Im m(E_1^{PV}) = k_{PV}\ \frac{Q_W}{N}, \tag{A.8}$$

where N is the number of neutrons (78 for ^{133}Cs), Q_W is the weak nuclear charge and k_{PV} is the electron matrix element of the electric dipole transition induced by the weak interaction between the $6S_{1/2}$ and $7S_{1/2}$ states of the cesium atom. Once we experimentally find how much is $\Im m(E_1^{PV})$, we still have to calculate k_{PV} in order to evaluate Q_W and confront it to the Standard Model prediction.

The precise numerical evaluation of k_{PV} is not trivial at all. In ref. [18], together with the measurement of β, S.C. Bennett and C.E. Wieman present a comparison of measured quantities, such as polarizabilities, dipole amplitudes and hyperfine

constants, with the theoretical predictions in ref. [88, 89] and some other papers from the same authors. Considering that these measured quantities show a better agreement with the calculations than the previous measurements did, they decide to take the average of the two values of k_{PV} of ref. [88, 89], with a smaller estimation of the error, $4 \cdot 10^{-3}$ instead of the initial 1%:

$$k_{PV}^{(1999)} = 0.9065(36) \cdot 10^{-11}\ e\ a_0.$$

This led to a Q_W which was 2.5 σ higher than the Standard Model Prediction.

Therefore, this apparent discrepancy motivated theoretical physicists to refine their calculations and check how accurate k_{PV} was. For example, Dzuba *et al.* [90] came back to their previous calculations [88], and with the help of improved theoretical methods, they managed to decrease the theoretical uncertainty on k_{PV} to 0.5% :

$$k_{PV}^{(0)} = 0.908(1 \pm 0.5\%) \cdot 10^{-11}\ e\ a_0.$$

Taking into account the Breit interaction and the neutron-distribution correction, they reached the following value:

$$k_{PV}^{(B,N)} = 0.901(1 \pm 0.5\%) \cdot 10^{-11}\ e\ a_0.$$

Then, the QED radiative corrections (vacuum polarization and self-energy) still had to be considered [19], which led in the 2003 year to:

$$\boxed{k_{PV} = 0.896(1 \pm 0.5\%) \cdot 10^{-11}\ e\ a_0} \tag{A.9}$$

This result is confirmed by the calculations of other groups (e.g. see [91]).

A.1.6 The weak charge Q_W

In their paper [88, 19], Flambaum *et al.* assume the value (A.9) for k_{PV}, and a value intermediate between (A.3) and (A.6) for β, i.e. $\beta = 26.99(5)\ a_0^3$. Then, using the $\frac{\Im m(E_1^{PV})}{\beta}$ measurement (A.7) and the equation (A.8), they deduce the following value for Q_W:

$$\boxed{\boldsymbol{Q_W = -72.84 \pm 0.29|_{expt} \pm 0.36|_{theor}}}$$

which is consistent with the Standard Model Prediction [92],

$$\boldsymbol{Q_W^{S.M.} = -73.10\ \pm\ 0.03,}$$

at 0.5 standard deviation.

Note that if we use $\beta = 26.96(5)\ a_0^3$ (cf. eq. (A.3)), we obtain

$$Q_W = -72.75 \pm 0.29|_{expt} \pm 0.36|_{theor},$$

which is 0.7 σ higher than $Q_W^{S.M.}$.

The use of $\beta = 27.22(11)\ a_0^3$ would lead to

$$Q_W = -73.46 \pm 0.39|_{expt} \pm 0.37|_{theor},$$

0.7 σ smaller than $Q_W^{S.M.}$. In both cases, the consistency with the Standard Model is good.

A.1.7 The electric quadrupole amplitude E_2

The electric quadrupole amplitude E_2 for the $6S \rightarrow 7S$ transition is much smaller than the other ones (presented in paragraph 1.3.1), but it can bring small corrections to some kind of measurements. For example, for the calibration of the longitudinal electric field (cf. paragraph 2.3.5), we have to deal with a correction factor $(1 + \frac{3}{2}\epsilon)$, with $\epsilon \equiv E_2/4M_1$ [40].

S.C. Bennett and C.E. Wieman [18, 85] evaluated the ratio $\frac{E_2}{M_1^{hf}}$ to be:

$$\frac{E_2}{M_1^{hf}} = (53 \pm 3) \cdot 10^{-3}.$$

From equation (A.1), it follows that

$$\frac{E_2}{M_1} = (1.010 \pm 0.057) \cdot 10^{-2}.$$

Therefore, the correction is given by:

$$\frac{3}{2}\,\epsilon \;=\; (3.79 \pm 0.21)‰$$

A.2 The case of francium atoms

Of course, since the forbidden $7S$-$8S$ transition in francium has not been observed yet, there is no experimental data of the interesting quantities for a parity violation experiment. Nevertheless, theoretical calculations are available, for M_1, α, β and of course $\Im m(E_1^{PV})$, which are necessary in order to define what can be the better scheme for a experiment on the $7S$-$8S$ francium transition, and estimate the signal to noise ratio. The future measurements of these quantities will allow to test the accuracy of the theoretical models used for the francium atomic structure.

A.2.1 The magnetic dipole amplitude M_1

M_1 was computed for francium (and several other alkalis) by I.M. Savukov *et al.* [93]. They find

$$\boxed{M_1 = -46 \cdot 10^{-5} \left|\frac{\mu_B}{c}\right|},$$

with a 16% quoted accuracy, corresponding to the difference between the experiment and their $M1$ theoretical value for cesium.

A.2.2 The scalar and vector polarizabilities α and β

M.S. Safronova *et al.* deduced their most precise values of α and β from semiempirical calculations [94]:

$$\boxed{\begin{array}{c}\alpha = (-375.3 \pm 3.6\ ) \cdot\ a_0^3 \\ \beta = (\quad 74.3 \pm 0.7\ ) \cdot\ a_0^3\end{array}}$$

A.2.3 $\Im m(E_1^{PV})$

The expected value of $\Im m(E_1^{PV})$ is deduced from the Standard Model prediction of the weak charge Q_W and the atomic structure factor k_{PV} (cf. equation (A.8)).

Two theoretical estimations of k_{PV} for francium have been performed: according to V.A. Dzuba *et al.* [12],

$$k_{PV}(^{223}\mathrm{Fr}) = 1.59\ (1\pm \sim 1\%) \cdot 10^{-10}\ e\ a_0,$$

whereas the value from M.S. Safronova *et al.* is slightly different (2.1σ) [13]:

$$k_{PV}(^{223}\mathrm{Fr}) = (1.541 \pm 0.017) \cdot 10^{-10}\ e\ a_0.$$

Safronova *et al.* also estimated k_{PV} for the ^{210}Fr isotope:

$$k_{PV}(^{210}\mathrm{Fr}) = (1.402 \pm 0.015) \cdot 10^{-10}\ e\ a_0.$$

From the values of the weak charge Q_W predicted by the Standard Model,

$$Q_W(^{223}\mathrm{Fr}) = -129$$
$$Q_W(^{210}\mathrm{Fr}) = -116 \quad \text{(at the tree level, cf. equation (1.1))},$$

we deduce that

$$\begin{array}{ll} \Im m(E_1^{PV}) \simeq -1.48(3) \cdot 10^{-10}\ e\ a_0 & \text{for } ^{223}\mathrm{Fr}, \\ \Im m(E_1^{PV}) \simeq -1.33(2) \cdot 10^{-10}\ e\ a_0 & \text{for } ^{210}\mathrm{Fr}. \end{array}$$

A.3 Summary table

In the following table the M_1, α, β and $\Im m(E_1^{PV})$ quantities are summarized for the $6S$-$7S$ cesium transition and the $7S$-$8S$ francium transition[1].

	Cesium	Francium
M_1	$-4.236(8) \cdot 10^{-5}\ \lvert\mu_B/c\rvert$	$-46\ (1 \pm 16\%) \cdot 10^{-5}\ \lvert\mu_B/c\rvert$
α	$-269.7(1.1) \cdot a_0^3$	$-375.3(3.6) \cdot a_0^3$
β	$26.957(51) \cdot a_0^3$	$74.3(7) \cdot a_0^3$
$\Im m(E_1^{PV})$	$-8.354(33) \cdot 10^{-12}\ e\ a_0$	$-1.48(3) \cdot 10^{-10}\ e\ a_0$ (^{223}Fr) $-1.33(2) \cdot 10^{-10}\ e\ a_0$ (^{210}Fr)

[1] In order to compare the presented quantities, the following relations can be useful: $1\ a_0^3\mathrm{V/cm} \simeq 1.03 \cdot 10^{-18}\ e$ cm and $1\ \mu_B \simeq 1.93 \cdot 10^{-11}\ e$ cm.

Acknowledgements

I wish to thank all the people who made possible this "adventure" of mine: three years of research in what I consider a most fascinating and involving field of modern physics. Since my first years of graduate studies in Pisa University, when I heard about parity violation I was captivated by this topic.

First of all, I am extremely grateful to my advisors. Prof. Paolo Minguzzi gave me the possibility of working in this field by initiating the collaboration with the Legnaro and Paris groups. I want to thank him for his helpfulness, his broad-mindedness and his trust in my work: his human and professional qualities were of fundamental help for my whole thesis. Prof. Philippe Jacquier helped me for all the French part of my Ph D. I thank him for his support in all the aspects of my stay in Paris: the help for the bureaucratic aspects of the 'cotutelle' (it was not obvious to set up from scratch this program between the French and Italian Universities and I believe it would have been much more difficult without Philippe's help and enthusiasm), the precious scientific advice, and also his sympathy and friendship.

In the Paris group, I would like to express my sincere gratitude to Prof. Marie-Anne Bouchiat who welcomed me in her research team. I admire her scientific competence, in particular her ability to confront theoretical and experimental aspects in order to improve both of them, the accuracy and rigour of her work and her talent in explaining "easily" even the most difficult facets of atomic parity violation. Dr. Jocelyne Guéna helped me and guided me in all the measurements performed on cesium. Almost all I have learned about this topic comes from my interaction with Jocelyne, who had the patience of explaining many aspects of the cesium setup to me, and made me able to "drive" PV measurements (several weeks of efforts being necessary due to the complexity of the setup) and to master the data analysis. I want to thank her and also to tell her my admiration about all the passion she gives to her work. I am grateful to Dr. Michel Lintz, for his valuable help and the meticulousness he tried to transmit to me, so useful for a high precision experiment. I also want to thank all the technical staff of the Laboratoire Kastler Brossel: I cannot mention all of them, but I would like to give a special thank to Lionel Pérennes, our electronic technician, for his interest and for helping us so many times.

In the Legnaro collaboration, I wish to thank Prof. Luigi Moi and Prof. Roberto Calabrese who allowed me to participate in the francium experiment from its early

stage, at the beginning of my thesis. I had the luck of working with Dr. Stefano Veronesi, who had the patience of explaining each part of the experiment to me. In particular he taught me all the important aspects of the francium production and transport (target and secondary beam line). Thank you also to Prof. Sergei Atutov, who takes care of the laser part of the experiment: even if in principle I was less involved in this section (it was not possible to do everything...), he taught me how to deal with the lasers and how to align the MOT. I also could directly participate in the optimization of the lock-in schemes on the rubidium MOT, and of course in the search of the francium MOT. The francium part is the result of a large collective work: I also have to thank Prof. Emilio Mariotti, Dr. Alessia Burchianti and Alen Khanbekyan from Siena, Dr. Giulio Stancari and Dr. Luca Tomassetti from Ferrara (who taught me the α-particle data acquisition), Dr. Lorenzo Corradi and Dr. Antonio Dainelli from LNL, for their contribution and all the interesting discussions about physics and else. I realized that the collaboration with researchers from different areas (nuclear and atomic physics in the present case) is very profitable from all the points of view.

Many thanks to Prof. Alberto Di Lieto, Prof. Mauro Tonelli, Francesco Cornacchia, Stefano Bigotta, Mohamed Al-Shourbagy, Piera Masia, Alessio Pirastu, Chiara Bertini, Daniela Parisi, Renzo Grassi, Dr. Alessandra Toncelli, Ilaria Grassini, Alessandro Masetti, also for their natural good mood: it is a real pleasure to work in such an enjoyable environment. Thank you also to our secretaries Patrizia Pucci and Michela Saviozzi, and Paola Cecchi, secretary of the Physics Ph D school in Pisa.

I express my gratitude to the people from the "Servizio Editoriale Universitario", who bound this thesis document, for their professional reliability: they made several tries with me in order to obtain a very nice result.

A very special thank to Cristina Lossi and Sandrine Lemoigne, from the International Relations Office, respectively of Pisa and Paris University: they had the patience of answering all my questions, and they set up this "cotutelle".

At the end, I want to thank all my French and Italian friends who supported me in these last years (Frédéric, Maurizio and all the others...), and my family for their encouragements and their constant help.

List of Figures

References

[1] M.A. Bouchiat and C. Bouchiat. 'Parity violation induced by weak neutral currents in atomic physics. Part I'. *J. Phys. (France)*, **35** 899 (1974) - Cited at p. 1, 7, 9, 10

[2] M.A. Bouchiat and C. Bouchiat. 'Parity violation induced by weak neutral currents in atomic physics. Part II'. *J. Phys. (France)*, **36** 493 (1975) - Cited at p. 1, 7

[3] S. L. Glashow. 'Partial symmetries of weak interactions'. *Nucl. Phys.*, **22** 579 (1961) - Cited at p. 1

[4] S. Weinberg. 'A model of leptons'. *Phys. Rev. Lett.*, **19** 1264 (1967) - Cited at p. 1

[5] A. Salam. 'Weak and electromagnetic interactions'. Originally printed in *Svartholm: Elementary Particle Theory, Proceedings Of The Nobel Symposium Held 1968 At Lerum, Sweden*, Stockholm 1968, 367-377 - Cited at p. 1

[6] S. Weinberg. 'Conceptual foundations of the unified theory of weak and electromagnetic interactions'. *Rev. Mod. Phys.*, **52** 515 (1980) - Cited at p. 1, 7

[7] A. Salam. 'Gauge unification of fundamental forces'. *Rev. Mod. Phys.*, **52** 525 (1980) - Cited at p. 1, 7

[8] S.L. Glashow. 'Towards a unified theory: Threads in a tapestry'. *Rev. Mod. Phys.*, **52** 539 (1980) - Cited at p. 1, 7

[9] J. Erler and M.J. Ramsey-Musolf. 'Low energy tests of the weak interaction'. arXiv:hep-ph/0404291 - Cited at p. 1

[10] S. Liberman, J. Pinard, H.T. Duong, P. Juncar, J.-L. Vialle, P. Jacquinot, G. Huber, F. Touchard, S. Büttgenbach, A. Pesnelle, C. Thibault, and R. Klapisch. 'First evidence of an optical transition in francium atoms'. *Comptes rendus hebdomadaires des séances de l'Académie des Sciences, Série B Sciences Physiques*, **286** 253 (1978) - Cited at p. 2, 103

[11] J.E. Simsarian, A. Ghosh, G. Gwinner, L.A. Orozco, G.D. Sprouse, and P.A. Voytas. 'Magneto-optic trapping of Fr-210'. *Phys. Rev. Lett.*, **76** 3522 (1996) - Cited at p. 2, 87, 103, 104, 123, 127

[12] V.A. Dzuba, V.V. Flambaum, and O.P. Sushkov. 'Calculation of energy levels, $E1$ transition amplitudes and parity violation in francium'. *Phys. Rev. A*, **51** 3454 (1995) - Cited at p. 2, 9, 87, 140

[13] M.S. Safronova and W.R. Johnson. 'High-precision calculation of the parity-nonconserving amplitude in francium'. *Phys. Rev. A*, **62** 022112 (2000) - Cited at p. 2, 9, 87, 140

[14] M.A. Bouchiat, J. Guéna, L. Hunter, and L. Pottier. 'Observation of a parity violation in cesium'. *Phys. Lett. B*, **117B** 358 (1982) - Cited at p. 2

[15] M.A. Bouchiat, J. Guéna, L. Pottier, and L. Hunter. 'New observation of a parity violation in cesium'. *Phys. Lett. B*, **134B** 463 (1984) - Cited at p. 2

[16] M.A. Bouchiat, J. Guéna, and L. Pottier. 'Atomic parity violation measurements in the highly forbidden $6S_{1/2}$-$7S_{1/2}$ caesium transition. I. Theoretical analysis, procedure and apparatus'. *Journal de Physique*, **46** 1897 (1985) - Cited at p. 2

[17] S.L. Gilbert, M.C. Noecker, R.N. Watts, and C.E. Wieman. 'Measurement of parity nonconservation in atomic cesium'. *Phys. Rev. Lett.*, **55** 2680 (1985) - Cited at p. 2

[18] S.C. Bennett and C.E. Wieman. 'Measurement of the $6S \rightarrow 7S$ transition polarizability in atomic cesium and an improved test of the standard model'. *Phys. Rev. Lett.*, **82** 2484 (1999); **82** 4153(E) (1999); **83** 889(E) (1999) - Cited at p. 2, 136, 137, 139

[19] M. Yu Kuchiev and V.V. Flambaum. 'Radiative corrections to parity nonconservation in atoms and test of the standard model'. *J. Phys. B: At. Mol. Opt. Phys.*, **36** R191 (2003) - Cited at p. 2, 138

[20] M.A. Bouchiat and C. Bouchiat. 'Parity violation in atoms'. *Rep. Prog. Phys.*, **60** 1351 (1997) - Cited at p. 9

[21] M. Poirier. *Contribution à la recherche d'une violation de la parité induite par les courants neutres faibles sur la transition 6S-7S du césium.* Thèse d'état, Université Paris VI (1979) - Cited at p. 11

[22] M. Lintz. *Spectroscopie à deux lasers sur un système interdit à trois niveaux : $6S_{1/2} - 7S_{1/2} - 6P_{3/2}$ dans le césium.* Ph.D. thesis, Université Paris XI (1987) - Cited at p. 11

[23] R.C. Jones. 'New calculus for the treatment of optical systems. I. Description and discussion of the calculus'. *J. Opt. Soc. Am.*, **31** 488 (1941) - Cited at p. 12

[24] J. Guéna, D. Chauvat, Ph. Jacquier, E. Jahier, M. Lintz, S. Sanguinetti, A. Wasan, M.A. Bouchiat, A.V. Papoyan, and D. Sarkisyan. 'New manifestation of atomic parity violation in cesium: a chiral optical gain induced by linearly polarized 6S-7S excitation'. *Phys. Rev. Lett.*, **90**(14) 143001 (2003) - Cited at p. 13, 69

[25] M.A. Bouchiat, J. Guéna, and L. Pottier. 'Absolute polarization measurements and natural lifetime in the $7S_{1/2}$ state of Cs'. *J. Physique Lett.*, **45** L523 (1984) - Cited at p. 14

[26] J. Guéna, D. Chauvat, Ph. Jacquier, M. Lintz, M.D. Plimmer, and M.A. Bouchiat. 'Sensitive pulsed pump-probe atomic polarimetry for parity violation measurements in caesium'. *Quantum Semiclass. Opt.*, **10** 733 (1998) - Cited at p. 14, 143

[27] E. Jahier, J. Guéna, Ph. Jacquier, M. Lintz, and M.A. Bouchiat. 'Implementation of a sapphire cell with external electrodes for laser excitation of a forbidden atomic transition in a pulsed E-field'. *Eur. Phys. J. D*, **13** 221 (2001) - Cited at p. 15, 16, 143

[28] E. Jahier. *Voies ouvertes par des cellules à césium en saphir pour des expériences de violation de parité détectée par émission stimulée.* Ph.D. thesis, Université Paris VI (2001) - Cited at p. 17, 18, 28, 34, 36, 44, 45, 46, 47, 48, 49, 50, 51, 52, 53, 54

[29] D. Chauvat. *Innovation et optimisation d'une méthode de polarimétrie pompe-sonde avec des faisceaux laser impulsionnels en vue d'une mesure précise de violation de la parité dans l'atome de césium.* Ph.D. thesis, Université Paris XI (1997) - Cited at p. 18, 25, 26, 28, 34, 35, 42, 43, 52, 73

[30] J. Guéna, E. Jahier, M. Lintz, A.V. Papoyan, S. Sanguinetti, and M.A. Bouchiat. 'Grooving an alumina surface as a mean to inhibit secondary electron emission under grazing incidence'. *App. Phys. B*, **75** 739 (2002) - Cited at p. 18

[31] M.A. Bouchiat, J. Guéna, Ph. Jacquier, and M. Lintz. 'Absolute measurements of the photoionization cross section of the $5D_{5/2}$ Cs excited state and of the photodissociation cross section of Cs_2 between 540 and 550 nm'. *Chem. Phys. Lett.*, **199** 85 (1992) - Cited at p. 19, 61

[32] A. Hrisoho, J. Guéna, Ph. Jacquier, M. Lintz, L. Pottier, and M.A. Bouchiat. 'Reaching the shot noise limit in the polarization measurement of individual nanosecond light pulses'. *Opt. Comm.*, **71** 6 (1989) - Cited at p. 20

[33] C. Bouchiat and M.A. Bouchiat. 'Amplification of electroweak left-right asymmetries in atoms by stimulated emission'. *Z. Phys. D*, **36** 105 (1996) - Cited at p. 23

[34] D. Chauvat, J. Guéna, Ph. Jacquier, M. Lintz, and M.A. Bouchiat. 'Amplification of L-R asymmetries by stimulated emission: experimental demonstration of sensitivity enhancement valuable for parity violation measurements'. *Eur. Phys. J. D*, **1** 169 (1998) - Cited at p. 23

[35] J. Guéna, D. Chauvat, Ph. Jacquier, M. Lintz, M.D. Plimmer, and M.A. Bouchiat. 'Differential-mode atomic polarimetry with pulsed lasers: High-precision zero adjustment'. *J. Opt. Soc. Am. B*, **14**(2) 271 (1997) - Cited at p. 32

[36] E. Jahier, J. Guéna, Ph. Jacquier, M. Lintz, A.V. Papoyan, and M.A. Bouchiat. 'Temperature-tunable sapphire windows for reflection loss-free operation of vapor cells'. *App. Phys. B*, **71**(4) 561 (2000) - Cited at p. 36

[37] M.A. Bouchiat, J. Guéna, and M. Lintz. 'Cylindrical symmetry discrimination of magnetoelectric optical systematic effects in a pump-probe atomic parity violation experiment'. *Eur. Phys. J. D*, **28** 331 (2004) - Cited at p. 42, 73, 74, 76

[38] M. Salehi and E.A. Flinn. 'Dependence of secondary-electron emission from amorphous materials on primary angle of incidence'. *J. Appl. Phys.*, **52** 994 (1981) - Cited at p. 45

[39] M.A. Bouchiat, J. Guéna, and L. Pottier. 'Atomic parity violation measurement in the highly forbidden $6S_{1/2}-7S_{1/2}$ caesium transition I'. *J. Physique*, **46** 1897 (1985) - Cited at p. 48

[40] M.A. Bouchiat and J. Guéna. 'The E_2 $6S-7S$ amplitude in Cesium and its importance in a precise calibration of E_1^{PV}'. *J. Phys. France*, **49** 2037 (1988) - Cited at p. 48, 135, 136, 139

[41] C.S. Wood, S.C. Bennett, D. Cho, B.P. Masterson, J.L. Roberts, C.E. Tanner, and C.E. Wieman. 'Measurement of parity nonconservation and an anapole moment in cesium'. *Science*, **275** 1759 (1997) - Cited at p. 51, 136, 137

[42] B. Bodermann, H. Knöckel, and E. Tiemann. *Basics and usage of the program IodineSpec.* Institut für Quantenoptik, Universität Hannover (2000) - Cited at p. 56

[43] D. Chauvat, J. Guéna, Ph. Jacquier, M.A. Bouchiat, M.D. Plimmer, and C.W. Goodwin. 'Magnification of a tiny polarisation rotation by a dichroic plate in balanced mode polarimetry'. *Opt. Comm.*, **138** 259 (1997) - Cited at p. 66, 67, 68, 83

[44] Z.-T. Lu, K.L. Corwin, K.R. Vogel, C.E. Wieman, T.P. Dinneen, J. Maddi, and Harvey Gould. 'Efficient collection of ^{221}Fr into a vapor cell magneto-optical trap'. *Phys. Rev. Lett.*, **79** 994 (1997) - Cited at p. 87, 103, 105

[45] M.A. Bouchiat. 'Atomic parity violation: past, present status and future perspectives'. In 'From parity violation to hadronic structure and more...', Workshop Pavi 2002, Mainz (6-8 June 2002). Ed. Franck Mass, World Scientific 2003, in press. - Cited at p. 87

[46] S. Sanguinetti, J. Guéna, M. Lintz, Ph. Jacquier, A. Wasan, and M.A. Bouchiat. 'Prospects for forbidden-transition spectroscopy and parity violation measurements using a beam of cold stable or radioactive atoms'. *Eur. Phys. J. D*, **25** 3 (2003). arXiv:physics/0101098 - Cited at p. 88, 103, 132

[47] J.D. Miller, R.A. Cline, and D.J. Heinzen. 'Far-off-resonance optical trapping of atoms'. *Phys. Rev. A*, **47** R4567 (1993) - Cited at p. 100

[48] K.L. Corwin, S.J.M. Kuppens, D. Cho, and C.E. Wieman. 'Spin-polarized atoms in a circularly polarized optical dipole trap'. *Phys. Rev. Lett.*, **83** 1311 (1999) - Cited at p. 100

[49] S. Aubin, E. Gomez, L.A. Orozco, and G.D. Sprouse. 'High efficiency magneto-optical trap for unstable isotopes'. *Rev. Sci. Instrum.*, **74** 4342 (2003) - Cited at p. 100, 103

[50] E. Biémont, P. Quinet, and V. Van Renterghem. 'Theoretical investigation of neutral francium'. *J. Phys. B*, **31** 5301 (1998) - Cited at p. 101

[51] S. Liberman, J. Pinard, H.T. Duong, P. Juncar, P. Pillet, J.-L. Vialle, P. Jacquinot, F. Touchard, S. Büttgenbach, C. Thibault, M. de Saint-Simon, R. Klapisch, A. Pesnelle, and G. Huber. 'Laser optical spectroscopy on francium D_2 resonance line'. *Phys. Rev. A*, **22** 2732 (1980) - Cited at p. 103, 105

[52] G. Gwinner, J. A. Behr, S.B. Cahn, A. Ghosh, L.A. Orozco, G.D. Sprouse, and F. Xu. 'Magneto-optic trapping of radioactive ^{79}Rb'. *Phys. Rev. Lett.*, **72** 3795 (1994) - Cited at p. 103, 104

[53] Z.-T. Lu, C.J. Bowers, S.J. Freedman, B.K. Fujikawa, J.L.Mortara, S.-Q. Shang, K.P. Coulter, and L. Young. 'Laser trapping of short-lived radioactive isotopes'. *Phys. Rev. Lett.*, **72** 3791 (1994) - Cited at p. 103

[54] L.C. Carraz, I.R. Haldorsen, H.L. Ravn, M. Skarestad, and L. Westgaard. 'Fast release of nuclear reaction products from refractory matrices'. *Nucl. Instr. and Meth.*, **148** 217 (1978) - Cited at p. 105

[55] Erich Kugler. 'The ISOLDE facility'. *Hyperfine Interactions*, **129** 23 (2000) - Cited at p. 105

[56] R.B. Firestone and V.S. Shirley, editors. *Table of Isotopes, 8th ed.* Wiley, New York (1996) - Cited at p. 106

[57] W. Reisdorf. 'Analysis of fissionability data at high excitation energies. I. The level density problem'. *Z. Phys. A*, **300** 227 (1981) - Cited at p. 106

[58] W. Reisdorf and M. Schadel. 'How well do we understand the synthesis of heavy elements by heavy-ion induced fusion ?' *Z. Phys. A*, **343** 47 (1992) - Cited at p. 106

[59] J.F. Ziegler, J.P. Biersack, and U. Littmark. *The stopping and range of ions in solids*. Pergamon Press, New York (1985). See `http://www.srim.org/` - Cited at p. 107

[60] The properties of gold are summarized in `http://www.webelements.com/webelements/elements/text/Au/index.html` - Cited at p. 108

[61] A.R. Lipski and M.R. Pearson. 'Development of thick gold targets for the production of radioactive beams of francium'. *Nucl. Instr. and Meth. in Phys. Res. A*, **480** 156 (2002) - Cited at p. 108

[62] R.N. Sagaidak, G.N. Kniajeva, I.M. Itkis, M.G. Itkis, N.A. Kondratiev, E.M. Kozulin, I.V. Pokrovsky, A.I. Svirikhin, V.M. Voskressensky, A.V. Yeremin, L. Corradi, A. Gadea, A. Latina, A.M. Stefanini, S. Szilner, M. Trotta, A.M. Vinodkumar, S. Beghini, G. Montagnoli, F. Scarlassara, D. Ackermann, F. Hanappe, N. Rowley, and L. Stuttgé. 'Fusion suppression in mass-asymmetric reactions leading to Ra compound nuclei'. *Phys. Rev. C*, **68** 014603 (2003) - Cited at p. 108

[63] S. Beghini, C. Signorini, S. Lunardi, M. Morando, G. Fortuna, A.M. Stefanini, W. Meczynski, and R. Pengo. 'An electrostatic beam separator for evaporation residue detection'. *Nucl. Instr. and Meth. in Phys. Res. A*, **239** 585 (1985) - Cited at p. 108

[64] D.A. Dahl. 'SIMION 3D Version 6.0'. In '43rd ASMS conference on mass spectrometry and allied topics', p. 717. Atlanta, Georgia (May 21-26 1995). See also `http://sisweb.com/simion/simrefer.htm` - Cited at p. 111, 117, 145

[65] E. Arnold, W. Borchers, M. Carre, H.T. Duong, P. Juncar, J. Lerme, S. Liberman, W. Neu, R. Neugart, E.W. Otten, M. Pellarin, A. Pesnelle, J. Pinard, J.L. Vialle, and K. Wendt. 'High-resolution laser spectroscopy of Fr ns and nd Rydberg levels'. *J. Phys. B*, **22** L391 (1989) - Cited at p. 111

[66] M.R. Schmorak. *Nucl. Data Sheets*, **31** 283 (1980) - Cited at p. 111

[67] L. Tomassetti. *Development of new techniques to improve the trapping efficiency of magnetooptic traps*. Ph.D. thesis, Università di Ferrara (2002) - Cited at p. 112, 113, 125, 126

[68] A.R. Lipski, L.A. Orozco, M.R. Pearson, J.E. Simsarian, G.D. Sprouse, and W.Z. Zhao. 'Gold and isotopically enriched platinium targets for the production of radioactive beams of francium'. *Nucl. Instr. and Meth. in Phys. Res. A*, **438** 217 (1999) - Cited at p. 114

[69] K.R. Crandall and D.P. Rusthoi. TRACE 3-D *Documentation*. Los Alamos National Laboratory Rep. LA-UR-97-886, third edition (1997) - Cited at p. 117

[70] G.H. Gillespie. *PBO Lab 2.0 User Manual*. Accelsoft Inc., San Diego (1999) - Cited at p. 117

[71] A.R. Lipski, M.R. Pearson, R.P. Fliller III, and G.D. Sprouse. 'Neutralizer for radioactive francium beam'. *Nucl. Instr. and Meth. in Phys. Res. A*, **521** 49 (2004) - Cited at p. 120

[72] S.G. Crane, X. Zhao, W. Taylor, and D.J. Vieira. 'Trapping an isotopic mixture of fermionic ^{84}Rb and bosonic ^{87}Rb atoms'. *Phys. Rev. A*, **62** 011402 (2000) - Cited at p. 120

[73] G. Stancari. 'Yttrium neutralizer: francium escape time and release efficiency vs heating current'. TRAPRAD Memo (2003) - Cited at p. 122

[74] F. James. MINUIT, *Function minimization and error analysis, Reference manual*. CERN Program Library Long Writeup D506 (1998) - Cited at p. 122

[75] J. Brewer, A. Burchianti, C. Marinelli, E. Mariotti, L. Moi, K. Rubahn, and H.-G. Rubahn. 'Pulsed laser desorption of alkali atoms from PDMS thin films'. *App. Surf. Science*, **228** 40 (2004) - Cited at p. 123

[76] A. Burchianti. *Light-induced atomic desorption general features and applications*. Ph.D. thesis, Univesità degli studi di Siena (2003) - Cited at p. 123, 126

[77] S.N. Atutov, R. Calabrese, V. Guidi, B. Mai, A.G. Rudavets, E. Scansani, L. Tomassetti, V. Biancalana, A. Burchianti, C. Marinelli, E. Mariotti, L. Moi, and S. Veronesi. 'Fast and efficient loading of a Rb magneto-optical trap using light-induced atomic desorption'. *Phys. Rev. A*, **67** 053401 (2003) - Cited at p. 123

[78] G. Stancari. 'Basic considerations for the choice of MOT coil geometry'. TRAPRAD Memo (2002) - Cited at p. 124

[79] A. Rossi, V. Biancalana, B. Mai, and L. Tomassetti. 'Long-term drift laser frequency stabilization using purely optical reference'. *Rev. Sci. Instr.*, **73** 2544 (2002) - Cited at p. 126

[80] S. Atutov and G. Stancari. 'Influence of the thermionic current from the target on the rubidium magneto-optical trap'. TRAPRAD Memo (2003) - Cited at p. 126

[81] S.N. Atutov, V. Biancalana, A. Burchianti, R. Calabrese, L. Corradi, A. Dainelli, V. Guidi, A. Khanbekyan, B. Mai, C. Marinelli, E. Mariotti, L. Moi, S. Sanguinetti, G. Stancari, L. Tomassetti, and S. Veronesi. 'Production and trapping of francium atoms'. To be published in *Nucl. Phys. A* - Cited at p. 129

[82] S.N. Atutov, R. Calabrese, R. Grimm, V. Guidi, I. Lauer, P. Lenisa, V. Luger, E. Mariotti, L. Moi, A. Peters, U. Schramm, and M. Stoessel. 'White-light laser cooling of a fast stored ion beam'. *Phys. Rev. Lett.*, **80** 2129 (1998) - Cited at p. 132

[83] C. Bouchiat and C.A. Piketty. 'Magnetic dipole and electric quadrupole amplitudes induced by the hyperfine interaction in the Cesium $6S$-$7S$ transition and the parity violation calibration'. *J. Phys. Paris*, **49** 1851 (1988) - Cited at p. 135

[84] V.A. Dzuba and V.V. Flambaum. 'Off-diagonal hyperfine interaction and parity nonconservation in cesium'. *Phys. Rev. A*, **62** 052101 (2000) - Cited at p. 136, 137

[85] S.C. Bennett. *High-precision measurements in atomic cesium supporting a low-energy test of the standard model.* Ph.D. thesis, University of Colorado (1998) - Cited at p. 136, 139

[86] A.A. Vasilyev, I.M. Savukov, M.S. Safronova, and H.G. Berry. 'Measurement of the $6s - 7p$ transition probabilities in atomic cesium and a revised value for the weak charge Q_W'. *Phys. Rev. A*, **66** 020101 (2002) - Cited at p. 137

[87] D. Cho, C.S. Wood, S.C. Bennett, J.L. Roberts, and C.E. Wieman. 'Precision measurement of the ratio of scalar to tensor transition polarizabilities for the cesium $6S - 7S$ transition'. *Phys. Rev. A*, **55** 1007 (1997) - Cited at p. 137

[88] V.A. Dzuba, V.V. Flambaum, and O.P. Sushkov. 'Summation of the high orders of perturbation theory for the parity nonconserving E1-amplitude of the 6s-7s transition in the caesium atom'. *Phys. Lett. A*, **141** 147 (1989) - Cited at p. 138

[89] S.A. Blundell, J. Sapirstein, and W.R. Johnson. 'High-accuracy calculation of parity nonconservation in cesium and implications for particle physics'. *Phys. Rev. D*, **45** 1602 (1992) - Cited at p. 138

[90] V.A. Dzuba, V.V. Flambaum, and J.S.M. Ginges. 'High-precision calculation of parity nonconservation in cesium and test of the standard model'. *Phys. Rev. D*, **66** 076013 (2002) - Cited at p. 138

[91] A.I. Milstein, O.P. Sushkov, and I.S. Terekhov. 'Calculations of radiative corrections to the effect of parity nonconservation in heavy atoms'. *Phys. Rev. A*, **67** 062103 (2003) - Cited at p. 138

[92] K. Hagiwara *et al.* 'Review of Particle Physics'. *Phys. Rev. D*, **66** 010001 (2002). `http://pdg.lbl.gov` - Cited at p. 138

[93] I.M. Savukov, A. Derevianko, H.G. Berry, and W.R. Johnson. 'Large contributions of negative-energy states to forbidden magnetic-dipole transition amplitudes in alkali-metal atoms'. *Phys. Rev. Lett.*, **83** 2914 (1999) - Cited at p. 139

[94] M.S. Safronova, W.R. Johnson, and A. Derevianko. 'Relativistic many-body calculations of energy levels, hyperfine constants, electric-dipole matrix elements, and static polarizabilities for alkali-metal atoms'. *Phys. Rev. A*, **60** 4476 (1999) - Cited at p. 139

glass, and had jumped lightly down into the Looking-glass room. The very first thing she did was to look whether there was a fire in the

From *Through the Looking-Glass and What Alice Found There*, by Lewis Carroll (1872): illustration by John Tenniel.